Investigations in MALDI-MSI using a high repetition rate laser

by

Rory Thomas Steven

A thesis submitted to the University of Birmingham for the degree of

DOCTOR OF PHILOSOPHY

UNIVERSITY OF BIRMINGHAM

Physical Sciences of Imaging in the Biomedical Sciences (PSIBS) Doctoral Training Centre

School Of Chemistry

University of Birmingham

September 2014

Abstract

Within these studies the properties of a high repetition rate (≤ 25,000 Hz) Nd:YVO_4 laser were investigated with a view to improving the throughput and quality of information obtained from MALDI MS data collected in continuous raster sampling mode.

Initially, the nature of the laser beam profile was investigated and a novel fluorometric method developed for imaging these profiles. Analysis of thin film samples of α-cyano-4-hydroxycinnamic acid (CHCA) and lipid standard phophatidylcholine (PC) 34:1 were carried out. Under most conditions a lower repetition rate and slow stage raster speed were found to be optimal. However, in tissue based investigations repetition rates of 5-10 kHz and faster raster speeds were found to increase the detected ion intensity. Subsequent to this, the use of para-nitroaniline (PNA) as an effective matrix for high-repetition rate laser MALDI MSI applications was investigated and compared to CHCA. PNA was found to provide high quality MSI data, comparable to or better than that obtained with CHCA. The utility of CHCA and PNA were then investigated for the repeat analysis of single tissue sections with a view to increasing the amount of information obtained. Up to five analyses of the same tissue section were demonstrated. Repeat analysis was then applied to the acquisition of both lipid and protein data from a single tissue section using multiple matrices and tissue washing.

Declaration

I hereby declare that the work presented within this thesis is entirely my own, except where indicated. Work presented within Chapters 2, 5 and 6 have been published in the following journal articles:

Steven, R. T., Race, A. M., Bunch, J. Para-Nitroaniline is a promising matrix for MALDI-MS imaging on intermediate pressure MS systems. Journal of the American Society for Mass Spectrometry, 2013. 24(5): p. 801-804.

Steven, R. T., Bunch, J. Repeat MALDI MS imaging of a single tissue section using multiple matrices and tissue washes. Analytical and Bioanalytical Chemistry,2013. 405(14): p. 4719-4728.

Steven, R. T., Palmer, A. D., Bunch, J. (2013). Fluorometric Beam Profiling of UV MALDI Lasers. Journal of the American Society for Mass Spectrometry, 2013. 24(7): p. 1146-1152.

Acknowledgements

I would like to acknowledge and thank the following people for the support, help and guidance I have received during completion of this work:

My primary supervisor Josephine Bunch for her excellent supervision, guidance and friendship; a great debt is owed.

My secondary supervisors and mentor G. Ed Rainger, Ata Kaban and Gerrard Nash for their help and supervision; Keith Oakes (Elforlight Ltd.) for help, useful discussion and loan of a laser power meter and beam profiler; the other members of the Bunch Group including: Andrew Palmer, Alan Race, Rian Griffiths and Claire Carter, always helpful and kind; Steve Thomas for the supply of samples; Anna Peacock, Hector Basevi, Jamie Guggenheim and all my other colleagues within the PSIBS doctoral training centre and the School of Chemistry for making Birmingham University an enjoyable place to work; the EPSRC for funding my studentship and to the University of Birmingham. In addition, I would like to thank Karl Collins for his advice, kindness and friendship.

Finally, thank you to my family: Miranda Mitchley, Robert Steven, Duncan Steven, Louis Steven, Mari Steven and Mia Steven. Without their love and support I wouldn't have begun this PhD, let alone finished it.

Table of Contents

List of Figures

List of Tables

List of Definitions and Abbreviations

μ	micro: 10^{-6}
CCD	charge couple device
CH_3OH	Methanol
CHCA	α-cyano-4-hydroxycinnamic acid
CMOS	complementary metal oxide semiconductor
Da	Dalton: atomic mass unit (synonamous with u)
DHB	2,5-dihydroxybenzoic acid
DPSS	diode pumped solid state laser
FAB	fast atom bombardment
fps	frames per second
H	fluence
HCCA	α-cyano-4-hydroxycinnamic acid
HPLC	high performance liquid chromatography
Hz	Hertz: unit of frequency (s^{-1})
J	Joules - unit of energy
k	kilo: 10^3
M	mega: 10^6
m	milli: 10^{-3}
m	meter
m/z	mass to charge ratio
MALDI	matrix assisted laser desorption ionization
mean	geometric mean

MHz	megahertz: 10^6 Hertz
mm s^{-1}	unit of speed: 10^{-3} meters per second
MS	mass spectrometry
MS/MS	tandem mass spectrometry - typically denoting the use of multiple mass analysers to perform fragmentation of a specific ion.
MSI	mass spectrometry imaging
n	nano: 10^{-9}
N2	molecular nitrogen
NA	numerical aperture
Nd:YAG	Nd:$Y_3Al_5O_{12}$ -describes make up of lasing medium within laser: Nd - neodynimym, Y - yttrium, A - aluminium, G – Garnet.
Nd:YLF	Nd:$YLiF_4$ - describes composition of lasing medium: Nd - neodynimym, Y - yttrium, L - Lithium, F – fluoride.
Nd:YVO_4	describes make up of lasing medium within laser: Nd - neodynimym, Y - yttrium, V - vanadium, O – oxygen.
PC	phosphotidylcholine
PNA	para-nitroaniline
QqToF	quodrupole time of flight
s	second
s.d.	standard deviation
SA	Sinapinic acid
SE	standard error of the mean
TEM	transmission electron microscopy
TFA	trifluoroacetic acid
TIC	total ion cromatogram - typically denoting the sum of all ions detected within a specific time period
ToF	time-of-flight mass analyser
UK	United Kingdon

UV	ultraviolet
VIS	visible
Y	ion yield

Chapter 1

Introduction and Literature Review

1.1. A Brief Historical Introduction to Matrix Assisted Laser Desorption Ionisation Mass Spectrometry (MALDI MS)

The detection of intact labile high-molecular-weight compounds, particularly peptides and proteins, by mass spectrometry has long been a significant driver of innovation. By the mid- to late-1980s techniques such as secondary ion mass spectrometry (SIMS), fast atom bombardment mass spectrometry (FAB MS) and plasma desorption mass spectrometry (PDMS) had enabled the detection of peptide and protein ions in the kilo-Dalton mass range [1-3]. However, these techniques suffered from issues such as poor sensitivity and a large degree of fragmentation when used for the analysis of these high molecular weight compounds. At this time laser desorption ionisation mass spectrometry (LDI MS) had also shown it could provide useful information regarding bio-relevant molecules but is too aggressive in its energy deposition to allow the detection of in-tact molecular ions in the kilo-Dalton mass-to-charge range.

In 1985 Hillenkamp, Karas and co-workers were investigating the influence of wavelength on ultraviolet laser desorption of organic molecules in LDI [4]. This study included an example of the utility of a highly UV absorbing matrix to aid the desorption and

ionisation of another co-crystallised molecule. Though both analyte and matrix in this case were single amino acids, the ability of one molecule to seemingly aid the ionisation of another in a mixed sample system was shown; a key element of what we now recognise as MALDI MS.

In 1988, the Yoshida group published the first mass spectrometric data demonstrating the detection of proteins of mass as high as 34,472 Daltons [5] by what they described as laser ionisation time-of-flight mass spectrometry. Unlike typical LDI MS methods in which the laser beam is incident directly upon the sample, this technique relied upon the mixing of the sample with a suspension of fine cobalt powder in glycerol. The addition of this "ultra fine metal plus liquid matrix method" to an LDI experiment enabled the desorption and analysis of large labile molecules in MS and these achievements were jointly awarded the 2002 Nobel Prize in Chemistry. The great potential of matrix enhanced methods was thus shown.

At the same time Karas and Hillenkamp demonstrated the use of nicotinic acid for the analysis of protein molecular ions up to ~67,000 Daltons [6, 7]. The use of a conjugated ring-structure organic acid such as this would soon become one of the defining features of MALDI MS and despite the driving factors of analysing labile high-mass molecules, MALDI MS has proven to have great utility for the desorption and ionisation of a wide range of molecular classes and masses.

1.2 Ultraviolet (UV) Matrix Assisted Laser Desorption Ionisation Mass Spectrometry (MALDI MS)

1.2.1 UV MALDI Matrix Irradiation

One of the defining features of UV MALDI-MS is the use of a ‘matrix’; usually a benzene related organic acid, exhibiting peak optical absorption in the region of 280 – 380 nm [8, 9]. The function of the matrix is to absorb the energy imparted by the laser and enable the creation of gas phase ions from the molecule or molecules which are the object of study. There are a number of issues surrounding the irradiation of a MALDI-MS sample with regards to the desorption / ablation and ionisation of the matrix and analyte molecules therein and some of these variables are summarised within Table 1.1.

Table 1.1. Some Important characteristics of the laser and matrix within UV MALDI-MS.

Characteristic	Comment
Laser Wavelength (λ)	Value depends upon laser used. Typical UV MALDI lasers are N_2 gas (337 nm) or Neodymium based solid state lasers (typically employed in frequency tripled mode at $\lambda \approx 355$ nm).
Laser Pulse Repetition Rate (Hz)	Number of laser pulses fired per second. Laser model dependent. Not arbitrary as is intimately linked to the energy state lifetimes of the lasing medium and the laser construction.
Fluence (J/m^2)	Number of photons incident within a given region of the sample surface per single laser pulse. Dependent upon the laser and focussing optics employed.
Laser temporal pulse width (s)	Measure of the time period over which the photons of each individual laser pulse will arrive at a surface.
Laser Beam Profile	The spatial distribution and number of photons as incident on the sample surface.
Matrix electromagnetic absorption (molar absorptivity)	Commonly measured in solution by UV/VIS spectroscopy. However, solid phase data is more appropriate for understanding MALDI MS processes.

1.2.1.1. Electromagnetic Absorption Properties of UV MALDI Matrices

Ultraviolet MALDI-MS is the most well studied wavelength regime within the field of MALDI-MS. It has been known since the very first MALDI-MS work by Karas *et al.* that the

wavelength of the laser used would have an influence on the mass spectra obtained [4]. There have been a number of studies considering the effect of matrix electromagnetic absorption and laser wavelength [8-17].

The absorption properties of crystalline matrices show peak broadening and a red shift as compared to the solution phase spectra [17, 18]. However, these studies only provided relative rather than absolute values for the absorption coefficients, preventing a fuller understanding of the processes observed. Quantitative solid phase absorption spectra were measured by Allwood *et al.* (1996) [12, 16]. The absolute absorption coefficient values for several MALDI matrices were studied and it was concluded that a stronger absorption coefficient at the wavelength of irradiation was conducive to an improved ion yield for the protonated ion of bovine insulin. It was, however, pointed out that different matrix molecules will have other physical characteristics which complicate this picture and a strong absorption at the wavelength used is unlikely to be the sole indicator of matrix performance. In fact it was noted that "The UV absorption of the matrix alone was not a sufficient criterion for selecting a useful matrix" [10]. Interestingly it was also suggested that some of the matrices exhibited absorption from doublet structures in the solid phase which were lacking in the liquid phase.

The topic of matrix optical absorption, laser wavelength and ion yields in MALDI MS has recently been revisited to great effect by the Dreisewerd group [9, 13, 14]. Overall it was concluded that use of laser wavelengths near to the peak absorption of the matrix used was favourable but a slight shift to the longer wavelength side of this peak improved ion yields further and movement to shorter wavelengths increased fragmentation of the analyte molecule, effectively lowering the useful ion yield. The absorption spectra and ion intensity

data for each of the matrices used in one of these studies are reproduced in Figures 1.1 and 1.2 [13].

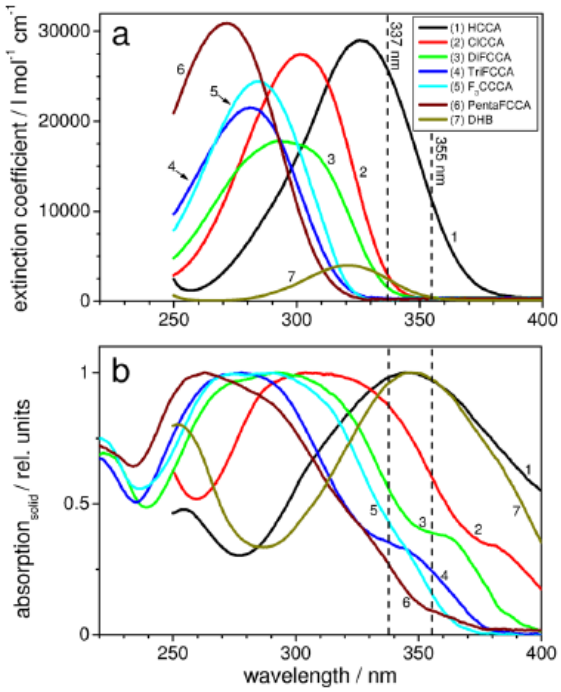

Figure 1.1. Absorption profiles of α-cyano-4- hydroxycinnamic acid (HCCA), chloro-α-cyanocinnamic acid (ClCCA), α-cyano-2,4-difluorocinnamic acid (DiFCCA), α-cyano-2,4,6-trifluorocinnamic acid (TriFCCA), α-cyano-4-trifluoromethylcinnamic acid (F_3CCCA), and α-cyano-2,3,4,5,6- pentafluorocinnamic acid (PentaFCCA), α –cyano-2, and 2,5-dihydroxybenzoic acid (DHB) in (a) solution and (b) in the solid state. Figure and caption reproduced and adapted with permission from [13].

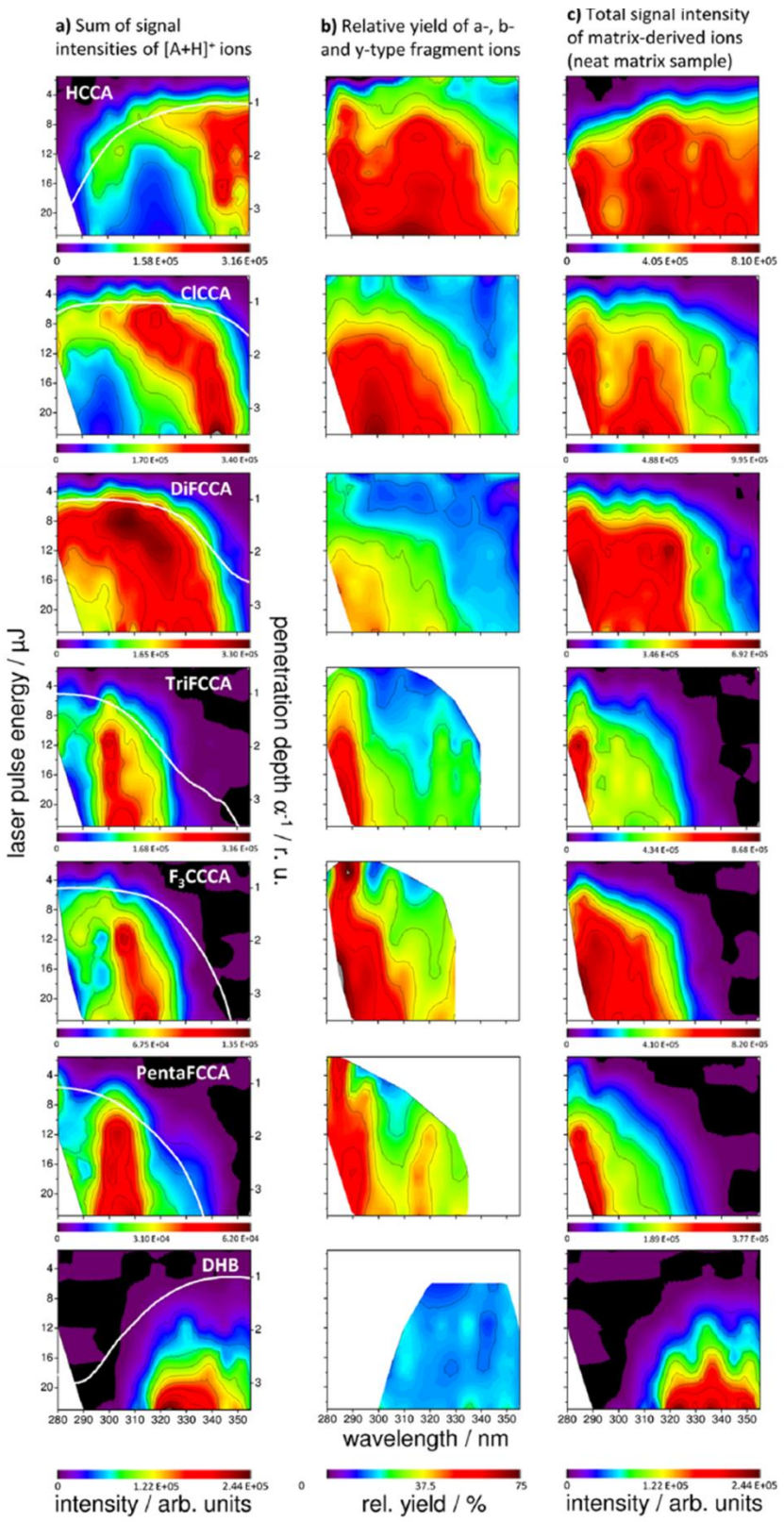

Figure 1.2. Heat maps displaying the signal intensities of different groups of ion species generated from two standard MALDI matrixes (HCCA and DHB) and five

halogenated CCA-derivatives, as a function of wavelength and laser pulse energy. (a) Combined intensities of the molecular ion signals $[A + H]^+$ of the five peptides contained in the peptide mix (5 pmol/peptide were prepared on target). The laser penetration depth (αsolid−1, normalized to the peak absorption) is shown as a white solid line (right ordinate). (b) Combined signal intensities of a-, b-, and y-fragments of the five peptides relative to the intensity sum of all analyte-derived ion signals ($[A + H]^+$ ion species plus those of a, b, y-fragments); wavelength−pulse energy combinations that produced no measurable analyte fragmentation (no single fragment ion signal with S/N > 5) are kept blank. (c) Total signal intensity of all matrix-derived ions generated from a neat matrix preparation. Figure and caption reproduced with permission from [13].

As in many of the earlier studies concerning optical absorption of MALDI matrices, the quantitative solid state absorption coefficients of the matrices were not measured [13]. The inverse of the relative normalised solid state molar extinction coefficients shown within Figure 1.1 (b) are displayed in Figure 1.2 as a white line. This is intended as a guide to the laser photon penetration depth for each matrix and implies that the larger the penetration depth the lower the relative absorption at that wavelength. Thus showing that the highest signal intensities ($[analyte+H]^+$) for all matrices are found at near to the minimum penetration depth – the wavelength at which the highest optical absorption is measured. The increase in analyte fragmentation to the left of these absorption peaks can also be clearly seen in Figure 1.2 and was largely blamed for the decrease in detected in-tact ion intensity towards the ‘blue’ side of the matrix peak-optical-absorption region.

1.2.1.2. Laser Energy and Fluence as Incident upon MALDI Samples

The fluence incident on a sample has been shown to be one of the most important parameters within MALDI MS. The earliest discussions of laser energy often centred on the concept of a threshold energy (per laser pulse) for a given matrix-analyte combination. The threshold irradiance is the fluence below which no ion signal is detected for a particular mass-to-charge value and above which an ion signal is detected. A study by Ingendoh *et al.* in 1994 demonstrated a decrease in mass resolution as the laser irradiance was increased, suggesting that the optimal operating conditions for linear or reflector type mass analysers are those only moderately above the measured threshold irradiance [19]. Values for threshold irradiance, and so fluence, vary considerably depending upon a number of factors such as the matrix-analyte system, the laser wavelength, and the dimensions of the irradiated area.

Published values for analyte ion detection threshold fluence cover a wide range of values from: ~20 - 1700 J m^{-2} [20-24]. Aside from the fact almost all of these studies were performed on different instruments, an obvious biasing factor when any ion intensity measures are compared, the area of irradiation was often very different for each value quoted. The dependence of threshold energy upon the area irradiated, as determined by Ingendoh *et al.*, is shown in Figure 1.3 [19].

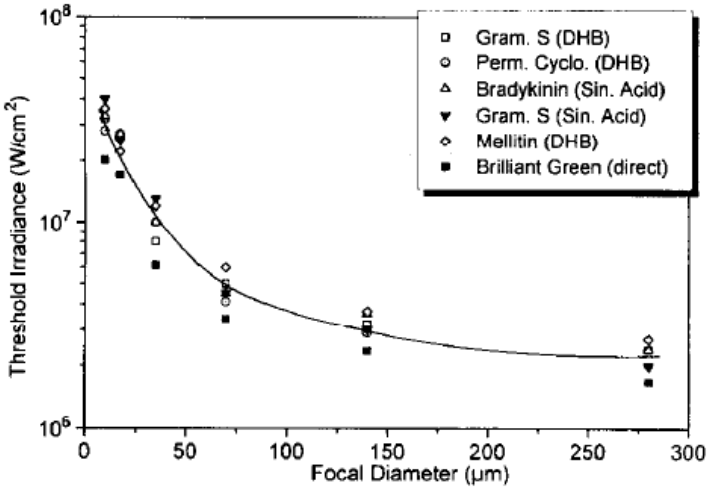

Figure 1.3. Plot of threshold irradiances vs. focal diameters for MALDI of different test compounds and matrices. Figure and caption reproduced and adapted with permission from [19].

This dependence of threshold irradiance (and so fluence) on the area irradiated was explained as being the result of the number of molecules available for ionisation. As the spot-size decreases this number decreases and so the amount of energy delivered must be increased so as to provide a larger portion of the irradiated area with sufficient energy for desorption-ionisation to occur. This result arises due to the Gaussian nature of the laser beam profile, within the study in question, delivering a different numbers of photons to different regions within the irradiated area. In addition, it was stated that these higher energies alter the conditions within the MALDI plume, changing the plume density, number and nature of collisions, causing changes in mass resolution seen. A subsequent study by Dreisewerd *et al.* [21] measured the detected ion intensity using a fibre-induced (pseudo) flat-top beam profile with fibres of diameter 200, 125, 60, 25 and 10 μm. The ion detection fluence thresholds also varied by over an order of magnitude depending upon the size of the irradiated area and at a

fixed irradiation area were found to be the same for both matrix and analyte ion detection. Within this study, laser post-ionisation of neutral matrix and analyte molecules was also carried out. It is interesting to note at this point that the desorption threshold energy, for detection of ions within the post-ionisation experiment, was about a fifth that of the MALDI (non-post ionisation) derived ions. It therefore seems likely that neutral molecules are ejected from the sample at fluences below the apparent MALDI threshold. The area dependence of detected ion intensity was found to follow a quadratic relationship for post-ionised neutral molecules and a cubic relationship for directly desorbed ions. This latter relation was subsequently confirmed for fluences near threshold within a study by Qiao *et al.* utilising fibre diameters of 200, 100, 50, 25, 10 μm [23]. However, it was also noted that the ion intensity dependence on irradiated area was closer to linear at higher fluences. The non-linear relation of threshold fluence with irradiated area is likely due to the requirement for a fixed number of ions to be created in order for an ion detection event to occur. Though the radius of the irradiated area decreases linearly, the area itself does not, therefore more material must be ablated from the smaller area (from deeper layers of the matrix and a larger portion of the irradiated area receiving high fluence) to provide the threshold detection level of ions. Elements of these relations are neatly summed up a study by Qiao *et al.* [23] which is reproduced here as Figure 1.4.

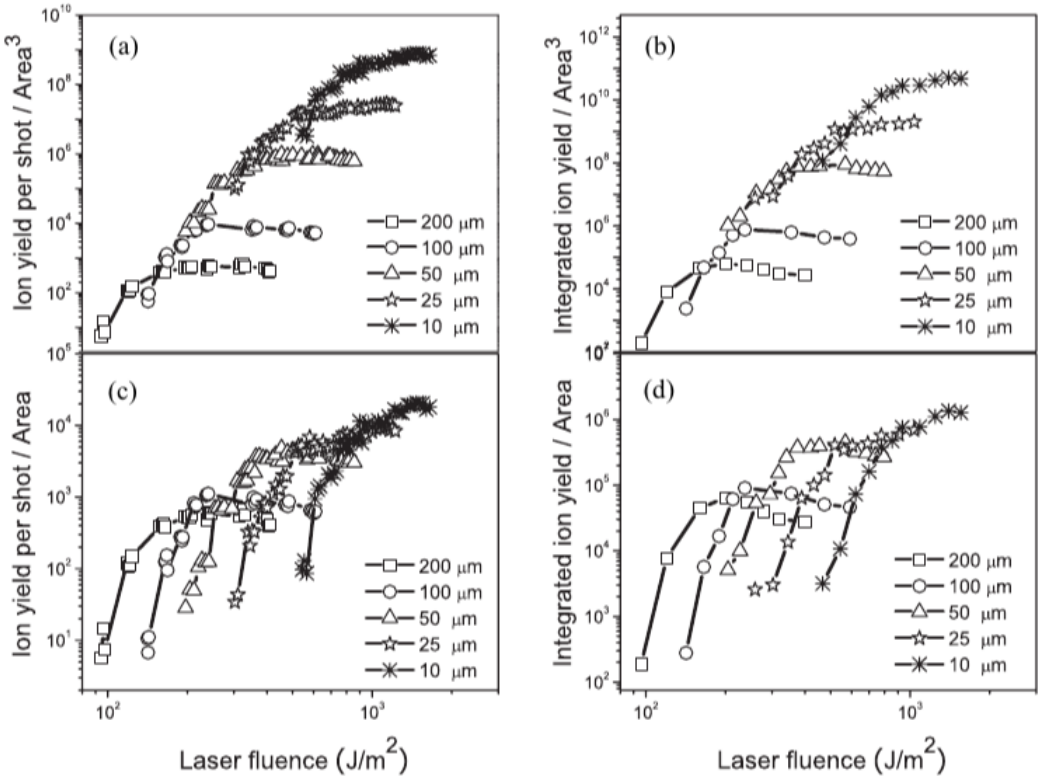

Figure 1.4. Illustration of the area dependence of the ion yield per laser pulse (a, c) and the integrated ion yield (b, d), using the same data shown in Fig. 10. In the top panels (a, b), the yields are divided by the cube of the spot area, and this indicates that yields measured at near-threshold fluence follow a cubic dependence on area. In the bottom panels (c, d), the yields are divided by the area, and this indicates that yields measured above saturation fluence have an approximately linear dependence on area. Figure and caption reproduced and adapted with permission from [23].

The presence of a true MALDI ion production threshold was called into question in a study by Westmacott *et al*. [25]. Within their work two different ion detection setups (analogue oscilloscope and time-to-digital signal recording methods), within two different instruments, were used to better probe the detection of ions at different fluences. A wide range of apparent ion detection threshold fluences were observed depending upon the instrument

used. This fact was used to conclude that the threshold commonly seen experimentally is simply a result of instrument (in)efficiencies in ion transmission and detection. Despite this, it was pointed out that there could still be a genuine ion creation threshold at fluences lower than those probed within their study.

Computational studies by Garrison and co-workers [26, 27] have suggested that there may be a change in the dominant molecular ejection process between desorption and ablation at a certain fluence. This may correspond to the apparent fluence threshold seen in MALDI experiments. Additionally, the Wang group [28] showed that photoelectrons are produced from common MALDI matrices at fluences considerably below those previously reported as threshold values. It seems likely, therefore, that the apparent threshold fluence is not one associated with a cessation in ionisation of the matrix crystals, but associated with a change in the dynamics of desorption / ablation of the sample and / or non-linear processes of giving the impression of an ionisation threshold energy.

The intensity of detected ions at fluences above threshold has also been studied by a number of research groups, including within studies discussed above [14, 21, 23-25]. The relation between fluence and detected ion intensity is linear on a log – log plot (prior to plateauing at higher fluence) and is commonly fitted to a power law relationship of the form:

$$Y \sim H^m \qquad (1)$$

where Y is the ion intensity or yield, H is the fluence (energy per unit area) and m is the exponent of the fit and is therefore the gradient of the linear fit in the log – log plot. An example of this relation fitted to experimental data is shown in Figure 1.5.

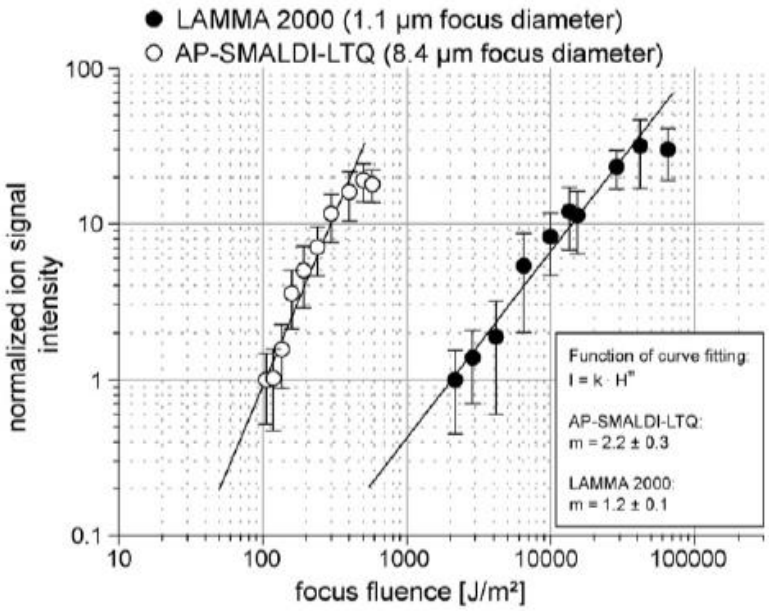

Figure 1.5. Dependence of Substance P ion signal intensity ([M+H]+) on laser focus fluence determined for the LAMMA 2000 and the AP-SMALDI-LTQ setup. Figure and caption reproduced and adapted with permission from [24].

The response of ion intensity to fluence incident upon the MALDI sample, like that of the threshold fluence, is dependent upon a number of factors such as the size of the irradiated area, matrix-analyte system and instrument utilised. The aforementioned study by Westmacott *et al.* probed these influences in great detail [25]; as well as utilising two different instruments and detector setups a number of matrices and analytes were also employed. The detected ion intensity of leutinizing hormone release hormone (LHRH) in CHCA, 2,5-DHB, SA and 2,6-dihydroxyacetophenone (2,6-DHAP) were compared over a range of fluences. It was found that the calculated exponent of the fit does have a dependence upon the matrix-analyte system used, with values varying from $m = 8$ to 9.1 for that data set. Reported values for m vary from around 1.2 up to above 10 [21, 24, 25]. The ion intensity increases rapidly from the threshold fluence in this manor until a maximum detected ion intensity is reached at a fluence which is

typically 2 – 3 [21, 29] times the threshold value but can be as much as 10 times higher [24]. At this point, the ion intensity will plateau and, if the fluence is further increased, will decrease [14, 23]. The reason for the reduction in detected ion intensity at these larger fluences is likely due to a combination of detector saturation, increased fragmentation of analyte ions and matrix modification effects [9, 23, 30-32].

The Dreisewerd group, within studies utilising a variable wavelength laser, looked into the effect on ion intensity with varying fluence over a range of wavelengths using multiple matrices (as discussed above) [9, 13, 14]. The data obtained within their studies provide the most complete data set so far collected regarding the response of analyte and matrix ion yields at different fluences (see Figure 1.2 for example data set). Whilst Equation 1 typically provides a good fit to a large portion of data points in ion intensity – fluence plots, it does not fit or describe a number of important physical phenomena such as the saturation of ion intensity as the fluence increases and the influence of spot size and wavelength. Based upon their data they propose a new model equation, of sigmoidal form, to describe the relation of ion yield to fluence [9]:

$$I = \hat{I}\frac{(H+H_{thr})^m}{(H_k+H_{thr})^m+(H+H_{thr})^m} \qquad (2)$$

where I is the ion intensity detected, $\hat{I}$ is the experimentally observed upper limit of ion intensity, H is the fluence, H_k is the fluence at the inflection point of the intensity - fluence relationship and scales approximately inversely with the absorption coefficient of the matrix in question, H_{thr} is the point at which the sigmoidal function intersects with the x–axis and therefore approximates the apparent threshold fluence and m is the fitting parameter used as above.

1.2.1.3. Influence of Laser Beam Profile in MALDI MS

The fluence ($J\ m^{-2}$) per laser pulse is discussed frequently as one of the most significant variables within MALDI MS. This global value, however, ignores the distribution of the laser photons with the sample area irradiated. As these global fluence values are clearly very important in determining the detected ion intensity then it follows that the photon density arriving at sub-regions of the laser spot on the sample must also play an important role. The laser spot will, in effect, be made up of regions of differing fluence. There has been little work done to understand the influence variation of the laser beam profile can have on ion intensities. Early MALDI MS studies typically focussed the laser beam directly onto the sample without use of fibre optic patchcords and therefore an approximately Gaussian beam profile was assumed. Latterly, Neodymium doped (commonly Nd:YAG) diode pumped solid state lasers (DPSS) have been introduced and the performance differences between these lasers and traditional Nitrogen (N_2) cell lasers became apparent. Holle *et al.* studied these differences in more depth by comparing MALDI MS ion intensities obtained with N_2 and Nd:YAG beam profiles modified by diffraction optics [33]. The messier Gaussian profile of the N_2 laser showed improved ion intensity over the smoother Gaussian profile of the Nd:YAG laser (beam profile images used are shown in Figure 1.6).

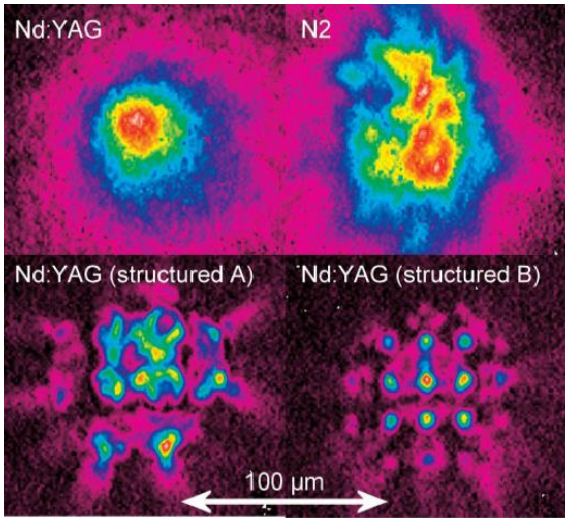

Figure 1.6. Direct comparison of the four beam profiles used for the experiments. Figure and caption reproduced and adapted with permission from [33].

By using the diffraction optics setup (specifically that shown in Figure 1.6 as structured A) they were able to obtain similar or improved performance for the Nd:YAG as compared to the N_2 laser.

Surprisingly Qiao *et al.* found that these differences in performance between N_2 and Nd:YAG lasers persist even after the destruction of the original beam profiles due to delivery through an optic fibre; suggesting that the original differences in beam profile were not completely 'forgotten' despite multiple mode mixing within the fibres during transmission (Figure 1.7 show the post fibre beam profiles as used in the study by Qiao *et al.*) [23]. It was found that, analogous to Holle *et al.*, the N_2 gave a higher ion intensity as compared to the Nd:YAG laser under normal operation (though fibre delivered in this case). However by twisting the fibre optic patchcord, and thus altering the pulse to pulse photon distributions, the ion intensity detected from each laser were approximately the same as each other and both similar to the non-twisted N_2 fibre delivered data.

Neither of these studies attempted to quantify the actual fluence difference for the beam profiles as incident upon the sample, or the changes in area within the irradiated region receiving different numbers of photons as dependent upon the beam modifications made. It seems likely that one area of the irradiated sample does not 'know' how many photons are incident upon another area of the sample, due to the timescales involve within the MALDI ablation process. Therefore, in both of these studies what is actually being seen is adjustment which brings the experimenter closer to the optimum division of the total number of delivered photons to each sub-area of the total irradiated area. Quantification of this energy division is necessary to further understand these phenomena. One route to better controlling the number of photons per unit area could be to use advance laser patterning optics to spatially modify the laser beam profile in a controlled manor [34].

1.2.1.4. Laser Temporal Pulse Width in Typical UV MALDI MS Studies

Within typical UV MALDI MS applications the lasers used have a temporal pulse width of between approximately 0.5 and 20 ns. A study by the Hillenkamp group utilised two N_2 lasers with pulse widths of 0.55 and 3 ns to probe this MALDI relevant region [35]. Fluences within the range of 10 to 300 J m^{-2} were employed for a range of matrices and analytes. It was concluded that there was little to no difference in the data obtained with each laser pulse width from any given matrix analyte combination, supporting the conclusion that UV MALDI MS is fluence rather than irradiance dominated. Though, in this author's opinion, there appear to be some differences in threshold fluence and fragmentation within the data sets shown.

The Vertes group used an N_2 (337 nm) and an Nd:YAG (355 nm) of pulse widths 4 nanoseconds (ns) and 22 picoseconds (ps) respectively, to further probe the influence of pulse width in MALDI [36]. Within their study the 'thermometer molecule' 3-methoxy-benzylpyridinium salt (3MO-BP), molecular salts for which no charge transfer reactions are necessary for detection, were used to decouple the energy transfer inherent in charge transfer reactions from that imparted in ablation and plume collision processes. Therefore, the detected molecular ion intensity of these molecules (as compared to the sum of all analyte related peaks within the mass spectrum) was, to the first order, considered a function of their fragmentation decay due to these collision based energy transfer processes. It was stated that the survival yield (SY: ratio of molecular ion intensity to fragment plus molecular ion intensity) was higher for the picosecond laser pulse but higher fluences were needed for this laser to achieve ion detection; e.g. an increase of approximately 25 compared to 42 mJ cm^{-2} for CHCA with ns and ps pulses respectively. Even needing higher fluences the SY was higher for the ps pulse, which is slightly counter intuitive. However, for each individual pulse length, increasing the fluence upwards from threshold caused a decrease in SY, an increase in fragmentation, suggesting that more energy was being transferred to the rotational and vibrational states (internal energy) of the analyte as fluence increased, regardless of the pulse width.

The timescale on which energy is deposited in MALDI MS is important for considering the underlying energy transfer pathways involved. Within ps / ns timescales the regimes of thermal and mechanical confinement need to be considered. Thermal confinement concerns the timescale of conduction of the absorbed energy in the form of heat. To exist within the thermal confinement temporal regime the time constant for heat transport, τ_{th}, must be longer or similar to the laser temporal pulse width; whereas for mechanical confinement

the laser pulse duration must be shorter or of the order of the characteristic transport time, τ_{ac}, for acoustic waves within the irradiated region. Dreisewerd [29] has calculated that for the matrix 2,5-DHB the values are approximately 10 ns and 30 ps for τ_{th} and τ_{ac} respectively, suggesting that typical MALDI MS experiments operate within the regime of thermal confinement and as a consequence that thermal processes are likely to dominate over mechanical ones.

In addition to experimental studies relating to laser temporal pulse width, there have been a number of theoretical studies of the relating to this subject [37-39]. The Garrison group's molecular dynamics (MD) simulations showed differing ablative mechanisms when operating within the regimes of thermal (150 ps pulse) or mechanical (15 ps pulse) confinement [38]. Thermal confinement was characterised by a phase explosion of the heated material and a mixture of liquid droplets and gas phase molecules are ejected. For mechanical (stress) confinement, material removal was observed at lower fluences due to a more efficient ablative process via pressure change and void nucleation, though with larger clusters and large spalled droplets. An example of images obtained from these simulations is shown in Figure 1.7. The Garrison group also studied two pulse widths lying within the regime of thermal confinement (150 ps and 1 ns) [37]. It was concluded that whilst the pulse width, within the regime of thermal confinement, does not significantly affect the ejection mechanism seen within their MD simulations, there are differences seen in plume make up and ablation threshold fluence. More specifically the longer pulse width increases both the number of monomers in the plume and the ablation threshold fluence.

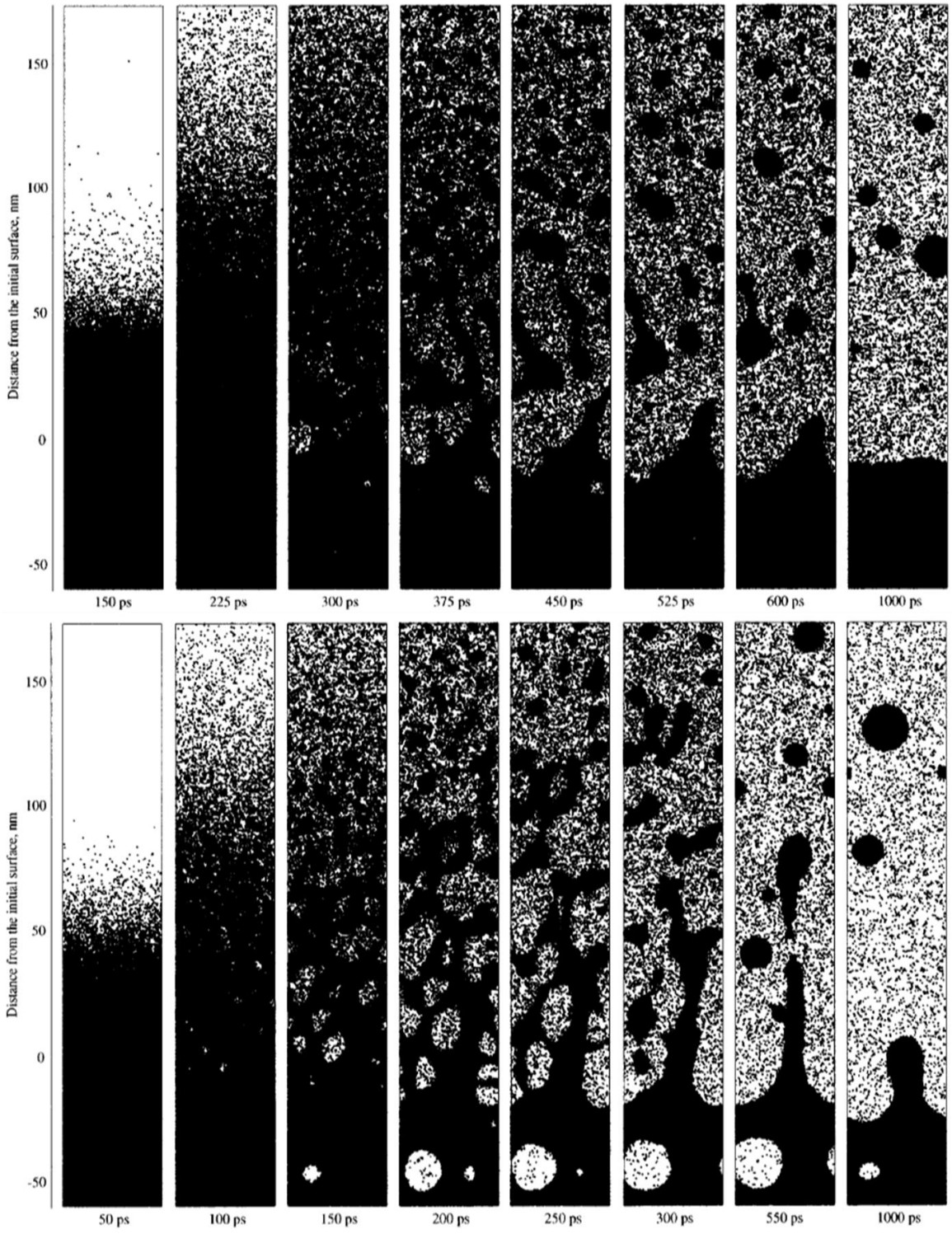

Figure 1.7. Snapshots from the MD simulation of laser irradiation of a molecular solid with: top - pulse duration of 150 ps, bottom – pulse duration of 15 ps, both with a fluence of 61 J/m^2. Figure and caption reproduced and adapted with permission from [38].

More recently Knochenmuss and Zhigilei used MD simulations to probe ionisation ejection and ionisation mechanisms for pulse widths of 35 ps, 350 ps and 3 ns [39]. The shorter pulse widths were found to produce higher pressures and rapid early acceleration with stratified ejection regions of molecules (first) and clusters (after) as compared to the longer pulse with a smoother transition between the molecular and cluster ejecta. However, these differences were seen to largely disappear due to plume interactions on the nanosecond timescale, agreeing with experiments which have suggested that the MALDI event is fluence not irradiance driven (within certain pulse width time-scales).

Further to the variation of the temporal width of single laser pulses in MALDI MS the use of multiple pulses with varying arrival time can be used to further probe the MALDI ablation / ionisation process. One such study by Knochenmuss and Vertes [40] used two ps pulses from an Nd:YAG laser to probe ablation and ion formation. Either pulse alone was shown to produce no detectable ions, however, when both were incident upon the same sample area within a suitably short timescale ions were produced. The relative detected ion intensity peaked at two time points (approximately 0 and 2 ns) suggesting both fast and slower energy conversion / storage processes and also showing that commonly used lasers in MALDI are well suited to the preferred energy deposition time scales for the 2,5-DHB matrix used. Tang *et al.* [41] also found optimum delay times for similar dual, sub-threshold, pulse experiments of 4.2 and 12.6 ns for SA and 2,5-DHB respectively.

1.2.1.5. Desorption / Ablation Plume Characteristics and Dynamics in UV MALDI MS

The ejected plume of a UV MALDI MS desorption / ablation event is a complex mixture of many processes where individual molecules, electrons, ions, clusters and large

particles are all present at different velocities and time points. The velocity of different plume components has been studied by a number of groups and reported values vary from ~ 100 to over 3000 m s^{-1} [42-53] and it is widely agreed that a super-thermal molecular jet like process is observed. A number of these studies found that there were two components to the detected velocity populations [17, 42, 50, 53]; that matrix associated ions were often found to have a higher velocity than that of the analyte studied [17, 50]; the angular velocity distribution of the plume is significantly forward peaked [47, 53, 54]; the velocities increase to some extent with fluence and have a dependence on the matrix / analyte system studied [44, 53, 55]; velocities are at weakly dependant on ion / molecule mass and charge (for any given matrix) [44, 48, 51, 55]. It also seems likely that the crystal morphology resulting from different sample preparation methods will have an effect upon the velocities seen during the MALDI process [46].

Imaging of MALDI plumes can provide valuable information regarding the dynamics and composition of the desorption / ablation ejecta. Geohegan and co-workers used laser induced fluorescence (LIF) imaging of the ablation plume to further study the dynamics involved [56, 57]. Two different forward propagating components were identified within the images and the axially dominant direction of the plume was clearly visible. The Dreisewerd group [52] used a combination of photoacoustic detection, fast-flash imaging (with 90 degree scatter and dark-field illumination setups) and laser post-ionisation to create a comprehensive picture of MALDI type ablation plumes using the liquid matrix 3-Nitrobenzyl Alcohol (3-NBA). Within their images the ejection of gaseous material is seen to occur at an earlier time compared to the emission of larger particles. The dark field images were judged to be a measure of the amount of gaseous material in the plume and these images were found to increase in intensity as the fluence was increased. Schmitz *et al.* [58] used shadowgraphic

imaging to study the early plume and shockwave dynamics for the laser ablation of some common MALDI matrices. An example of a time series of these images is shown in Figure 1.8. Within these images a number of features can be observed e.g. the external shockwave due to rapid heating originating at the sample surface; the ionized shock front made of ionised gas; a product front consisting of the ejected material from the sample.

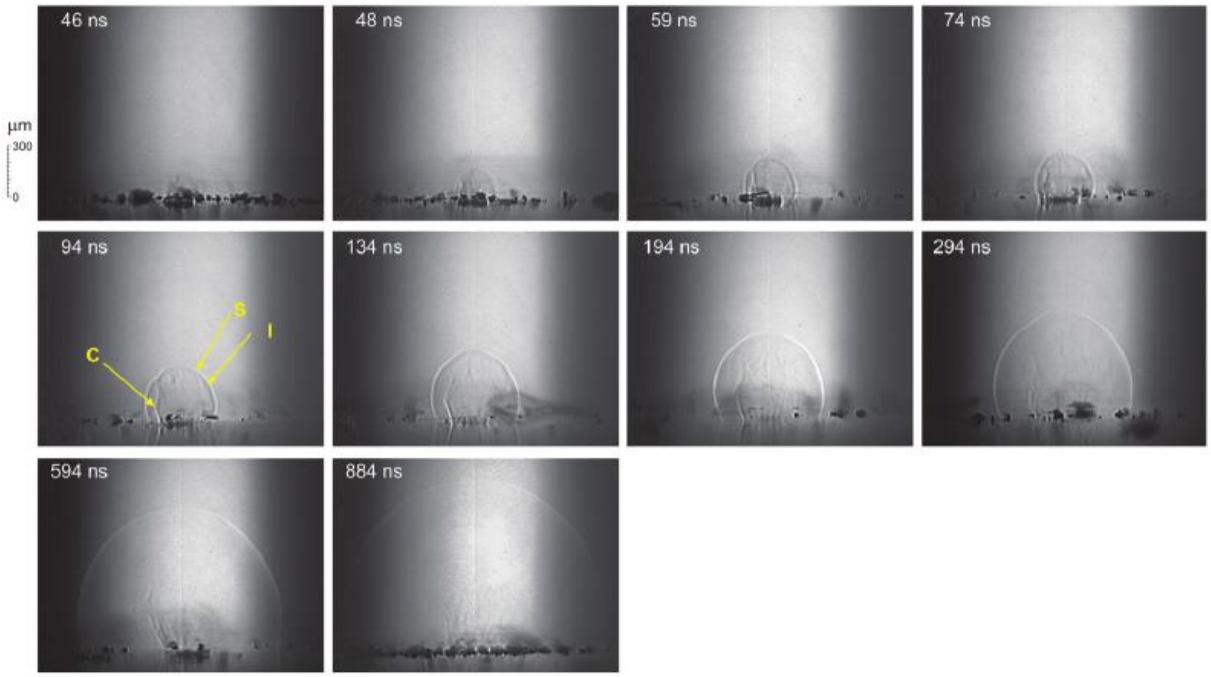

Figure 1.8. Shadowgraphs for UV-laser ablation of 2,5-DHB, obtained at the indicated delay times Δt. Laser energy 126.5 µJ/ pulse, S = External shock wave (SWe), I = Ionization front; C = Contact/Product front. Figure and caption reproduced and adapted with permission from [58].

After around 200 ns the product front is seen to move from propagating equally in all direction from the centre of irradiation and become much more directional, in agreement with the studies discussed above. Velocities for the shockwave expansion were estimated at

between 1 and 8 km s^{-1} and were found to have some fluence dependence. In common with other studies, a threshold fluence was found; in this case for the onset of a detectable shockwave front.

1.2.2. Sample Preparation and Associated Phenomena in UV MALDI MS

1.2.2.1. Matrix Choice in UV MALDI MS

The choice of molecule to act as matrix in UV MALDI MS experiments is an important one. An effective MALDI matrix must display some or all of the following characteristics: a suitably strong absorption at the wavelength of the laser being used; an ability to crystallise in intimate contact with the analyte of choice at a suitable molecular ratio; the ability to participate in charge transfer reactions with the analyte; typically it must be soluble in the same solvent systems as the analyte; it's crystallisation and ablation characteristics must be robust to salts and contaminants; the matrix must not be so reactive as to significantly alter the analyte structure beyond recognition; the energy decay pathways after excitation by the laser pulse must enable a desorptive / ablative event conducive to releasing molecules / ions of interest into the gas phase. Despite these specific requirements, or perhaps because of their number and interdependence, the discovery of MALDI matrices has often proceeded by a brute force method with attempts to rationally choose or design matrices having mixed, or even limited, success. The first MALDI matrices were known to absorb well at suitable wavelengths due to having been successfully desorbed and analysed by laser desorption ionisation mass spectrometry (LDI-MS) [4, 6, 59]. This provided an important start point for many of the subsequent investigations in MALDI MS: the

importance of absorption wavelength [60] and ablation / desorption of the molecules under study was already recognised. Therefore, the start point of many subsequent studies was the highly conjugated aromatic ring molecular structures which provide these absorption properties in the UV region.

Fitzgerald *et al.* [61] screened 37 basic amino containing highly substituted pyrimidine, pyridine, and benzene derivatives for their ability to act as matrices for the analysis of proteins and oligonucleotides with a focus on the importance of pH. Of these compounds surveyed only two were ultimately recommended and no general rules for the success or failure of any given molecule were put forward. The approach of focussing matrix discovery efforts on one or a few compound classes has been the most common tactic for MALDI matrix discovery [62-73]. Krause *et al.* investigated benzene related carboxylic acid containing compounds by varying the isomer moiety location and type through *ortho*, *meta* and *para* locations and qualitatively assessing the efficacy of these compounds as MALDI matrices [62]. Compounds which performed intramolecular proton transfer under UV irradiation were found to more readily act as MALDI matrices and additionally the *ortho*-hydroxy isomers were found to outperform the *meta* and *para* varieties. Salicylamide, salicylanilide, 2,5-dihydroxyacetophenone and 2,6-dihydroxy-acetophenone were found to be particularly useful new matrices. More recently statistical approaches have been employed by Meier *et al.* in an attempt to widen the search for new matrices without the requirement of screening the MALDI MS results of many hundreds of compounds [74]. Within their study 11,000 molecules from the Aldrich Catalog were screened for: mass (100 – 500 g/mol) and presence of at least one aromatic ring. In addition, inorganics and organometallics were removed from consideration and various descriptors were calculated from the physical properties of the compounds. PCA was then used then used to select 59 potential compounds

which described the largest variance within this chemical property landscape. Ultimately, ten new matrix compounds were recommended for the analysis of synthetic polymers. The hope of MALDI MS researchers for precise performance prediction from molecular structure and corresponding physiochemical properties still remains some way off.

1.2.2.2 Matrix – Analyte Co-Crystallisation

The co-crystallisation of matrix and analyte was initially, and in many cases still is, thought to be necessary for optimal desorption / ablation and ionisation of the analyte molecule(s). Whilst this concept seems likely to be a good rule of thumb, the true picture is somewhat confused; a more appropriate, if slightly vague, statement would perhaps be that analyte molecules must be in intimate contact with the matrix crystals for MALDI like phenomena to occur. Early work on these concepts was carried out by Strupat and co-workers [8, 75]. DHB isomers 2,4-, 2,5-, 2,6-, 3,4- and 3,5- were used to study the influence of incorporation of analyte into matrix crystals on MALDI MS detection of cytochrome c from single large crystals, dried droplet (premixing of analyte and matrix solutions) and "thin layer" (over-layer method: matrix pipetted first, allowed to dry, analyte pipetted on top) preparation methods [8]. The protein incorporation into single large crystals was determined by spectrophotometry and compared to the subsequent MALDI MS data. Cytochrome ions were detected with all matrices despite some having no detectable analyte incorporation; consequently, analyte incorporation was deemed helpful but not necessary. In subsequent studies by the same group electrospray and compressed dry pellet (dry crushing of matrix / analyte and subsequent compression into pellet form) sample preparation methods were used to further investigate analyte incorporation into matrix crystals [75, 76]. It was concluded that incorporation of analyte molecules into the crystal lattice was not a prerequisite for MALDI

like desorption / ablation and ionisation. However, analyte dependent behaviours were observed, as was a reduction in spectral quality for the dryer preparations. Consequently it was speculated that a transition from 'hard' laser desorption ionisation (LDI) like behaviour from the matrix crystal surfaces (where analytes are not incorporated) to the 'soft' MALDI like desorption / ablation from fully incorporated analytes could be observed depending upon the sample preparation method used. Trimpin *et al.* also investigated the issue of analyte / matrix co-crystallisation and concluded that, due to the inverse relationship between crystal size and signal to noise for a given laser energy (i.e. larger crystals required a larger energy to obtain the same signal to noise for a given analyte), crystallinity was not beneficial for the MALDI process [77]. The reduction of the lattice energy of the matrix crystals by increasing the number of defect surfaces (by reducing the size of the matrix crystals used) was deemed beneficial.

Despite the complex picture of analyte / matrix preparation it is still the case that much of the fundamental work in MALDI MS is done utilising 'wet' preparations such as dried droplet. Within this and similar wet preparations the analyte and any contaminants will likely be incorporated into the matrix crystal and their location in the subsequent dried preparation will therefore be effected by the process of drying and crystallisation. Separate investigations by Owens, Heeren and Spengler [78-80] investigated the phenomena of matrix, analyte and salt distributions within MALDI type sample preparations. In all three of these studies movement and segregation of the molecules was observed to occur; a potentially significant issue for spatially resolved studies (imaging) and also for the optimisation of sample preparation methods. An example image from the study by Bouschen and Spengler is shown in Figure 1.10.

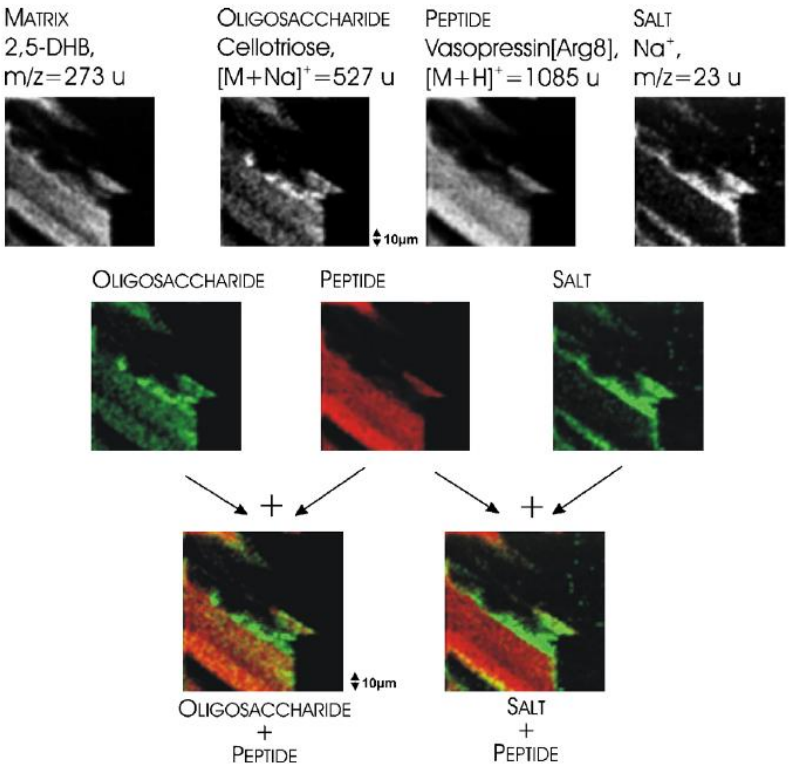

Figure 1.9. MALDI MS images of matrix DHB, cellotriose, vasopressin and sodium. Sampled area was 100 µm × 100 µm, scanning step size was 1 µm. (First row) Gray scale distribution images. (Second row) Colored distribution images. (Third row) Red/green overlay images. Figure and caption reproduced and adapted with permission from [78].

In addition to the (de)localisation of species within single crystals, different MALDI matrices will (as would be assumed from their differing physical properties) form crystals of different sizes, shapes and structures. Furthermore variables such as solvent choice / evaporation and sample substrate properties will influence the crystal properties. There have been a number of investigations into these and similar phenomena for a range of matrices, analytes and additives [81-87] and issues such as crystal size and 'hot spots' are directly attributable to these features of sample preparation. A further, important, factor in sample preparation is the matrix-to-analyte molar ratio. This value will not only have an effect upon

the nature of the crystals formed but will also dictate, to some extent, the subsequent charge transfer reactions in the expanding plume and so the ability of a certain sample preparation to function successfully for MALDI MS. Therefore, optimisation of the matrix-to-analyte ratio is an important consideration for successful MALDI MS [88-90].

1.2.3 MALDI MS Desorption / Ionisation Mechanisms and Models

So far, much discussion within this literature review has been devoted to a somewhat empirical summary of the current knowledge of UV MALDI MS. It is now important to discuss attempts which have been made to unify this knowledge into mechanistic frameworks which are able to qualitatively and quantitatively describe the MALDI MS process, accounting for as many or all of the experimental variables [91]. The current view in MALDI MS is largely unified with respect to the treatment of the MALDI mechanism(s) as a two-step process. With the primary mechanisms occurring on a nanosecond time scale, leading to the creation / release of a set of initial ions and secondary charge transfer and phase change processes occurring on a microsecond timescale. These primary mechanisms consist of photon absorption by the matrix and conversion of this energy to heat, sound (pressure waves) and, depending upon the model one subscribes to, creation of a population of primary matrix ions. The secondary reactions will typically refer to the exchange of protons, cations and electrons between molecules in the expanding desorption / ablation plume. It is these secondary reactions from which the detected ions emerge to create the subsequent mass spectrum.

There are currently two major models describing the MALDI MS process: the ‘lucky survivor’ or ‘cluster’ model [92-94] and the ‘gas phase’, ‘two step’ or, more recently,

'coupled photophysical and chemical dynamics (CPCD)' model [91, 95, 96]. Both of these models require gas-phase (though this process will occur throughout the explosive phase change from solid through to the gas phase) charge transfer reactions for the second phase reaction processes. The nature of these reactions will depend upon the physical properties, such as the proton affinity and gas-phase basicity, of the molecules in question. These reactions are typically of the form:

$$mH^+ + A \leftrightarrow m + AH^+ \qquad (3)$$

$$AH^+ + B \leftrightarrow A + BH^+ \qquad (4)$$

where *m* is a matrix molecule, *A* and *B* are analyte molecules and *H* is a proton. In addition, the final makeup of the detected mass spectrum will also be highly dependent upon other charge recombination reactions, neutralising previously existing ions.

The Lucky Survivor model relies on ion pairs being pre-formed within the solid crystalline sample (like a salt), with these charge states having been created during the liquid phase of sample preparation [97, 98]. Upon radiation, clusters consisting of these ion pairs and neutral matrix and analyte molecules will be released, these clusters must then undergo a rapid disintegration (desolvation / decay) leaving an excess of charge, resulting in the ions detected by mass spectrometry. Therefore, within the Lucky survivor model, the laser simply serves to provide the energy for the creation and decay of these clusters and is assumed to cause little or no ionisation by absorption of photons in either the matrix or analyte. During the decay process charge exchange reactions between matrix and analyte will also occur; it has been shown experimentally that the extent to which the preformed analyte ion or the 'gas-phase' protonated ion are detected can be altered depending upon experimental conditions [94]. This model has not yet been formalised to enable quantitative predictions to be made.

Though there is a body of evidence building from work by the Trimpin group which suggests clusters are a key factor, not only in MALDI like processes but in a number of photon and voltage free ionisation methods developed by her group [99, 100].

The CPCD model, on the other hand, states that under 'normal' MALDI conditions, the analyte and matrix will (largely) not exist as preformed ion pairs but as neutral molecules. The laser photons are absorbed by the matrix, causing mobile electron excited singlet (S_1) states (excitons) to exist within and between the overlapping π-bond orbitals of the crystalline matrix. Single and even two photon absorption events are not typically sufficient to ionise single matrix molecules at common UV MALDI wavelengths (337 or 355 nm). For example 2,5-DHB has an ionisation energy of about 8 eV and the energy of one 337 nm photon is 3.7 eV [101, 102]. Therefore, exciton hopping is proposed to enable the creation of matrix ions, allowing exciton pooling events of sufficient number to occur at single molecule sites (e.g. $S_1 + S_n$ where n = 2 or more) [91]. Pooling events have been evidenced by fluorescence quenching behaviour where the presence of a fluorophore in appropriate concentration ranges will act as a exciton trap, preventing the necessary energy pooling for matrix ionisation, resulting in reduced ion yields of matrix related ions [103]. Subsequent to these processes the heat resulting from rotational and vibrational energy decay pathways (as with other models) leads to desorption and ablation processes and the transition from a solid through to the gas phase, during which time the secondary charge transfer reactions will occur [104]. The CPCD model has largely been developed by Richard Knochenmuss and it is currently the only quantitative mode which attempts to account for all MALDI MS phenomena.

All proposed models require thermal effects to enable the phase change necessary for the desorption / ablation event. Recently, thermal effects have even been proposed to be the behind the dominant ionisation mechanism due to the thermal dependence of ion abundance

observed by the Kim group [105]. Though this apparent thermal dependence is also a property of the CPCD model within certain fluence regimes [106].

1.3 MALDI Mass Spectrometry Imaging (MSI)

The spatially discrete nature of laser-sample interrogation lends itself well to the concept of probe based imaging; by allowing the user to collect mass spectra over an array of known locations the abundance of a given molecule in the sample can be mapped. MALDI MSI was invented by, amongst others, Richard Caprioli in the late 1990s [107]. Since this time it has evolved and spread rapidly, moving quickly from the niche research area to a widely used technique which features in many different types of research setting, including routine use within areas such as drug discovery / development where MALDI MSI is not the main research focus. The reason for this is the relative ease with which certain molecular classes are detected from plant and animal tissue sections and so the uptake has been enthusiastic.

1.3.1. Theoretical and Practical Considerations for MALDI MSI

1.3.1.1. MALDI MSI Methodology

A typical MALDI MSI workflow consists will consist of: tissue preparation; sectioning and subsequent application to the sample plate; matrix application onto sample; loading of the sample and subsequent interrogation within the mass spectrometer. This protocol is summarised in Figure 1.11.

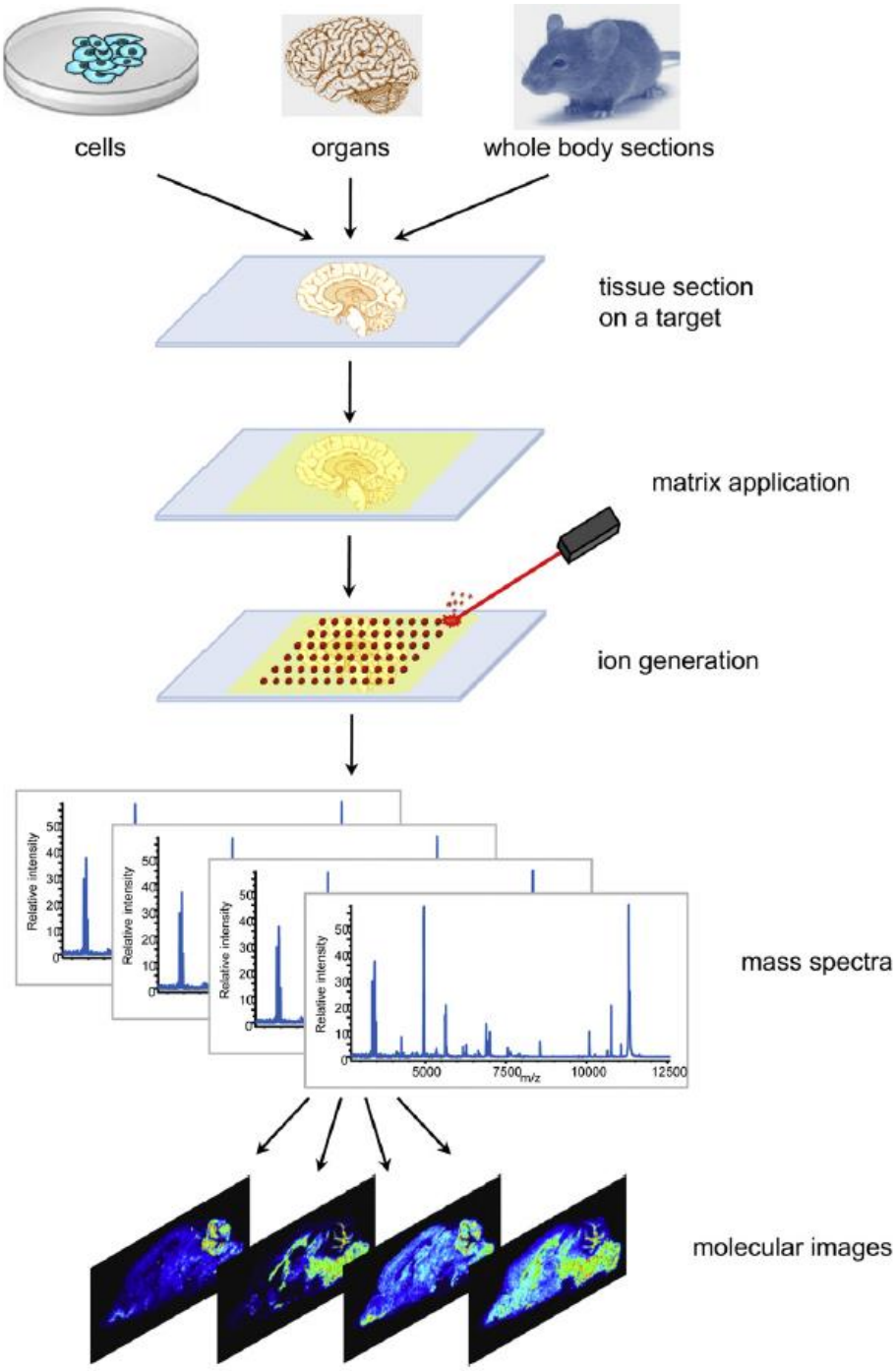

Figure 1.10. Schematic outline of a typical workflow for an IMS experiment. Sample pretreatment steps include cutting, mounting the sample on a target and matrix application. Mass spectra are generated in an ordered array at each x, y coordinate. Individual spectral features can be visualized within the tissue to generate protein images. Figure and caption reproduced and adapted with permission from [108].

There has been limited work regarding the effect of tissue section thickness studies regarding tissue sectioning in MALDI MSI. There may be some improvement in detected ion intensity with analysis of thinner tissue sections at 2 – 5 μm [109], though there is also evidence suggesting this makes little difference in the range of 10 – 40 μm [110], where good results are still obtained. Therefore, sectioning thickness is largely a compromise between the ease of handling provided by thicker tissue sections and the desire to section to the approximate thickness of one cell to prevent sample charging and ensure the detected molecular distributions are reflect and compliment the kind of data traditionally obtained by histological staining and light microscopies. Consequently MALDI MSI practitioners will typically section tissue at a thickness of between 10 and 20 μm [111].

1.3.1.2. MALDI MSI Matrix Application

The need to coat larger areas of a sample with a homogenous and isotropic layer of matrix of sufficiently small crystal size has led to the development of a number of MALDI MSI specific matrix deposition techniques. Caprioli and co-workers, in their study introducing MALDI MS imaging of tissue / biological samples, employed two methods: electrospray and pipetting of the matrix onto tissue [107]. The matrix crystal size resulting from electrospray deposition were measured as < 1μm by light microscopy; much smaller than the pixel size employed. Electrospray matrix deposition has been used for matrix deposition in a number of instances [111, 112] though is rarely used for imaging based sample preparation probably due to its relative complexity, the lack of a commercially available robotic electrospray device and the difficulty of coating large areas with a homogenous matrix layer due to needle blockage.

Perhaps the most commonly used in MALDI MSI matrix deposition methods are air-spray / air-brush / capillary nebulisation techniques. These techniques will typically involve the use of a nebulising spray device enabling a constant stream of matrix solution to be directed at the sample surface [111, 113, 114]. These will typically be a thin layer chromatography (TLC) sprayer or an artist's paint air-brush. The TLC sprayer uses a hand pump to enable the nebulising airflow whereas the airbrush will use a gas cylinder. The use of a gas cylinder will enable a higher pressure, resulting in smaller spray droplets and so the potential for smaller matrix crystals. Additionally the constant pressure / gas flow velocity allows a more reliable and reproducible coating to be achieved. Using hand held devices requires practice and a care to enable reproducible coating of samples due to the scope for human error. For example, the wetting of the sample is heavily dependent upon the distance of the spray nozzle from said sample. Over-wetting can cause large crystal formation and substantial analyte migration. An illustration of air-spray matrix deposition is shown in Figure 1.12.

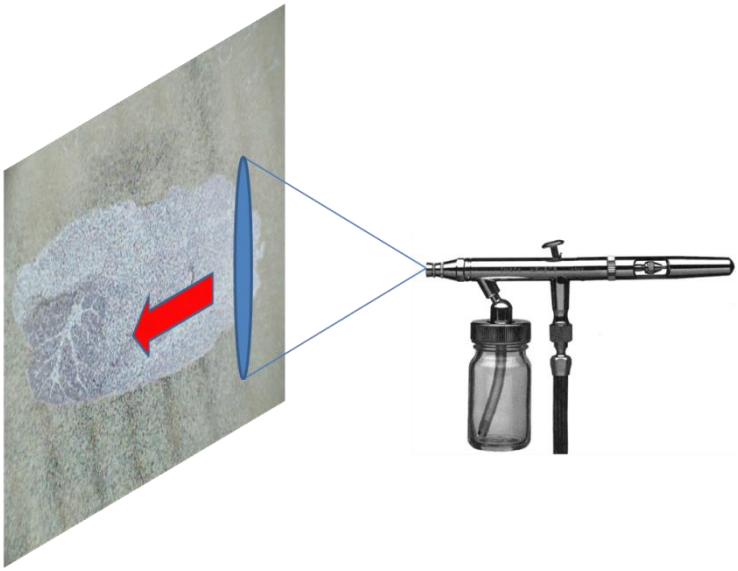

Figure 1.11. Schematic diagram of the air-spray method of matrix deposition in MALDI MSI (not to scale). Sample shown is a mouse brain tissue section on a stainless steel sample plate with CHCA matrix coating performed by air-spray deposition. The nebulising artist's air-brush spray device is hand-held in front of the sample and moved back and forth, coating the sample in the chosen matrix.

Due to the scope for human bias within this method of sample preparation it is difficult to draw general conclusions about the typical crystal sizes obtained. However, within our group, crystals of the order 1- 10 µm have been measured by secondary ion microscopy (SEM) for a standard preparation protocol of CHCA by air-spray deposition (Figure 1.13). This method is cheap, relatively easy to implement and provides high quality data and consequently remains widely used.

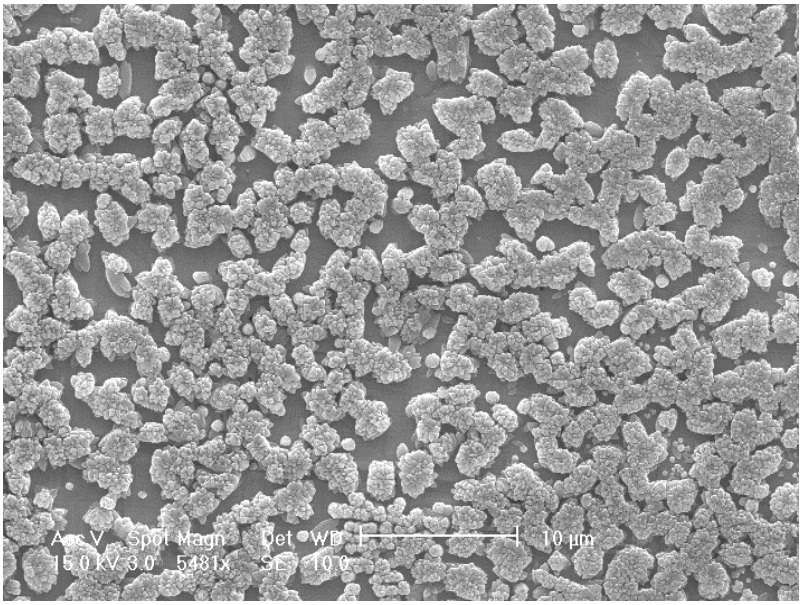

Figure 1.12. Scanning electron microscopy (SEM) image of CHCA crystals on a stainless steel MALDI MSI sample plate. Sample was coated with angstrom thick layer of platinum prior to imaging to improve conductivity, as is necessary for SEM imaging of insulating samples. Scale bar shows 10 µm.

A number of automated matrix solution deposition strategies have been explored such as the oscillating capillary nebuliser [115], heated capillary nebuliser [116, 117], vibrational aerosol [118] and robotic spray [119] devices. Rather than coating large portions of the sample with a broad spray of matrix solution the tactic of micro-spotting matrix onto the sample has also been explored through chemical printer [120], adapted inkjet printer [121], micro-spotter [122] and acoustic spotter [123] devices. Due to the relative complexity and expense of these systems, each type / model of these devices (commercial or otherwise) are typically only used in a handful of laboratories. Therefore, despite the increased capacity for reproducible sample preparation, the low take-up of any particular device has hindered the comparability of data between research groups. As yet, there has been no rigorous

examination of the crystal sizes obtained from use of these methods, however, it is likely that for the nebulising devices a similar size will be produced as for the air-spray methods i.e. approximately 1- 10 μm. The spotting devices are likely to result larger crystal sizes as each droplet may have a volume of ~ 100 pL and will result in therefore likely cover an area ~ 100 μm when deposited [123] thus restricting the image pixel size to a similar order.

The above matrix deposition methods all require the matrix be dissolved in an appropriate combination of solvents prior to deposition. Whilst these 'wet' methods typically work well, the pursuit of smaller crystal sizes and or solvent free matrix application has led to the development of sublimation [124] and sieving [125] based methods. The potential advantage of a solvent-free approach is that the analyte of interest need no longer be soluble in the system used for the matrix solution [126]. Though this is not the primary motivation of sublimation deposition for tissue imaging applications; the small (< 1 μm), regular and reproducible crystal sizes are. Matrix sublimation deposition is now routinely used by many labs, primarily for imaging of lipids in mammalian tissue sections [127, 128]. The downside of these dry preparation methods for typical tissue imaging applications is that there is poor incorporation of certain analyte classes 'into' the matrix crystals upon crystallisation; a step commonly thought to be aided by the presence of solvent and the time allowed for crystal formation i.e. how 'wet' the preparation protocol is. Consequently these 'dry' coating methods are not suitable for protein analysis and as a result a re-crystallisation method has been developed [129]. This method uses matrix vapour deposition (roughly equivalent to sublimation) to deposit the matrix, the sample is then left in a humidity controlled atmosphere to allow some reforming of the matrix crystals. The idea being that by careful control of this re-crystallisation the small crystal size can be preserved whilst still benefitting from the presence of solvent for analyte extraction from the tissue. The potential for sensitivity

improvements provided by this method has led to other groups employing similar methods of recrystallization or seeding by using both dry and wet protocols in combination [130].

1.3.1.3. Irradiated Area, Pixel Size and Resolution

Pixel size and stage movement settings are important characteristics of any MALDI MSI experiment. A typical MALDI MSI protocol will utilise one of two sampling modes: a continuous or discrete rastering of the stage underneath a fixed laser position [131]. A discrete, spot-to-spot, raster sampling mode (the most commonly utilised sampling mode) consists of a number of laser pulses incident within a single pixel region where the sample stage is either stationary or wanders to enable a fuller ablation of the sample within said pixel region. The pixel to pixel data in this mode will be distinguished by the data acquired by the number of laser pulses incident upon each pixel. A literature example exploring this form of data acquisition is shown in Figure 1.14 [132]. Specifically these concepts are demonstrated in sub-figure (b) of Figure 1.14. Though this example is from an investigation into infra-red matrix-assisted laser desorption electrospray ionisation (IR MALDESI), it is a good example of the nature of discrete raster mode sampling under different specified pixel dimensions / pulse numbers and is exactly parallel to the sampling methodology utilised within UV MALDI MSI applications. It can therefore be seen where the pixel size is reduced the laser pulse area will begin to overlap, a concept known as oversampling [133]. Oversampling is typically considered legitimate if the sample is entirely exhausted in one location prior to moving onto the next overlapping location, so each newly interrogation provides data from a unique area of the sample. In the case of this IR MALDESI example the tissue is completely removed in each new location, within UV MALDI the matrix in each consecutive area of irradiation will be ablated fully, allowing the same conditions to be met.

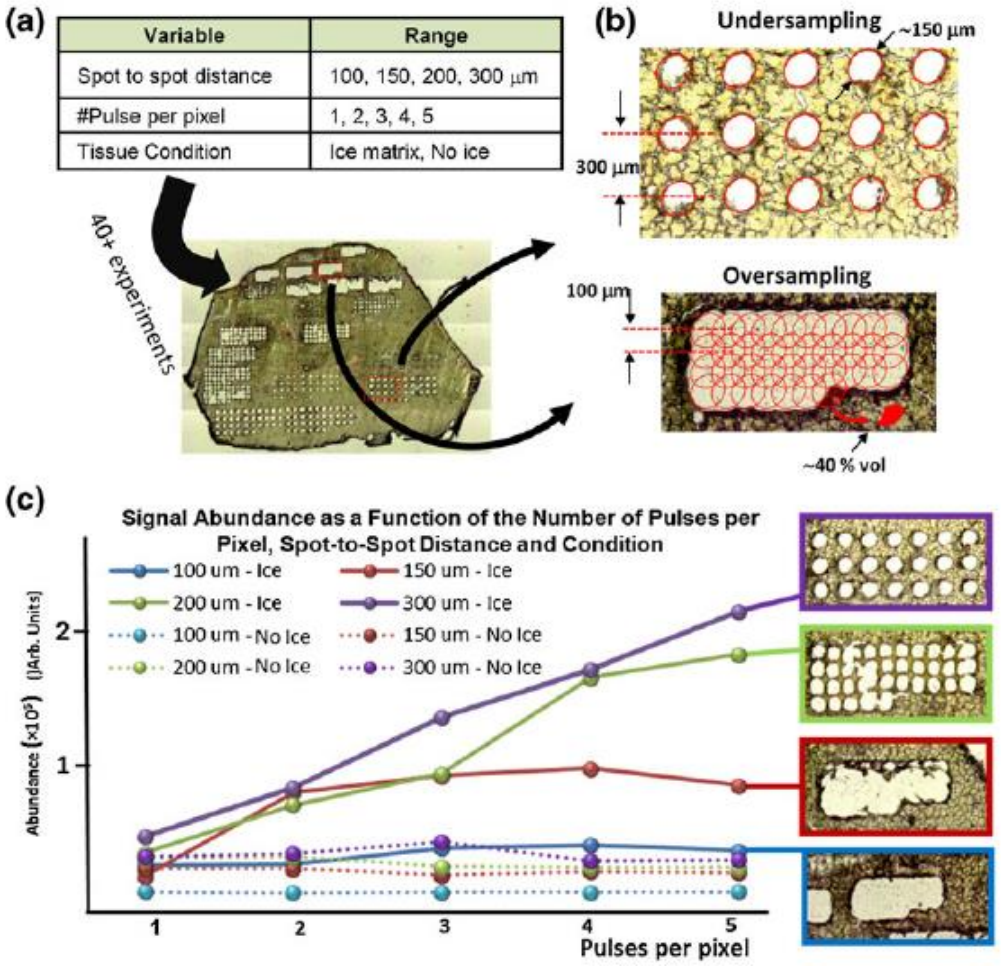

Figure 1.13. (a) Combination of parameters tested on a liver tissue section (50 µm). For each condition, abundance of selected peaks were computed and optical image of the tissue section captured. (b) Undersampling versus oversampling techniques and how overlapping pixels can lead to better spatial resolution. (c) Optical images of ablated tissue and corresponding average abundance for different spot-to-spot distances and number of pulses per pixel. As expected, multi-pulse imaging of tissue sections without an ice matrix did not result in greater signal since all material is ablated after first pulse (also confirmed with optical images). Greater signal can be achieved using ice as a matrix where it becomes a trade-off between spatial resolution and sensitivity. Figure and caption reproduced and adapted with permission from [132].

Continuous raster mode sampling entails the continuous movement of the sample stage under the irradiated region. Here the data ascribed to any particular pixel is distinguished by the ions detected within the time period corresponding the stage velocity combined with the prescribed pixel size. Each mass spectrum, consequently, may contain data in each pixel which in fact originates from the pixels either side. A graphical depiction by the Caprioli group [134] of this sampling process is shown in Figure 1.15. The practical result of the differences between these imaging modes are immaterial for typical MALDI MSI applications, though one can speculate that a certain blurring could occur with continuous raster mode sampling. Oversampling in the y-axis may still be employed in continuous raster mode sampling to reduce the effective pixel size.

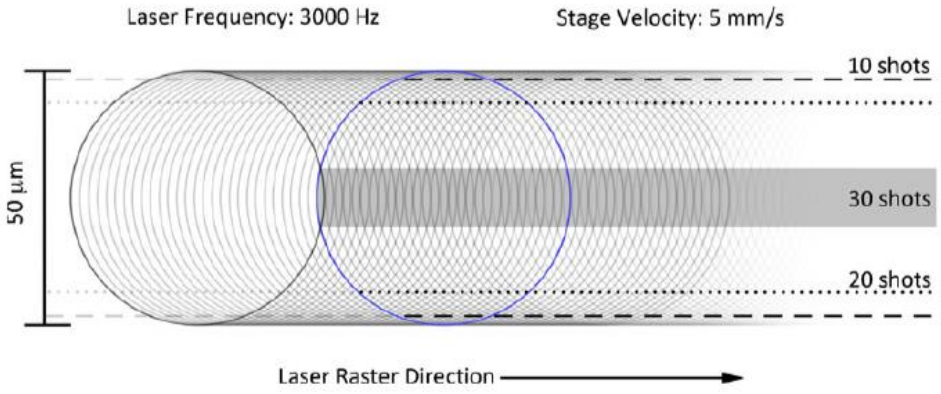

Figure 1.14. An illustration of continuous laser raster MALDI sampling highlighting the number of laser pulses/unit area for a representative laser frequency (3 kHz), laser spot diameter (50 µm) and stage velocity (5 mm s^{-1}). After an initial distance roughly equal to the diameter of the laser beam, the sampling conditions become constant (blue circle) with a maximum of 30 pulses/unit area. Laser pulse overlap decreases for areas further away from the center of the raster path (grey bar). Figure and caption reproduced and adapted with permission from [134].

1.3.2. Applications of MALDI MSI

The unique merits of MALDI MS when translated into imaging applications have led to a rapid take-up of MALDI MSI making it the front-running mass spectrometric imaging technique for biologically relevant applications. The applications of MALDI MSI can largely be grouped into the following areas: pharmaceuticals and their metabolites, lipids, peptides and proteins. MALDI MSI has been used extensively for monitoring the localisation of drugs and their metabolites in multiple organs within test animals [135]. Prideaux *et al.* monitored the spatial distribution of moxifloxacin (MXF) in rabbit lung tissue sections in a post-dose time-course study [136]. The incorporation and removal of the drug in the granulomas was shown over a period of 5.14 hours (Figure 1.16).

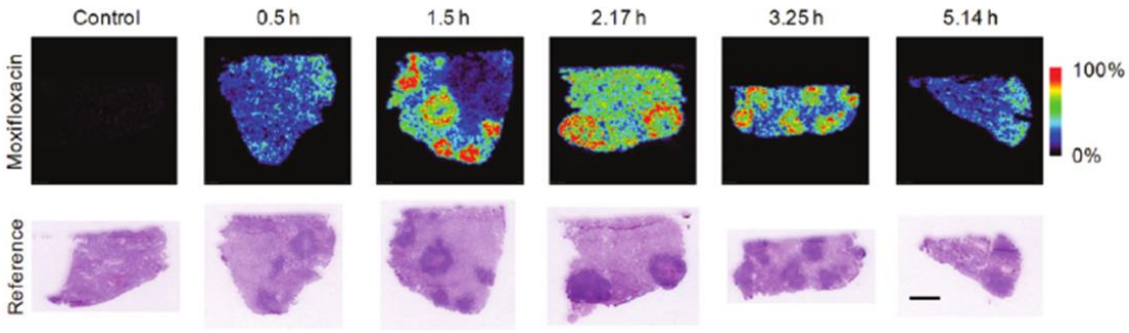

Figure 1.15. MS images showing MXF distributions within the rabbit lung biopsy sections at a defined range of post dose times. A subsequent H&E stained reference tissue section is displayed below these images. MXF is uptaken rapidly into the lung, and accumulation within granulomas occurs from 1.5 h. Granuloma drug levels remain higher than surrounding lung tissue over the remaining time points monitored. Lower levels of MXF are observed within the central caseous necrotic areas of the granulomas in the 1.5 and 2.17 h tissues (necrosis is visible as a light pink centre in the H&E stained reference tissue). Signal intensities are shown as a fixed scale. Scale bar = 5 mm. Figure and caption reproduced and adapted with permission from [135].

Recent advances in instrumentation were utilised by Rompp *et al.* to enable imaging of the drug imatinib at a cellular length (10 μm pixel size) scale in mouse kidney sections [137]. As well as imaging drug distributions in single organs a number of studies have demonstrated drug distributions within single human hairs [138] and in whole animal tissue sections [139].

Peptide and protein distribution studies have featured since the inception of MALDI MSI [107] and much work has been performed on analytes of these classes [140]. Peptide and protein studies in MALDI MSI will typically differ from those of other analyte classes as a tissue wash is likely to be used prior to matrix application [141] to remove unwanted competition for ionisation from other molecular classes such as lipids. Further to this, the large mass of many different protein molecules creates a problem for desorption and ionisation, which is increasingly difficult for these large labile molecules. Currently, in-tact peptides and small proteins detected directly from tissue by MALDI MSI will be below 20,000 Daltons in mass [117, 140, 142]. For example, Elsner *et al.* analysed Barrett's adenocarcinoma tissue sections enabling the discovery of several potential biomarkers distinguishing cancerous and non-cancerous tissue regions [143]. Problems with detecting higher mass proteins have led to a number of other tactics being employed. One method is to perform on-tissue digestion; allowing the characteristic digested fragments of these proteins to be detected, thus inferring the presence of the whole original molecule [144, 145].

Although protein and peptide analysis was one of the main applications in the development of MALDI MS and MSI, the imaging of lipid distributions is now one of the most common applications of this technology, likely due to the large number of distinct lipids which can be readily ionised and detected within a relatively small mass-to-charge window

(~300 – 4500 *m/z* [140]). Lipid distributions have been detected from a large variety of tissue samples, for a wide variety of investigative purposes [146] including: lipid atherosclerotic legions from murine aorta [147]; murine brain samples as part of an investigation of blast induced trauma [148]; whole-body *Xiphosphorus maculatus* fish [128]; insect wing and plant leaf lipid distributions [149]. In addition to these studies of large scale lipid distributions the excellent performance of MALDI MSI for lipid ion detection has been exploited for single cell imaging [150]. For example, Schober *et al.* analysed human HeLa cells with a pixel size of 7 μm to show sub cellular lipid distributions [151].

1.4. Mass Analysis

1.4.1. Time-of-Flight (ToF) Mass Analyser

After their creation, ions will be travelling with some velocity depending upon the kinetic energy imparted to them in the process of desorption / ablation and ejection from the sample. An electric field, between sample plate and extraction grid or orifice, is then applied. The ions will then be accelerated to some velocity dependent on the field strength, the length of time the ion is in the field and the mass-to-charge ratio of the ion. The mass-to-charge ratio of the ion can then be determined by the time taken to travel a known distance i.e. the field free region. A schematic of a linear MALDI-ToF setup is shown in Figure 1.17.

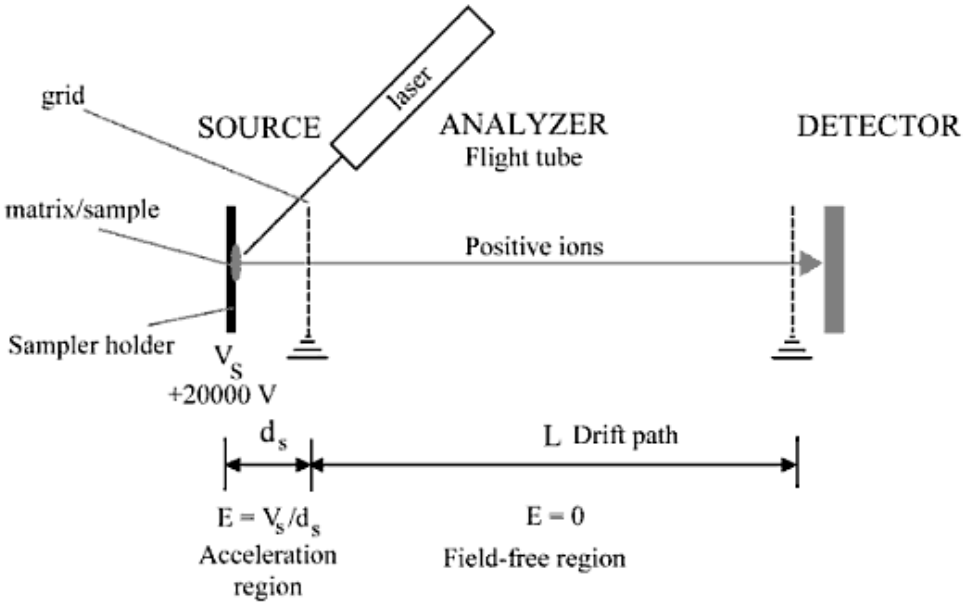

Figure 1.16. Schematic of a linear time-of-flight instrument setup. Figure reproduced with permission from [152].

After an ion leaves the extraction area it will have approximate kinetic energy, E, according to Equation 5.

$$E = \frac{mv^2}{2} = ZeV \qquad (5)$$

Where *m* is the ion's mass, *v* its velocity, *z* is its charge, *e* is one unit of elementary charge and *V* is the potential difference of the electric field. The time-of-flight, *t*, is then calculated from

$$t = \frac{d}{v} \qquad (6)$$

where *d* is the length of the analyser's field free region. Then by combining Equations 5 and 6 the mass to charge ratio of the ion in question can be calculated.

$$t^2\left(\frac{2Ve}{d^2}\right) = \frac{m}{z} \qquad (7)$$

Equation 7 shows that the smaller the mass to charge ratio of the ion the faster it will reach the detector .

The mass resolution and mass accuracy of ToF mass analysis can be affected by, amongst other things, initial variations in the temporal and spatial distribution of the ions within the desorbed plume, causing an increased temporal spread of ions of the same *m/z* arriving at the detector. This can be mitigated to a certain extent with the use of techniques such as delayed extraction and reflectron time-of-flight. Both of these techniques can improve the mass resolution of ToF-MS by helping negate time of flight differences, for ions of the same *m/z*, created by initial differences in kinetic energy / velocity and start-position (height) of desorbed ions [152-154]. Delayed (pulsed) ion extraction is commonly implemented in linear or reflectron ToF instrumentation due to the strong dependence of mass resolution on phenomena such as initial molecule/ion velocity, sample height variation or sample charging effects. Delayed extraction allows some fixed time period between the ion creation event, in MALDI MS the arrival of the laser pulse at the sample, and the application of an electric field to extract those ions into the mass analyser. An example of the improvement in mass resolution bought about by delayed extraction is shown in Figure 1.18.

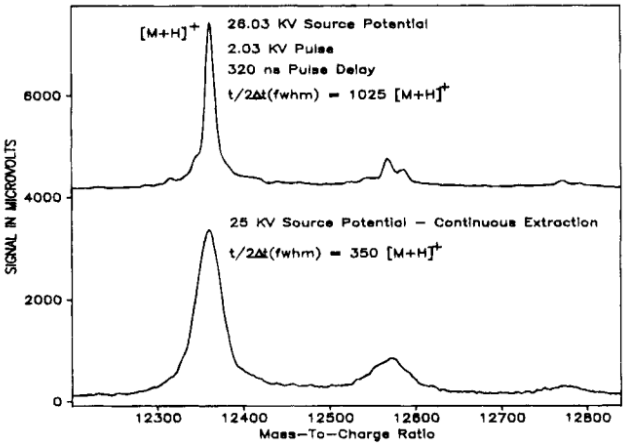

Figure 1.17. Typical MALDI (sinapinic acid matrix) mass spectra comparing the protonated molecular ion region of cytochrome c obtained with pulsed ion extraction (top) versus continuous ion extraction (bottom). Figure and caption reproduced with permission from [153].

Reflectron ToF enables improvements in mass resolution due to similar concepts of ion acceleration (and deceleration) balancing differences in kinetic energy for ions of the same *m/z*. A schematic showing these concpets is shown in Figure 1.19.

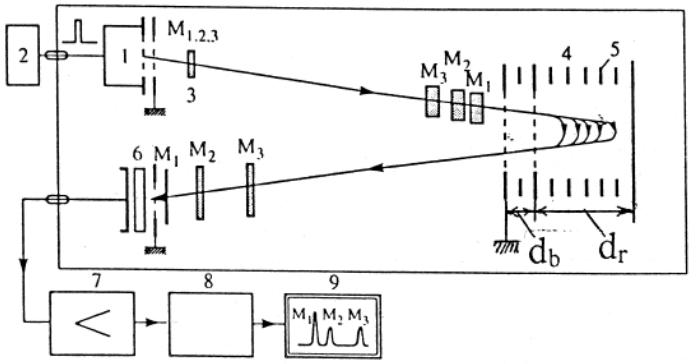

Figure 1.18. TOF mass spectrometer with a two-section reflector with plane electric fields. 1-pulsed ion source; 2-power supply (laser); 3-focused ion packet near the ion source; 4-double sectional reflector; 5-electrodes for creation of plane electric fields; 6-detector; 7-wide band amplifier; 8-computer; 9-display; d_b—the ion deceleration section; and d_r—the ion reflection section. Figure and caption reproduced and adapted with permission from [154].

Ions of the same *m/z* entering the reflectron (ion-mirror) portion of the reflectron ToF instrument will have a kinetic spread, as represented by the width of the boxes $M_{1,2,3}$ in Figure 1.19. Ions with a larger kinetic energy will penetrate further into the ion-mirror compared to those with less kinetic energy, causing the lower energy ions to reflect at an earlier point in space and time. Those ions penetrating further into the ion-mirror will acquire a correspondingly larger amount of kinetic energy upon re-acceleration due to the larger potential difference experience within the ion-mirror after reflection. By tuning the electric fields within the ion mirror the focal plane of ions of the same *m/z* can be tuned to sit at the detector surface, minimising the temporal spread of the ions as they arrive there and thus improving the mass resolution.

1.4.2. Quadrupole Mass Analyser

Quadrupole mass analysers (or ion guides) consist of four precisely aligned, parallel conducting metal rods and are similar in theory and operation to hexapole and sextapole mass analysers. An electric field is applied between these rods enabling the transmission of ions through the quadrupole ion guide. The quadrupole will typically operate in one of two modes: radio frequency (r.f.) only mode or mass filter mode. When operating in r.f. only mode the quadrupole will transmit ions with a wide range of *m/z* values and effectively acts as an ion transmission and focussing device. When operating in mass filter mode both direct (DC) and r.f. currents are applied between the rods. An ion passing through the quadrupole will be attracted to the rod with electrical charge opposite to its own. When this potential is switched the direction of attraction will change accordingly. Thus, the path of the ion oscillates as it passes through the length of the quadrupole. A schematic of this set up is shown in Figure 1.20.

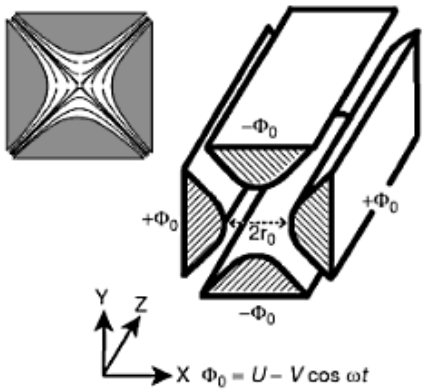

Figure 1.19. Hyperbolic quadrupole rods with applied electric potentials, Φ_0, equipotential lines shown in top left. $2r_0$ is the distance between neighbouring rods. U is the d.c. potential, V is the amplitude of the RF voltage, ω is the angular frequency of the RF field, Φ_0 is the applied electrical potential, r_0 is the distance between neighbouring rods and t is the time of flight. Figure and caption reproduced with permission from [152].

By adjusting the strength of these fields and the frequency of the RF potential, the path stability for ions of a given *m/z*, passing through the quadrupole, can be tuned. Therefore, an ion of specific *m/z* can be given a stable path through the quadrupole, where ions of differing *m/z* will have unstable trajectories and so will not reach the mass analyser [155]. Quadrupole analysers are not high mass accuracy devices and are usually set to transmit ions with $\Delta m/z$ = 1 or 2 atomic mass units to ensure the passing of the ions of interest. This feature of quadrupole ion guides allows the selection of a specific *m/z* (and so molecule) by a first quadrupole (Q1), this molecule can then be transmitted to another quadrupole (the collision cell quadrupole, q) operating in r.f. only mode. The collision cell is supplied with an inert gas, often nitrogen or argon and will be at a higher pressure than Q1. The collision of the selected precursor ion with this gas will result in the creation of fragment ions. These ions can then be separated by a second mass analyser, for example another quadrupole or time-of-flight, allowing further structural characterisation of the selected precursor ion. This type of analysis is known as tandem mass spectrometry and is abbreviated as MS/MS.

Quadrupoles are traditionally used as ion-guides, ion mass filters and collision cells in triple quadrupole (QqQ) and quadrupole time-of-flight (QqToF) instruments. A schematic of the QSTAR XL (AB Sciex) QqToF MS setup of the type used within this thesis is shown in Figure 1.21.

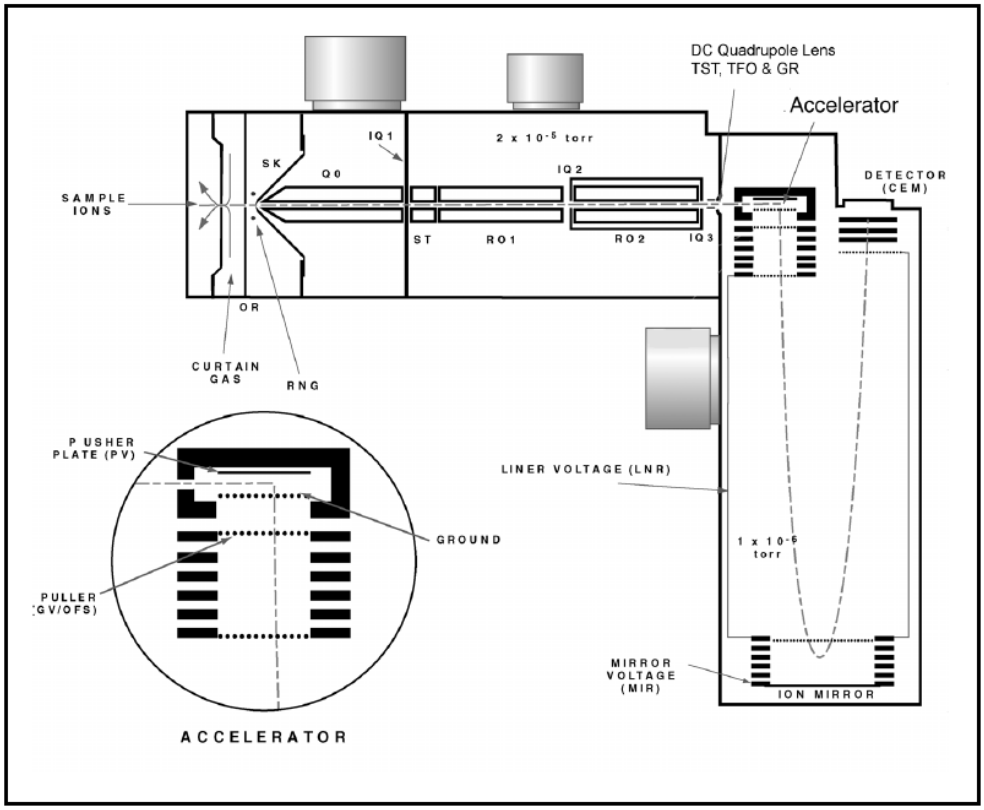

Figure 1.20. Schematic of a QSTAR XL QqToF instrument of the type used within this thesis. Figure reproduced from QSTAR XL hardware manual.

1.5 – Introduction to Thesis

This thesis reports a series of investigations into MALDI MSI related issues with particular relevance to the use of laser repetition rates above 1000 Hz. As improvements in throughput are sought within MALDI MSI applications, the use of high repetition rate lasers is becoming increasingly common. This thesis involves the investigation into parameters relevant to the use of a Nd:YVO_4 high repetition rate laser (1 – 25 kHz) and the subsequent application of the laser to MALDI MSI investigations. It is split into seven chapters with the first being this introductory literature review.

The second chapter of this thesis investigates the spatial profile of the laser beam using CCD and fluorometric methods to enable imaging of the profile both outside and inside the MALDI MS ion source. A comparison was made between the CCD and fluorometric methods and a practical application of the use of laser beam profiling in MALDI is demonstrated.

Chapter 3 concerns the comparison of a high repetition-rate Nd:YVO_4 laser and a N_2 laser for MALDI MS in continuous raster sampling mode. Here, the influence of laser pulse repetition rate and stage raster speed on detected ion intensities are systematically investigated for both lasers. The Nd:YVO_4 laser is shown to enable improved ion intensity as compared to the N_2 laser; though some counterintuitive trends are seen within this data. Consequently the influence on the ion intensity of varying repetition rate, raster speed and laser attenuation are investigated for the Nd:YVO_4 laser to better understand the trends seen in the earlier comparison. The complexity of the data and trends therein, as investigated within Chapter 3, led to a further investigation into the variation of repetition rate and raster speed in continuous raster sampling mode with the Nd:YVO_4 laser. Chapter 4 incorporates improved control of the energy per laser pulse with the aim of simplifying the system under investigation. The influence of the stated variables on the molecular ion form (i.e. $[M+H]^+$ versus $[M+Na]^+$) or the amount of analyte fragmentation seen are examined. Further to this, the investigation was carried out in tissue samples where similarly complex trends were evident.

The knowledge acquired within Chapters 3 and 4 regarding the optimal conditions for high throughput tissue imaging using the Nd:YVO_4 laser is put to use within Chapter 5. Here the matrix *para*-nitroaniline (PNA) is investigated as a suitable matrix for MALDI MSI of mouse brain tissue sections using the Nd: YVO_4 laser is. A comparison of the image data is

made to equivalent data acquired using α-cyano-4-hydroxycinnamic acid (CHCA), a common matrix for high throughput MALDI MSI applications.

Chapter 6 explores the fact that high repetition-rate lasers, when operated in oversampling continuous raster mode imaging, may remove most or all of the matrix coating. The opportunity this provides to repeatedly analyse a single tissue section, with the aim of improving the quality and amount of information obtained from said tissue section, is thereby explored.

Finally, within Chapter 7, the conclusions of each chapter are expanded upon with regards to the possibilities for further experimentation and studies.

Chapter 2

Fluorometric Beam Profiling of UV MALDI Lasers

2.1. Introduction

The ion yield detected via matrix assisted laser desorption ionization mass spectrometry (MALDI MS) is heavily dependent upon the fluence of the laser incident upon the sample surface. Ion yields, Y, in MALDI-MS depend upon the incident fluence, H, according to the power law relation $Y \sim H^m$ where m is the gradient on a log-log axis [29]. Consequently the distribution of photons within the laser spot as projected onto a sample is of fundamental importance to the process of MALDI MS [23, 33]. Additionally, in order to calculate the fluence, a measure of the dimensions of the incident laser beam profile is required.

Holle *et al.* [33] and Qiao *et al.* [23] both reported upon the significance of the beam profile with respect to the MALDI MS ion yield. In these two studies the photon distribution of the incident laser beam profile was manipulated to determine and optimize its effect on the detected ion yield. In order to measure these profiles the source optics were replicated and / or modified to allow measurements of the beam profile, a tactic which is beyond the scope of most MALDI researchers. There are a number of reported methods for measurement of aspects of laser beam positioning and profile including: burn marks [156], accurate calibration

of beam profiling setup [24], scanning knife edges or slits [157], pinhole [158], charge couple device (CCD) [33, 159] and ablation of matrices [23, 133] or other substances [160]. All methods will suffer from some ambiguity as to the proportion and distribution of the area measured which is above the effective MALDI fluence threshold for a given matrix [24, 25] but it is nonetheless necessary to obtain this information. The majority of beam profiling methods listed above require relatively expensive specialist equipment / modifications to the MALDI ion source and typically the beam profile will be acquired off line and out of source.

It is known in many fields that certain substances will fluoresce when irradiated by certain wavelengths of light. Lasers used in MALDI MS typically operate at ultraviolet (UV) wavelengths. Standard CCD / complementary metal oxide semiconductor (CMOS) type imaging systems may not work efficiently at these wavelengths. Therefore, one route toward the imaging of ultraviolet laser beam profiles is to image the fluorescence emitted from an appropriate material illuminated by the UV laser; provided the Stokes shift is such that the emitted wavelength is detected efficiently by the imaging setup used. This has been performed in other in non-MALDI MS applications [161] with the use of doped fluorescent glass and a standard CCD imaging setup, allowing the capture of beam profile information at a relatively low cost. Other materials also fluoresce under UV light including the whitening chemicals commonly used in the production of card and paper [162] and also MALDI-MS matrices themselves [103, 130].

2.2. Experimental Methods

2.2.1. Materials

Methanol (HPLC grade) used in preparation of all matrix solutions was purchased from Fisher Scientific (Leicestershire, UK). The water used was purified by an ELGA Option 3 system (Marlow, UK). Trifluoroacetic acid (TFA, 99 % purity) and MALDI matrices α-cyano-4-hydroxycinnamic acid (CHCA) and *para*-nitroaniline (PNA) were purchased from Sigma Aldrich (Dorset, UK). The TEM grid (G2400C) was purchased from Agar Scientific Ltd. (Essex, UK). Lipid standard phosphatidylcholine (PC) 34:1 (18:1 / 16:0) with mass of 759.578 was purchased from Avanti Polar Lipids Incorporated (Delf Zyl, Netherlands). The VRC1 UV/VIS detector card (250 to 540 nm excitation; 525 to 650 nm emission) was purchased from ThorLabs (Ely, UK) and the Lumilass fluorescent glass filter type B (peak excitation at 365 nm; peak emission at 405 nm) was purchased from Edmund Optics (York, UK). The MALDI MS sample plates used were smooth surfaced stainless steel imaging plates from AB Sciex (Ontario, Canada)

2.2.2. Laser Beam Profiling

Firstly, the beam profile was measured using a Spiricon LBA 300 beam profiling system with a Pulnix TM6 camera. Secondly, the laser was directed at a sheet of A4 paper (Office Depot, Leicester UK – Green Paper, high white recycled paper, 80 gm^{-2}). The distance of the laser focusing optics (for pre-fibre) or fibre exit-aperture (for-post fibre) dictates the size of the projected image and therefore the whole beam profile was imaged in all cases. The resulting fluorescent emission was then photographed using a ThorLabs DCC1545M monochrome CMOS camera. The beam intensity per unit area was attenuated such that no

paper degradation was observed for the entire duration of data acquisition (> 30 minutes). To image single pules beam profiles the above CMOS camera was replaced with a Casio EX-FH100 operated in high speed video mode of 1000 frames per second (fps).

The beam spot size as incident on the MALDI plate in-source was measured via the same fluorometric method using paper as well as using the UV/VIS detector card and fluorescent glass filter. The existing source view camera supplied with the QSTAR XL was removed and replaced with the CMOS camera listed above. This was used in conjunction with a neutral density filter to image the beam profile on the sample plate, within the ion source. Again the beam was attenuated such that there was no observed photo-bleaching during the course of the acquisition. The in-source beam profile dimensions were also estimated from the ablation of matrix. CHCA was applied to a microscope slide via the air-spray method. The ablated raster tracks and spot were then imaged in bright field (Zeiss LSM 710 ConfoCor 3) at 10 × magnification.

2.2.3. Tissue Preparation and Sectioning

Mice were sacrificed humanly at the School of Cancer Sciences, University of Birmingham in accordance with the Home Office Animals (Scientific Procedures) Act 1986 [163]. Mouse brains were flash frozen in liquid nitrogen immediately after excision (fresh frozen). Tissue sections were acquired at 12 μm thick and thaw mounted onto an AB Sciex MALDI imaging plate (Warrington, UK). Sectioning was performed on a Leica CM 1850 Cryostat (Milton Keynes, UK).

2.2.4. Matrix Application

For the lipid standard analysis PC 34:1 (1 mg mL^{-1} in 80 % CH_3OH, 0.1 % TFA) was mixed 1:9 (*v:v)* with 10 mL of CHCA (20 mg mL^{-1} in 80 % CH_3OH, 0.1 % TFA) and for prior to airspray deposition of a thin homogenous layer on MALDI imaging plate. For tissue analysis 15 mL of PNA (20 mg mL^{-1} in 85 % CH_3OH, 0.1 % TFA) was dispensed in total using an artist airbrush purchased from Draper Air Tools Airbrush Kit (Hampshire, UK) propelled by dry N_2. The airbrush nozzle was held approximately 20 cm from the plate. Three consecutive spray passes were followed by fifteen seconds dry time. This process was repeated four times then the plate was rotated on the clamp stand by ninety degrees. This sequence was repeated until all matrix solution was used.

2.2.5. Mass Spectrometry

Mass spectrometric data were acquired with an AB Sciex QSTAR XL QqTOF instrument with an oMALDI 2 ion source using Analyst QS 1.1 with oMALDI server 5.1 (AB Sciex). Ion focusing within the mass spectrometer was optimized prior to data acquisition. Data was accumulated for 1 second per mass spectrum and acquired in manual tuning mode. An Nd:YVO_4 (Elforlight: SPOT-10-100-355) DPSS laser with λ = 355 nm, operated at a 5 kHz repetition rate and > 1.5 ns pulse length was used in this study. The Nd:YVO_4 laser was triggered by a Thurlby Thandar Instruments (Huntingdon, Cambridgeshire) TGP110 10MHz Pulse Generator. The laser was coupled to the MALDI source via a 100 μm core diameter fibre-optic patchcord (Edmund Optics, NA = 0.22). All fibres used were of this specification and brand.

2.2.6. Data Analysis

MALDI data analysis was carried out using Analyst QS 1.1 and MATLAB. The data were converted from AB Sciex proprietary file format (.wiff) to .mzML using AB MS Data Converter (AB Sciex version 1.3) and then converted to imzML using imzMLConverter [164] and processed in MatLab (version 7.8.0 (2009a), Math Works Inc., USA). Beam profile images were also processed in MatLab. Further image processing was performed in GIMP (GNU Image Manipulation Program) 2.6.11.

2.3. Results and Discussion

2.3.1. Laser Beam Profiling Outside of the MALDI Ion Source

In MALDI-MS, the beam profile as incident on a sample is extremely important when considering the detected ion yield [23-25]. Therefore, it is instructive to investigate the influence (if any) that selected variables have on the spatial intensity distribution of the laser beam profile. This can inform the inclusion or exclusion of the beam profile as a variable parameter in a given MALDI-MS experiment. It has previously been shown that UV laser beam profile information can be obtained using a non-UV-sensitive imaging setup with the aid of fluorophore doped glass [161]. This idea can be implemented using any substance that fluoresces under the laser wavelength used (355 nm in this case) and has a large enough Stokes shift to enable detection of the emitted radiation by the camera used. Standard white office paper will fluoresce with a peak at around 420 nm when exposed to wavelengths in the approximate region 300-400 nm [162]. The emitted fluorescence from paper after illumination with the Nd:YVO_4 laser used in this study was imaged as projected from the laser (pre-fibre) and after transmission through an optic fibre (post-fibre) at repetition rates of

5, 10, 15, 20 and 25 kHz; these images are displayed in Figure 2.1. Single line pixel intensities through the centre of each image A through F of Figure 2.1 are displayed in Figure 2.2. The consistency of pre-fibre beam profile shape can be seen, especially where the intensity is normalized as shown in Figure 2.2 B.

The pre- and post-fibre beam profile at laser pulse repetition rates of 1, 5, 10, 15, 20 and 25 kHz were also imaged using a specialist beam profiling CCD setup for comparison to the fluorometric method (Figure 2.3). In agreement with previous publications we find a Gaussian beam profile pre-fibre (Figures 2.1 A-E, 2.2 and 2.3 rows A and C) and speckle pattern beam profile post-fibre (Figure 2.1 F-J and Figure 2.3 rows B and D) [21, 23, 33, 165]. The beam profiles appear to be consistent across the range of repetition rates, though slight differences in the speckle pattern can be seen across the repetition rates. Asymmetries in the pre-fibre profiles shown in Figures 1 and 3 are due to the slight deviation from orthagonality of the laser beam as incident to the fluorescent screen. It is worth noting that the exposure used for every image was 1 / 60^{th} of a second. Accordingly images at each repetition rate are the average of approximately 83, 167, 250, 333 and 417 pulses at 5, 10, 15, 20 and 25 kHz respectively. Due to the large number of pulses contributing to even the 5 kHz,

images the different pulse numbers contributing to the images are not considered to be a biasing factor to the shape of the profiles seen. Further to this, the energy per pulse delivered by the Nd:YVO_4 is dependent upon the repetition rate selected (see next chapter for further discussion on this topic). This too will contribute to intensity differences between beam profile images at different repetition rates. Due to these issues each beam profile image shown in Figures 2.1, 2.2 B and 2.3 are normalized to the same intensity scale for ease of comparison.

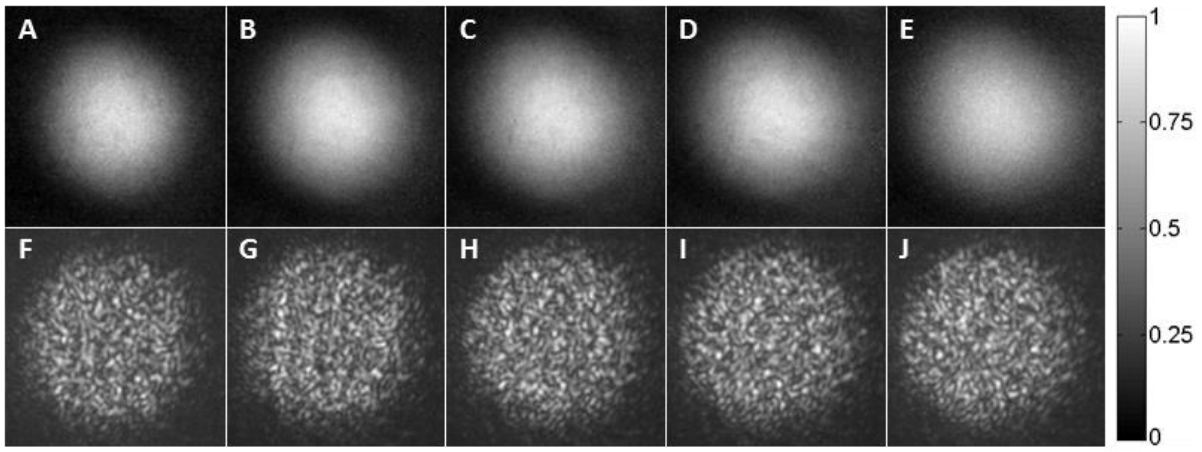

Figure 2.1. A-E) pre-fibre and F-J) post-fibre beam profiles of the Nd:YVO_4 laser at 5, 10, 15, 20, 25 kHz respectively. The physical diameters of each image shown are approximately: top row = 4 cm and bottom row = 8 cm. Detailed information regarding speckle patterns can be obtained easily from imaging laser induced fluorescence.

Another way to view the similarity of the pre-fibre beam profiles is to plot the intensity of a single line of pixels through the centre of the beam profile image at each repetition rate. This data is shown in Figure 2.2 for the profiles in Figure 2.1 A - E. The difference caused by the intensity scale normalization is demonstrated by the difference between Figures 2.2 A and B.

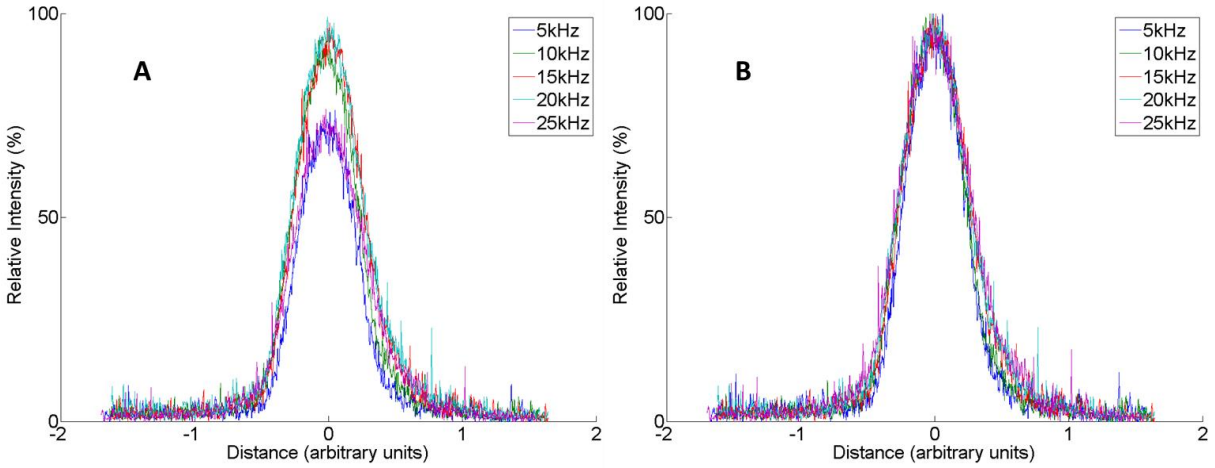

Figure 2.2. Intensity detected from single line of pixels through the centre of each image in Figure 1 A-E. Intensity differences due to differing pulse number and pulse energy can be seen in A but normalization of the intensity scales to the same maximum value largely removes these differences (B) and demonstrates the similarity of the pre-fibre profiles across the repetition rates investigated. Distance along the x-axis relates to the number of pixels in the original images; as these were not precisely calibrated an arbitrary (linear) distance value is displayed.

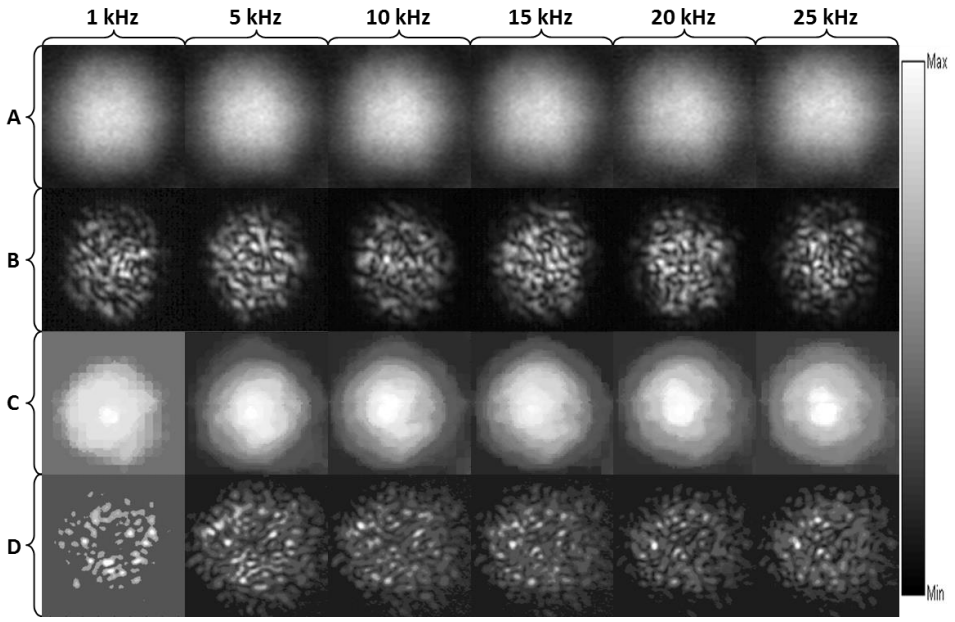

Figure 2.3. Laser beam profile imaged using: paper fluorescence A - pre-fibre and B - post-fibre; CCD beam profiling system for C - pre-fibre and D - post-fibre. The physical diameters of each image shown are approximately: row A – 5 cm, row B – 10 cm, rows C & D – 4 mm. The intensity scale represents the normalized range of intensities detected in each image. The fluorometric method performs well in comparison to the commercial system used here.

Beam profiles shown at 1 kHz in Figure 2.3 C, D appear different due to the reduced energy output of the laser at this repetition rate in combination with the neutral density filters used resulting in a reduced portion of the beam reaching the CCD threshold power. Other variations in speckle pattern in this experiment were likely due to slight variations in fibre position between image acquisitions altering photon paths within the fibre and consequently the nature of the mode mixing. The laser beam profile is therefore not thought to change as a result of the repetition rate used in this study, but is likely to change to some extent on a pulse to pulse basis due to slight movement of the optic fibre with instrument vibration and air

currents. The similarity of the images shown in Figure 2.3 demonstrates that the results obtained using the fluorometric method are reliable and may even, under certain conditions, give improved contrast and detail over the CCD beam profiling system used here.

To determine whether the post-fibre beam profile changes on a pulse to pulse basis we can first consider the beam profiles shown in Figures 2.1 and 2.3. The fact that the speckle images show well defined maxima and minima suggests that any changes in beam profile on a pulse to pulse basis will at least vary around some average position; if this were not the case and any pulse to pulse change were random then we would likely see an approximately Gaussian post-fibre pattern like that observed by Trim *et al.* [165] upon vibration of the fibre. Alternatively, we could assume there were no changes on a pulse to pulse basis. To further check this single pulse images were acquired using a 1000 fps camera. The laser was operated at 400 Hz to comply with the Nyquist rate when sampling at 1000 fps, preventing aliasing of the sampled profiles from pulse to pulse. Despite this, the information obtained at 400 Hz should be valid for the same processes at the other, higher, repetition rates studied within this work. Four single pulse profiles are displayed in Figure 2.4. When acquiring these images effort was made not to induce movement of the optic fibre.

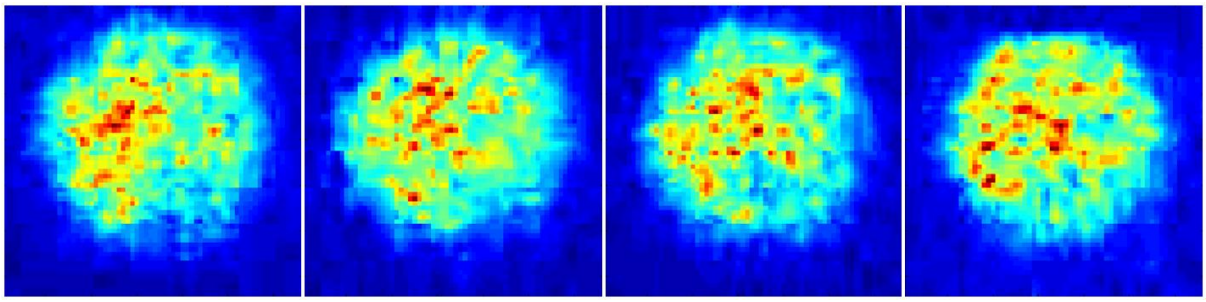

Figure 2.4. Images of the fluorescence emission from paper of four sequential single laser pulses from the Nd:YVO_4 laser operated at 400 Hz were acquired with a 1000 fps camera. Pulse to pulse differences in the intensity distribution are seen. No size scale calibration was carried out for this image acquisition but the height of the visible fluorescent area within these images is ~ 10 cm.

The camera used to acquire the images in Figure 2.4, when operating in high frame rate mode, bins a number of pixels together to increase the signal-to-noise ratio and decreasing the pixel digitization readout time. This enables the higher frame rate to be sufficiently sensitive to produce useful images, though this comes with a corresponding reduction in image resolution. Despite this, the images in Figure 2.4 still provide useful information. The four single laser pulse images in Figure 2.4 each show differences suggesting that pulse to pulse changes in beam profile are present during normal operation of the laser system used. To provide further insight into these phenomena the beam profile was imaged with the Spiricon system to demonstrate the consistency of profile when many pulses (~1000 in this instance) are summed as well as the influence of the fibre's position on the profile. These images show very similar beam profiles in two frames (Figure 2.5 A is similar to B and C is similar to D). Between B and C the fibre was bent into a different position and remained in this position for the remainder of time in which data (including images C and D)

was collected. The influence of the fibre's position, and the consequent nature of the mode mixing, is clearly shown, as is the consistency in beam profile photon distribution when the fibre is not moved. Therefore, it seems likely that under normal operation, where the fibre undergoes no visible movement, the beam profile will remain a stable distribution on average but will actually change on a pulse to pulse basis around said average, giving the appearance of stability where many pulses are summed for one image (like those in Figures 2.1, 2.3 and 2.5).

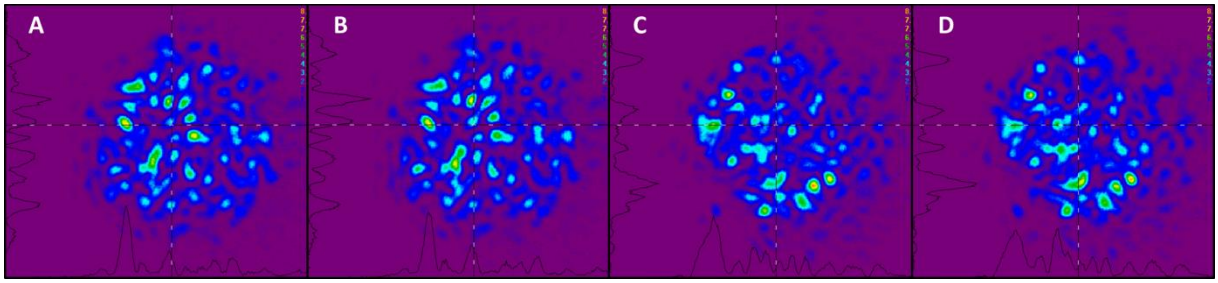

Figure 2.5. Beam profile images taken from a video acquired with the Spiricon beam profiling system of Nd:YVO_4 laser operated at 5 kHz and delivered through a 100 µm fibre. Profiles A and B are different frames separated by several seconds, as are C and D. Between A, B and C, D the fibre was held still. Between B and C the fibre was bent into a different shape, changing the mode mixing within, causing a different beam profile to be projected. No size scale calibration was carried out for this image acquisition but the diameter of the beam profile within these images is ~ 0.5 cm.

A surface plot of the speckle pattern (taken from data shown in Figure 2.3 B at 15 kHz) is shown in Figure 2.6 alongside images showing the 3-D speckle patterns corresponding to the area of the beam profile with intensity above 40, 50, 60 and 70 % of the

maximum value (Figure 2.6 B, C, D, and E respectively). Additionally a graph of the relationship between the incident pulse energy and detected fluorescence intensity is shown (Figure 2.6 F). This shows the impact of the beam profile when considered in light of the threshold fluence and power law dependence. If, for example, the threshold energy of a matrix sits at 40 % of the peak energy of the recorded profile then ions will be generated from the area shown in Figure 2.6 B. Whereas if the matrix requires 70 % of the peak energy to produce ions then only the area shown if Figure 2.6 E will be sampled from; an order of magnitude decrease in the area actually being interrogated or ~ 29 % of the total image area in Figure 2.6 B compared to ~ 2.3 % in Figure 2.6 E.

The linear response of the fluorescence from paper *vs*. incident energy shows that the emitted fluorescence can be used as a measure of the incident power and therefore the incident energy per pulse (when the attenuation and repetition rate of the laser is held constant, as in this case). This is important as it provides validation for the fluorometric profiling methodology. As the fluorescence response to incident energy is linear then the relative detected intensities are quantitative: the profiles shown in the obtained images are a true reflection of the incident laser beam profile. The linear response of fluorescence with incident laser energy over a given intensity range has been shown previously for laser induced fluorescence applications [161].

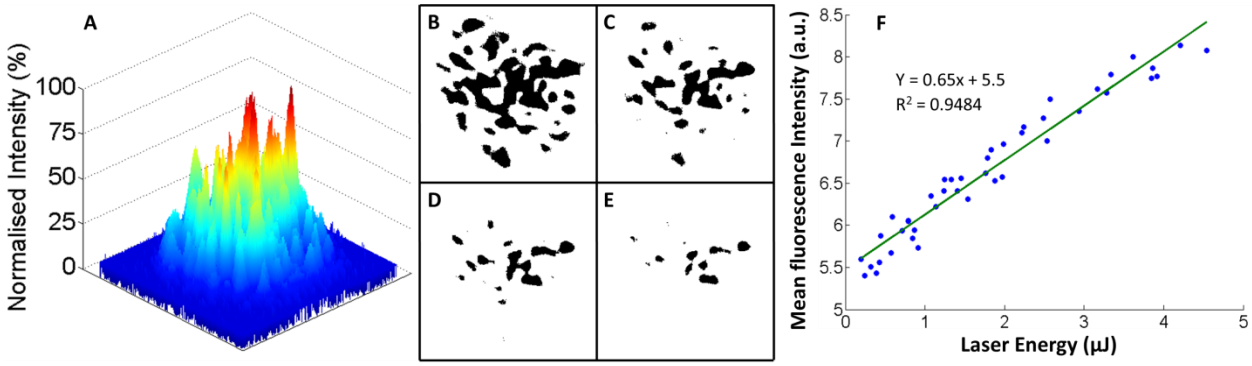

Figure 2.6. A - Surface plot of beam profile shown in Figure 1 B at 15 kHz. The portion of profile delivering above 40, 50, 60 and 70 % of peak intensity are shown in B, C, D and E. They illustrate potential regions of speckle pattern above threshold energy accentuating the possible impact of the speckle pattern on the ion yield. Graph F shows the good linear fit between incident energy and the mean of the total fluorescence intensity from the corresponding beam profile image. The intercept of the fitted line in graph F is not at zero due to detected background light.

This raises an important issue regarding the consideration of the beam profile as incident upon the sample surface. Due to the relationship between fluence and ion yield in MALDI-MS, the spatial distribution of incident photons will directly influence the number of ions created from different areas within the laser spot itself. If the total fluence incident on the sample in the area of the laser spot directly translates to a given number of ions, then the same rule will hold for smaller areas within the laser spot itself. A study by Holle et al. [33] showed that certain photon distributions within the beam profile result in superior ion yields. It has also been shown that manipulating the patchcord in fibre-optic delivered MALDI-MS systems can improve the ion yield [23, 165]. These studies show that the distribution of photons within the beam profile can be optimized and, by extension, that knowledge of these factors

can inform a greater understanding of the MALDI-MS process. Measurement of the beam profile is vital to performing both of these functions.

When using commercial systems to measure laser beam profile and pulse energy both an energy sensor and a CCD camera are required. The linearity of the CCD response used to measure the laser profile is relied upon to allow the measured profile to be related to the energy / power of the laser incident on the detector. The linearity between total image fluorescence and laser power shown in Figure 2.6 demonstrates that these considerations are also valid when using the fluorometric beam profiling technique in conjunction with an energy / power meter, at least within the energy density range considered here.

Due to the importance of the beam profile in relation to the ion yield within MALDI-MS the fluorometric method can be used to give further information in certain experiments *e.g.* fibre manipulation [165], alteration of fibre diameters or lengths [23], also issues of fibre misalignment or damage. An illustrative example of investigation into the effects on ion yield of differences in beam profile is shown in Figure 2.7. Six fibres with identical specifications but different amounts of previous usage were used to acquire data by MALDI MS under identical operational parameters. The total ion count resulting from the use of each fibre (A-C) is seen to increase according to the fluorescence intensity relation of each corresponding fibre's beam profile (graphs 1 and 2 in Figure 2.7) *i.e.* the brightest fluorometric beam profile (total fluorescence) corresponds to the fibre which provides the data with the largest mean TIC and best quality spectra (largest signal to noise). This relation results from the fluorescence intensity – energy relationship shown in Figure 2.6 - F in conjunction with the ion yield vs. fluence relation discussed in the introduction ($Y \sim H^m$ [29]). The fluorometric method provides a route by which changes in the ion yield caused by an alteration of the laser beam profile can be monitored in an easy, low cost fashion. In addition to the fibres with

relatively similar profiles yet differing transmissions (A-C) three other fibres were also investigated (fibres D, E and F). These fibres have damage causing more dramatic changes to the beam profile itself. The total ion counts obtained in MALDI MS experiments from both thin layer CHCA and lipid standard and from CHCA on mouse brain tissue sections when using each of these fibres (D-F) are shown in graph 3 of Figure 2.7. It is interesting to note that despite potential inhomogeneity in the tissue molecular composition, the ion counts for the lipid standard and tissue follow similar trends. This is what would be expected if the dominant variable within the experiments was the fibre used (and consequently the energy deposited per pulse). The fluorometric method is therefore shown to provide useful information, allowing the relation of the beam profile of the fibre used within a MALDI MS experiment to be related to the ion intensities detected within said experiment.

To further demonstrate the differences seen in ion count due to use of fibres A, B and C example spectra are shown in Figure 2.8. The difference in overall intensity for specific peaks can be seen. In addition, there appears to be some change in the relative abundances of detected ions depending upon the fibre used. This may be because of the differences in fluence delivered per pulse due to the different damage and therefore transmission of light within each fibre. Alternatively, the differences in tissue location from which each spectrum is acquired may be causing the differences. However, as large areas were summed from during the data acquisition, the differences in total ion count causing the trends seen within Figure 2.7 are not thought to be due to tissue inhomogeneity. Whilst spectral differences due to variations in fluence and beam profile (as in this study) are of interest, and may be worthy of further study, the main issue in this instance is the ability of the fluorescence intensity emitted from paper to provide an indication of fibre damage as correlated with detected ion intensities.

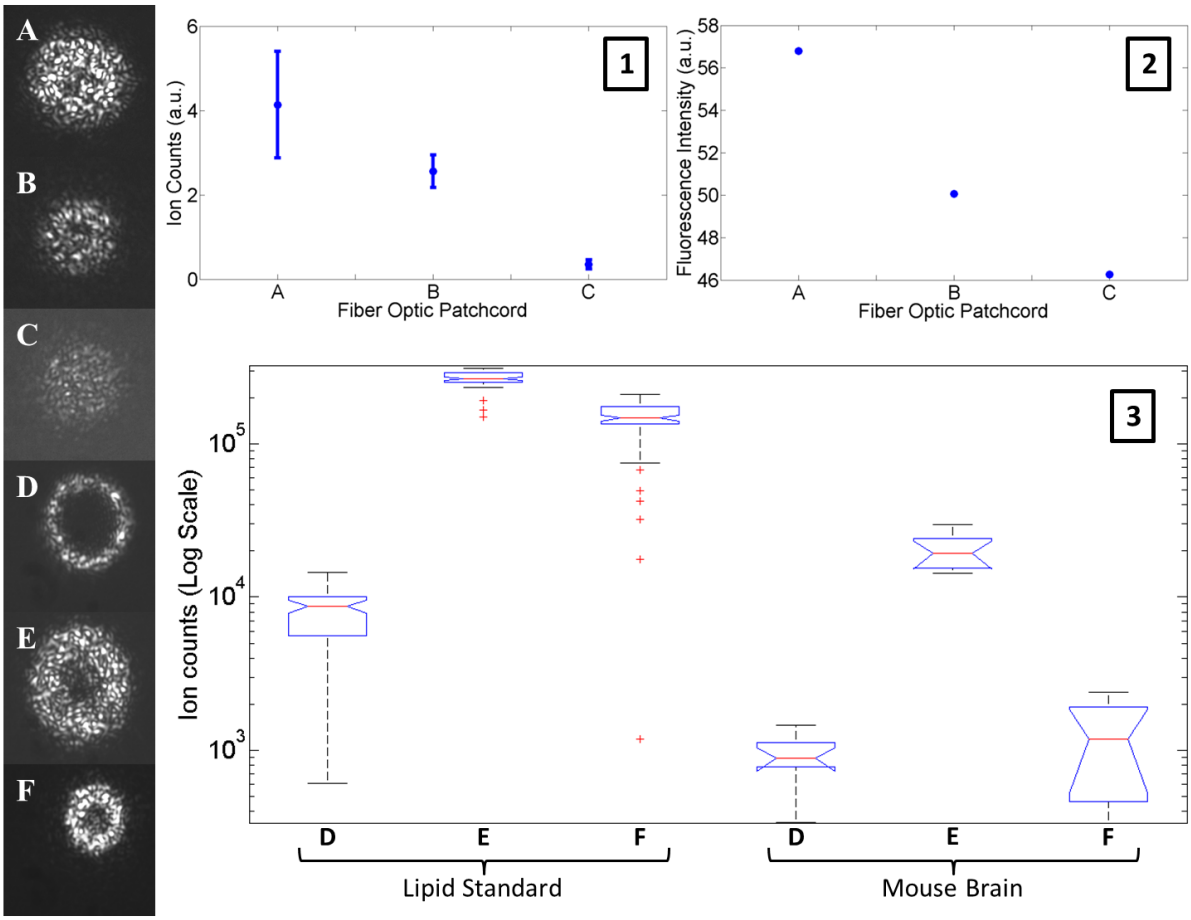

Figure 2.7. Post-fibre laser beam profile from six fibres (A-F) each with differing amounts of damage. Profile images are shown on separate scales so as to be visible within this figure. Graph 1 shows the mean ion counts per pixel ± standard error (SE) acquired from fibres A, B and C for identical MS acquisitions of PNA on tissue. Graph 2 shows the total fluorescence intensity from images A, B and C. Similar trends are observed for graphs 1 and 2. Graph 3 shows total ion counts per pixel from a continuous raster mode MALDI-MS data acquisition from mouse brain tissue and thin layer lipid standard with CHCA. Fluorometric beam profiling provides a cheap, quick method of determining fibre profile differences and aids understanding of their influence on MALDI-MS ion yield.

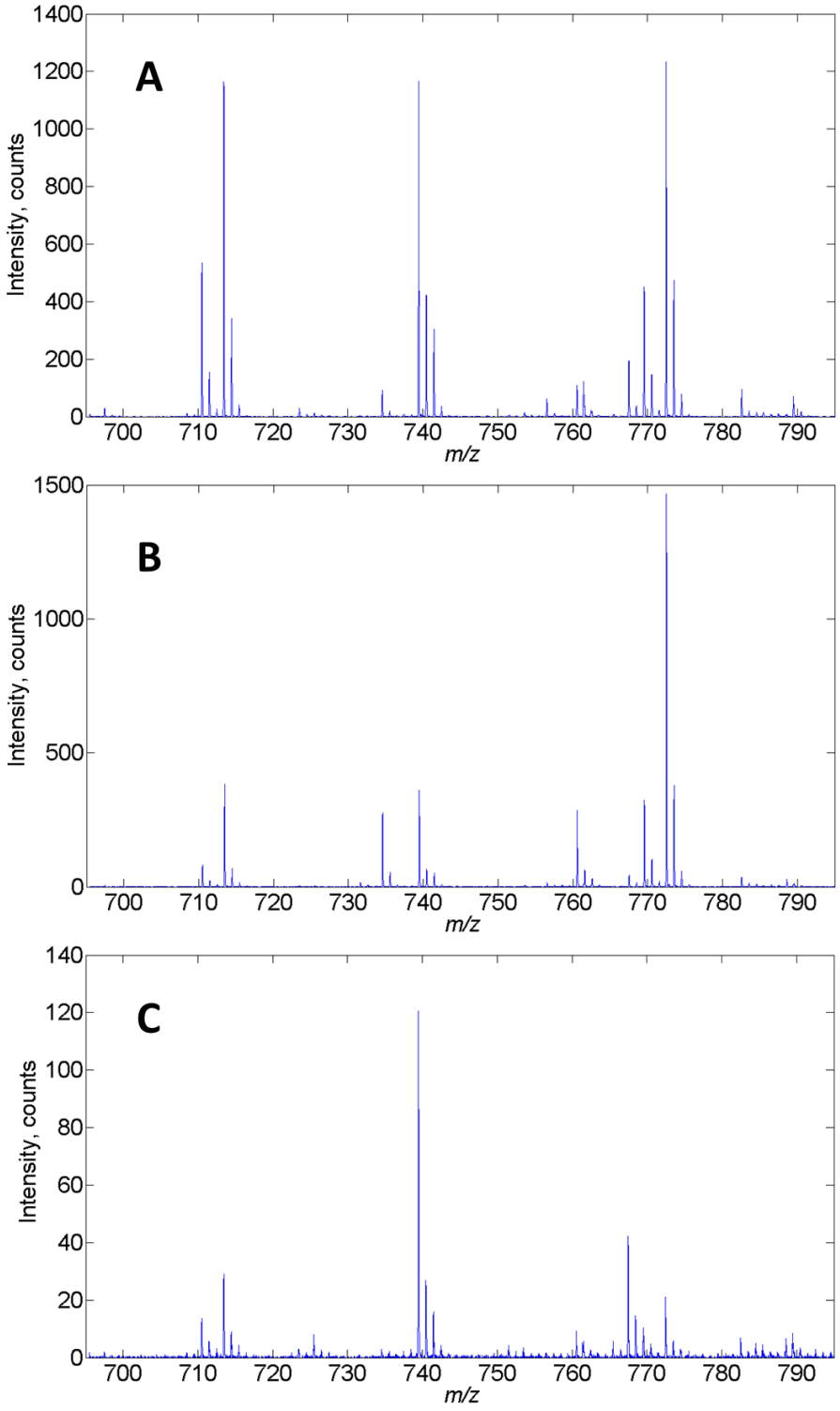

Figure 2.8. Example spectra from analyses shown in Figure 2.7 for fibres A, B and C (labeled A, B and C within Figure 2.7). Single peak intensity differences as well as changes in ratio between different peaks are observed between spectra from different fibres.

Frequent or excessive fibre damage could be an indication of: poor fibre coupling alignment; the focal spot on the fibre face being larger than the aperture itself (overfilling); the focal spot on the fibre face being too small and so exceeding the energy density damage threshold; the use of fibres which accrue damage under the laser pulse energy / pulse width / repetition rate / wavelength used. These issues can easily be remedied with fibre couple optimization and realignment or purchase of a more appropriate or larger diameter fibre. However, without the ability to diagnose these issues, other causes such as a reduction in instrument transmission efficiency may be blamed as it can produce similar effects. A full clean and tune of a mass spectrometer is a much more costly and / or time consuming endeavor than replacing or mending an optic fibre.

2.3.2. Laser Beam Profiling Inside the MALDI Ion Source

Typically, commercially available mass spectrometry instruments do not contain provision for the direct estimation of incident laser beam profile size. They will however have a camera view of the sample plate at the point of incidence of the laser. These cameras are routinely used for sample alignment and positioning by photographing the reflected light from stainless steel or emission from matrix coated spots. An example of the type of detailed information that could potentially be gathered by in source photography was presented by Moskovets *et al.* (2002) as an alignment checking step within a study of ionization kinetics [166]. The fluorometric method was not used in this instance and it is unclear whether the CCD employed was specially adapted for efficient detection at the 337 nm wavelength of the N_2 laser used.

In this study we investigate capture of laser induced fluorescence as a beam profiling tool. The original sample view camera was replaced with a low cost CMOS camera to allow greater control over image acquisition. A schematic of the in-source image acquisition setup is shown in Figure 2.9.

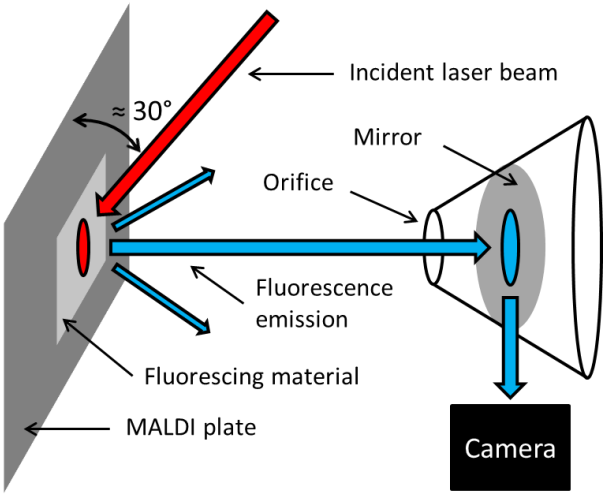

Figure 2.9. Schematic of in-source beam imaging setup used in present study. This setup (or one like it) is replicated in virtually all commercial mass spectrometers meaning the fluorometric profiling technique employed in this study could be easily implemented by other groups.

The fluorometric beam profiling technique was applied in the QSTAR XL oMALDI 2 ion-source. To provide scale to the in-source images a transmission electron microscopy (TEM) grid of known dimensions (bar width = 15 μm, hole width = 47 μm) was secured to the sample plate upon which white paper was also affixed. This provided the necessary scale measure to allow the fluorescence induced by the laser beam to become a measure of the in-source beam profile dimensions (images shown in Figure 2.10 A, B and C). The in-source

image of the TEM grid can be seen in Figure 2.10 A. The in-source laser beam profile image from paper fluorescence emission can be seen in Figure 2.10 B. An overlay, maintaining the correct relative scales, of images A and B is shown in Figure 2.10 C; this image allows a measure of the size of the beam profile incident on the sample plate in the MALDI ion source to be made. The scale bars, vertical and horizontal, represent a distance of 200 μm in each of those directions. This allowed an estimate of the x and y diameters of the spot size to be made at approximately 185 μm and 395 μm respectively.

A useful comparison of the measurement of laser beam profile dimensions in MALDI-MS is the ablation [133] of a thin layer matrix preparation (ablated thin layer matrix preparation shown in Figure 2.10 D, E and F). Using this method the x and y laser beam diameters were estimated at approximately 150 μm and 300 μm respectively.

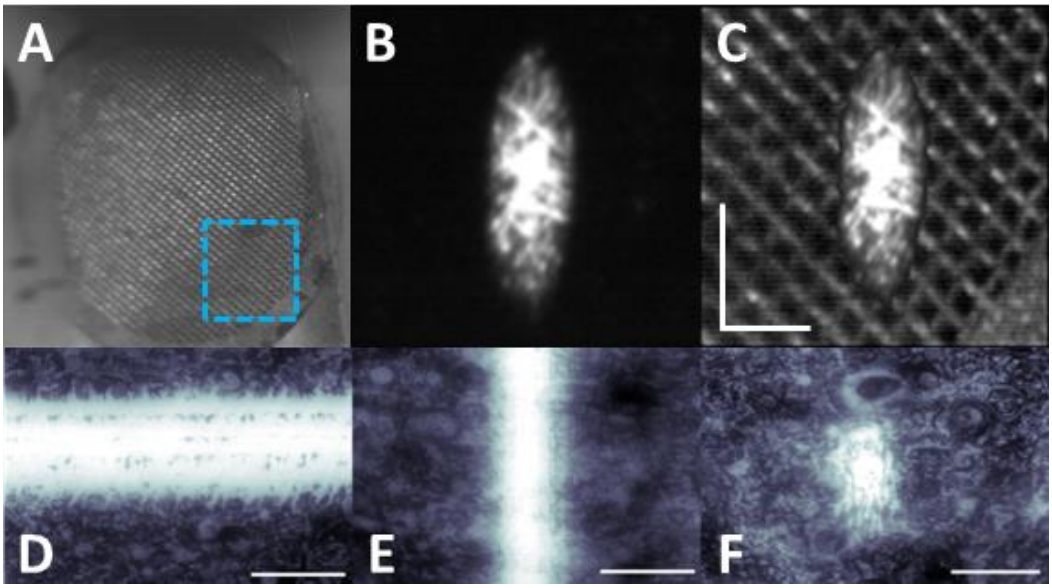

Figure 2.10. In-source beam profiling and size calibration via the fluorometric technique alongside beam profile measure from thin film CHCA. A: in-source view of TEM grid with bar width = 15 μm and hole width = 47 μm. B: in-source fluorometric beam profile on white paper; the full beam profile induced fluorescence is visible. C: overlay of highlighted region of A and beam profile in B retaining relative scale. D: horizontal raster ablation of thin film CHCA revealing height beam profile in-source. E: vertical raster ablation of thin film CHCA revealing width beam profile in-source. F: single position ablation of CHCA revealing beam profile and dimensions. All scale bars (both vertical and horizontal) represent 200 μm. Different methods for quantifying beam profile dimension provide different results.

It is worth noting the spatial intensity distribution within the beam profile image shown in Figure 2.10 B and C. It is clearly quite different to the out of source beam profile images shown in Figures 2.1 and 2.3. This is likely due to the fibrous structure of the paper and the distribution of the fluorophores within it; which at the length scales being imaged in Figure 2.10 become visible as the dominant features within the beam profile, preventing the

speckle pattern being viewed effectively. The ablation beam profiles shown in Figure 2.10 D and F have regions within the beam profile in which the matrix has remained un-ablated. This provides a link to Figure 2.6 in which the fluence maxima and minima of the speckle pattern are discussed. The un-ablated regions within Figure 2.10 are a direct result of these fluence minima within the speckle pattern.

The problems encountered with imaging the speckle pattern in-source, rather than just the beam dimensions, led to other fluorescent surfaces being trialed. Both a fluorescent UV/VIS detector card (absorption maxima ~ 400 nm; emission maxima ~ 575 nm) and a fluorescent glass filter (absorption maxima ~ 250-350 nm; emission maxima ~ 410 nm) were used in place of paper for in source beam profiling (example images shown Figures 2.11 and 2.12). The UV/VIS detector card suffered from similar issues to the paper in that the surface topology / fluorophore location were the dominant features; the severity of this is further exemplified by the acquisition of beam profile images at different locations on the detector card (Figure 2.11 A, B and C). The detector card proved even less useful than the paper as no well-defined edge of the laser induced fluorescence was observed.

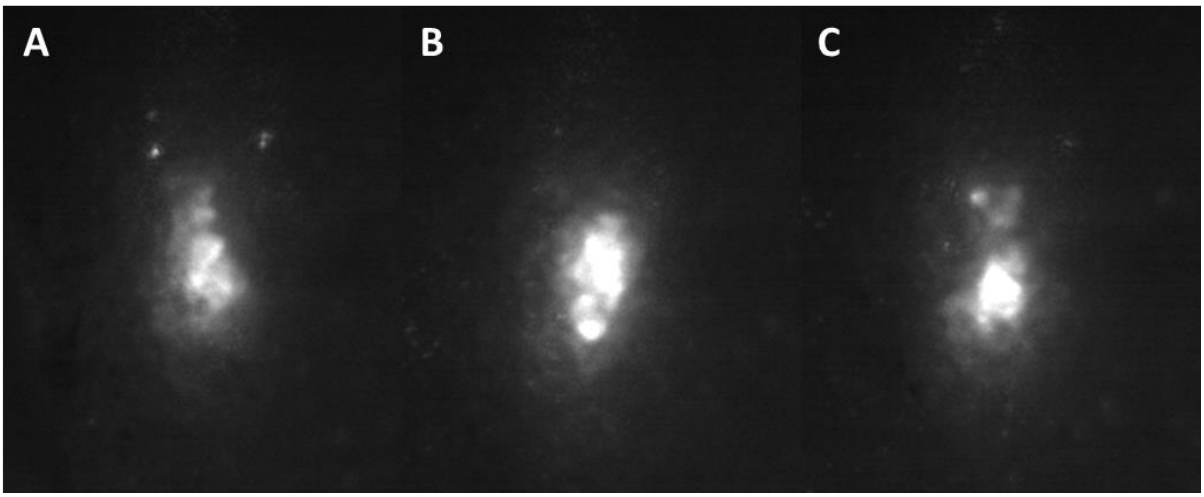

Figure 2.11. In-source laser beam induced fluorescence profile at three different locations (A – C) upon UV/VIS detector card. Different apparent beam profiles are observed at different locations due to the inhomogeneous surface topology of the fluorescing surface of the card. No size scale calibration was carried out for this image acquisition but the height of the visible fluorescent area within these images is ~ 400 μm.

The filter glass, however, was even more problematic and no beam profile information was observed at all. The path of the laser beam through the glass was clear and well defined by its fluorescence emission but due to the thickness (3 mm) of the glass and the fact that fluorescence is induced throughout the path of the laser beam, the beam profile cannot be observed as incident upon a flat surface as was necessary for our purposes.

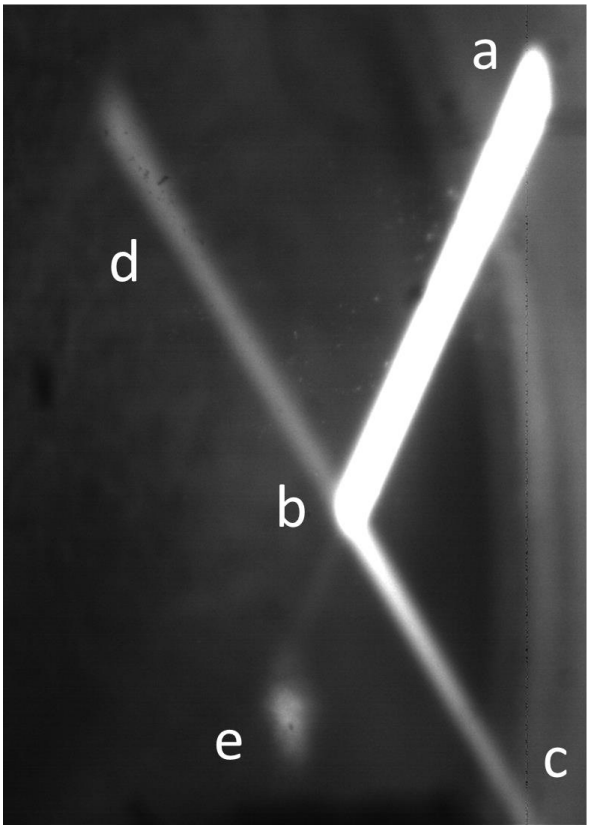

Figure 2.12. In-source laser induced fluorescence within the fluorescing filter glass. Though it is difficult to be certain the features within the image are believed to be: a) point of entry of laser beam to upper surface of glass; b) reflection of beam from lower surface of glass; c) exit of beam from glass after reflection from b; d) reflection of beam travelling along path *ab* from surface under the glass; e) projection of fluorescence induced emission from light travelling along path *ab* giving rise to beam profile like feature. Fluorescent filter glass is not suitable for in source beam profiling of this kind.

The differences between the two beam profile dimension estimates shown in Figure 2.10 provide for an interesting point of discussion. Fibre induced beam profiles are often described as flat-top. There will, however, still be an underlying Gaussian shape to the beam profile as a whole and for every peak within the profile as shown in Figure 2.6. Additionally

the visible gradient from the fully ablated to the un-ablated region in Figure 2.10 D and E suggests this is the case. Consequently the outer and pattern minima regions of a fibre delivered speckle pattern will be delivering a lower fluence than a more central or pattern maxima region, as with a Gaussian beam profile. This fact, in conjunction with the fluence dependent relationship of ion yield in MALDI, results in the ablation measured beam dimensions giving lower estimated values than those given by other methods, including the fluorometric method shown here. In this particular case the beam area given by the ablation of CHCA was ≈ 35342 μm^2 and by the fluorometric method was ≈ 57392 μm^2. In this particular case the observed difference would also result in fluence estimates differing by approximately × 1.6 i.e. for pulse energy of 10 μJ fluences of 283 $J\,m^{-2}$ and 174 $J\,m^{-2}$: a considerable disparity. Whilst this is a noteworthy finding it is not to suggest that other methods of estimating beam dimension are wrong, simply that they measure different things. For example, the method of using burn marks on heat sensitive paper may overestimate beam dimensions if heat is conducted too readily to the surrounding surface during irradiation. Despite this, the variation of fluence estimates due to differing beam dimension measures could well have significant implications in the consideration of areas such as matrix ion production threshold measurements [24] especially as these values appear to have a strong dependence upon the laser spot size [21].

The uncertainty in useful beam dimension is also of potential significance when performing oversampling [133]. With oversampling it is assumed that the entirety of the matrix / analyte at one location is ablated, and thus removed from the sample, prior to the next analysis. The problem with the differing beam profile size estimates then becomes important. If, as shown above, the beam diameter in fact extends beyond that which is shown by ablation of matrix then it cannot be assumed with absolute certainty that all ions are coming from only

the area ablated away during oversampling. It is well evidenced that significant ion counts can be obtained from discrete locations without removing all the matrix / analyte [23]. This implies that the outer regions of the laser beam profile may well be causing desorption and ionization of molecules without removing all matrix / analyte and therefore not providing the clean edge necessary for true oversampling. The significance of this in practical terms remains unclear though, as these unaccounted for ions may still be a small fraction of the overall ion yield per pixel, preventing this from undermining the practical use of oversampling.

2.4. Conclusions

The measurement of beam profile is an important factor in MALDI-MS and the fluorometric technique investigated here could provide a quantitative in-source method for on-line beam profiling. Beam profile information can be readily obtained by all users of MALDI-MS equipment in and easy and low cost fashion where no specialist equipment need be purchased. The work shown here also highlights the need for the use of multiple beam profiling techniques when estimating the beam profile dimensions for MALDI-MS studies as the information provided by different beam profiling techniques may relate to different physical phenomena and will therefore provide different and potentially complementary information.

Whilst the use of paper for fluorometric beam profiling can provide in-source beam profile dimension information there is a clear need for a fluorescing thin layer substance where the fluorophores and topology are homogenous across the surface down to the length scales needed to provide accurate information regarding the photon distribution within the

beam profile. It would, in addition, be necessary to choose fluorescing substances which undergo minimal photo-bleaching at the energies and irradiances typical within MALDI MS to allow effective imaging of the profile under true operating conditions. Additional future work would be to perform the single pulse beam profiling measurements on the in-source beam profile as pulse to pulse variations in beam properties would be of great interest to MALDI MS researchers. This would require the ability to acquire pulse images at a sampling rate complementary to the pulse repetition rates actually used when interrogating a sample for MALDI MS and MSI. The laser used with this study operates at up to ~ 50 kHz. The useful operating rate is, however, unlikely to extend across the full range available as the energy delivered per laser pulse, and so the fluence delivered, will change depending upon the repetition rate used. Therefore, in addition to the knowledge of the beam profile, knowledge of other laser parameters such as the fluence and laser repetition rate must be investigated.

Chapter 3

Evaluation and optimization of a N_2 and an Nd:YVO_4 laser for use in MALDI MSI with continuous raster mode sampling

3.1. Introduction

When operating at a fixed wavelength (typically 337 or 355 nm) in MALDI MS the number of photons per unit area (fluence, J m^{-2}) incident upon a sample per laser pulse is usually considered the most important laser parameter influencing the resulting ion yield. Development of techniques to further measure and understand the distribution of photons emitted from the laser used in MALDI MS was investigated in the previous chapter. Despite the distribution of photons and fluence incident upon the sample being critical, other laser and instrument parameters will also have a considerable influence upon the data acquired by MALDI MS. For example, the sample stage raster speed and laser pulse repetition rate will jointly determine the throughput of sampling and will have a strong influence upon the sensitivity obtained.

As MALDI mass spectrometry imaging (MSI) moves toward high throughput imaging of large sample areas, the use of continuous raster mode sampling for imaging becomes

increasingly important [134, 165]. This provides throughput benefits over spot mode image acquisition due to the continuous movement of the sample under the laser [131]. It has generally been assumed, due to the intuitive nature of sampling dwell times, that a shorter dwell time per pixel will result in a lower ion yield and, consequently, that there is a direct trade-off between throughput and sensitivity. One approach to improving the sensitivity and so throughput is to explore the used of lasers that offer higher pulse repetition rates, allowing a larger number of pulses per pixel, potentially enabling a sensitivity improvement.

The N_2 laser has been traditionally employed in UV MALDI applications due primarily to their comparatively low cost. With an increased need to image large areas the shorter lifetime [165], lower repetition rate (1-60Hz) and reduced pulse to pulse stability of N_2 lasers has caused researchers to look toward diode pumped solid state lasers (DPSS) [167]. To date the UV DPSS lasers used in MALDI-MS are all variations of neodymium doped lasers: Nd:YAG [147, 168], Nd:YLF [169, 170] and Nd:YVO_4 [165]. All are likely to have similar beam profiles but their other properties (repetition rate, energy per pulse, temporal pulse width) may vary. Repetition rates up to 15 kHz with energies in the region of ~ 10 µJ have been reported [134, 165, 171-173]. The benefit of increased repetition rate for faster data acquisition has been demonstrated for spot data acquisition [171] and has also been shown in conjunction with improved sensitivity over a standard N_2 laser [172].

The use of high repetition rate (defined here as lasers able to operate at > 3 kHz) lasers for improved throughput in MALDI MSI has twice been studied. Trim *et al.* investigated the use of an Nd:YVO_4 laser operated at between 1 and 20 kHz in continuous raster sampling mode [165]. Within this work the sample stage raster speed was held constant and the optimum repetition rate was found to be between 1 and 10 kHz. Spraggins *et al.* investigated the use of an Nd:YLF laser operated at between 1 and 5 kHz in continuous raster sampling

mode [134]. Within the study it was found that the ion yield per pixel was compromised by high laser pulse repetition rates and / or fast stage raster speed, both of which lead to 'severe oversampling'. An upper limit of 50 pulses per unit area was recommended.

3.2. Experimental Section

3.2.1. Materials

Methanol (HPLC grade) used in preparation of all matrix solutions was purchased from Fisher Scientific (Leicestershire, UK). The water used was purified by an ELGA Option 3 system (Marlow, UK). Trifluoroacetic acid (TFA, 99 % purity) and MALDI matrix α-Cyano-4-hydroxycinnamic acid (CHCA) were purchased from Sigma Aldrich (Dorset, UK). The MALDI MS sample plates used were smooth surfaced stainless steel imaging plates from AB Sciex (Ontario, Canada). Lipid standard PC 34:1 (16:0/18:1) with isotopic mass of 759.578 g $mole^{-1}$ was purchased from Avanti Polar Lipids Incorporated (Delf Zyl, Netherlands). Smooth, stainless steel MALDI MS imaging plates were purchased from AB Sciex

3.2.2. Tissue Preparation and Sectioning

Rat brain samples were supplied by AstraZeneca (Alderley Park, UK) and were stored at -80 $^{\circ}$C until sectioned. Brain hemispheres were mounted onto the cryostat chuck using purified water-ice slush. Beginning within ≈ 0.5 mm parallel to the sagittal midline 8 serial sections of 12 μm were collected and thaw mounted onto two MALDI imaging plates. Six sections were mounted onto plate A for the repetition rate and raster speed study and two sections onto plate B for whole tissue section imaging. Sectioning was performed on a Leica CM 1850 Cryostat (Milton Keynes, UK).

3.2.3. Complex Lipid Solution

Lipid extraction from whole rat brain was performed using Folch's method [174]. The resulting lipid fraction was used without further processing.

3.2.4. Matrix Application

CHCA (20 mg mL^{-1} in 80 % CH_3OH, 0.1 % TFA) was mixed 1:3 (*v:v, lipid:matrix*) with the complex lipid extract solution. Solutions were applied to their respective imaging plates using an artist airbrush purchased from Draper Air Tools Airbrush Kit (Hampshire, UK) with Badger Airbrush propellant (bought from Amazon.co.uk). The MALDI plate was held vertically and 16 spray passes of the air brush were carried out with 3 seconds in between and one 90 degree turn of the MALDI plate every 4 passes. 10 mL of matrix / lipid solution was dispensed in total. For the tissue imaging experiments 15 mL CHCA (20 mg mL^{-1} in 80 % CH_3OH, 0.1 % TFA) was deposited by the same method.

3.2.5. Mass Spectrometry

MALDI TOF MS analysis was carried out on a QSTAR XL Qq-ToF mass spectrometer using Analyst QS 1.1 with oMALDI server 5.1 (Applied Biosystems). An N_2 (Spectra Physics: VSL-337ND-S) laser with λ = 337 nm, 1-60Hz repetition rate, < 100 μJ energy per pulse (post-fibre), < 4 ns pulse length and an Nd:YVO_4 (Elforlight: SPOT-10-100-355) DPSS laser with λ = 355 nm, < 50 kHz repetition rate, < 14 μJ energy per pulse (post-fibre) at 10kHz and < 1.5 ns pulse length were used in this study. These data are taken from the information supplied by the laser manufacturers and were not measured as part of this study. The Nd:YVO_4 laser was triggered by a Thurlby Thandar Instruments (Huntingdon,

Cambridgeshire) TGP110 10MHz Pulse Generator. All data were acquired in positive ion mode with continuous raster mode sampling.

3.2.6. MALDI MS Continuous Raster Mode Sampling

The five different stage raster speeds are labeled slowest (0.2 mm s^{-1}), slower (0.3 mm s^{-1}), slow (0.5 mm s^{-1}), medium (1 mm s^{-1}) and fast (2.8 mm s^{-1}) in oMALDI software raster imaging setup; these are the only raster speeds available with this instrument. The speed of each raster setting was established from software specified pixel size and the corresponding acquisition time for that pixel. Dividing these two values gave the stage raster speed values quoted above.

3.2.7. MALDI MS Continuous Raster Mode Sampling of Complex Lipid Extract

The repetition rate of the N_2 laser was varied from 10 to 60 Hz at 10 Hz intervals. The repetition rate of the Nd:YVO_4 laser was varied from 5 to 25 kHz at 5 kHz intervals. The energy per pulse was held at 20 % (~ 20 μJ) and 36 % (~ 5 μJ at 5 kHz) for the N_2 and Nd:YVO_4 lasers respectively. Data were acquired at a pixel size (*x*, *y*) of 250 × 250 μm for raster speeds of 0.2, 0.3, 0.5 and 1.0 mm s^{-1} and at 340 × 250 μm for 2.8 mm s^{-1}. A resolution of 340 × 250 μm was used for the 2.8 mm s^{-1} speed setting due to minimum allowed acquisition time in Analyst 1.1 method editor options and was subsequently normalized for comparison to other data. One raster line of 30 mm in length was acquired for each combination of raster speed and repetition rate for both lasers.

3.2.8. MALDI MS and MSI with Continuous Raster Mode Sampling on Tissue

The lipid extract experimental method was repeated in tissue with the following modifications. A resolution of 310 × 250 μm was used for the fast raster speed (2.8 mm s^{-1}) in this case and was subsequently normalized as above. Each data set was comprised of one raster mode image ~ 10 mm wide (depending upon the width of the tissue section) and 1 mm deep which corresponds to ~ 150 pixels. This experiment was performed for all combinations of raster speed and repetition rate at energies of 100, 77, 55 and 18 % (approximately 14, 10.8, 7.7 and 2.5 μJ). The whole tissue section images were acquired using a 100 μm core diameter fibre optic patchcord (Edmund Optics, NA = 0.22) at 100 % energy with 100 × 100 μm pixel size at a raster speed of 0.5 mm s^{-1} and a repetition rate of 5 and 10 kHz respectively. Both tissue sections were mounted on the same imaging plate and CHCA was applied as described above.

3.2.9. Processing of MALDI MS and MSI Data

The data were converted from AB Sciex proprietary file format (.wiff) to .mzML using AB MS Data Converter (AB Sciex version 1.3) and then converted to imzML using imzMLConverter [164] and processed in MatLab (version 7.8.0 (2009a), Math Works Inc., USA). The mean ion counts (peak area ± 0.1 Daltons) for selected mass-to-charge values were calculated along with the standard error of the mean (SE) and are plotted as mean value ± SE in all bar charts.

3.3. Results and Discussion

3.3.1. Acquiring Data in Continuous Raster Mode

During a MALDI MS or MSI experiment the laser is incident upon the sample plate and will form an elliptical spot on the sample (with a circle being a special case of an ellipse), unless otherwise modified. The shape of the laser beam, as incident upon the sample plate, within the instrument used in this study was shown within Chapter 1. The sample is rastered continuously under the pulsed laser during data acquisition. The speed the stage is moved at, in combination with the laser pulse repetition rate, will result in a series of overlapping ellipses where, due to the distribution of the incident laser pulses, different points on the sample will receive a different number of pulses. This concept is demonstrated graphically in Figure 3.1.

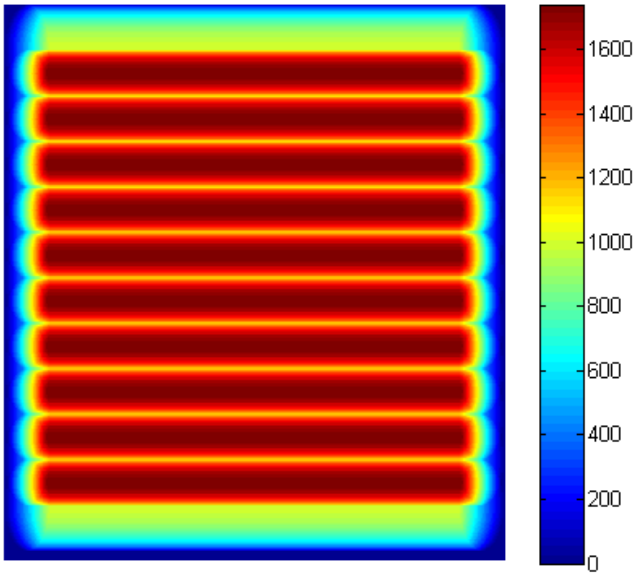

Figure 3.1. Heat map showing the theoretical number of laser pulses received per unit are of a sample where the stage is rastered at a speed of 1 mm s^{-1}, the laser pulses arrive at a repetition rate of 1 kHz, a pixel size of 100 µm is set and the incident beam profile dimensions are an ellipse with diameters (major and minor axis) of 200 µm and 100 µm.

In direct correlation to this, a pixel of a fixed size will receive a different number of pulses depending on the repetition rate of the laser and the speed at which the stage is rastered. The pulses per pixel resulting from these different combinations and can be calculated using Equation 8:

$$shots\ per\ pixel = \left(\frac{x_p}{v}\right) R \qquad (8)$$

where x_p is the pixel size in the x-dimension, v is the stage velocity and R is the laser pulse repetition rate used. In this instance the number of pulses per pixel is defined as the number times any given fixed point along the minor axis of the laser spot hits the area within the pixel. The pulses per pixel as defined by Equation 8 due to the raster speeds and repetition rates available within this study are shown in Table 3.1.

Table 3.1. Number of pulses per pixel for Nd:YVO_4 and N_2 lasers at different raster speeds and repetition rates for a pixel size of 100 µm.

	N_2						Nd:YVO_4					
Raster Speed (mm s^{-1})	Repetition Rate (Hz)											
	10	20	30	40	50	60	1000	5000	10000	15000	20000	25000
2.8	0.4	0.7	1.1	1.4	1.8	2.1	35.7	178.6	357.1	535.7	714.3	892.9
1.0	1.0	2.0	3.0	4.0	5.0	6.0	100.0	500.0	1000.0	1500.0	2000.0	2500.0
0.5	2.0	4.0	6.0	8.0	10.0	12.0	200.0	1000.0	2000.0	3000.0	4000.0	5000.0
0.3	3.3	6.7	10.0	13.3	16.7	20.0	333.3	1666.7	3333.3	5000.0	6666.7	8333.3
0.2	5.0	10.0	15.0	20.0	25.0	30.0	500.0	2500.0	5000.0	7500.0	10000.0	12500.0

3.3.2. Laser energy per pulse: Repetition rate dependence

The manufacturer's information supplied with the Nd:YVO_4 laser shows that the energy per pulse varies with repetition rate peaking at ~ 5 kHz with a value of ~ 18 µJ per pulse (pre-fibre). The energy decreases to ~ 83, 50, 33, 17 % of this for 10, 15, 20, 25 kHz

respectively (Figure 3.2). The temporal laser pulse width will also vary as the repetition rate is altered. The manufacturer's information states that over the range of 1 – 25 kHz this value is 1.40 ± 0.03 ns (mean ± 1 s.d.). Deviations on this order are believed not to have any effect upon MALDI MS data [35]. Any change in energy per pulse over the operating range of 1 – 60 Hz for the N_2 laser is not known and the manufacturer's information does not mention this. The laser pulse width is listed as being < 4 ns and is also thought to remain constant to within acceptable errors over the operating range of repetition rates, though again this is not mentioned in the manufacturer's information.

This is important as the number of ions desorbed / detected depends strongly upon the fluence of the laser (typically defined in MALDI MS as energy per unit area per pulse) [22-24, 29]. The effective laser spot size will also change as the repetition rate is altered due to the increased portion of the laser spot which delivers sufficient energy to cause desorption of ions [23, 175] (so causing widening as a result). Therefore, the alteration of the repetition rate when using the Nd:YVO_4 laser is a potentially complex issue and will need careful consideration.

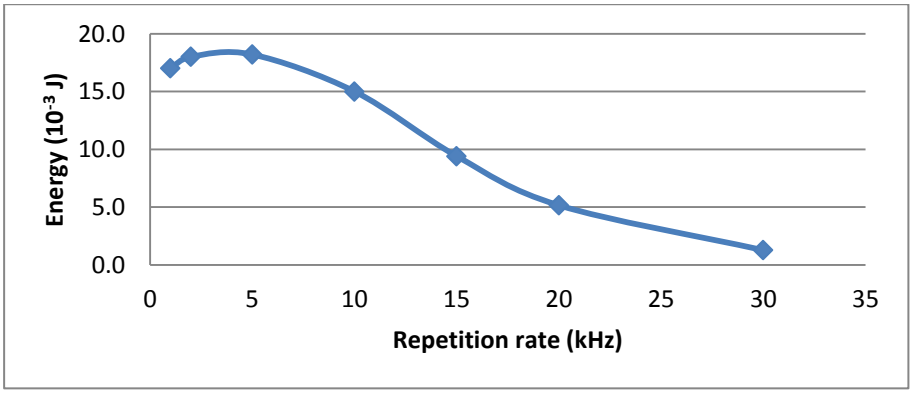

Figure 3.2. Energy per pulse delivered at different repetition rates by the Nd:YVO_4 laser (pre-fibre) used in this study as supplied by the manufacturer. Line fitted is to guide the eye only. The choice of repetition rate may have a big impact upon the data obtained by MALDI MS.

3.3.3. Variation of Repetition Rate and Raster Speed in MALDI MS Continuous Raster Mode Sampling of CHCA and Complex Lipid Extract

Investigation into the effect of stage raster speed and laser pulse repetition rate is necessary in order to optimize data acquisition and enable the improvement of throughput within MALDI MS imaging applications. This study utilises a novel (within the field of MALDI MS) high repetition rate (< 50 kHz) Nd:YVO_4 laser and a more commonly used nitrogen laser with low repetition rate (1-60 Hz). To probe the relation between laser pulse repetition rate and raster speed with a view to optimizing MALDI MSI performance, a homogenous layer of complex lipid extract and CHCA was studied initially. This reduced any issues which may arise from heterogeneity of lipid distribution within tissue sections whilst helping replicate the type of lipid species complexity within murine tissue sections.

The most commonly detected lipid species in murine brain by MALDI MS in positive ion mode are phosphatidylcholine (PC) lipids with mass values commonly in the range of 700 to 900 Daltons [128, 176, 177]. The intact ions from these lipids may be detected as one or multiple peaks depending on the charge adduct associated with that lipid: addition of a proton $[M+H]^+$, a sodium cation $[M+Na]^+$ or a potassium cation $[M+K]^+$. The presence of $[M+H]^+$ ions is deliberate and to be expected in positive ion mode MALDI MS as proton donating species such as the matrix molecule and TFA are added to the sample prior to analysis. The presence of sodium and potassium are due to both contamination of samples and their natural occurrence in tissue. Therefore, within this mass-to-charge region (*m/z* 700 – 900) there are a large number of peaks detected, some of which will be characteristic of the same lipid molecule. To simplify the analysis of this complex lipid extract the most abundant lipid ion at *m/z* = 760.6 (tentatively assigned from literature as PC 16:0/18:1 [178, 179]) was chosen for

data analysis. The thin layer sample of CHCA and lipid standard was rastered at different velocities under the laser at a variety of repetition rates to explore as much of this combined variable space as possible. The mean ion counts detected per pixel alongside the mean counts per pixel per pulse for the Nd:YVO_4 and N_2 lasers are shown in Figure 3.3 and 3.4.

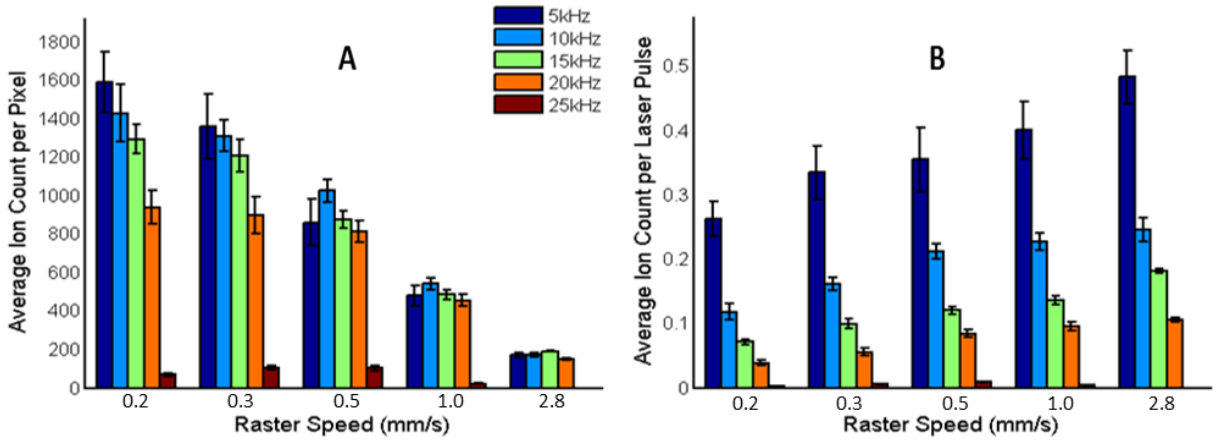

Figure 3.3. Variation of average ion counts per pixel of *m/z* = 760.6 (tentatively assigned as PC 16:0/18:1 $[M+H]^+$ [178]) from complex lipid mixture at different raster speeds and repetition rates with Nd:YVO_4 laser. **A)** Average ion counts per pixel ± SE. **B)** Data from A, normalized to number of laser pulses per pixel.

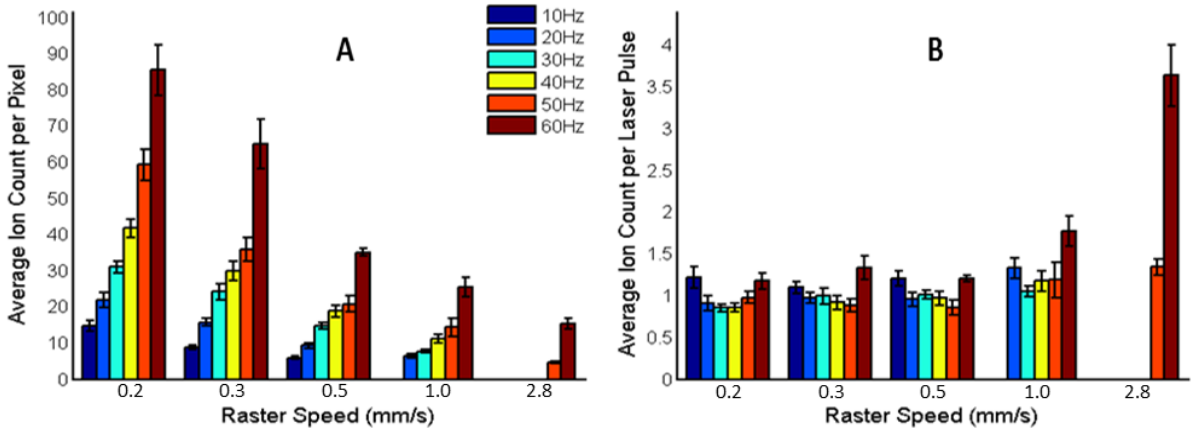

Figure 3.4. Variation of average ion counts per pixel for *m/*z = 760.6 (tentatively assigned as PC 16:0/18:1 $[M+H]^+$ [178]) from complex lipid mixture at different raster speeds and repetition rates with N_2 laser. **A)** Average ion counts per pixel ± SE. **B)** Data from A, normalized to number of laser pulses per pixel. Due to the low number of pulses per pixel the N_2 laser benefits from each extra pulse per pixel.

The first comparison of note is the improved ion counts offered by the Nd:YVO_4 laser compared to the N_2 laser within our instrumental setup. This is particularly pertinent when considering the use of faster raster speeds for high throughput imaging. It seems likely that the difference in laser pulses per pixel is a major factor in this, although issues such as laser wavelength, beam profile and energy per pulse may all be contributing factors [9, 23, 29, 180]. The superior performance of the Nd:YVO_4 laser under most conditions tested here, in particular at 5 kHz and 0.2 mm s^{-1}, means it would be the optimal choice for further use in MALDI MS and MSI in continuous raster mode.

For the Nd:YVO_4 laser at a given repetition rate: ion counts are found to increase as raster speed decreases (Figure 3.3-A). This means that an increase in pulses per pixel

corresponds to an increased ion count. Mass spectra obtained at 0.2 and 2.8 mm s^{-1} for repetition rates of 5 and 20 kHz are shown in Figures 3.5 and 3.6.

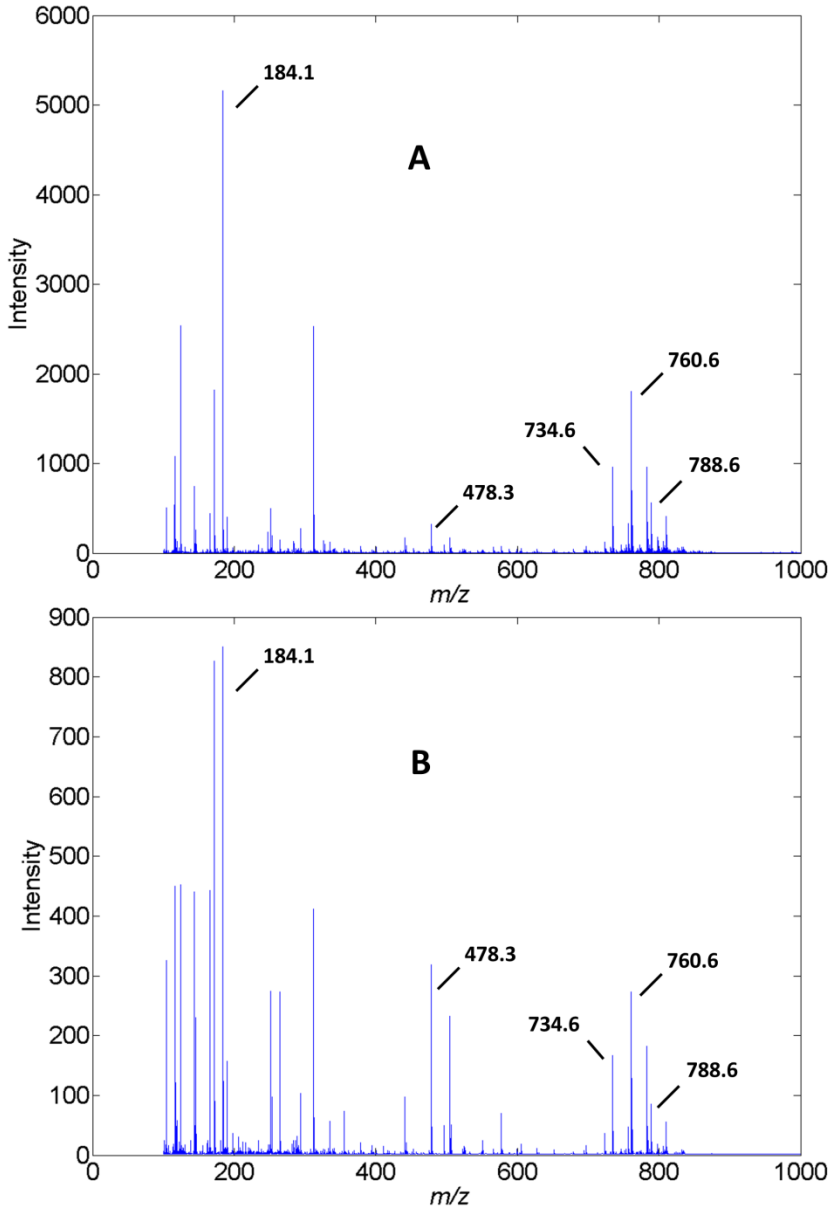

Figure 3.5. Representative single pixel spectra acquired under different conditions from thin layer CHCA and lipid extract preparation using the Nd:YVO_4 laser. A and B were acquired with a laser pulse repetition rate of 5 kHz at 0.2 and 2.8 mm s^{-1} raster speed respectively. Labelled lipid peaks are tentatively assigned: *m/z* = 184.1 PC head group fragment $[PO_4HC_2H_4N(CH_3)_3]^+$, *m/z* = 478.3 palmitic acid containing PC lipid fragment $[M+H-C_{18}H_{34}O_2]^+$ *m/z* = 788.6 PC (18:0/18:1) $[M+H]^+$, PC (16:0/18:1) $[M+H]^+$ and *m/z* = 734.6 PC (16:0/16:0) $[M+H]^+$. The potential for improved throughput is apparent.

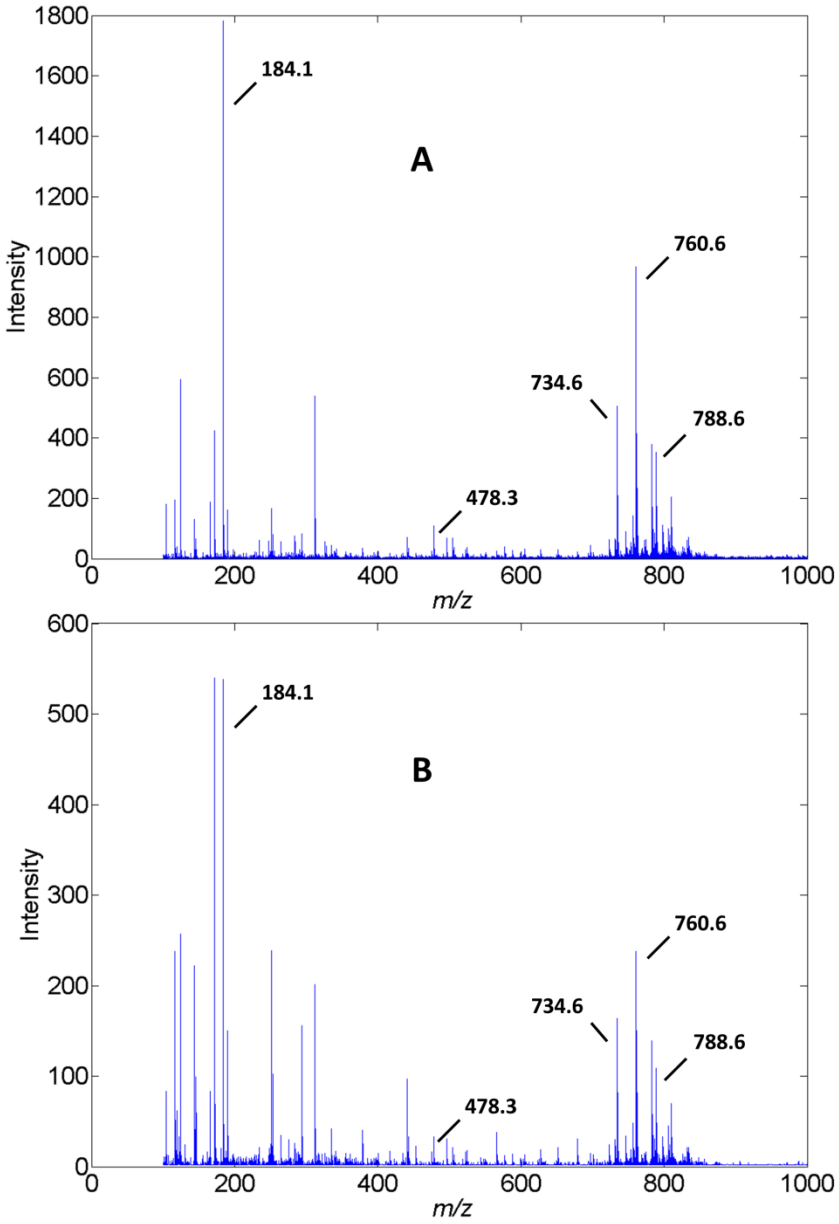

Figure 3.6. Representative single pixel spectra acquired under different conditions from thin layer CHCA and lipid extract preparation using the Nd:YVO_4 laser. A and B were acquired with a laser pulse repetition rate of 20 kHz at 0.2 and 2.8 mm s^{-1} raster speed respectively. Labelled lipid peaks are tentatively assigned: *m/z* = 184.1 PC head group fragment $[PO_4HC_2H_4N(CH_3)_3]^+$, *m/z* = 478.3 palmitic acid containing PC lipid fragment $[M+H-C_{18}H_{34}O_2]^+$ *m/z* = 788.6 PC (18:0/18:1) $[M+H]^+$, PC (16:0/18:1) $[M+H]^+$ and *m/z* = 734.6 PC (16:0/16:0) $[M+H]^+$. The potential for improved throughput is apparent.

At both 5 and 20 kHz the peak intensity within the lipid region and for the common PC lipid head-group fragment at *m/z* = 184.1 is larger where a slower raster speed is used (Figures 3.5 and 3.6). Interestingly there is increased intensity within the lipid fragment *m/z* region at the faster raster speed at 5 kHz as highlighted by the peak at *m/z* = 478.3. However, sensitivity at the faster raster speed is still sufficient and so the potential for improved throughput is demonstrated.

Spectral quality and signal to noise ratio remains reasonable under all conditions barring those data acquired at a repetition rate of 25 kHz. The optimum repetition rate at a raster speed of 0.2 mm s^{-1} is 5 kHz. The mean ion counts at raster speeds of 0.2 and 0.3 mm s^{-1} appear to scale inversely with the increasing repetition rate and so scale with relative energy per pulse delivered at these repetition rates (Figures 3.2 and 3.3). Trends of this nature would likely be expected for this relative energy change [29] but the decrease in ion counts with increasing number of laser pulses per pixel is counter-intuitive; suggesting that the change in energy at these raster speeds dominates the trend, not the repetition rate. As the raster speed is increased, the influence of the repetition rate (between 5 and 20 kHz) lessens until at 1 and 2.8 mm s^{-1} there is very little effect of altering the repetition rate. Given the range of energies involved this is also a counter-intuitive result and suggests that the effect of the stage raster speed is able to reduce the influence of the energy delivered per pulse / repetition rate at these faster speeds. However, without precise control and measurement of the energy it is difficult to apportion significance to its influence within these experiments.

Normalizing this data reveals that larger numbers of ions are detected per pulse as the stage is rastered faster under the laser (Figure 3.3-B). This may be due to the larger area of un-interrogated sample interrogated by each new pulse as the raster speed is increased.

The spectra obtained for the Nd:YVO_4 laser are largely similar and of a reasonable quality. Peaks detected in the *m/z* region 400 – 600 (typically associated with lipid fragments and matrix clusters) are more intense relative to the lipid peaks in the *m/z* region 700 - 900 at the faster stage raster speeds. This is particularly apparent in Figure 3.5 suggesting a change in the physic-chemical interactions where the stage velocity is in increased. A similar trend can also be observed for peaks in the *m/z* region (100 – 400): as the stage raster speed is increased the relative intensity of many peaks in this region increases. Issues regarding lipid fragment and matrix related ion intensities and ratios will be discussed in more detail in Chapter 4.

The information within Table 3.1 enables further insight into the trends seen within Figure 3.3. For example, those pixels receiving a similar number of pulses may be expected to provide similar mass spectra. The data acquired at 0.5 mm s^{-1} and 10 kHz will have the same number of pulses per pixel as the data acquired at 1 mm s^{-1} and 20 kHz; however the mean ion counts detected per pixel at these two setups differ by a factor of 2 (Figure 3.3). Furthermore, data points at raster speeds of 1 mm s^{-1} or 2.8 mm s^{-1} have similar mean ion counts despite very different numbers of pulses per pixel having been incident upon the sample.

Considering this in conjunction with the differing energy per pulse delivered by the Nd:YVO_4 laser at each repetition rate is particularly pertinent. Whilst knowledge provided by Figure 3.2 can help explain broad trends within the data, the lack of proper control and measurement of the energy delivered makes the complex trends here difficult to unravel. Use of a laser power meter and more precise control of the laser energy are employed in Chapter 4.

The N_2 laser produces the highest ion counts at a given raster speed when using the highest repetition rate (60 Hz). In addition, the slower the raster speed used, the higher the ion

counts obtained (Figure 3.4 A). The variation of energy per pulse over the range of repetition rates is not known in this instance for the N_2 laser but the data presented suggests there is little difference, or that any change is not enough to counteract the benefit derived from the increased pulse rate. Similar ion counts per laser pulse are obtained at all repetition rates and raster speeds (Figure 3.4 B), though there is an apparent increase as the speed is increased for the 60 Hz data. The reason for this is unclear but is likely due to the low signal-to-noise at these settings, resulting in anomalous values when normalised. The increased ion counts per pixel for the slower raster speeds are therefore largely attributable to the increased number of laser pulses per pixel. The spectra obtained with the N_2 laser were, however, not of a very high quality, even for the 60 Hz / 0.2 mm s^{-1} data (Figures 3.7 and 3.8).

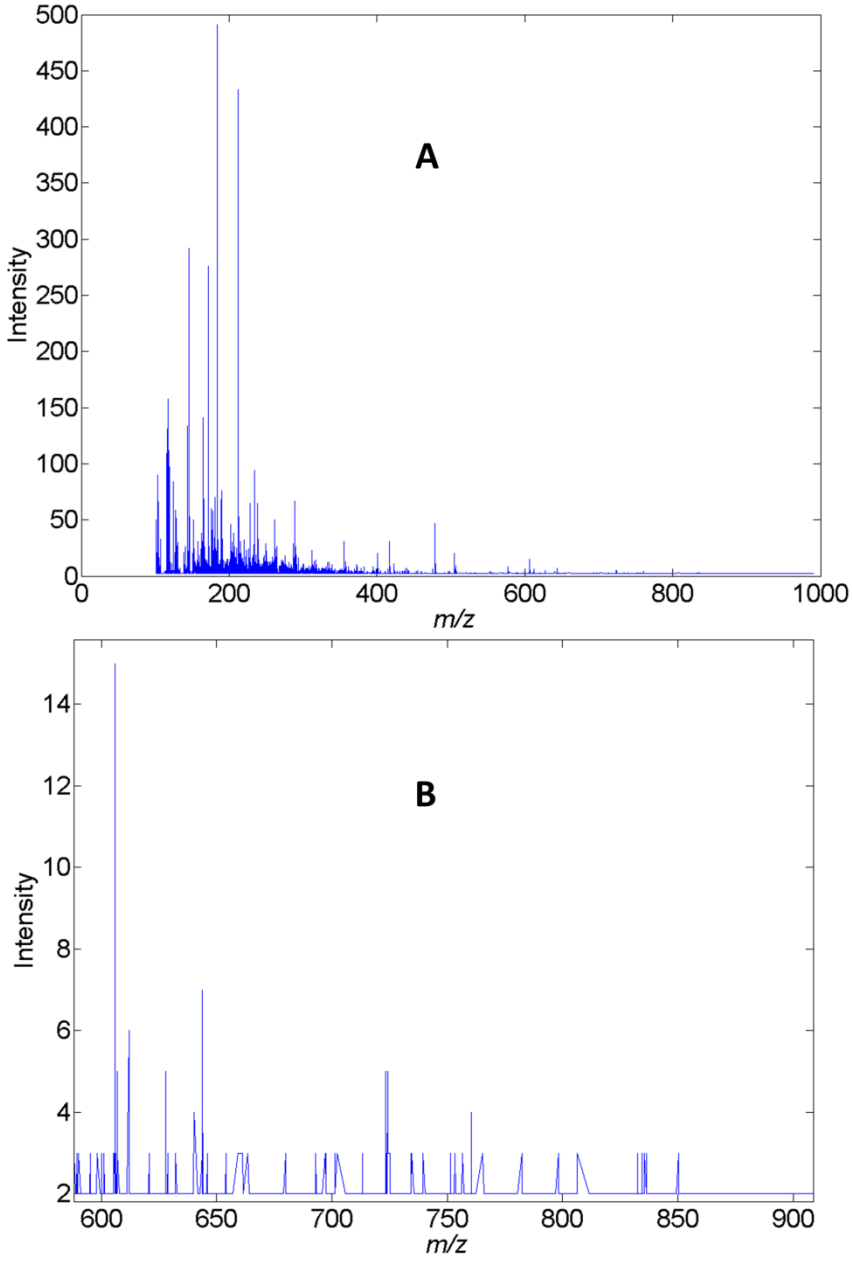

Figure 3.7. Representative single pixel spectra acquired under different conditions from thin layer CHCA and lipid extract preparation using the N_2 laser. A shows full *m/z* region detected and B shows lipid associated *m/z* region. Data acquired at a repetition rate of 10 Hz and a raster speed of 0.2 mm s^{-1}. Spectral quality is poor at 10 Hz particularly in the lipid mass-to-charge region.

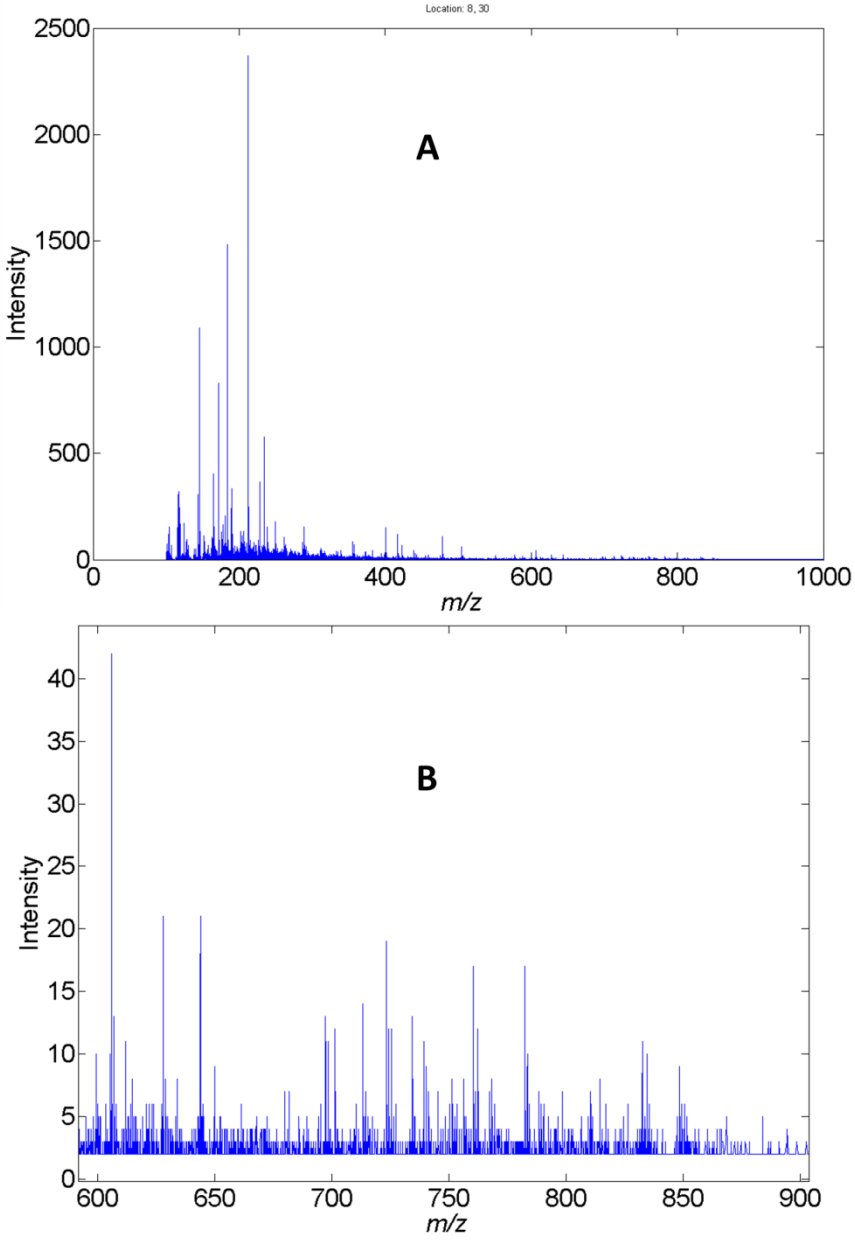

Figure 3.8. Representative single pixel spectra acquired under different conditions from thin layer CHCA and lipid extract preparation using the N_2 laser. **A** shows full *m/z* region detected and **B** shows lipid associated *m/z* region. Data acquired at a repetition rate of 60 Hz and a raster speed of 0.2 mm s^{-1}. Signal to noise is improved as compared to data acquired at 10 Hz (Figure 3.7.).

The intensity of the detected lipid region ions at lower repetition rates (for example 10 Hz as shown in Figure 3.7) and faster speeds are too low to be distinguished from potential noise. At the slower raster speeds and higher repetition rates the ion count and corresponding peak shape were improved, but still had relatively low signal to noise as compared to the Nd:YVO_4 data. As such, the N_2 laser is largely unsuitable for analysis of this sample type in continuous raster mode sampling and consequently the N_2 laser was not used for the remainder of these studies.

3.3.4. Distribution of lipids at m/z = 798.5 and 739.5 in saggital rat brain sections

The lipid peak at *m/z* = 798.5 (tentatively assigned in agreement with lipid standard work above and literature as PC16:0/18:1 $[M+K]^+$ [173, 181, 182]) and its fragment *m/z* = 739.5 (tentatively assigned from literature as PC 34:1 $[M+K-N(CH_3)_3]^+$ [178]) were detected homogenously in sagittal rat brain tissue sections within this study. Consequently, this lipid peak (*m/z* = 798.5) was used to monitor the effects of changing laser parameters. An example MALDI-MS image showing its distribution is presented in Figure 3.9. This lipid has both been shown to be homogenously and heterogeneously distributed in sagittal rat brain tissue sections within other studies [125, 183, 184]. From these studies and ours it would seem that the distribution of detected ions varies depending upon the sample preparation methods and instrumentation used. In addition, the spread of data as indicated by the standard error on Figure 3.10 indicates that the detected distribution of the lipid in question is sufficiently homogeneous for the purposes of this investigation.

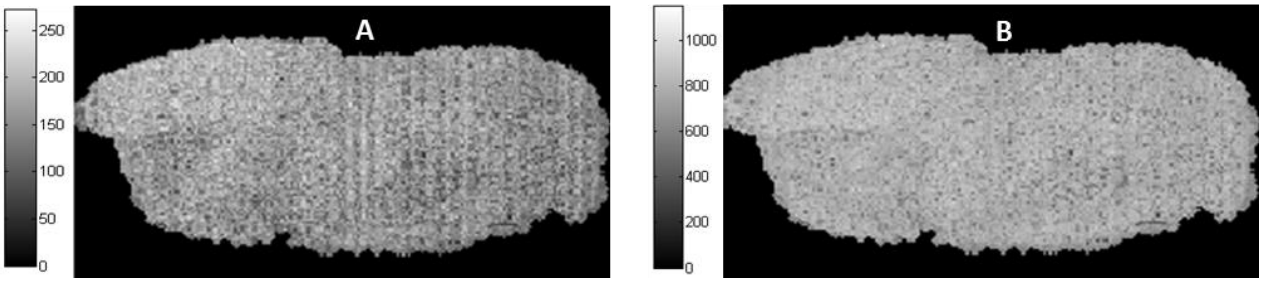

Figure 3.9. 100 μm spatial resolution lipid ion image of **A**) m/z = 739.5 (tentatively assigned as PC (34:1) $[M+K-N(CH_3)_3]^+$ [178]) and **B**) m/z = 798.5 (tentatively assigned as PC 16:0/18:1 $[M+K]^+$ [178]) in a sagittal rat brain tissue section. A homogenous distribution is observed for these ions.

3.3.5. Variation of Repetition Rate and Raster Speed in MALDI MS Continuous Raster Mode Sampling of Murine Brain Sections

The raster speed and repetition rate were varied across a series of raster imaging acquisitions in sagittal rat brain tissue sections (Figure 3.10). In addition, the laser attenuation was varied to give results under four different energy regimes and whilst this is not a substitute for measurement and control of the laser energy as a variable across all repetition rates, it may provide some clue as to the influence of energy in these experiments. Much like the spectra from the lipid extract analysis, spectra obtained from murine brain sections by MALDI MS will exhibit many peaks within the *m/z* region of 700 – 900. The peak at *m/z* = 798.5 (tentatively assigned from literature as PC 34:1 [177, 185]) was chosen for the plotting of Figure 3.10, as discussed in section 3.3.4.

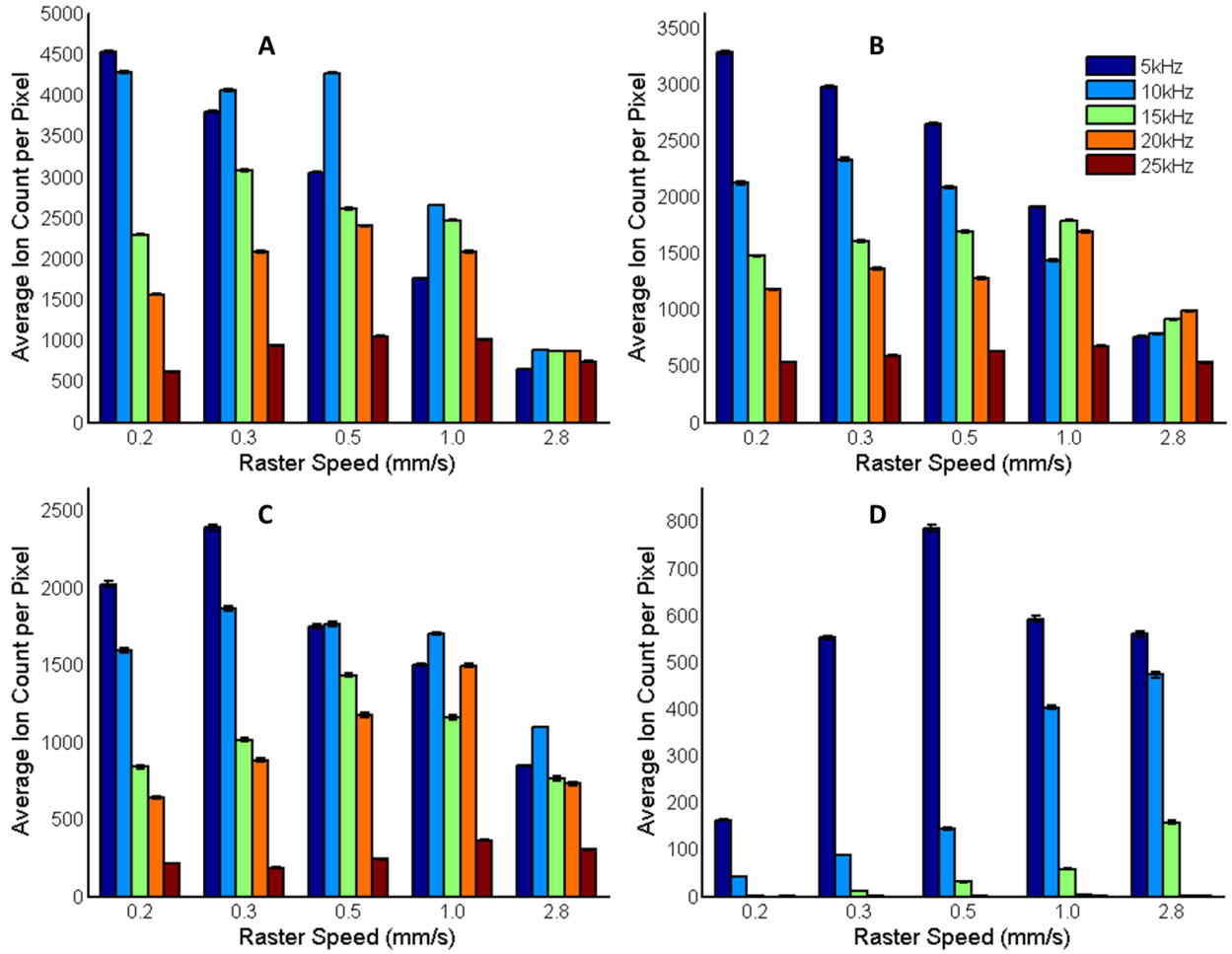

Figure 3.10. Variation of average ion counts per pixel in rat brain tissue at different raster speeds and repetition rates with Nd:YVO_4 laser for PC 16:0/18:1 $[M+K]^+$ (*m/z* = 798.5). A) 0 %, B) 23 %, C) 45 % and D) 82 % power attenuation.

The data from analysis in tissue shows some correlation with the trends seen in the lipid extract analyses above. As one would expect, there is often an increase in ion counts as the attenuation is decreased. The optimum repetition rate varies as the raster speed changes, though in the case of the on-tissue data there is more variability in the trends seen. This is likely due to the reduced homogeneity within this sample type, notwithstanding the reasonable homogeneity shown in Figure 3.9. At the lower three attenuation settings (Figure

3.10 A, B and C) the ion intensity depends strongly upon the repetition rate, where slower raster speeds are employed, whereas at the higher raster speeds this influence is lessened.

These trends also shift as the attenuation of the laser is altered. With decreasing attenuation, it can broadly be seen that the optimum raster speed at a given repetition rate will decrease. For example, at 23 % attenuation (Figure 3.10-B) the optimum raster speed at 5 kHz repetition rate is the slowest available (0.2 mm s^{-1}). These value shifts as the attenuation is increased to 82 %, resulting in the optimum raster speed for 5 kHz being 0.5 mm s^{-1}.

As previously, the data shown in Figure 3.10 was also normalized to pulses per pixel and plotted (Figure 3.11).

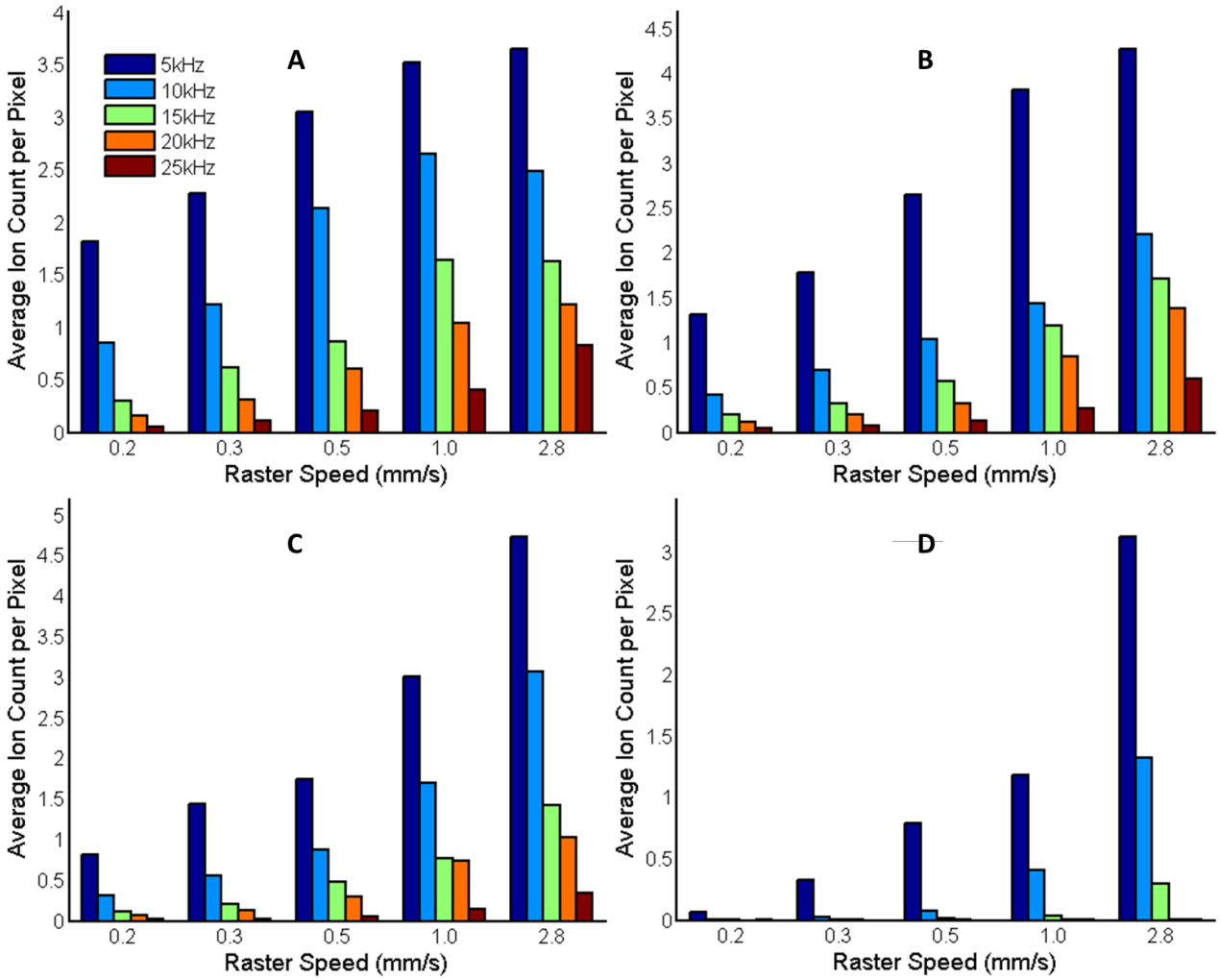

Figure 3.11. Variation of average ion counts per pixel normalized by pulses per pixel in rat brain tissue at different raster speeds and repetition rates with Nd:YVO_4 laser for *m/z* = 798.5 PC 16:0/18:1 $[M+K]^+$ (*m/z* = 798.5).). A) 0 %, B) 23 %, C) 45 % and D) 82 % power attenuation.

These graphs show similar trends as observed for the lipid standard data set: increasing counts per pulse with increasing raster speed. As the attenuation is decreased, more ions per pulse are seen at the lower raster speeds, though this increase is not mirrored by the faster raster speeds. The most interesting aspect of the trends within Figure 3.11, as an addition to Figure 3.3, is the largest number of ions per pulse shifts from significantly

favoring the highest raster speed to being much more similar across the raster speeds as the attenuation is decreased. The reason(s) for this are not clear but it appears that a more efficient ionization process occurs at the lower raster speeds where the attenuation is lower (and so energy is higher). Again, a greater understanding of these factors may be obtained with precise energy control and measurement. The change in the optimum setup for the maximum ion counts per pixel is further illustrated by the spectra shown in Figures 3.12, 3.13, 3.14. The changing in influence of raster speed at different repetition rates (and consequent energy per pulse) within the 0 % attenuation data set is highlighted by the spectra shown within Figures 3.12 and 3.13.

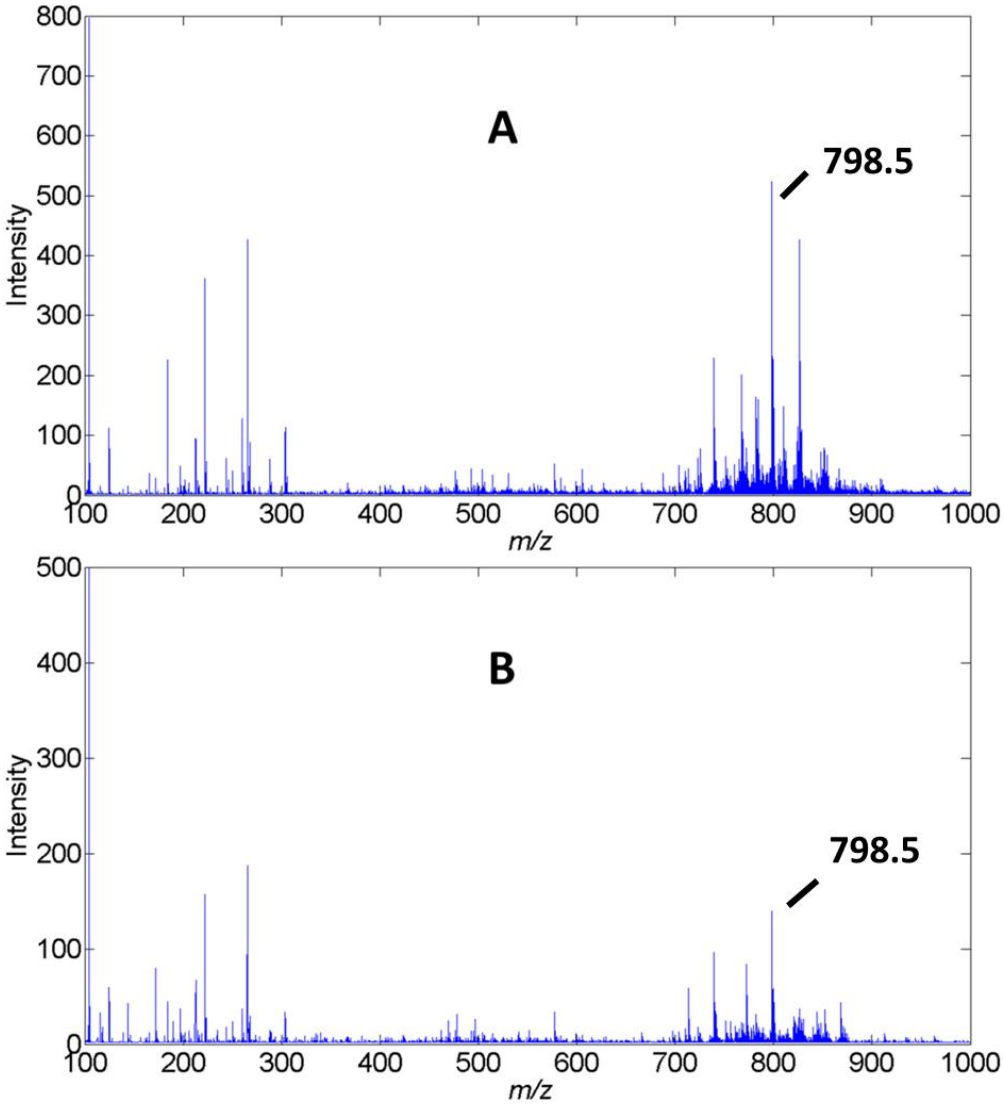

Figure 3.12. Representative region mean spectra from CHCA and rat brain tissue 0 % attenuation. Data were acquired at a repetition rate of 5 kHz at raster speeds of 0.2 mm s^{-1} (A) and 1 mm s^{-1} (B). When operating at 0 % attenuation

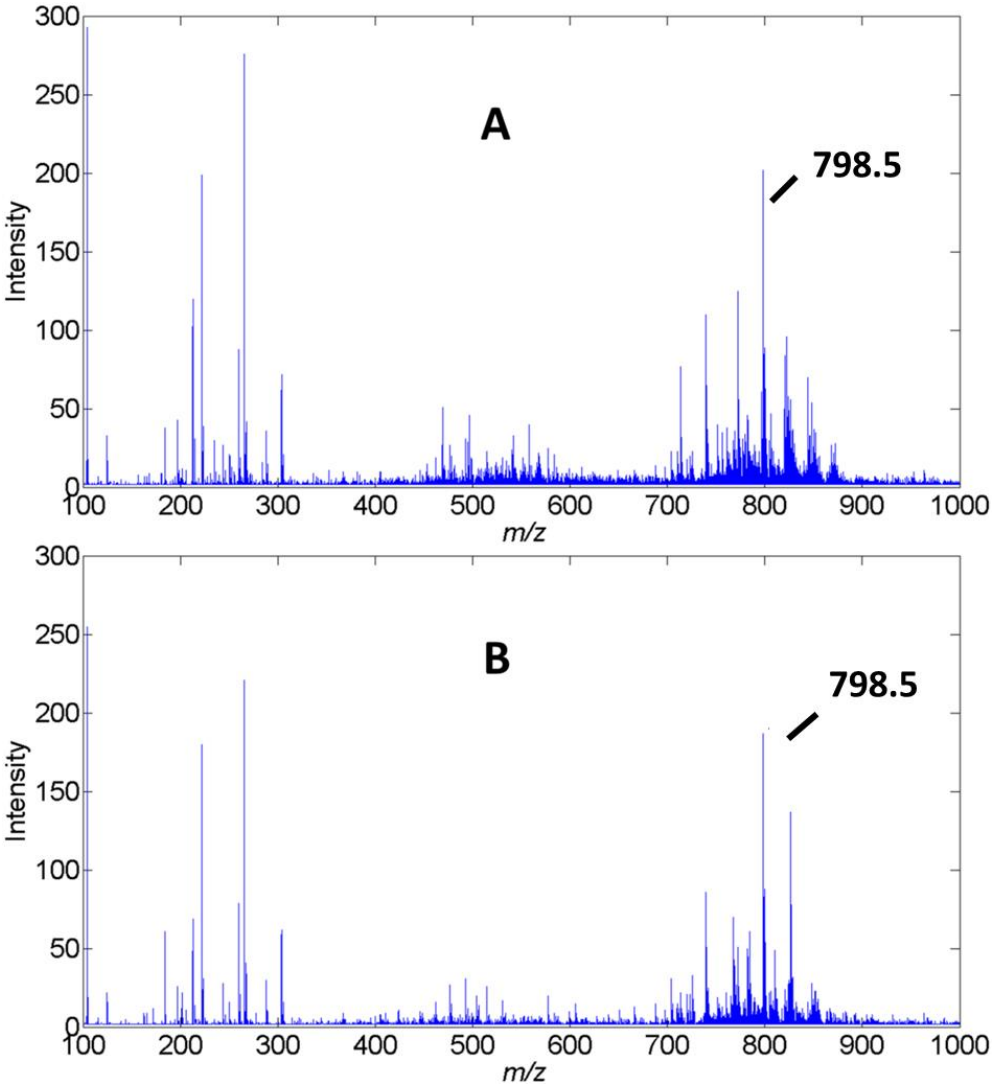

Figure 3.13. Representative region mean spectra from CHCA and rat brain tissue 0 % attenuation. Data were acquired at a repetition rate of 15 kHz at raster speeds of 0.2 mm s^{-1} (A) and 1 mm s^{-1} (B). Approximately equivalent ion intensity is seen for the lipid rich *m/z* region 700 – 900 Da.

More ions are detected within the lipid mass to charge region (including the *m/z* = 798.5 peak used for Figures 3.10 and 3.11) at lower speeds when operating at 5 kHz as oppose to 15 kHz (Figures 3.12 and 3.13 spectra A). Whereas, at 1 mm s^{-1} these two repetition rates give rise to similar ion intensities within the lipid *m/z* region (Figures 3.12 and 3.13 spectra B). The most obvious difference between the spectra for 5 and 15 kHz at 1 mm s^{-1} is a slight increase in intensity for the lipid fragment related ions at *m/z* = 450 – 600 at 15 kHz and the PC lipid head-group fragment ion at *m/z* = 104.1 [186] at 5 kHz. This could point to changing fragmentation pathways or amounts of fragmentation as being responsible for some of the trends seen but there is sufficient variability within these data to make this unclear. Furthermore, the different energies delivered at these two repetition rates make these changes in fragmentation both more likely and more difficult to assess from these data.

The similarity of spectra acquired at 25 kHz, regardless of the raster speed, is shown within Figure 3.14. The lipid rich *m/z* region 700 - 900 shows particular similarity across these raster speeds at 25 kHz repetition rate. The reason for the reduced influence of raster speed at this repetition rate is unclear and is not echoed in the trends of the other repetition rates investigated (Figure 3.10). It does, however, suggest that at higher repetition rates, some aspect of the processes causing the trends within these data is no longer a significant influence upon the ion yield.

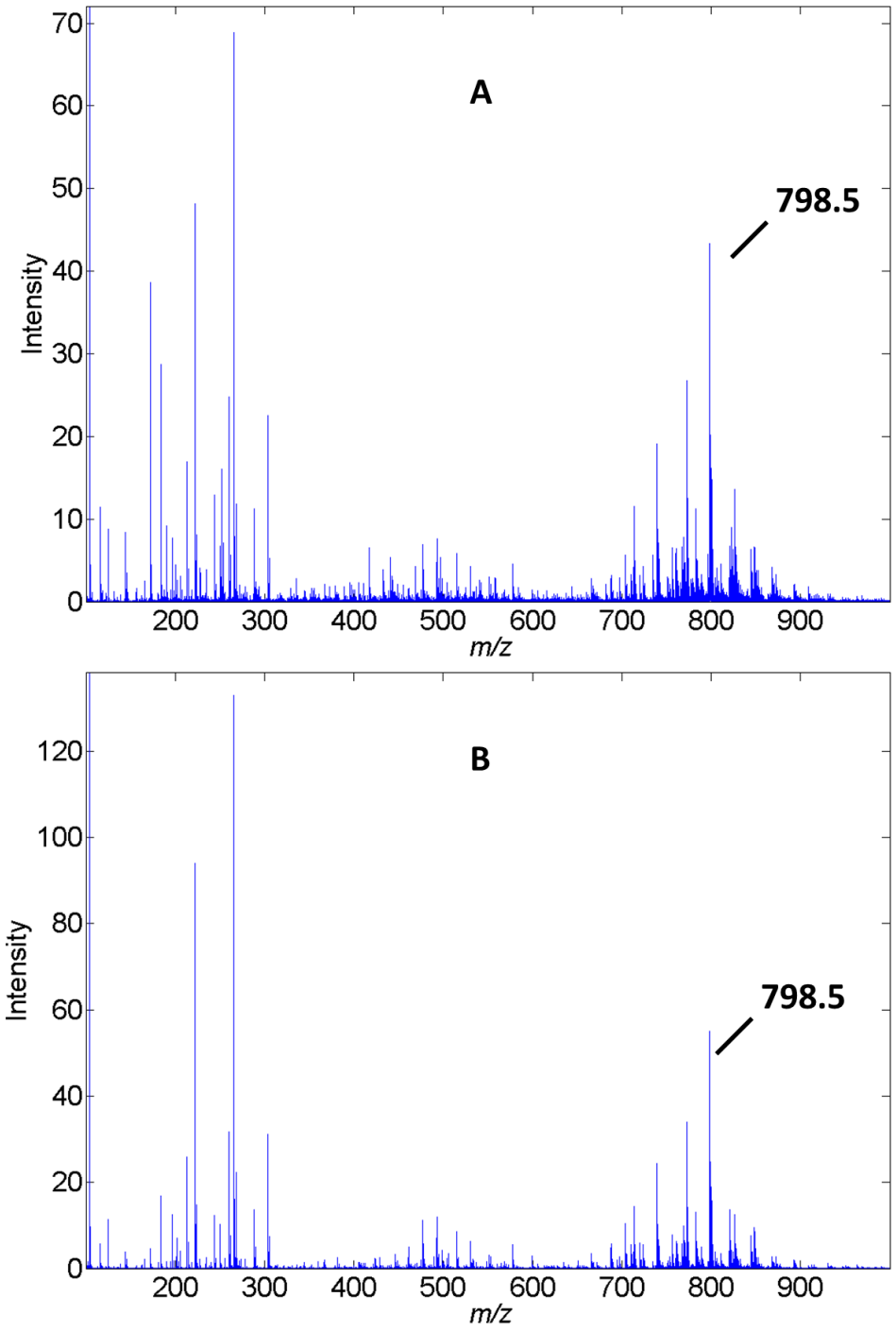

Figure 3.14. Representative region mean spectra from CHCA and rat brain tissue 23 % attenuation. Data were acquired at a repetition rate of 25 kHz at raster speeds of 0.2 mm s^{-1} (A) and 2.8 mm s^{-1} (B). Minimal lipid region (*m/z* = 700-900) spectral differences are seen for data collected at different raster speeds for a repetition rate of 25 kHz.

The trends seen within this study will inevitably be influenced by the fluence delivered at each repetition rate. As noted earlier, increasing the repetition rate between 5 and 25 kHz decreases the fluence delivered, though true measurement of this was not carried out within this study. In general, as the raster speed is increased, the influence of the repetition rate on the ion yield is reduced. This corresponds to a decrease in the influence of fluence on the ion yield as well, contradicting some aspect of MALDI mechanism theory and experimental evidence [9]. This strongly suggest that additional factors are influencing the ion yield; likely the same phenomena causing the trends observed by Spraggins *et al*. [134]. Additionally, the trends seen do not appear to be a result of the repetition rate independent of the fluence, as evidenced by the data shown in Figure 3.10 A-D. As the attenuation is increased independent of the repetition rate, shifts in optimum frequency occur for any given repetition rate.

It is known that within a certain range an increased number of laser pulses gives an increased ion count and a higher fluence will increase the number of ions generated per pulse and in total, for interrogation of a fixed spot [23]. It may be possible to apply these concepts to raster imaging: at faster raster speeds the reduced time spent per pixel may be compensated for by an increased number of laser pulses (at a lower energy) within that pixel. But if the repetition rate is even higher (at corresponding lower energies) better results will not continue to be seen as the benefit of higher energy and fewer pulses will outweigh the lower energy but increased pulses option. It has previously been reported that as the fluence drops further an ion desorption / detection threshold will be reached and no ions will be detected at all [21, 23].

It is reasonable to assume that the number of ion counts per pixel will level out as the number of pulses increases to the point where no more ions are available at that fluence. This

has been shown for interrogation of fixed spots [23] but is not sufficient to explain the decrease seen here. To the authors knowledge no similar effect has been observed in dried droplet MALDI-MS, though a leveling out and reduction in ion signal is observed as fluence is increased; where fragmentation, plume effects and detector saturation have been thought to be the cause [21, 23, 25, 29]. The Caprioli group [134] also saw a decrease in ion signal at repetition rates higher than an optimum value. Their proposal that the decrease in signal is due to severe oversampling does not appear to hold true in all cases within this study. For example, higher ion counts per pixel are seen at 10 and 15 kHz as compared to 5 kHz at some raster speeds within Figures 3.3 and 3.10. However, the effect discussed in this paragraph does appear to be caused by some aspect of overlapping pulses as the stage is moved. One possibility which is not ruled out by our results is that surface modification effects occurring at different rates and to different extents could possibly be the cause of or a contributing effect to this phenomenon [23, 30-32].

3.4. Conclusion

In order for MALDI-MS to excel as a high throughput technique for tissue imaging not only must improvements in instrumentation be introduced but a deeper understanding of underlying factors must also be sought. This study of the relationship between laser repetition rate and raster speed for a new Nd:YVO_4 laser shows the optimum configuration for different imaging considerations (e.g. throughput vs. sensitivity) which is clearly very important for any given instrumental setup. The use of a 5 kHz was found to be optimum under most conditions at lower raster speed and the use of 10 kHz may be preferable at higher raster speeds. In addition the results presented provide a deeper insight into this relation which can help direct the use and further development of MALDI imaging systems. These results

demonstrate that for a given raster speed there is an optimum repetition rate and raster speed at which the ion counts obtained per pixel will be maximized. This repetition rate depends upon the fluence and raster speed in question and will therefore vary from instrument to instrument, depending upon the operational setup available, meaning optimisation is vital for improved imaging performance. This study does not show that there is a fixed optimum repetition rate above which ion counts suffer as a result of extreme oversampling. Whilst this does appear to exist for a specific raster speed it can shift to higher repetition rates as the raster speed is increased.

The complexities of the trends observed within this study make progress toward a fundamental understanding of their cause problematic. The change in fluence at different repetition rates with the laser used is unfortunate and clouds the interpretation of the influence of repetition rate and raster speed within the data. Controlling the energy per pulse so it was uniform across all values of repetition rate would help allow a more rigorous investigation of the phenomena seen here. Furthermore, the potential changes of spectral properties such as fragmentation, which could be contributing to the trends seen, are difficult to interpret due to the presence of many lipid species within the sample. Use of a lipid standard would enable the monitoring of this and related issues in an unambiguous fashion.

Chapter 4

A systematic survey of the effects of repetition rates up to 25 kHz in continuous raster mode MALDI MS

4.1. Introduction

In order to access the fastest image acquisition times it is now considered necessary to employ high repetition rate lasers for MALDI-MSI in continuous raster sampling mode. This provides throughput benefits over spot mode image acquisition due to the continuous movement of the laser over the sample [131]. The performance of high repetition rate lasers in MALDI-MSI in raster mode was the topic of two recent publications [134, 165]. Both studies suggest that there was an optimum repetition rate for use in raster imaging and that a decrease in signal was observed when exceeding this rate. In one case it was suggested that this was due to excessive laser pulse to pulse overlap and that a limit of 50 laser pulses per unit area should be observed for optimum performance [134]. This limit was not observed within the experiments carried out within Chapter 2 of this thesis and although the same matrix was used in all three of these studies, the analytes used were different. Despite not agreeing that an oversampling limit of 50 pulses per pixel exists; previously unreported trends were observed in Chapter 2 and the underlying mechanisms causing these phenomena are likely to be the same as those investigated by Caprioli *et al* [134].

The MALDI ionization process is typically described as depending upon the number and nature of photons incident upon the matrix-analyte crystals within each laser pulse. Therefore, the characteristics of the laser which are deemed to be important are the temporal pulse width, the wavelength, the number of photons delivered per pulse and the size and distribution of the photons as incident upon the sample (the beam profile) [9, 39]. In the previous chapters the monitoring and effect of laser beam profile and the optimization of repetition rate and raster speed were investigated with a view to improving understanding of some of these fundamental influences within MALDI MS. Whilst novel effects due to repetition rate and raster speed were observed within the analyses in Chapter 2, further study is needed to uncover the reasons and mechanisms behind those trends. The control of energy / fluence and the use of a more easily understood analyte were deemed the crucial factors in extending the work in Chapter 2 from an optimisation study to one which can potentially reveal further insights into fundamental aspects of the MALDI MS technique.

4.2. Experimental Section

4.2.1. Materials

Methanol (HPLC grade) used in preparation of all matrix solutions was purchased from Fisher Scientific (Leicestershire, UK). The water used was purified by an ELGA Option 3 system (Marlow, UK). Trifluoroacetic acid (TFA, 99 % purity) and MALDI matrix α-cyano-4-hydroxycinnamic acid (CHCA) were purchased from Sigma Aldrich (Dorset, UK). The MALDI MS sample plates used were smooth surfaced stainless steel imaging plates from AB Sciex (Ontario, Canada). Lipid standard PC 34:1 (18:1 / 16:0) with mass of 759.578 was purchased from Avanti Polar Lipids Incorporated (Delf Zyl, Netherlands).

4.2.2. Tissue Preparation and Sectioning

Mice were sacrificed humanly at the School of Cancer Sciences, University of Birmingham in accordance with the Home Office Animals (Scientific Procedures) Act 1986 [163]. Mouse brains were flash frozen in liquid nitrogen immediately after excision (fresh frozen). Beginning within ~ 0.5 mm parallel of the sagittal midline, serial sections at 12 μm thick were collected and thaw mounted onto MALDI imaging plates. Sectioning was performed on a Leica CM 1850 Cryostat (Milton Keynes, UK).

4.2.3. Matrix Application

The lipid standard (1 mg mL^{-1} in 80 % CH_3OH, 0.1 % TFA) was mixed 1:9 (*v:v)* with CHCA (20 mg mL^{-1} in 80 % CH_3OH, 0.1 % TFA). The solution was then applied to the imaging plate using an artist airbrush purchased from Draper Air Tools Airbrush Kit (Hampshire, UK) propelled by dry N_2. 10 mL of matrix / lipid standard solution was dispensed in total. For the tissue imaging experiments 15 mL CHCA (20 mg mL^{-1} in 80 % CH_3OH, 0.1 % TFA) was deposited onto the thaw mounted tissue section by the same method.

4.2.4. Mass Spectrometry

MALDI TOF MS analysis was carried out on a QSTAR XL QqTOF instrument using Analyst QS 1.1 with oMALDI server 5.1 (Applied Biosystems). An Nd:YVO_4 (Elforlight: SPOT-10-100-355) DPSS laser with λ = 355 nm, < 50kHz repetition rate and < 1.5 ns pulse length was used in this study. The Nd:YVO_4 laser was triggered by a Thurlby Thandar Instruments (Huntingdon, Cambridgeshire) TGP110 10 MHz Pulse Generator. The laser was

coupled to the MALDI source via a 100 μm core diameter fibre optic patchcord (Edmund Optics, NA = 0.22). All data were acquired in positive ion mode.

4.2.5. Laser Beam Profiling and Energy Measurement

The laser power was measured using a Molectron PM10 detector in conjunction with a Molectron PM5200 power meter (Molectron are now Coherent Inc. (Ely, UK)). The fluence was subsequently calculated from these results. The fluence was calculated using the laser beam dimensions determined within Chapter 1 using the fluorometric method.

4.2.6. MALDI MS Continuous Raster Mode Sampling of Lipid Standard

The repetition rate of the Nd:YVO_4 laser was set to 1, 5, 10, 15, 20 and 25 kHz ± 10 %. The raster speed was varied across the five pre-set values available (0.2, 0.3, 0.5 1.0 and 2.8 mm s^{-1}). Data was acquired at a pixel size of 350 × 350 μm for all variable combinations. One raster line of 38.5 mm in length was acquired for each combination of raster speed and repetition rate with the Nd:YVO_4 laser. The energy of the laser was measured before and after each of these acquisitions. The average of these values are discussed in the text and used in the fluence calculation. This experiment was repeated four times where the energy per pulse (0.6, 0.8, 1.0, 1.2 μJ) was held constant across all variable combinations. This was achieved by altering the attenuation (Brewster's angle attenuator) of the laser beam under each new combination of variables.

4.2.7. MALDI MS Raster Imaging on Tissue

The lipid standard experiment was repeated in tissue with the following modifications. Each data set was comprised of one raster mode image ~ 10 mm wide (depending upon the

width of the tissue section) and 1.05 mm deep which corresponds to ~ 85 pixels. This experiment was performed for all combinations of raster speed and repetition rate at energies 1 and 1.1 μJ per pulse. Off tissue pixels were excluded from the statistical analysis.

4.2.8. Processing of MALDI MSI Data

The data were converted from AB Sciex proprietary file format (.wiff) to .mzML using AB MS Data Converter (AB Sciex version 1.3) and then converted to imzML using imzMLConverter [164] and processed in MatLab (version 7.8.0 (2009a), Math Works Inc, USA). The mean ion counts (peak area ± 0.1 Daltons) for selected mass-to-charge values were calculated along with the standard error of the mean (SE) and are plotted as mean value ± SE in all bar charts.

4.3. Results and Discussion

4.3.1. Variation of Repetition Rate and Raster Speed in Continuous Raster Sampling MALDI MS

The variation of mean ion counts per pixel for the protonated molecule of PC 34:1 (18:1 / 16:0) $[M+H]^+$ under varying repetition rate, raster speed and fluence is shown in Figure 4.1. At a fluence of 34 J m^{-2} (Figure 4.1 D) broad trends seen are as follows: the mean analyte ion yield is observed to decrease as the repetition rate increases, regardless of the raster speed used; the trends between repetition rates approximately hold independent of the raster speed used; the optimum raster speed for all repetition rates is 0.2 mm s^{-1}. Where optimum refers to largest ion yield produced. Similar general trends are evident in Figure 4.1 C (28 J m^{-2}), with the exception that as the raster speed increases the difference in mean ion

counts afforded by the various repetition rates reduces. Further departures from these trends are seen in Figure 4.1 B (23 J m^{-2}): the mean ion counts no longer improve with decreasing repetition rate at a given raster speed. Instead the optimum repetition rate has increased to 10 kHz and 1 kHz is one of the poorest performing frequencies, particularly at the slower raster speeds. The repetition rate trends stay roughly consistent across the raster speeds with a decrease in the impact of repetition rate as the raster speed increases. In addition, the optimum raster speed for a given repetition rate is no longer solely 0.2 mm s^{-1}; 1 kHz now shows improved ion counts at the faster speed of 0.3 mm s^{-1}. Whilst this change is minimal in this example, it is worth noting with a view to the trends in Figure 4.1 A. The optimum repetition rate at 17 J m^{-2} is 15 kHz across nearly all raster speeds. Different trends are observed at different raster speeds and there does not appear to be a clear pattern in their shift as the speed changes. The optimum raster speed varies depending upon the repetition rate in question. 0.2 mm s^{-1} is optimum for 15 kHz, 0.3 mm s^{-1} is for 5 and 10 kHz and 0.5 mm s^{-1} is optimum for 20 and 25 kHz.

At the higher fluences investigated the trends seen do appear to agree with previous literature on high repetition rate MALDI-MS in raster mode, [134] whereby increasing the repetition rate was found to result in reduced ion yields. However, additional relationships are seen when the lower two fluences are considered. At a given raster speed there appears to be an optimum repetition rate; this rate is dependent upon the fluence used and broadly speaking shifts to higher values as the fluence decreases. In addition at the lowest fluence considered a given repetition rate has an optimum raster speed above and below which ion yields decrease. Finally, overall, as the fluence is increased from 17 to 23 J m^{-2} the mean ion counts also increase (Figure 4.1 A, B). Contrary to what may be expected, further increase of the fluence does not appear to result in higher ion counts [21, 23].

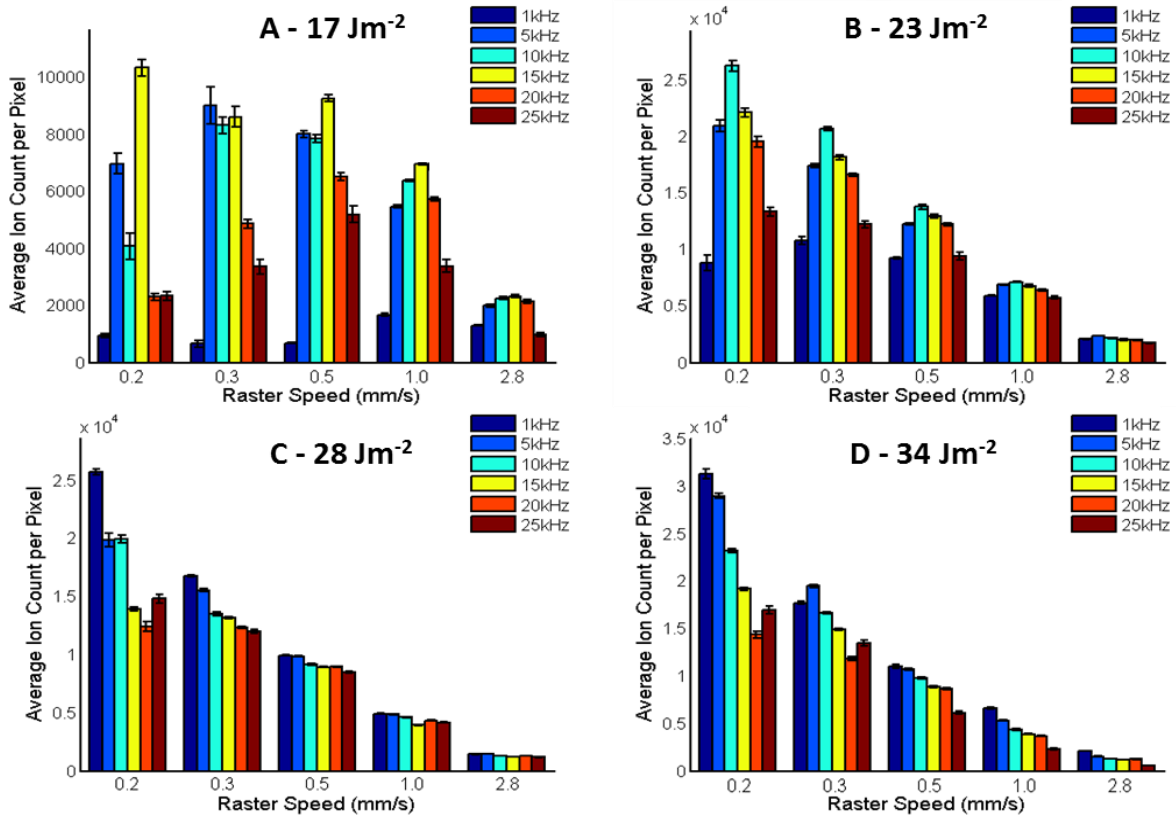

Figure 4.1. Mean ion count per pixel from thin layer preparation of CHCA and lipid standard of *m/z* = 760.6 PC 34:1 $[M + H]^+$ due to variation of repetition rate and raster speed at fluence A = 17 J m^{-2}, B = 23 J m^{-2}, C = 28 J m^{-2}, D = 34 J m^{-2}. Markedly differing relationships are found under different repetition rate, raster speed and fluence combinations.

The lipid standard (PC 16:0/18:1) surveyed in these experiments is readily detected in positive ion mode as a number of *m/z* values depending upon the charge adduct present: *m/z* = 760.6 $[M + H]^+$, *m/z* = 782.6 $[M + Na]^+$, *m/z* = 798.5 $[M + K]^+$, *m/z* = 822.6 $[M + K + Na+ H]^+$. In addition a number of fragment ions from this lipid are observed at *m/z* = 104.1 $[OH(CH_2)_2N(CH_3)_3)]^+$, *m/z* = 184.1 $[PO_4HC_2H_4N(CH_3)_3]^+$, *m/z* = 478.3 $[M+H-C_{18}H_{34}O_2]^+$, *m/z* = 504.3 $[M+H-C_{16}H_{32}O_2]^+$, *m/z* = 577.5 $[M+H-C_5H_{15}O_4PN]$ and *m/z* = 723.6 $[M+Na-N(CH_3)_3]^+$. An example spectrum highlighting these ions and some example structural

assignments are shown in Figures 4.2 and 4.3. Elements of the dramatic alteration in trends between the 17 and 34 J m^{-2} data sets shown in Figure 4.1 are further demonstrated by the spectra shown in Figure 4.4.

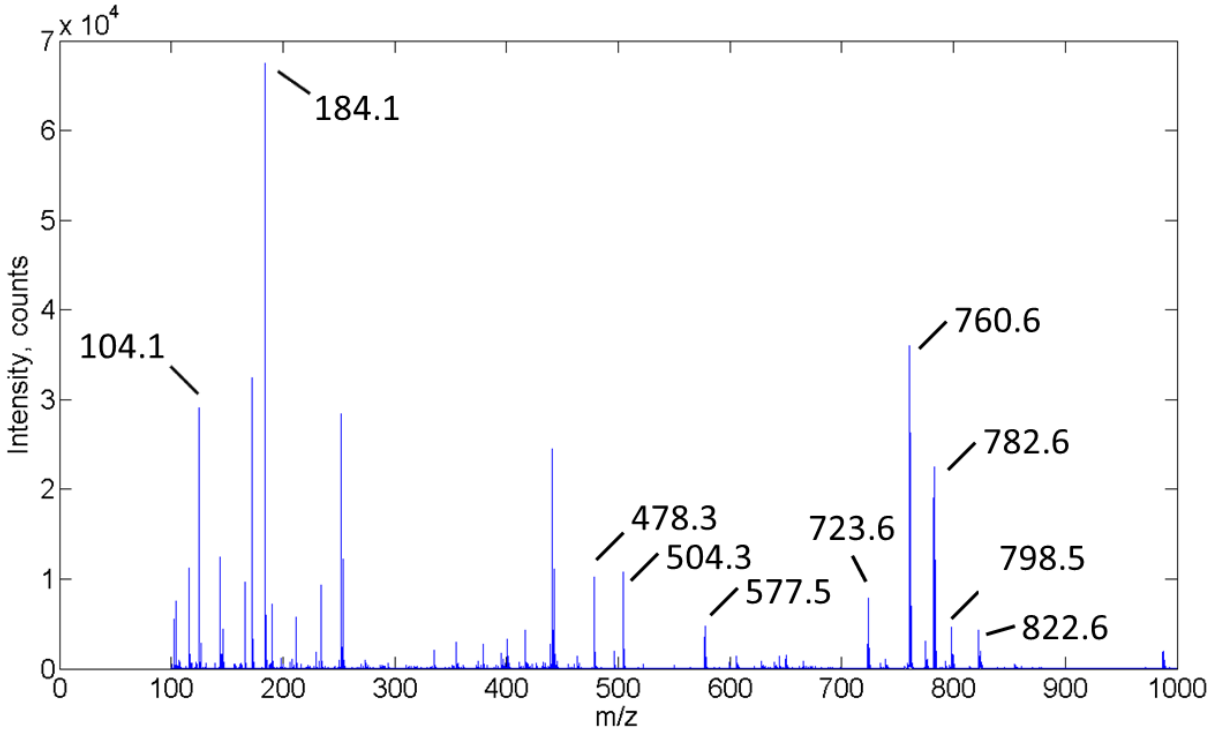

Figure 4.2. Mean spectra from thin layer preparation of CHCA and lipid standard (PC 34:1) acquired at a repetition rate of 1 kHz, a raster speed of 2.8 mm s^{-1} and a fluence of 34 J m^{-2}. Peaks of main lipid related peaks are labeled.

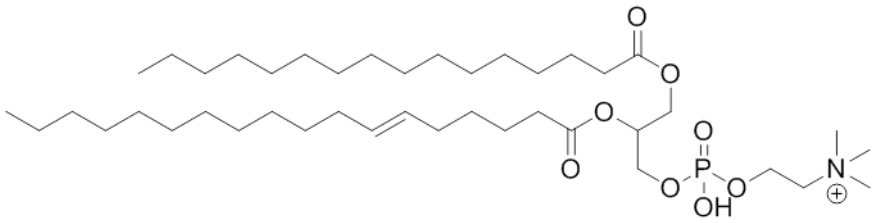

Exact Mass: 760.59

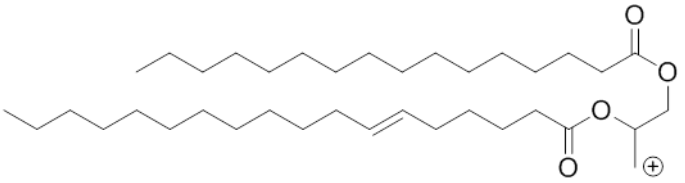

Exact Mass: 577.52

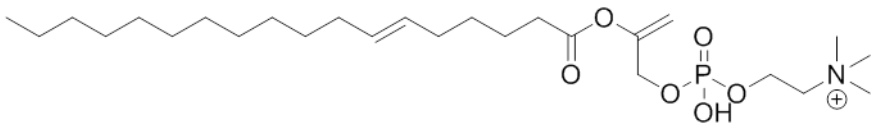

Exact Mass: 504.34

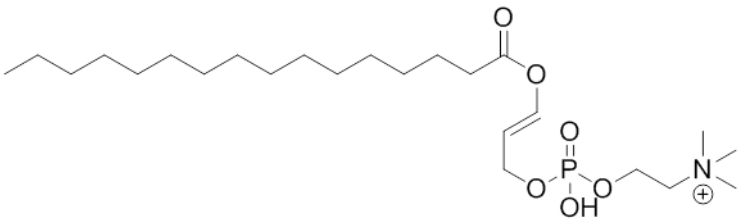

Exact Mass: 478.33

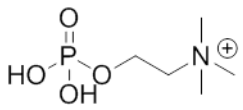

Exact Mass: 184.07

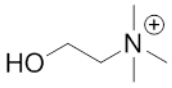

Exact Mass: 104.11

Figure 4.3. Proposed molecular structures for lipid standard PC 16:0/18:1 and some commonly observed fragment ions as labeled in Figure 4.4.

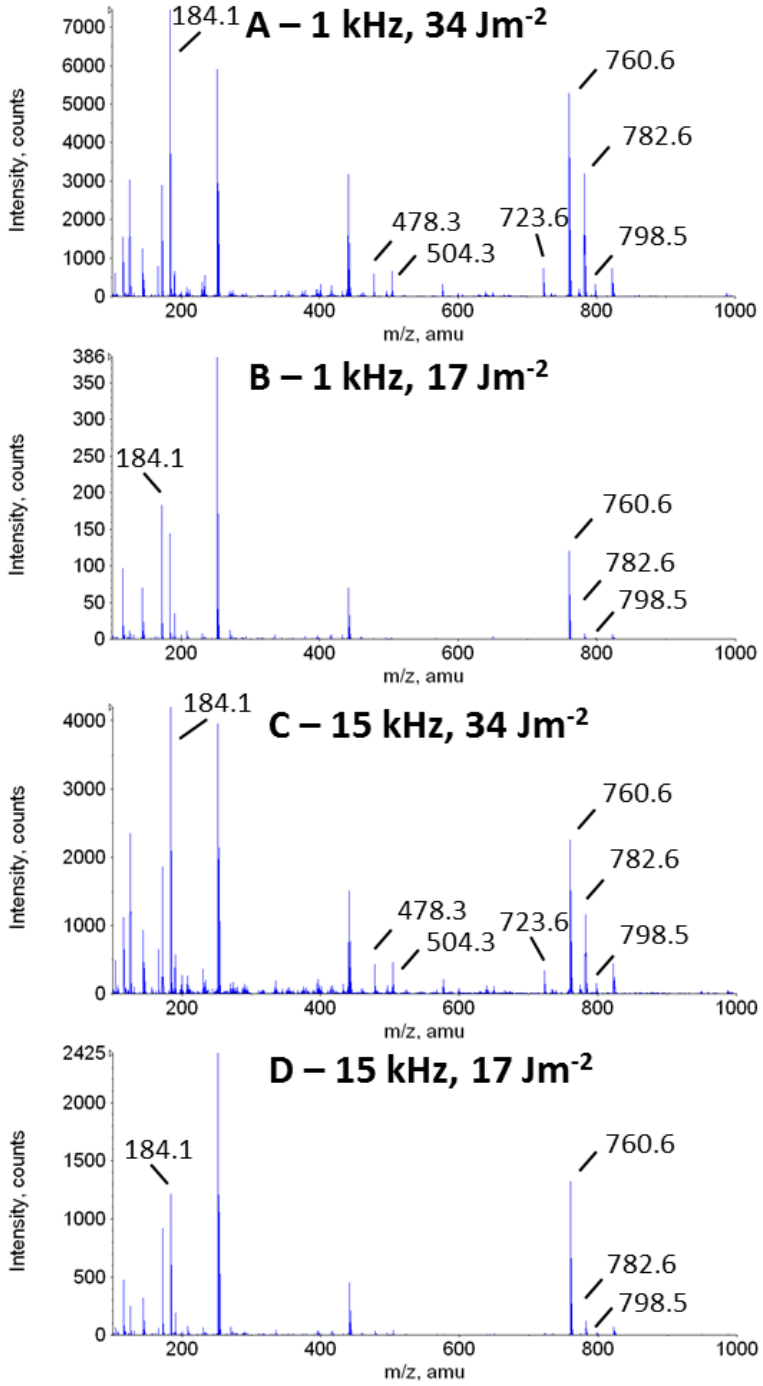

Figure 4.4. Mean spectra from thin layer preparation of CHCA and lipid standard at 1 kHz (A, B) and 15 kHz (C, D) at 17 (B, D) and 34 J m^{-2} (A, C). Raster speed was 0.2 mm s^{-1}. Spectra highlight the impact of fluence and repetition rate with respect to ion yield, lipid adduct ratios and fragmentation.

The large improvement in ion yield for peaks at *m/z* = 760.6, 782.6 and 798.5 at 1 kHz when the energy is increased is clear but the same comparison for the 15 kHz data shows a less significant improvement despite the energy difference (Figure 4.4). In addition, the improvement in ion counts at the higher repetition rate at 17 J m^{-2} is contrasted with the corresponding reduction in the 34 J m^{-2} data. There is a clear change in adduct peak ratio of *m/z* 760.6 to 782.6 from ~ 1.5 to ~ 10 at 34 J m^{-2} and 17 J m^{-2} respectively. This change is further demonstrated within Figure 4.5. Although not fully explained there are some reports in the literature discussing changing cation adduct formation [60, 187]. Within a study by Spengler *et al.* [60] sodium adducts of the dipeptide valylleucine were observed to be more intense than the protonated molecule at lower fluences and less so at higher fluences for a laser wavelength of 248 nm. However, the opposite trend was observed at a wavelength of 193 nm. The reason for these behaviors was proposed to be changes in surface vs. volume material ejection effects dependent upon the fluence observed. Differing behaviors for different wavelengths and analytes make this study complex and difficult to compare directly with the work shown here.

In addition to the changing ion adduct ratio, there is an increase in intensity for lipid fragment peaks at *m/z* = 478.3, 504.3 and 723.6 as the energy is increased (Figure 4.4). Levels of analyte fragmentation have been observed to increase with fluence due to increased internal ion energy and plume collision effects [188-190].

These features of the data could account for some element of the trends seen within Figure 4.1 and so need to be looked at. Re-plotting the graph in Figure 4.1 as the sum of $[M+H]^+$, $[M+Na]^+$ and $[M+K]^+$ shows similar trends to those in Figure 4.1 but the ion yield increases with increasing fluence as would be expected (Figure 4.6). Therefore, it does seem that the analyte ion yield increases as the fluence increases but the proportion of ions

corresponding to each of these *m/z* values changes depending upon the fluence and, to a much lesser extent, the repetition rate and raster speed.

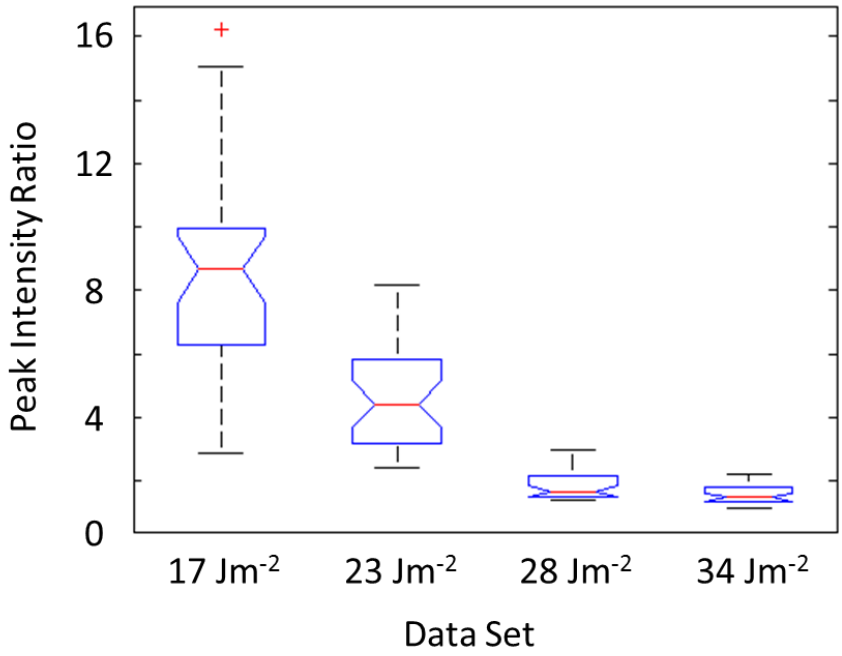

Figure 4.5. Ratio of peaks at *m/z* = 760.6 PC 16:0/18:1 $[M+H]^+$ and 782.6 PC 16:0/18:1 $[M+Na]^+$ across all four data sets. All combinations of repetition rate and raster speed are included. An increase in ion counts for $[M+Na]^+$ as compared to $[M+H]^+$ is seen as the fluence is increased. The features of each boxplot are: the red line is the median, blue lines parallel to this are the first and third quartiles, the notch around the median represents the 95 % confidence interval, the 'whiskers' represent +/- 2.7 σ and red + symbols are data points outside of this range.

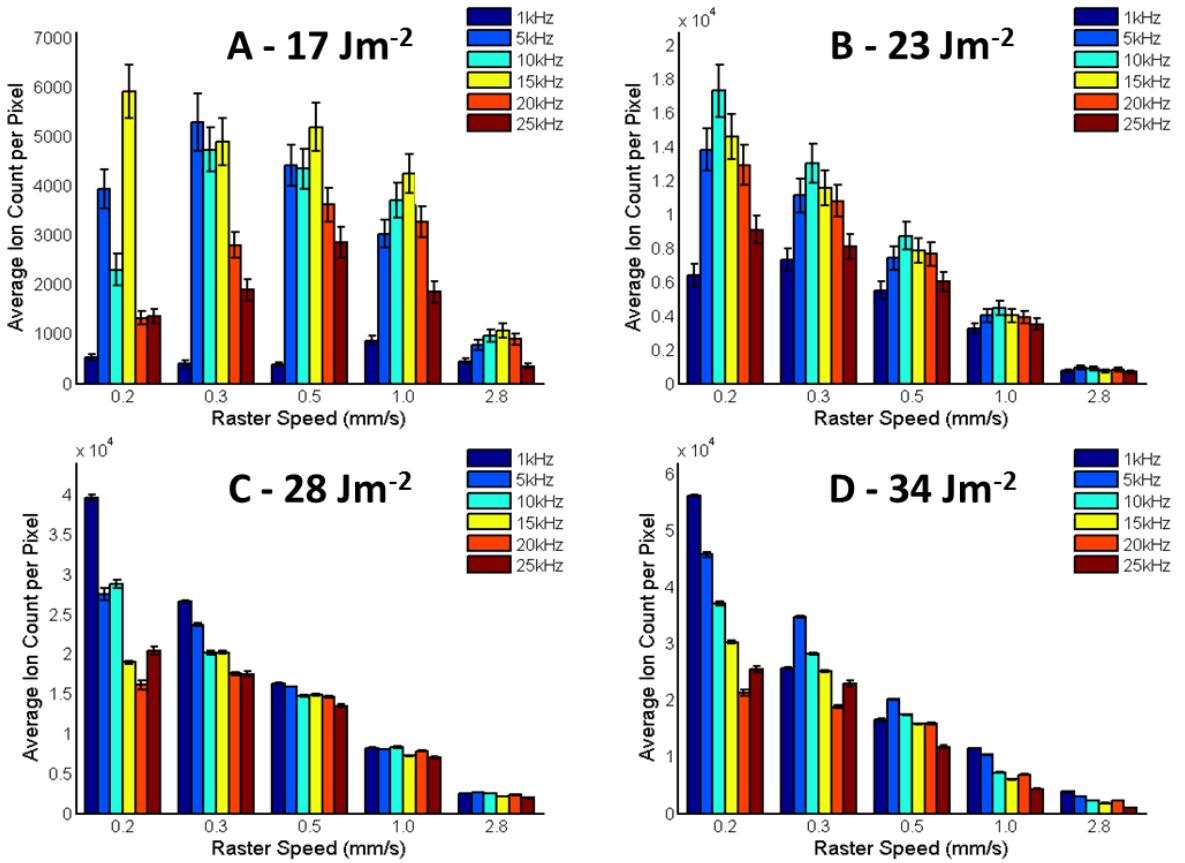

Figure 4.6. Mean ion count per pixel from thin layer preparation of CHCA and lipid standard of *m/z* = 760.6 PC 34:1 $[M + H]^+$ *m/z* = 782.6 PC 34:1 $[M + Na]^+$ *m/z* = 798.5 PC 34:1 $[M + K]^+$ due to variation of repetition rate and raster speed at fluence A) 17 J m^{-2}, B) 23 J m^{-2}, C) 28 J m^{-2}, D) 34 J m^{-2}. Markedly differing relationships are found under different repetition rate, raster speed and fluence combinations.

There are some departures from the trends seen within Figure 4.1 when all three main lipid adduct peak intensities are plotted together (Figure 4.6), however, the trends remain very similar. This strongly suggests that, despite the clear alteration in adduct peak ratio at different fluences (Figures 4.5 and 4.6), the changing adduct peak ratio is not responsible for the trends seen within Figure 4.1.

The apparent increase in fragmentation at 34 J m^{-2}, seen within Figure 4.4, may also be influencing the trends within Figures 4.1 and 4.6. This increase in fragmentation with increasing fluence is further demonstrated within Figure 4.7. Re-plotting Figure 4.1 as the combined ion counts of all major lipid related peaks (*m/z* = 760.6 $[M+H]^+$, *m/z* = 782.6 $[M+Na]^+$, *m/z* = 798.5 $[M+K]^+$, *m/z* = 104.1 $[OH(CH_2)_2N(CH_3)_3)]^+$, *m/z* = 184.1 $[PO_4HC_2H_4N(CH_3)_3]^+$, *m/z* = 478.3 $[M+H-C_{18}H_{34}O_2]^+$, *m/z* = 504.3 $[M+H-C_{16}H_{32}O_2]^+$, *m/z* = 577.5 $[M+H-C_5H_{15}O_4PN]$, *m/z* = 723.6 $[M+Na-N(CH_3)_3]^+$, *m/z* = 822.6 $[M+H+Na+K]^+$) will give an insight into the role of fragmentation in determining the trends seen within Figures 4.1 and 4.6 (Figure 4.8).

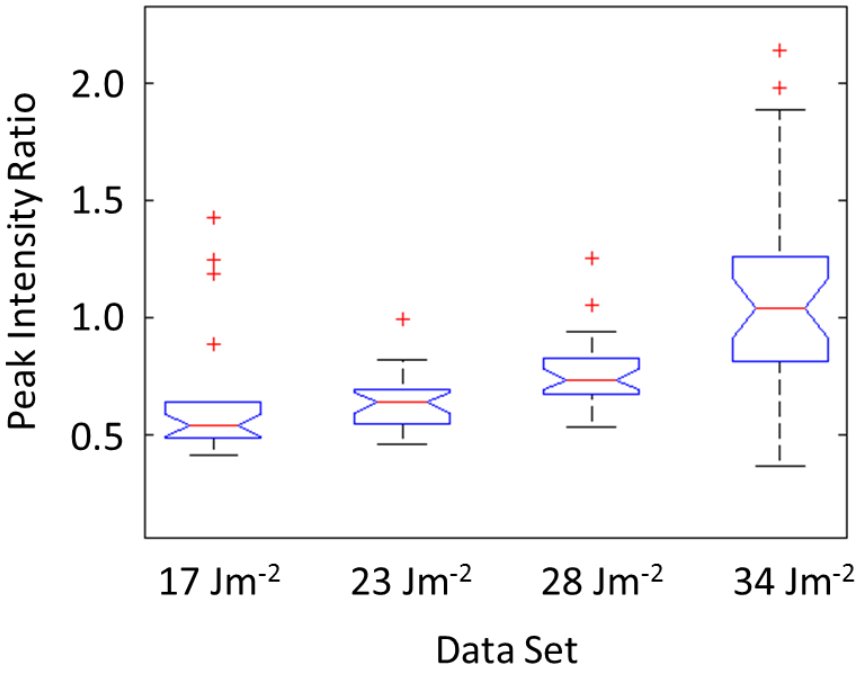

Figure 4.7. Sum of main PC 16:0/18:1 fragment peaks at *m/z* = 104.1 $[OH(CH_2)_2N(CH_3)_3)]^+$, *m/z* = 184.1 $[PO_4HC_2H_4N(CH_3)_3]^+$, *m/z* = 478.3 $[M+H\text{-}C_{18}H_{34}O_2]^+$, *m/z* = 504.3 $[M+H\text{-}C_{16}H_{32}O_2]^+$, *m/z* = 577.5 $[M+H\text{-}C_5H_{15}O_4PN]$, *m/z* = 723.6 $[M+Na\text{-}N(CH_3)_3]^+$ across all four data sets divided by the sum of the intact lipid peaks at *m/z* = 760.6 $[M+H]^+$, *m/z* = 782.6 $[M+Na]^+$, *m/z* = 798.5 $[M+K]^+$ and *m/z* = 822.6 $[M+H+Na+K]^+$. All combinations of repetition rate and raster speed are included. An increase in detected lipid related fragment ions is seen as the fluence is increased. The features of each boxplot are: the red line is the median, blue lines parallel to this are the first and third quartiles, the notch around the median represents the 95 % confidence interval, the 'whiskers' represent +/- 2.7 σ and red + symbols are data points outside of this range.

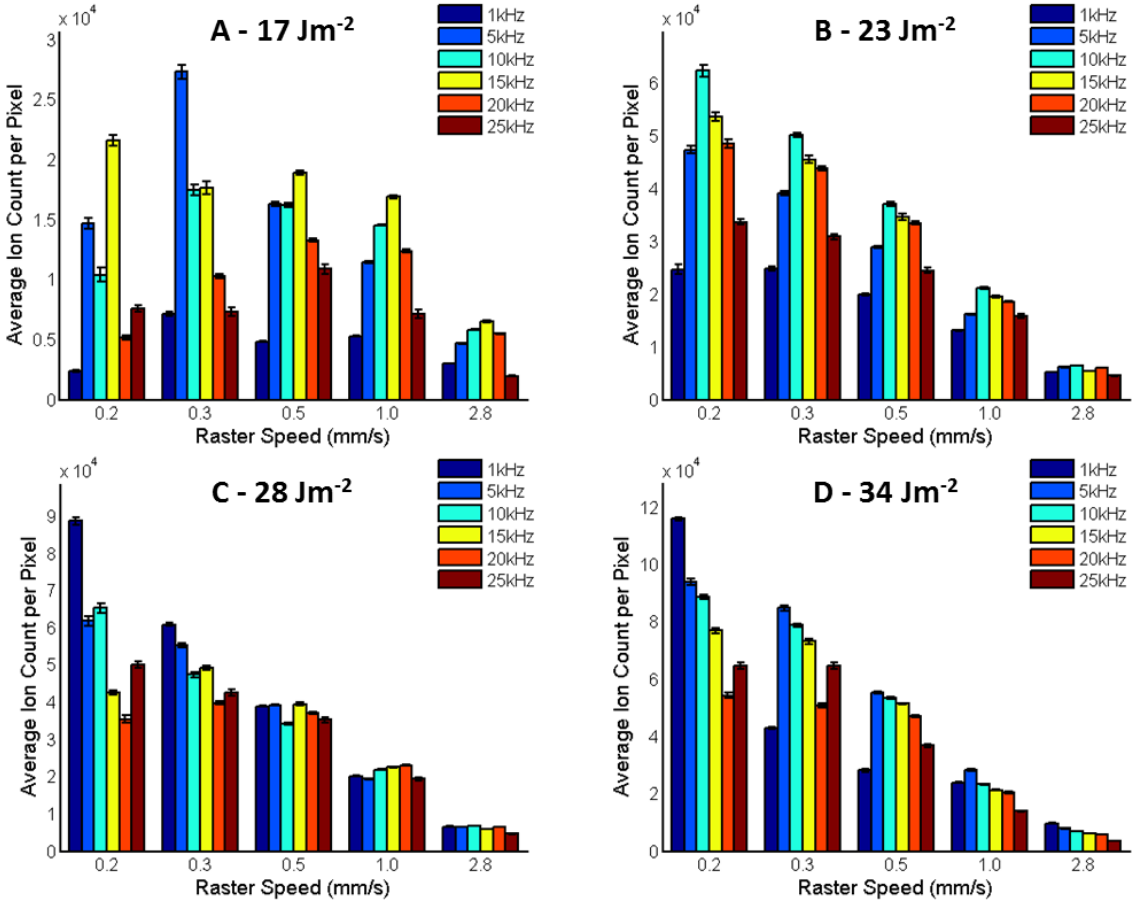

Figure 4.8. Mean ion count per pixel from thin layer preparation of CHCA and lipid standard for the summed ion counts of peaks detected at *m/z* = 760.6 $[M+H]^+$, *m/z* = 782.6 $[M+Na]^+$, *m/z* = 798.5 $[M+K]^+$, *m/z* = 104.1 $[OH(CH_2)_2N(CH_3)_3)]^+$, *m/z* = 184.1 $[PO_4HC_2H_4N(CH_3)_3]^+$, *m/z* = 478.3 $[M+H-C_{18}H_{34}O_2]^+$, *m/z* = 504.3 $[M+H-C_{16}H_{32}O_2]^+$, *m/z* = 577.5 $[M+H-C_5H_{15}O_4PN]$, *m/z* = 723.6 $[M+Na-N(CH_3)_3]^+$, *m/z* = 822.6 $[M+H+Na+K]^+$ due to variation of repetition rate and raster speed at fluence A) 17 J m^{-2}, B) 23 J m^{-2}, C) 28 J m^{-2}, D) 34 J m^{-2}.

Again, the trends remain very similar to those within Figure 4.1 (and so Figure 4.6). This leads to the conclusion that, despite the change in fragmentation with fluence, variation in fragmentation behavior is not the dominant factor responsible for the trends seen within Figures 4.1, 4.6 and 4.8.

Another way to place these results in context and enable further understanding is to plot the change in total ion count (TIC) across the repetition rates, raster speeds and fluences tested (see Figure 4.9). The variation of TIC is not hugely different to that of PC 16:0/18:1 and its associated fragments (Figures 4.1, 4.6 and 4.8), however there are some departures from the trends seen previously.

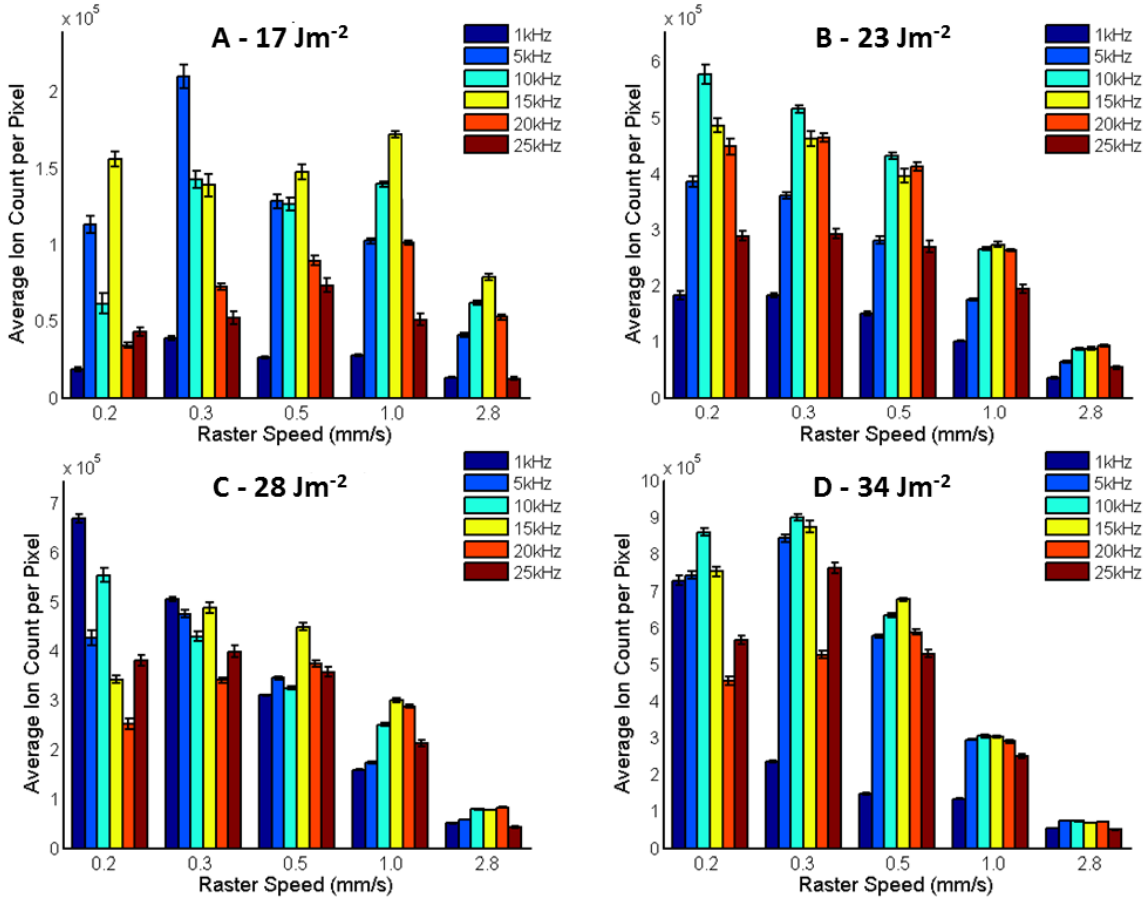

Figure 4.9. Mean total ion count (TIC) per pixel from thin layer preparation of CHCA and lipid standard (PC 16:0/18:1) due to variation of repetition rate and raster speed at fluence A = 17 J m^{-2}, B = 23 J m^{-2}, C = 28 J m^{-2}, D = 34 J m^{-2}. Some differences between the trends observed here and those seen in Figures 4.1, 4.3 and 4.6 are observed.

The trends at fluences of 17 and 23 J m^{-2} appear similar for TIC as for the lipid associated peaks. However there are departures from the trends seen previously at the two higher energies and particularly at 34 J m^{-2} where the highest ion counts are now obtained at 0.3 rather than 0.2 mm s^{-1} at all repetition rats bar 1 kHz. As the previous analysis has attempted to account for the various contributions of the major lipid and lipid fragment peaks it could be that at the fluences causing the most fragmentation (i.e. the larger ones) there may be a higher frequency of lower intensity fragment ions present within the spectra which aren't accounted for by the above summing of major peaks. Regardless, the incorporation of all detected ions into this graphical consideration does not provide an answer to the cause of the observed trends.

At a fluence of 34 J m^{-2} a 1 kHz repetition rate gives approximately twice the ion yield as at 15 kHz. Whereas at 17 J m^{-2} 15 kHz gives approximately an order of magnitude increase in ion yield over those at 1 kHz (Figures 4.1 and 4.4). These data correspond to an increase in pulses per unit area from 750 (Figure 4.1 C) to 11250 (Figure 4.1 D) as shown in Table 4.1.

Table 4.1. Number of laser pulses per point as defined by the combinations of repetition rate and raster speed used in thie study.

Raster Speed (mm/s)	Laser Pulse Repetition Rate					
	1kHz	5kHz	10kHz	15kHz	20kHz	25kHz
2.8	54	268	536	804	1071	1339
1.0	150	750	1500	2250	3000	3750
0.5	300	1500	3000	4500	6000	7500
0.3	500	2500	5000	7500	10000	12500
0.2	750	3750	7500	11250	15000	18750

To further analyze the data it may be instructive to consider the number of pulses delivered per unit area under the different combinations of repetition rate and raster speed used. For example, data collected at 1 kHz, 0.2 mm s^{-1} and 5 kHz, 1 mm s^{-1} received the same number of pulses (750 and 750 respectively). The fluence was held constant across the different repetition rates for all iterations of the experiment, as shown in Figure 4.1 A to D. Consequently, the only difference in experimental conditions was the rate at which they arrive and the area of unirradiated matrix available to each pulse due to differences in raster speed. In order to better understand these issues, the data may be normalised by the number of pulses per unit area (Figure 4.10).

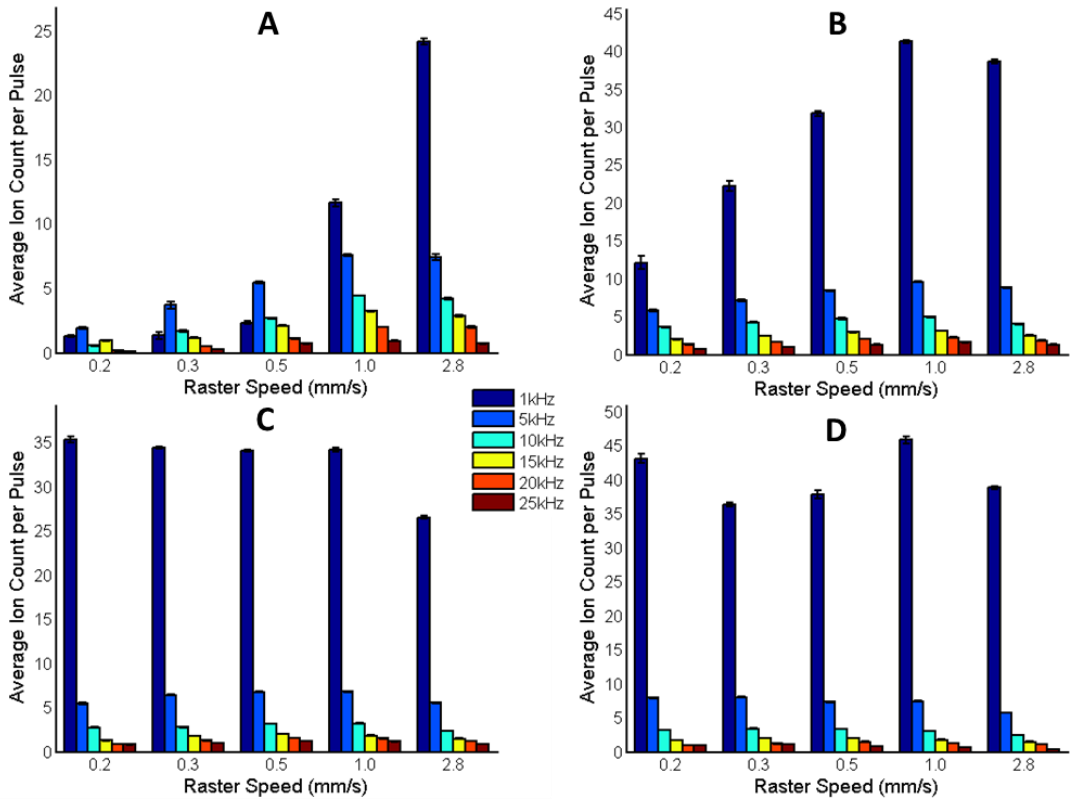

Figure 4.10. Mean ion count per pulse for PC 34:1 (18:1 / 16:0) *m/z* = 760.6 $[M+H]^+$ due to variation of repetition rate and raster speed at fluence **A** – 17 J m^{-2}, **B** - 23 J m^{-2}, **C** - 28 J m^{-2}, **D** - 34 J m^{-2}.

When the data obtained at 34 J m^{-2} are normalized to the number of pulses per pixel, the ion counts at a given repetition rate are roughly consistent across the raster speeds investigated (Figure 4.10 D). This relation appears to broadly hold for Figure 4.10 C as well. However at the lower fluences (Figure 4.10 A, B) the ion counts per pulse appear to improve as the raster speed increases. The ion yield per pulse decreases with increasing repetition rate with the exception of the three lower speeds in Figure 4.10 A. Consequently the different fluences employed appear to give rise to two phenomena.

The broadly independent relationship between raster speed and ion yield per pulse (at a given repetition rate) in Figure 4.10 C and D gives rise to the trends seen in Figure 4.1 C and D where the increased number of pulses delivered due to slower raster speeds translates into improved mean ion counts per pixel. Conversely, the increase in ion yield per pulse (observed to increase with raster speed) and the reduced ion count difference between different repetition rates (Figure 4.7 A and B) results in higher raster speeds and repetition rates being optimum, as seen in Figure 4.1 A.

A further phenomenon which could introduce effects dependent upon the rate of pulse arrival is potential interaction of the incident laser pulse with the expanding MALDI plume from the previous ablation event. Based upon fast flash imaging and UV laser post ionization studies of the MALDI plume [52] as well as typical plume velocities [39, 191] this would seem unlikely due to the distance the plume would travel between laser pulses. For example: the time period between the pulses at the highest repetition rate of 25 kHz is 40 µs and literature values for the speed of molecules in MALDI plume type events are above 100 m s^{-1}. Taking the plume velocity to be the minimum value of 100 m s^{-1} this gives a distance travelled between pulses of 4 mm, taking the plume away from the path of the next incoming laser pulse (bearing in mind the laser pulse is focused to a spot size of less than 500 µm).

4.3.2. Variation of Repetition Rate and Raster Speed in Tissue using Continuous Raster Sampling MALDI MS

The influence of repetition rate and raster speed was investigated in tissue at fluences of 28 and 31 J m^{-2}. The mean ion yields of *m/z* = 798.5 were then used to create the graphs in Figure 4.11. The validity of using the intensity of the ion at *m/z* = 798.5 to monitor these variables in rat brain tissue was discussed in Chapter 2. The trends presented here largely reflect those seen in Figure 4.1 A despite the fluences used being closer to those used in Figure 4.1 C, D. This is to be expected as tissue imaging will typically require higher fluences than thin film analysis. It can once again be seen that for many repetition rates the optimum raster speed is not the slowest available and that for many raster speeds the optimum repetition rate has also shifted to higher values (particularly within Figure 4.11 B). The exception is the trend for 1 kHz in Figure 4.11 A where, despite being at the lower of the two fluences, the ion counts relative to the other repetition rates are surprisingly high in comparison to that seen within Figure 4.1, 4.6, 4.8 and 4.9. The main lipid region of mean spectra for several data points in Figure 4.11 are shown in Figure 4.12.

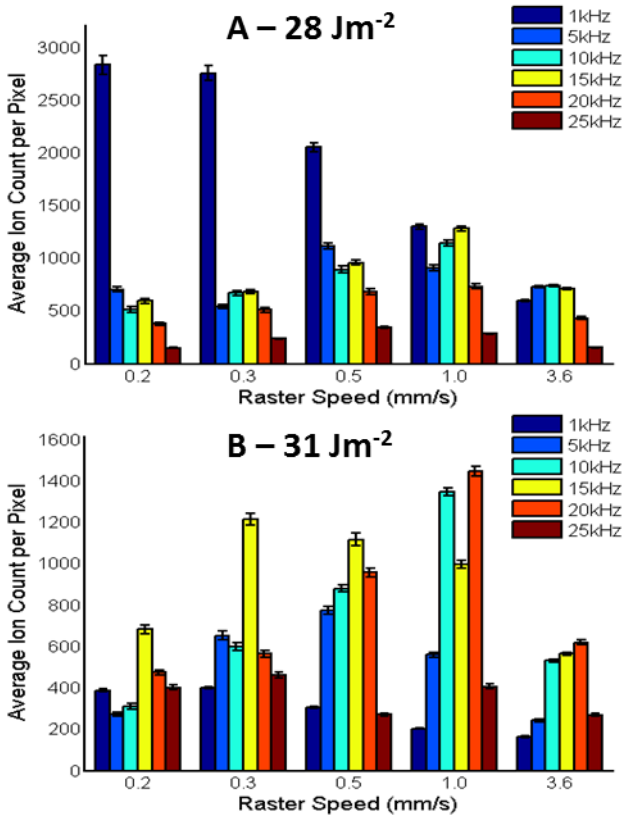

Figure 4.11. Mean ion count per pixel from sub-regions of rat brain tissue section with CHCA for *m/z* = 798.5 PC 34:1 $[M + K]^+$ at fluence of 28 J m^{-2} (A) and 31 J m^{-2} (B). The optimum raster speed varies considerably depending upon the repetition rate used and underlying trends appear to show some fluence dependence.

Spectra were chosen to illustrate the change in performance afforded by increasing the repetition rate at a fixed raster speed. In this case, repetition rates of 1 kHz (Figure 4.12 A, C) and 20 kHz (Figure 4.12 B, D) at a raster speed of 1 mm s^{-1} are displayed. At a fluence of 28 J m^{-2} the ion yield is seen to decrease by approximately 25 % as the repetition rate is increased (Figure 4.12 A, B) whereas at 31 J m^{-2} the ion yield increases by approximately an order of magnitude as the repetition rate is increased from 1 to 20 kHz. Due to the presence of a large number of lipid peaks within these spectra, it is not possible to ascribe the influence of changes in adduct formation or fragmentation to the trends seen in tissue. However, the

spectra within Figure 4.12 are similar to one another and the relative peak intensity relationships appear to hold under the different variable combinations examined.

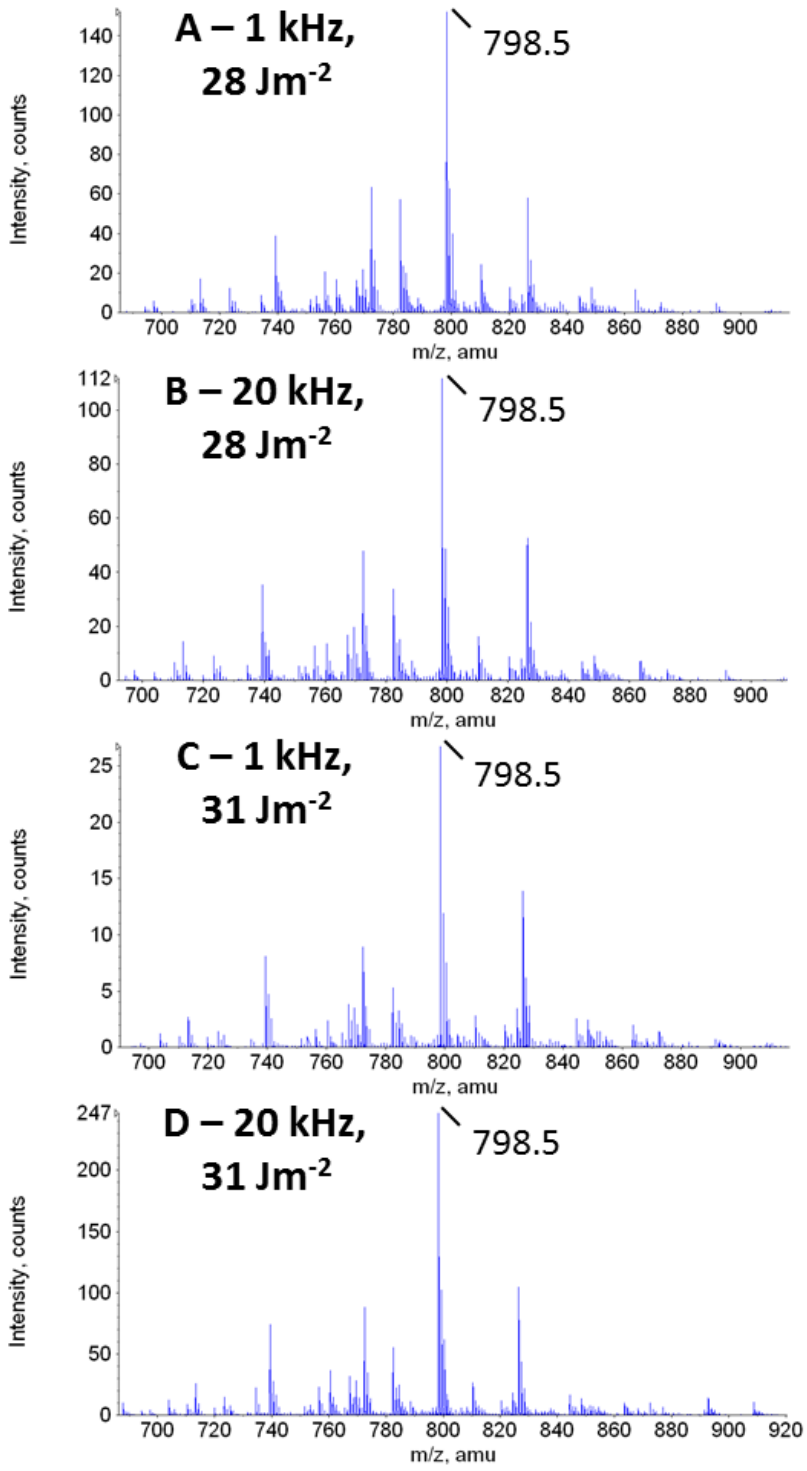

Figure 4.12. Mean spectra from sub-regions of rat brain tissue section with CHCA at 1 kHz (A, C) and 20 kHz (B, D); 28 J m^{-2} (A, B) and 31 J m^{-2} (C, D) all at raster speed of 1 mm s^{-1}. At 31 J m^{-2} a repetition rates of 20 kHz display order of magnitude improvement compared to 1 kHz (C, D). Highlighted peak correspond to PC 34:1 *m/z* = 798.5 $[M + K]^+$.

Although the trends observed from analysis of lipid standard and tissue (Figures 4.1, 4.6, 4.8, 4.9 and 4.11) provide great insight into the complex relations between fluence, raster speed and repetition rate within these studies, they do not in themselves reveal the underlying mechanisms causing these phenomena; though they do appear to rule out changing lipid adduction and alteration of fragmentation levels as the cause. Research on the variation of raster speed and repetition rate by *Spraggins et al.* showed a decrease in ion yield when approximately 50 pulses per unit area were exceeded [134]. Whilst this study does, in places, broadly support their conclusions, at no point were less than 50 pulses per unit area employed and in most cases vastly exceeded this value (Table 4.1). At the lower fluences, repetition rates of above 1 kHz were found to be optimum and higher repetition rates as well as higher raster speeds were often found to be beneficial. This suggests the picture is more complex than a simple pulse per unit area limit above which performance is reduced.

Qiao *et al.* investigated issues relating to number of laser pulses and fluence for spot mode analysis using Nd:YAG and N_2 lasers [23]. They found that the ion yield of substance P (1347 Da) with CHCA matrix at 560 J m^{-2} reached its maximum of ~ 1.4×10^4 after ~ 150 laser pulses and the sample was visibly depleted. At 320 J m^{-2} the maximum ion yield of ~ 4×10^4 was reached after ~ 300 laser pulses but there was no accompanying visible depletion of the sample. It was suggested that the decay of the signal at lower fluences despite the remaining visible sample could be due to surface modification / heating / hysteresis effects [30-32]. This effect was seen by *Fournier et al.* in a single large protein doped sinapinic acid (SA) crystal [31]. Ion yield per pulse was observed to halt after ~ 30 pulses at energy of 1.5 – 2 μJ but several 8 – 9 μJ pulses allowed further ion acquisition at the lower fluence setting. Structural changes to the crater surface, as well as decarboxylation of the matrix and the effect of this on the UV absorption were thought to be the cause; it was further mentioned that a

similar effect was also observed in CHCA [31]. Aspects of this phenomena were further investigated by Tarzi et al. who investigated the effects of temperature on various UV MALDI-MS matrices [192]. It was shown that heating of CHCA and SA led to chemical changes in the matrix. Decarboxylation of these matrices was again found to be present though to a much greater extent in CHCA than in SA. It was proposed that the observed thermochemical degradation of SA and CHCA was likely to blame for the phenomena seen by *Fournier et al* [31, 32]. Evidence obtained by the Zenobi group [193], amongst others, shows that matrices such as 2,5 DHB and nicotinic acid, will experience temperatures as high as 1000 K during MALDI MS analyses. It is worth noting that due to the speckle pattern of the laser spot used in this study there may be similar low / high energy pulse variation to that to that utilized by *Fournier et al.* and so surface modification effects may well be occurring naturally within this study and other MALDI-MS studies; though the data from Figure 2.3 would appear to rule out a changing beam profile as being the cause of the trends within this article.

4.4. Conclusions

Here a high repetition rate (< 50 kHz; Nd:YVO_4) laser was used in conjunction with a hybrid orthogonal MALDI-QqToF mass spectrometer to probe the relationship between beam profile, repetition rate, raster speed and fluence within raster mode MSI of lipids.

Analysis of thin layer CHCA and lipid standard preparations show complex relationships with several underlying trends evident within the data. Similar relationships are also show to be present in tissue data sets. A fluence dependence of the relationship between repetition rate and raster speed was also shown. Repetition rates of 20 kHz were seen to provide optimum ion yield under certain fluences in tissue with continuous raster mode

analysis. Despite not uncovering the mechanism(s) causing the observed trend it can be concluded that ion adduct variation, fragmentation and variation of beam profile at different repetition rates (Chapter 1) are not the sole causes nor are they likely to be significant contributors.

The influence of both repetition rate and raster speed are shown to be extremely important when optimizing raster imaging experiments for increased sensitivity and or throughput. These considerations are also crucial for the improved understanding and implementation of high repetition rate lasers, high throughput and high sensitivity MALDI-MS imaging. Once the operator or experimenter understands the role these variables play in influencing the sensitivity of MALDI MS, this knowledge can be implemented in applications such as tissue imaging. In addition, a better understanding of these variables allow one to move their investigations into other important areas of MALDI MS, such as studying the influence of new matrices, with a better overall understanding of the influence on the data obtained.

Chapter 5

para - Nitroaniline is a Promising Matrix for MALDI-MS Imaging on Intermediate Pressure MS Systems

5.1. Introduction

As MALDI-MSI moves forward, it is important that the performance of different matrices is assessed as instrumental characteristics progress and alter. The use of high-repetition-rate lasers in MALDI-MS is currently thought to be necessary to enable improvements in data acquisition speed and therefore to increase the potential throughput of the technique. Within the previous chapters of this report certain fundamental aspects of laser and instrumental variables were studied with a view to improving their understanding and optimising their setup for MALDI MSI application. Once these factors are optimised for a given instrumental setup the improvements obtained can then be utilised to improve throughput for tissue imaging applications.

Certain classes of diode-pumped solid-state (DPSS) high repetition-rate lasers (*e.g.* Nd:YFL [134] and Nd:YVO_4 [165]) have gained increased interest as a route to delivering

sufficient pulse numbers per pixel to allow faster stage speeds, increasing MALDI-MS imaging throughput as a result [134, 165]. These lasers may, however, deliver a lower energy-per-pulse as compared to more commonly used lasers (*e.g.* N_2 or Nd:YAG).

To date, high repetition-rate lasers, operating at significantly above 1 kHz, have largely been used in conjunction with CHCA [134, 165, 194]. The quest for matrices other than this is ongoing and a number of matrices have been evaluated for MALDI-MSI of lipids in tissue. These include: DHB [173], CHCA [195], 1,5-diaminonaphthalene (DAN) [128], 9-aminoacridine (9-AA) [196], 2-mercaptobenzothiazole (MBT)[197], dithranol (DT) [198] and 2,6-dihydroxyacetophenone, (DHA) [199]. Additionally 1,8,9-anthracentriol (DIT), 2',4',6'-trihydroxyacetophenone (THAP), sinapinic acid (SA), 3-hydroxypicolinic acid (3-HPA) and 1,8-bis(dimethylamino)naphthalene (DMAN) were all recently evaluated by Thomas et al. for sublimation deposition and lipid imaging. *p*-Nitroaniline (PNA) was not considered viable using the methodologies and instrumentation described in their study [128]. However, there has been little or no work focused on the use of matrices, novel or existing, with high repetition-rate lasers for rapid data acquisition MALDI-MS imaging.

PNA was first presented as a potential matrix for MALDI-MS analysis of proteins / nucleotides in 1993 [61] and for lipids in 1995 [200]. PNA was revisited in 2004 for the analysis of lipids in porcine and bovine lens tissue [201-203]. The authors found PNA to be superior to DHB, producing higher signal-to-noise ratios in both the positive and negative modes, as well as performing better under conditions of high salt concentration (typical in tissue MSI applications). Unfortunately, PNA has been shown on a number of occasions to sublime readily under the vacuum conditions commonly used in MALDI-MSI [204]. Consequently PNA has been considered to be unsuitable for MALDI-MSI [205].

Whilst many MALDI-MSI instruments do operate under vacuum conditions which preclude the use of PNA, there are a considerable number of commercial instruments (Thermo Scientific [206], AB Sciex [116] and Waters [207]) and home built instruments [156] whose sources operate at intermediate or atmospheric pressure. Third-party atmospheric pressure sources are also available for some commercial MALDI-MS systems.

5.2. Experimental Section

5.2.1. Materials

Methanol (HPLC grade) used in preparation of all matrix solutions was purchased from Fisher Scientific (Leicestershire, UK). The water used was purified by an ELGA Option 3 system (Marlow, UK). Trifluoroacetic acid (TFA, 99% purity) and MALDI matrices α-cyano-4-hydroxycinnamic acid (CHCA) and *para* - nitroaniline (PNA) were purchased from Sigma Aldrich (Dorset, UK). The MALDI MS sample plates used were smooth surfaced stainless steel imaging plates from AB Sciex (Ontario, Canada).

5.2.2. Tissue Preparation

Mice were sacrificed humanly at the School of Cancer Sciences, University of Birmingham in accordance with the Home Office Animals (Scientific Procedures) Act 1986 [163]. Mouse brains were flash frozen in liquid nitrogen immediately after excision (fresh frozen). Mouse brain was sectioned (Leica CM 1850 Cryostat (Milton Keynes, UK)) at 12 μm thick and thaw mounted onto the stainless steel MALDI imaging plate. Tissue sections were simultaneously mounted onto the imaging plate to prevent potential biasing of the results due to differential time periods spent at ambient conditions. To simultaneously mount multiple

tissue sections, each section was held at -18 °C within the cryostat until all sections were acquired then all thaw mounted in a single action.

5.2.3. Matrix Application

Matrix solutions of PNA or CHCA (20 mg/mL in 85 % CH_3OH, 0.1 % TFA) were applied to the imaging plate using an artist airbrush purchased from Draper Air Tools Airbrush Kit (Hampshire, UK) propelled by dry N_2. When imaging in negative ion mode with PNA, no TFA was included within the matrix solution. A total of 15 mL of matrix solution was dispensed for each sample plate, for each matrix used. The airbrush nozzle was held approximately 20 cm from the plate. Three consecutive spray passes were followed by fifteen seconds dry time. This process was repeated four times then the plate was rotated on the clamp stand by ninety degrees. This sequence was repeated until all matrix solution was used. To achieve dual matrix application on single plate the appropriate half of the plate was masked during spraying and the spray was subsequently repeated with the other matrix.

5.2.4. Mass Spectrometry

MALDI-MSI analysis was carried out on an AB Sciex QSTAR XL QqTOF instrument with an oMALDI 2 ion source using Analyst QS 1.1 with oMALDI server 5.1 (AB Sciex). An Elforlight (Daventry, UK) Nd:YVO_4 (SPOT-10-100-355) DPSS laser with λ = 355 nm operated at 5 kHz was used in this study. The Nd:YVO_4 (< 50,000 Hz repetition rate and < 1.5 ns pulse length) laser was triggered by a Thurlby Thandar Instruments (Huntingdon, Cambridgeshire) TGP110 10 MHz Pulse Generator. The laser was coupled to the MALDI source via a 100 μm core diameter fibre optic patchcord (Edmund Optics, NA = 0.22). All

data was acquired at energy per pulse of ≈ 8 μJ in positive ion mode over the *m/z* range 50-1000 using a focussing potential (FP) of 85 and a declustering potential (DP2) of 35. All images collected in continuous raster mode at a speed of 1 mm s^{-1}. For the peak at *m/z* = 772.5 the mass resolving power (*m/Δm*) was calculated to be ~ 9500. MS/MS data employing collision induced dissociation (CID) was carried out using a collision energy of 40 (arbitrary units) and unit resolution (+/- 1 *m/z* unit) transmission centered around the mass of the parent ion.

Further MALDI MSI data was acquired on a Bruker Daltonics UltrafleXtreme ToF/ToF instrument. Serial mouse brain tissue sections were analysed over a period of approximately 50 minutes at a pixel size of 200 × 200 μm in positive and negative ion mode respectively.

5.2.5. Data Conversion and Analysis

MALDI data analysis was carried out using Analyst QS 1.1 and MATLAB. The data were converted from the AB Sciex .wiff proprietary file format to mzML using AB MS Data Converter (AB Sciex version 1.3) and then converted to imzML using imzMLConverter [164] and processed in MATLAB (version 7.8.0 (2009a), Math Works Inc, USA).

For all images displayed peak information is the summed ion intensity from within a 0.1 Dalton window centred on the peak of interest.

5.3. Results and Discussion

5.3.1. MALDI MSI using PNA – Utility under different Source Vacuum Conditions

The oMALDI 2 ion source on the QSTAR XL used for this work operates at ~1 Torr (≈ 1.3 mbar) pressure, but there is no in-source vacuum gauge. It was therefore necessary to empirically determine whether PNA could provide consistent high quality data over time periods long enough to be useful for effective MALDI-MS imaging. Fourteen tissue sections were successfully imaged with an acquisition time of approximately six hours (≈ 25 minutes per tissue section). A representative composite image of all fourteen tissue sections, displaying the intensity of the peak at *m/z* = 826.6, is shown in Figure 5.1.

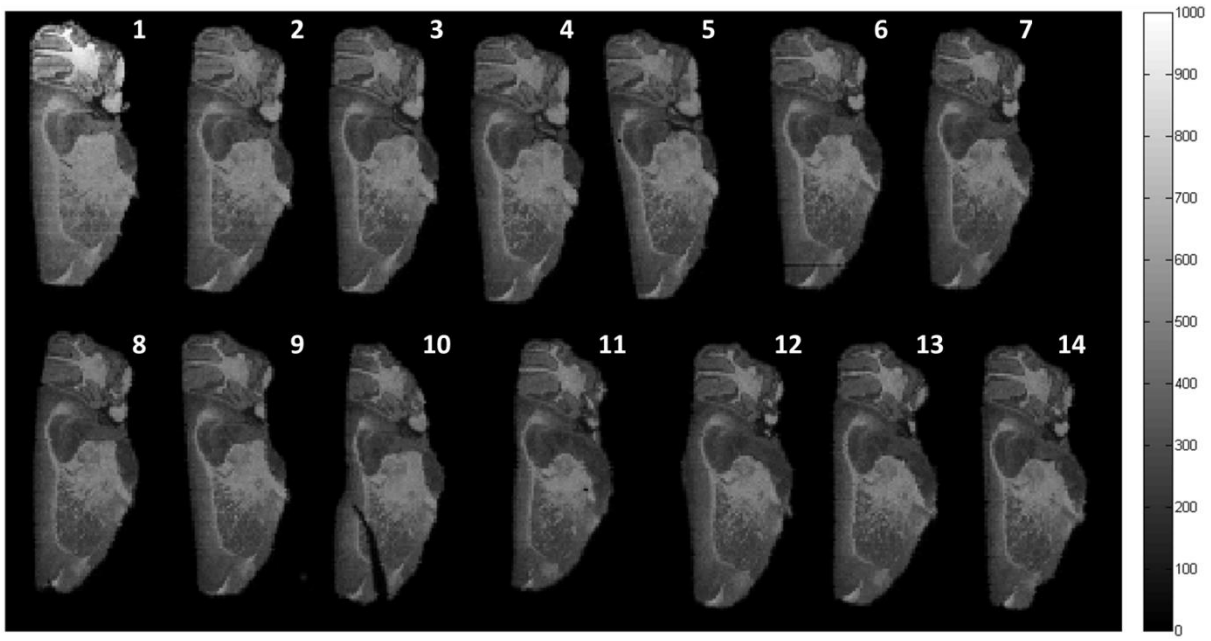

Figure 5.1. Images of *m/z* = 826.6 (PC 36:1 $[M+K]^+$) in mouse brain tissue sections using PNA. Data was acquired at a pixel size of 100 × 100 µm. Each section took 25 minutes to image resulting in a total imaging time of ~ 6 hours. Ion distributions are consistent over total time of data acquisition, demonstrating good analyte signal intensity throughout the acquisition.

The spatial distribution of *m/z* = 826.6 is consistent across all 14 images. Similar lipid ion peak intensities can be seen for all tissue sections with particular consistency seen from section 2 onwards. The reason for the slightly increased signal seen within the upper portion of section 1 (Figure 5.1) is not clear. It could have occurred for a number of reasons including: sublimation effects, inconstancies in tissue thickness or matrix coverage, differences in MALDI imaging plate contact with stage (e.g. bent at corner), fluctuation in laser energy delivered throughout the experiment. Whether any or all of these potential causes is truly responsible is not clear. What is clear is that the utility of PNA remains of a high quality throughout the image acquisition time. Representative single-pixel mass spectra from similar tissue regions of images 1, 5, 10 and 14 in Figure 5.1 are displayed in Figure 5.2.

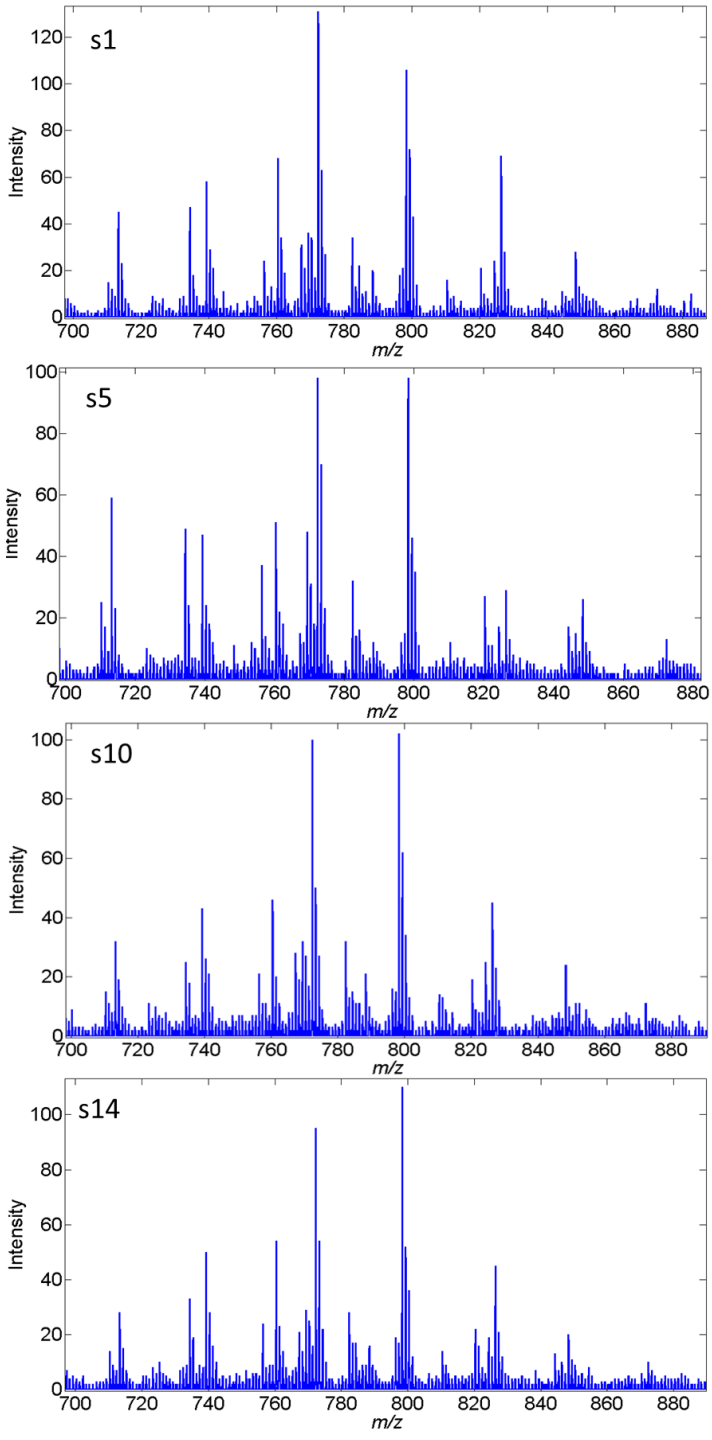

Figure 5.2. Representative single-pixel mass spectra from similar region of tissue sections 1, 5, 10 and 14 shown in Figure 5.1. Spectral data acquired are similar across the 6 hour time period in source. Similar high-quality spectra were obtained throughout the acquisition period.

The stability and utility of PNA as a matrix for MALDI-MSI in intermediate-source-pressure instrumentation is thereby confirmed. PNA can also be used in high vacuum instrumentation for *in-situ* work but the detected ion intensity will be affected by sublimation over relatively short time periods. In this study, PNA was also tested as a matrix for MALDI-MSI in a Bruker Daltonics UltrafleXtreme, with a source pressure of ~ 10^{-6} mbar, to provide comparison with the intermediate pressure data. Images and mass spectra from MALDI-MSI on-tissue in both positive and negative ion mode (200 x 200 µm pixel size; taking ≈50 minutes per image) are displayed in Figures 5.3, 5.4 and 5.5.

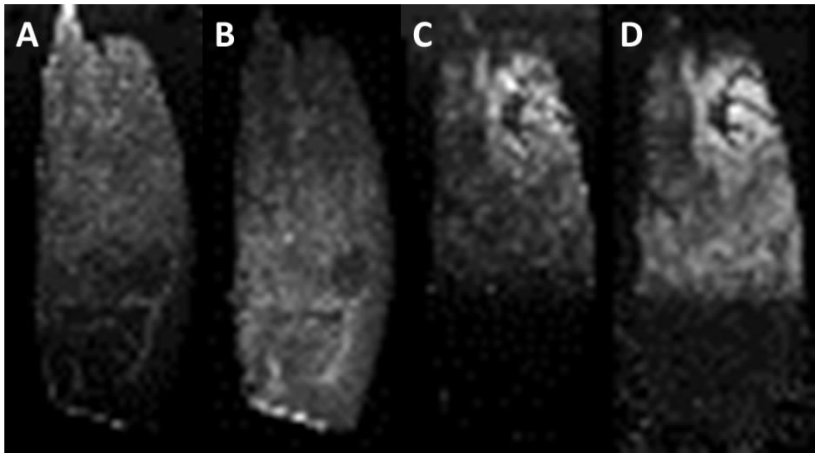

Figure 5.3. Images acquired from mouse brain tissue section using PNA as matrix. A high source vacuum Bruker ultrafleXtreme was used to acquire data. Images A and B are raw and TIC normalized intensity of ion at *m/z* = 826.5 in positive ion mode. Images C and D are raw and TIC normalized intensity of ion at *m/z* = 767.9 in negative ion mode.

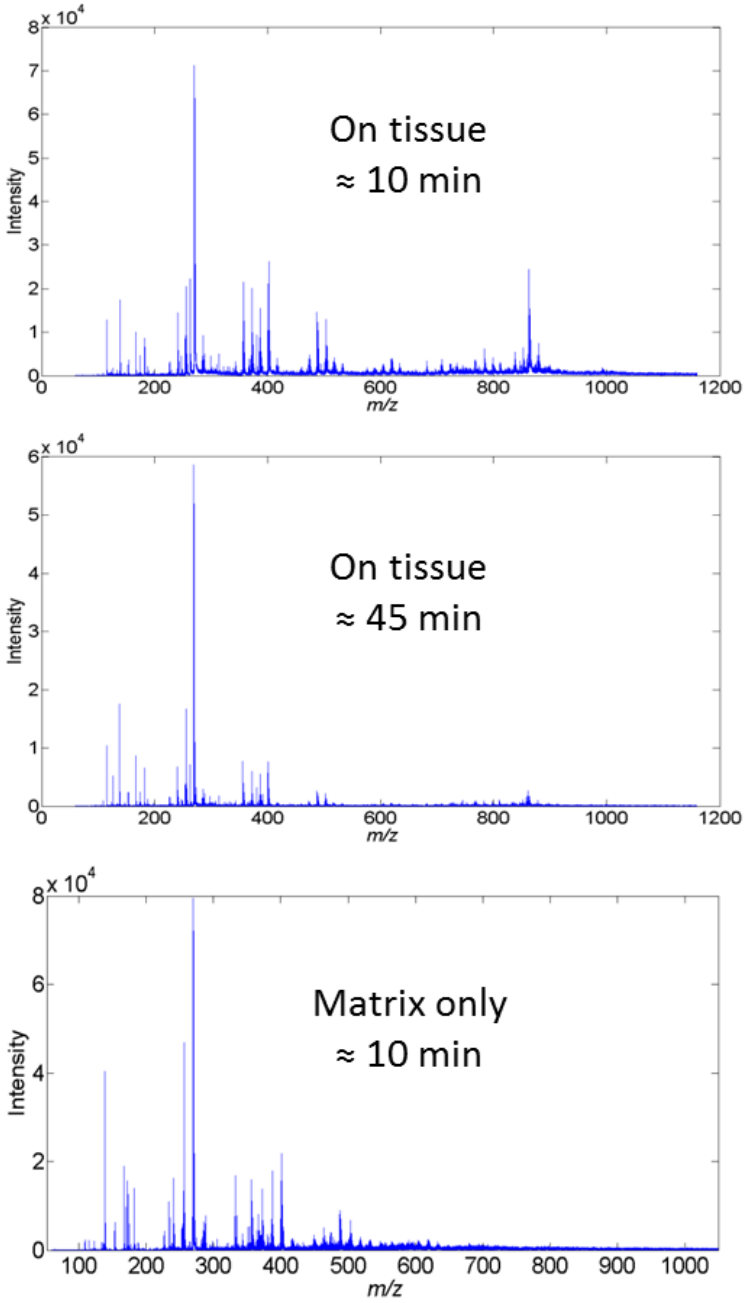

Figure 5.4. Negative ion mode on-tissue spectra from mouse brain tissue section image acquisition shown in Figure 5.3. PNA was used as the matrix. The top spectrum was acquired after approximately 10 minutes of the acquisition and the middle after approximately 45 minutes. The bottom spectrum is a matrix only, off tissue spectrum; provided for reference. A decrease in observed lipid signal is seen (*m/z* = 700-950 Da) over the time in the vacuum due to the sublimation of the matrix.

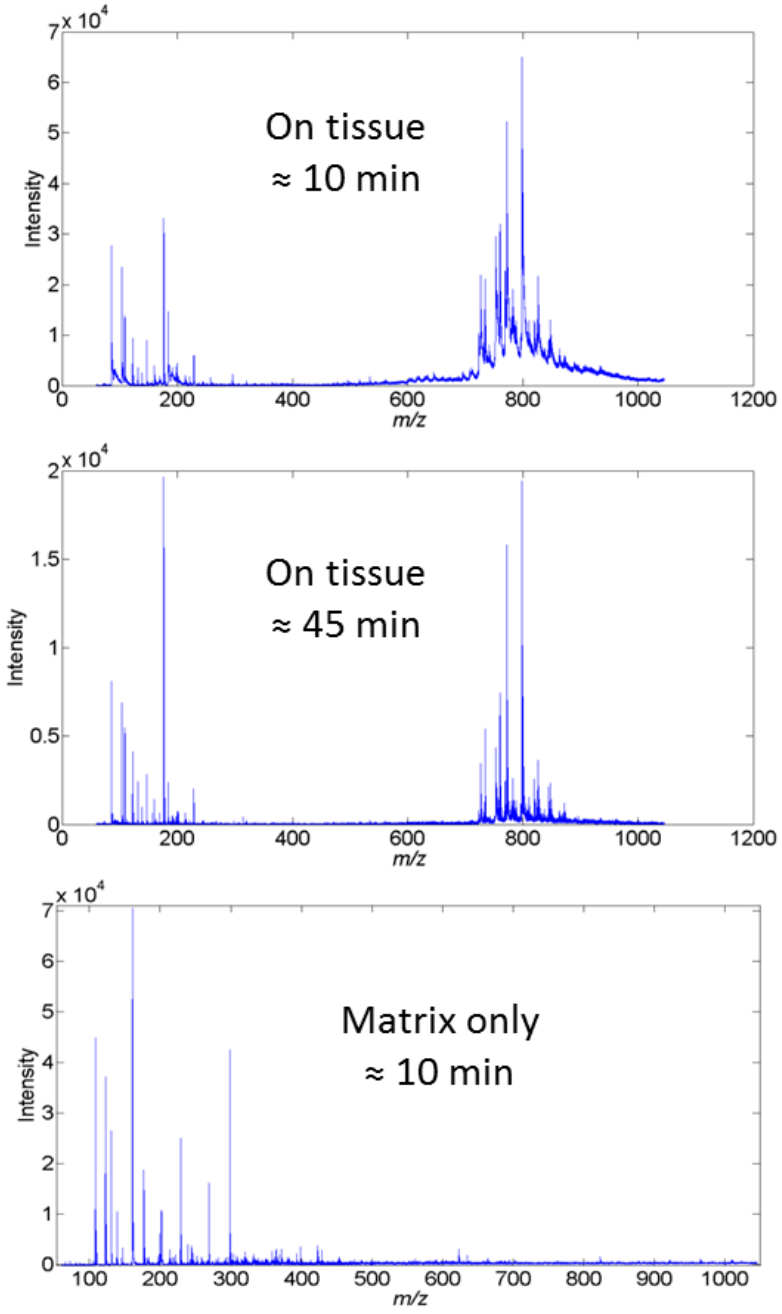

Figure 5.5. Positive ion mode on-tissue spectra from mouse brain tissue section image acquisition shown in Figure 5.3. PNA was used as the matrix. The top spectrum was acquired after approximately 10 minutes of the acquisition and the middle after approximately 45 minutes. The bottom spectrum is a matrix only, off tissue spectrum; provided for reference. A decrease in observed lipid signal (*m/z* = 700-900 Da) can be seen over the time in the vacuum due to the sublimation of the matrix.

Abundant lipid ion signals were obtained throughout the image acquisition but the sublimation of matrix throughout this time did introduce sublimation related peak intensity reduction artefacts into the image mass spectral data (Figures 5.4 and 5.5). Little matrix interference in the lipid *m/z* region is seen when comparing the off tissue spectra to those from on the tissue (Figure 5.5). Unlike the data from the QSTAR (Figures 5.1 and 5.2) where minimal sensitivity in negative ion mode prevented any meaningful data acquisition, negative ion mode images were acquired using the Bruker instrument, which, alongside the literature [201-203], demonstrate the additional utility of PNA.

5.3.2. MALDI MSI using PNA – Scope of Detected Species

Having shown the promise of PNA as a matrix for MALDI MSI in the intermediate pressure ion source of the QSTAR mass spectrometer, the nature of the lipid species detected must be considered. An image data set using PNA on a single mouse brain tissue section was acquired at a pixel size of 50 x 50 µm in positive ion mode (taking approximately 180 minutes). A mean on-tissue spectrum of the lipid rich *m/z* region is displayed in Figure 5.6. An image corresponding to the ion intensity of each peak marked with a star in Figure 5.6 is shown in Figure 5.7. Potential assignments from literature of all ions labelled and displayed in Figures 5.6 and 5.7 are shown in Table 5.1.

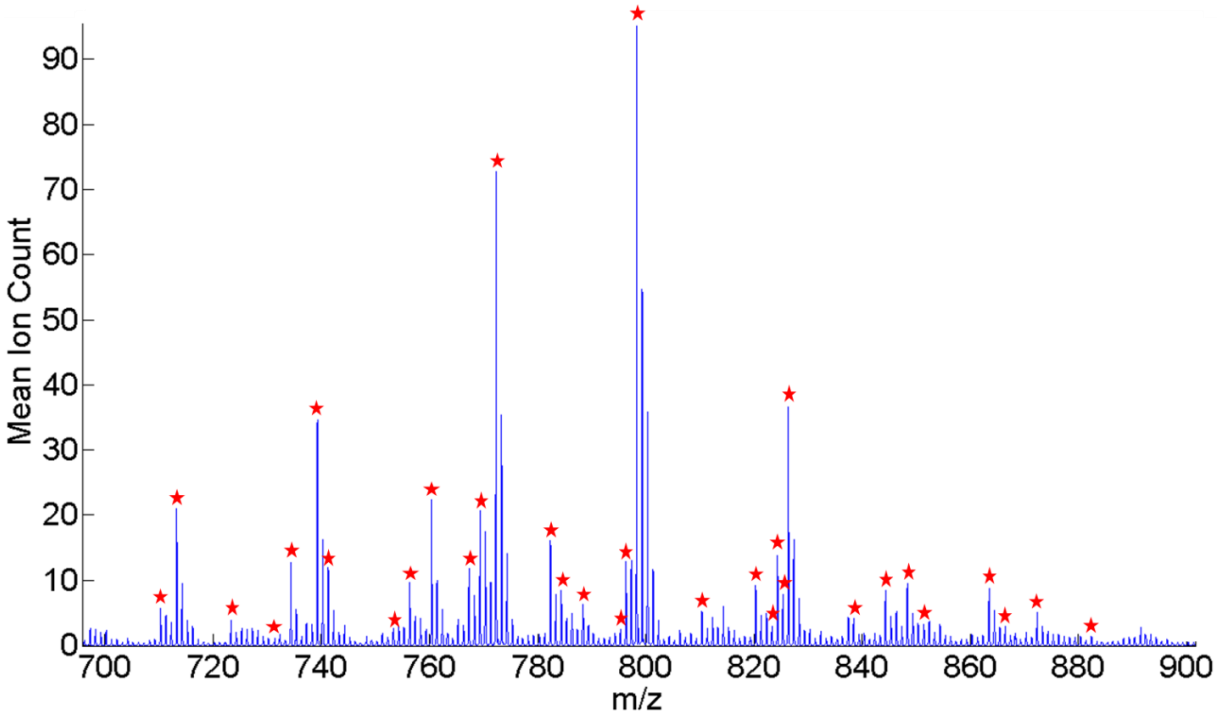

Figure 5.6. Mean spectrum from lipid rich *m/z* region taken from a murine tissue imaging data set where PNA was used as matrix. The data was acquired in ~ 90 minutes at a pixel size of 50 × 50 μm. Starred peaks are displayed as images in Figure 5.7 and potential assignments listed in Table 5.1.

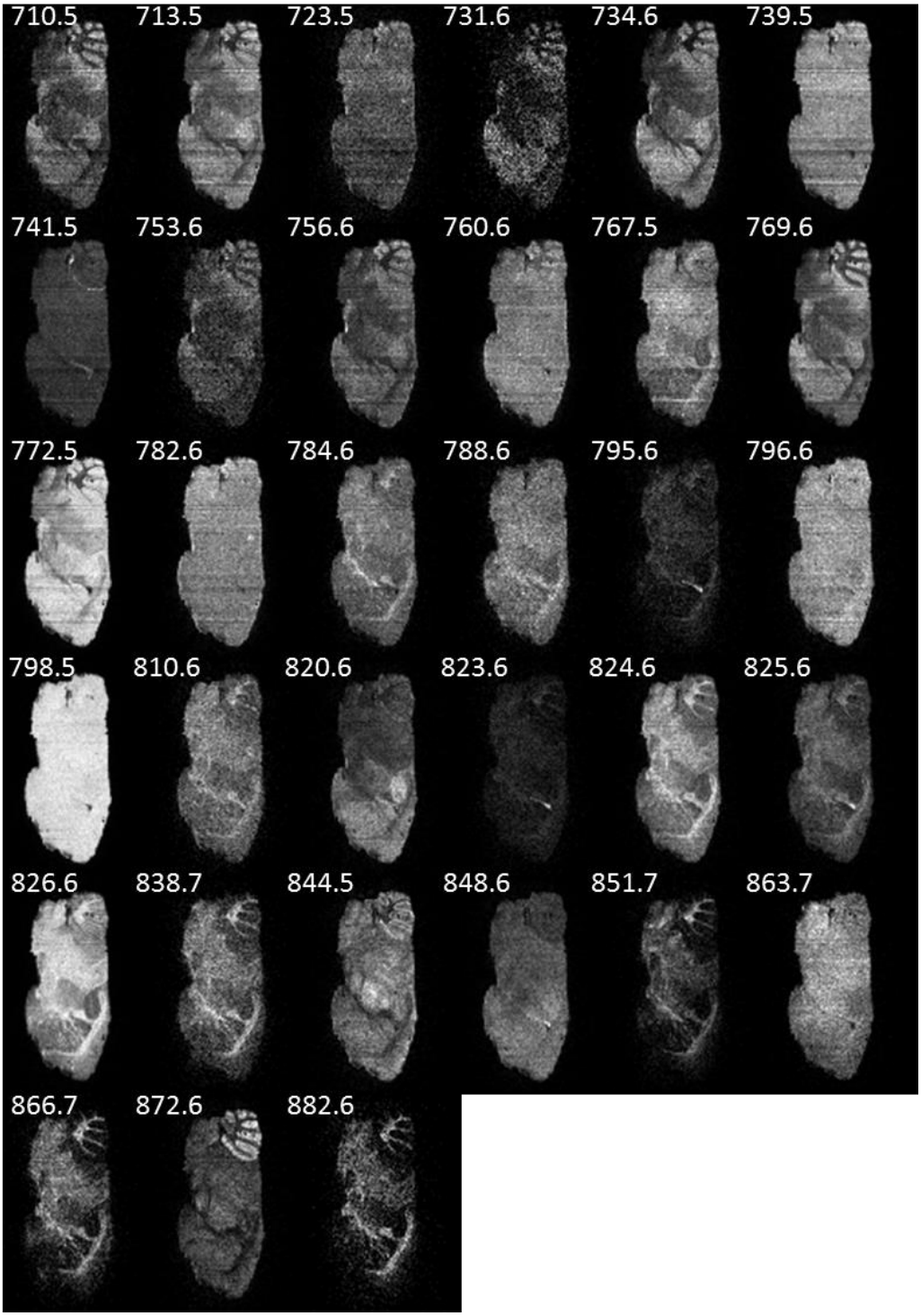

Figure 5.7. A selection of MALDI-MS images acquired from a single mouse brain tissue section in 25 minutes using PNA as the matrix. All are normalized to TIC. A large number of detected ions produce informative images.

Table 5.1. Table of potential assignments for peaks and images shown in Figures 5.6 and 5.7.

Experimental *m/z*	Potential Assignment
710.51	SM (18:0) $[M+K-N(CH_3)_3]^+$ [178]
713.48	PC (32:0) $[M+K-N(CH_3)_3]^+$ [178, 195]
723.51	PC (34:1) $[M+Na-N(CH_3)_3]^+$ [178]
731.62	SM (36:1) $[M+H]^+$ [178, 179, 195]
734.59	PC (16:0/16:0) $[M+H]^+$ [178, 179, 185]
739.49	PC (34:1) $[M+K-N(CH_3)_3]^+$ [178]
741.50	SM (d18:1/16:0) $[M+K]^+$ [195]
753.55	SM (36:1) $[M+Na]^+$ [178, 195]
756.57	PC (16:0/16:0) $[M+Na]^+$ [178, 179, 185]
760.58	PC (16:0/18:1) $[M+H]^+$ [178, 179, 185]
767.53	PC (36:1) $[M+K-N(CH_3)_3]$ [178]
769.58	SM (d18:1/18:0) $[M+K]^+$ [178, 179, 185]
772.53	PC (16:0/16:0) $[M+K]^+$ [178, 179, 185]
782.59	PC (16:0/18:1) $[M+Na]^+$ [178, 185] PC (36:4) $[M+H]^+$ [179]
784.58	PC (34:0) $[M+Na]^+$ [178]. PC (36:3) $[M+H]^+$ [179]
788.61	PC (18:0/18:1) $[M+H]^+$ [178, 179, 185]
795.53	No literature reference found.
796.55	PE (18:0/22:4) $[M+H]^+$ [208] PC (34:2) $[M+K]^+$ [209]
798.54	PC (16:0/18:1) $[M+K]^+$ [178, 179, 185]
810.61	PC (18:0/18:1) $[M+Na]^+$ [185] PC (38:4) $[M+H]^+$ [179]
820.55	PC(16:0/20:4) $[M+K]^+$ [179, 185]
823.56	SM (18:1/22:1) $[M+K]^+$ [195]

824.58	PC (18:0/18:2) $[M+K]^+$ [185]
825.57	SM (18:1/22:0) $[M+K]^+$ [195]
826.58	PC (18:0/18:1) $[M+K]^+$ [179, 185]
838.66	PC (38:1) $[M+Na]^+$ [116]
844.54	PC (16:0/22:6) $[M+K]^+$ [179, 185]
848.58	PC (18:0/20:4) $[M+K]^+$ [179, 185]
851.65	SM (18:1/24:1) $[M+K]^+$ [195]
863.71	No literature reference found.
866.68	No literature reference found.
872.57	PC (18:0/22:6) $[M+K]^+$ [185]
882.65	No literature reference found.

A large number of peaks within the lipid *m/z* region produce images of good quality (Figure 5.7). Most of the ions displayed have previously been assigned within the literature (as shown in Table 5.1) but very few of those assignments are accompanied by a full structural assignment from MS/MS spectra, and as those analyses were not performed within this study, a comparison cannot be made with certainty. Despite this, it seems likely that the use of PNA within MALDI MSI experiments enables ionization of very similar classes of lipid as those detected when using matrices such as CHCA and DHB, when operating in positive ion mode.

5.3.3 MALDI MSI using PNA – Comparison to CHCA

To further assess the performance of PNA as a useful matrix for rapid MALDI MS imaging, an experiment was conducted to compare it to the more common MSI matrix CHCA. Eight serial sections were mounted on a single imaging target: Four sections were coated with PNA, four with CHCA. The sections were analysed in a random order taking ≈ 25 minutes per section at a pixel size of 100 µm. Images taken from this analysis are shown in Figure 5.8 and mean spectra from regions shown in Figure 5.8 are displayed in Figures 5.9 and 5.10.

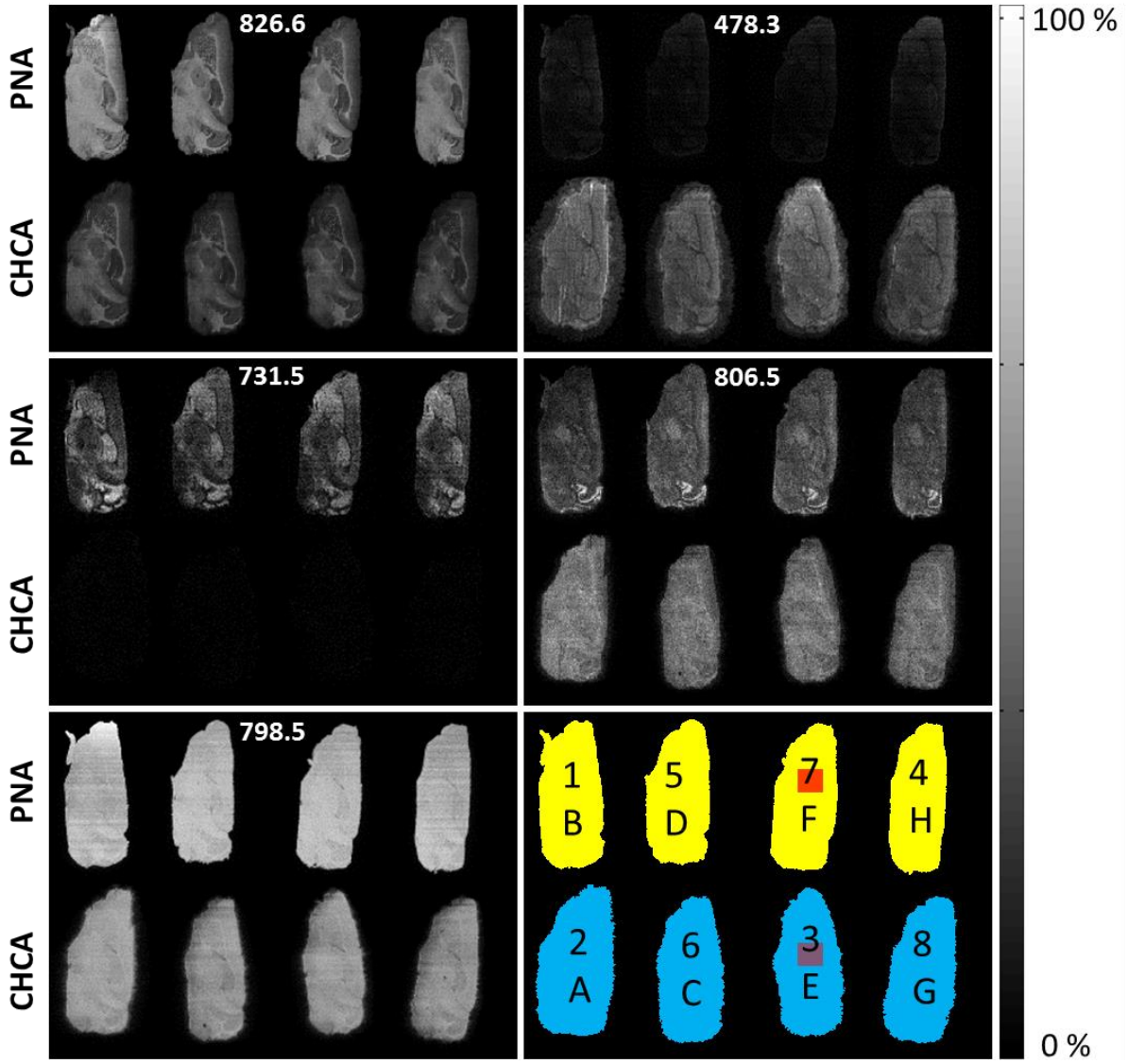

Figure 5.8. Ion images (*m/z* = 826.6 PC 36:1 $[M+K]^+$, *m/z* = 478.3 PC 34:1 $[M+H-C_{18}H_{34}O_2]^+$, 731.5 SM 18:0 $[M+H]^+$, 806.5 PC 36:3 $[M+Na]^+$ or PC 38:6 $[M+H]^+$ and 798.5 PC 34:1 $[M+K]^+$) from the analysis of eight serial sections. Pixel size is 100 x 100 µm. The centre right panel shows: the sectioning order from A–H; the image acquisition order 1–8; the matrix used, yellow (top four sections) represents PNA and blue (bottom four sections) CHCA; the red regions indicate the areas from which the mean spectra (Figures 5.9 and 5.10) were calculated.

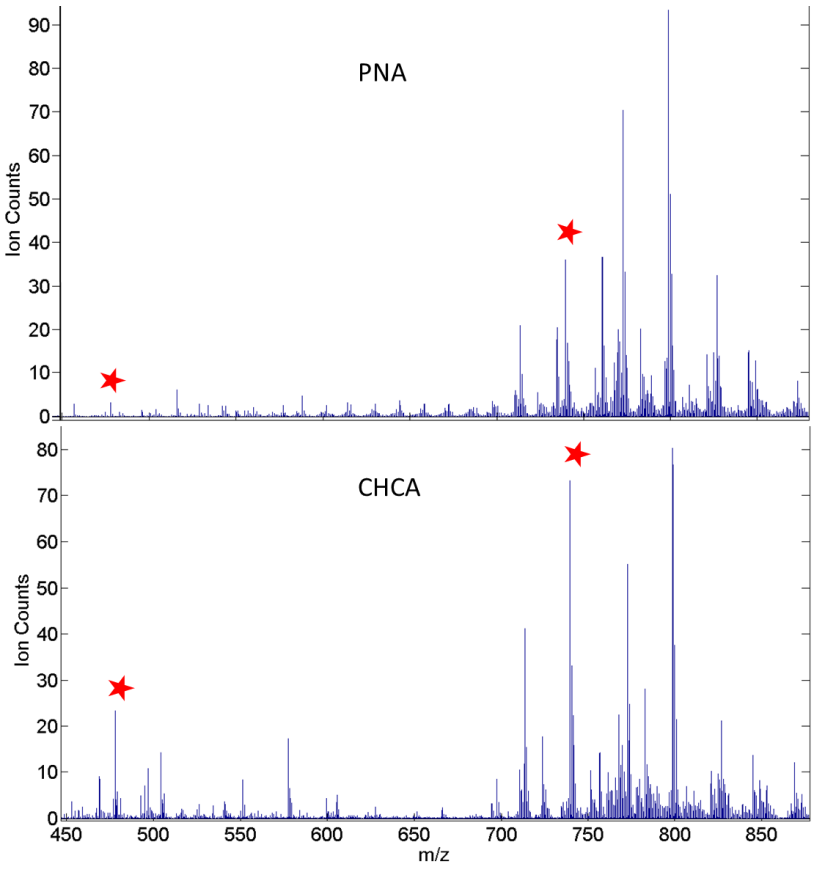

Figure 5.9. Mean on-tissue spectra taken from pixels indicated within Figure 5.8 (red highlighted regions within bottom right panel) from PNA and CHCA coated mouse brain tissue sections. Starred peaks correspond to the lipid fragment peaks *m/z* = 478.3 (PC 34:1 $[M+H-C_{18}H_{34}O_2]^+$) and *m/z* = 739.5 (PC 34:1 $[M+K-N(CH_3)_3]^+$). A reduction in observed fragmentation is evident when using PNA as compared to CHCA.

Examination of the data acquired using both PNA and CHCA revealed similar spatial distributions of the majority of the most abundant ions within the lipid rich *m/z* region (700-870 Da). In addition to this, the intensity of detected ions within this *m/z* region are approximately similar and both matrices appear to predominately facilitate the ionization of the same commonly detected phospholipids (see Figures 5.8, 5.9 and 5.10). The ions at *m/z* = 826.6 and 798.5 are displayed to as examples of these similarities (Figure 5.8). These ions

were assigned, based on the literature (Table 5.1), as phosphotidylcholine (PC) 36:1 $[M+K]^+$ and PC 34:1 $[M+K]^+$ respectively.

With PNA, the abundance of sodium and potassium adducts is approximately similar to that seen with CHCA but the protonated adducts appear to be more intense with PNA. Therefore, lower abundance protonated species are detected when using PNA and are not detected when using CHCA. This is illustrated by the image of the less spectrally abundant lipid at *m/z* = 731.6 (tentatively assigned as SM 36:1 $[M+H]^+$ - see Table 5.1 and Figure 5.11) in Figure 5.8. Whilst formation / detection of multiple adducts of the same lipid molecule are not necessarily a problem for many applications, it is not a desirable situation for most analytical scenarios as the spectra will be more complex and peaks from different species are more likely to overlap. This issue can be overcome to varying extents by using additives to drive the detected species toward a single desired adduct [176]. Whilst this method for reducing spectral complexity has been shown to work well for CHCA the extent to which PNA performs with salt additives for the reduction of spectral complexity in MALDI MS of lipids has not been studied.

Interestingly, not all ion images show the same distribution with both matrices, as can be seen in the images for *m/z* = 806.5 (tentatively assigned as PC 36:3 $[M+Na]^+$ and / or PC 38:6 $[M+H]^+$ [179]). The phenomenon of differing detected ion distributions arising from the use of different matrices has not been studied in depth. An example can be found in the graphical abstract of work by Shanta *et al.* [184] but is not commented upon within the main body of the article. In the case presented here, as well as the work by Shanta *et al.*, the mass resolving power of the MS instrumentation used is not sufficient to resolve many lipid ions detected in tissue due to their minimal *m/z* difference [210]. The two lipids potentially assigned as the ion at *m/z* = 806.5 within this work are a case in point. Therefore, it may well

be that more than one ion is contributing to a given peak within these data and these two ions may then contribute to the peak area to different extents, depending upon the matrix used (as mentioned above with regard to the ion at 731.6 Da). If these two ions also have different endogenous spatial distributions, different apparent spatial distributions within the MALDI images for this peak and any others like it could therefore be obtained, when different matrices are used for each MALDI MSI analysis.

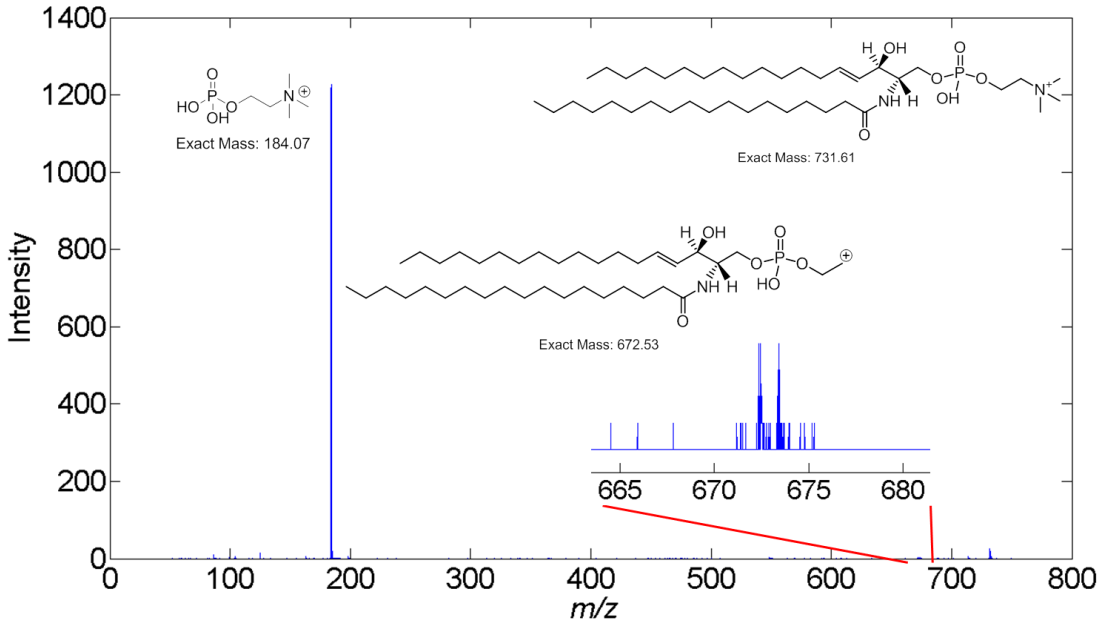

Figure 5.10. Product ion spectrum acquired by collision induced dissociation of parent molecule at *m/z* = 731.6 tentatively assigned as SM 36:1 $[M+H]^+$ [178, 179, 195]. The proposed structure of the parent and fragment molecule are shown. Double bond position is unknown and shown here only as an example. Neutral loss of amine head-group fragment and PC head-group fragment are observed, supporting this assignment.

The ion at *m/z* = 478.3 (marked with an asterisk in Figures 5.9 and 5.10) is tentatively assigned as the PC fragment resulting from the loss of oleic acid from PC 34:1 (16:0/18:1) and PC 32:0 (16:0/16:0) [176, 181, 211]. The assignment as a loss from PC 34:1 (16:0/18:1) is also supported by the presence of the presence of a peak at 478.3 Da within the ToF and MS/MS CID mass spectrum of lipid standard PC 16:0/18:1 $[M+Na]^+$ (Figures 5.12 and 5.13) and by the relevant literature [146, 176, 181, 212]. Additionally, it is a potential fragment of any PC lipid with alkyl group 16:0 (palmitic acid side chain).

The amount of fragmentation may give an indication of the relative "heat" [188] of a matrix i.e. the amount of internal energy transferred from the matrix to a particular analyte ion during the ablation / ionisation process of MALDI MS. Therefore, the difference in fragmentation behaviour seen between the two matrices used here suggests, in this instance, that CHCA is the "hotter" of the two at the laser energy used. The differing levels of fragmentation are further highlighted by the two mean spectra displayed in Figures 5.9 and 5.10, where an increased intensity can be seen for a number of peaks in the *m/z* region below 650, a region commonly associated with the fragments of lipid ions. Additionally the peak at *m/z* = 739.5 is seen to be significantly more abundant in the CHCA mean spectra (marked with a star in Figures 5.9 and 5.10). This peak is assigned in the literature as PC 34:1 $[M+K-N(CH_3)_3]^+$ (Table 5.1), which further supports the finding of increased PC lipid fragmentation with CHCA. Other PC fragment ions demonstrating this relationship are shown in as images in Figure 5.12 and as labeled peaks within Figures 5.13 and 5.14.

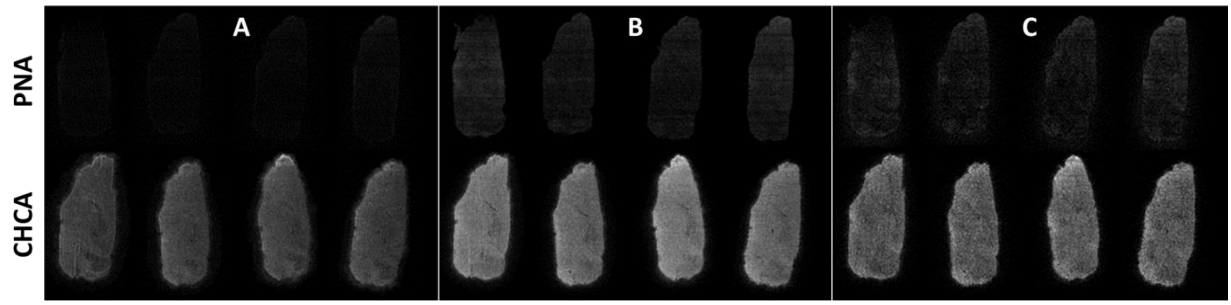

Figure 5.11. Images from dataset shown in Figure 5.8 of ion at *m/z* = 504.3 (A), 577.5 (B) and 599.5 (C) which correspond to known fragments of PC 34:1, shown in Figure 5.14. This further supports the hypothesis of increased lipid fragmentation when using CHCA as oppose to PNA.

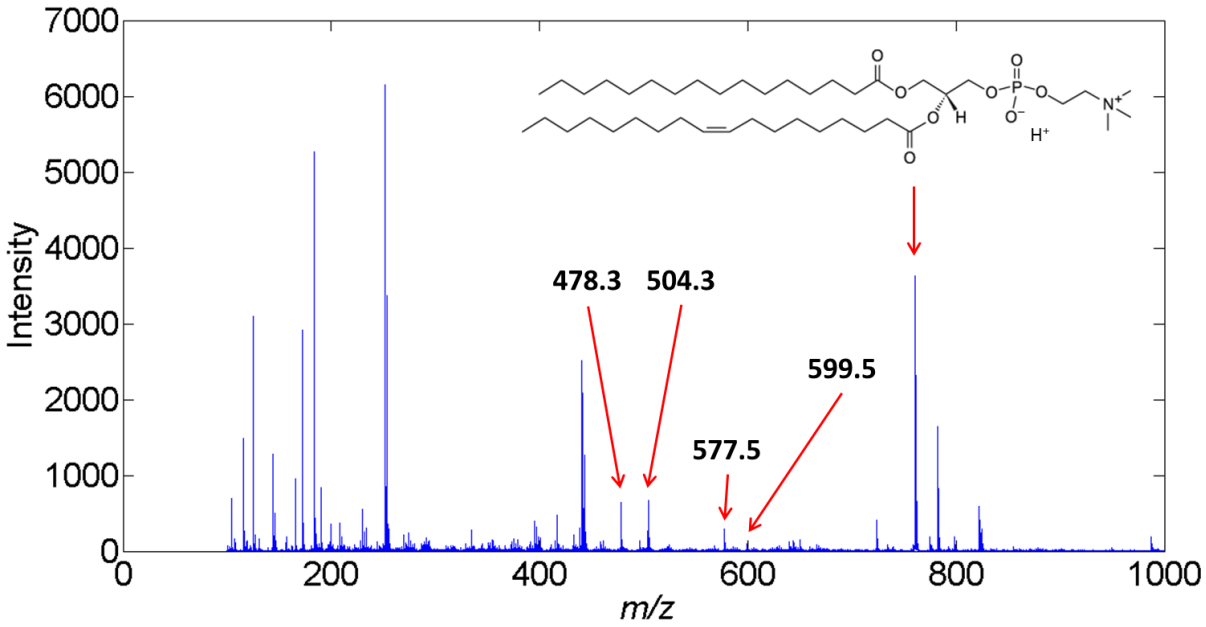

Figure 5.12. MALDI-ToF-MS spectrum of lipid standard PC 34:1 (16:0/18:1) with CHCA as matrix. Lipid fragment peaks at *m/z* = 478.3 $[M+H-C_{18}H_{34}O_2]^+$, *m/z* = 504.3 $[M+H-C_{16}H_{32}O_2]^+$ and *m/z* = 577.5 $[M+H-C_5H_{15}O_4PN]$, as well as the intact protonated ion, are labeled.

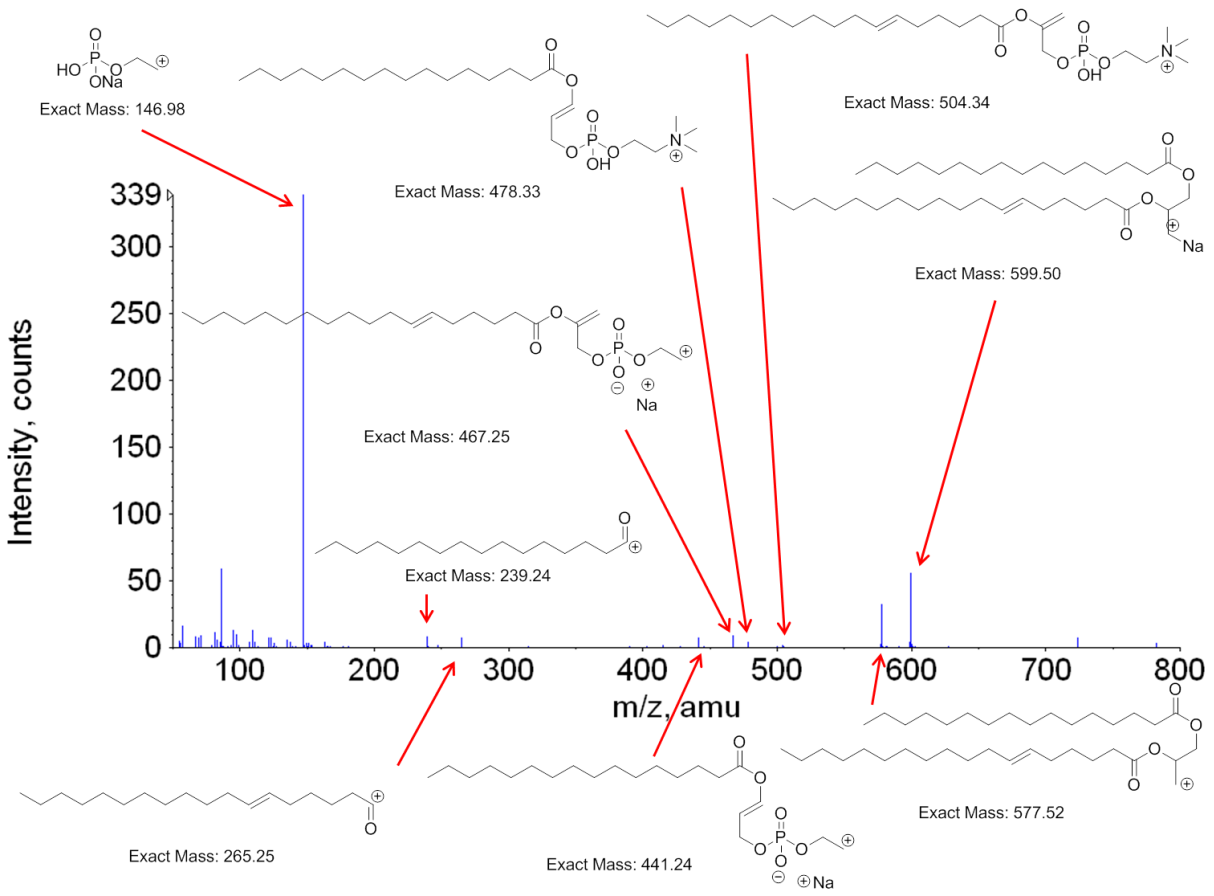

Figure 5.13. MS/MS spectrum of lipid standard PC 34:1 (16:0/18:1) $[M+Na]^+$ and possible structural assignments. Double bond locations are representative only as exact locations cannot be determined within analyses of this type. Fragment at *m/z* = 478.3 is seen in CID MS/MS studies of PC 34:1 and so may also contribute to the peak at 478.3 in tissue MALDI ToF-MS spectra.

The images of *m/z* = 478.3 intensity (Figure 5.8) also appears to show a halo around the edge of the tissue for the CHCA coated sections. In this study, the use of CHCA was found to result in higher levels of analyte migration during matrix application as compared to the use of PNA, indicating a potential advantage of PNA over CHCA for *in-situ* tissue analysis. The problem of analyte migration in MALDI MSI can be an issue for some matrix

application methods including the air-spray method used in this study. This phenomenon is potentially due to over-wetting of the sample during matrix application. It is interesting to note that tissue features are still observed in the ion images despite this.

Plotting the ion count along a single line of pixels from an on-tissue to an off-tissue region can give a measure of the sharpness of the tissue edge and by extension the presence of any analyte migration (see Figure 5.15). PNA shows a sharp drop for both *m/z* = 734.5 (PC 32:0 $[M+H]^+$) and 772.5 (PC 32:0 $[M+K]^+$) (both assigned tentatively from literature [179]) reaching approximately 0 after three or four pixels. Conversely those same two ions in the CHCA data set have significant ion counts up to 12 pixels outside the tissue region. Each pixel in this dataset corresponds to 100 μm so the difference seen is significant. This phenomenon is not necessarily always present when using these two matrices with air-spray deposition but it is worth noting due to the frequency with which it is seen to occur. PNA appears to demonstrate a greater resilience to the effects of over-wetting in airspray matrix deposition.

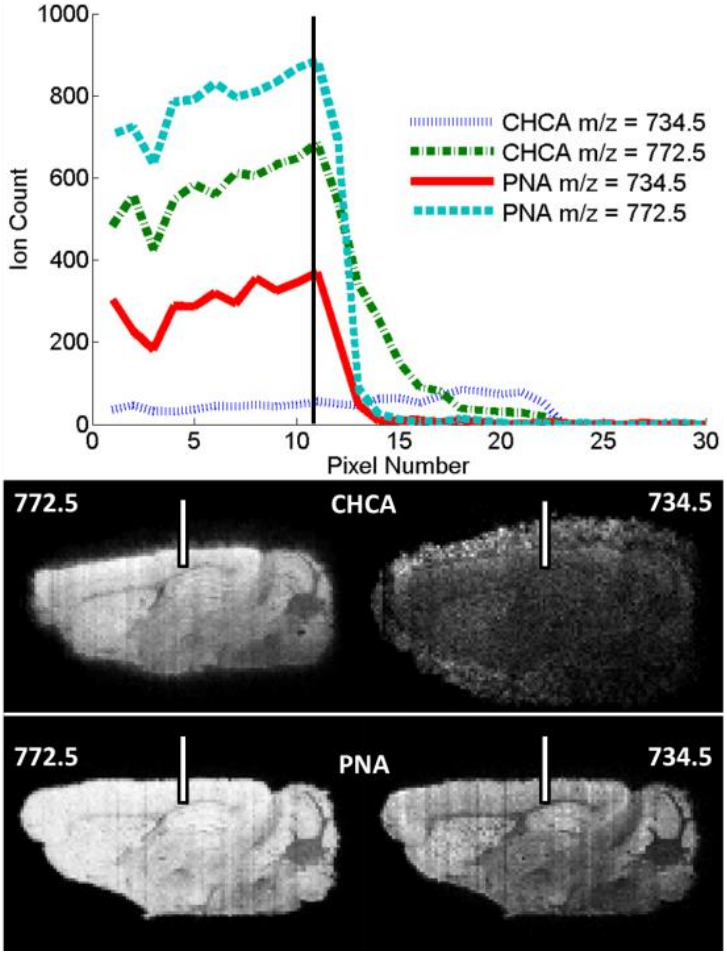

Figure 5.14. Investigation of analyte migration from tissue edge when using PNA and CHCA for *m/z* = 772.5 (PC 34:0+K) and *m/z* = 734.5 (PC 34:0+H) [179]. The white bar in the tissue images show the pixel region used to produce the graph. The graph shows the ion count for a line of pixels off and on tissue for two serial sections sprayed with CHCA and PNA. The location of the tissue edge is marked on the graph by the black vertical line. It is seen that the tissue edge is less well defined for the CHCA images.

5.4. Conclusion

PNA is shown to be useful for the acquisition of high-quality, high-throughput MALDI-MS imaging data in an intermediate pressure ion source using a high repetition-rate

Nd:YVO_4 laser. The use of a high repetition-rate laser is an important issue as the lower energy per pulse delivered by lasers, like that used within this study, may prohibit the use of matrices which exhibit higher ion detection threshold energy requirements. The number of molecules tentatively assigned is also reasonable, though, as is common in positive ion-mode MALDI MS, the vast majority of those detected lipids ions are positively charged amine group containing phosphatidylcholines molecules. Little breadth is seen in the variety of species detected / assigned. However, the utility of PNA in negative ion mode makes it potentially a very interesting candidate for further MSI studies as this would likely broaden the scope of species detected and further demonstrate its benifit compared to CHCA.

The comparison of PNA to CHCA within this work demonstrates that different results may be obtained depending upon which matrix is used, for a given analysis. Without a ground truth to compare the results of a MALDI MSI experiment to, it is reasonable to treat these different results as illuminating different angles of the same unknown ground truth. With this in mind, increasing the number of available matrices which work effectively at lower energy-per-pulse for MALDI MS and MSI experiments is a positive step. The more angles one can view a problem from, the more informative the overall picture obtained is likely to be.

Chapter 6

Repeat MALDI MS Imaging of a Single Tissue Section using Multiple Matrices and Tissue Washes

6.1. Introduction

Researchers are constantly pursuing improvements in the information obtained from tissue in MALDI MSI. Routes toward improving the information obtained from tissue include: increasing the signal-to-noise ratio of peaks of interest; increasing the ion yield; improving the number of informative MS/MS peaks; reducing the level of unwanted fragmentation; increasing the variety of molecular species detected. These improvements usually involve altering the instrumentation, instrumental setup, matrix and solvent system used.

The pursuit of new and improved matrix molecules has been a consistent feature in MALDI MS and many candidates have been tested and recommended for MSI applications; the work within Chapter 4 of this document being an example of this. The choice of matrix will directly affect a number of factors including the ion yield / sensitivity [13], the diversity of molecular species detected [184], the amount of analyte fragmentation seen [188] and the polarity of ions which can be created and detected [213]. Despite advances in this area, the

pursuit of new and improved matrices has limitations. It seems distinctly unlikely that one matrix will ever perform optimally under all variable combinations. The matrix, therefore, is likely to remain a restriction to the way in which any given sample can be analysed i.e. the analyte classes most easily detected or the polarity the instrument is used in. This makes the analysis of serial sections necessary if multiple matrices are required to survey all species of interest.

There have been a number of examples regarding the use of multiple mass spectrometry analyses carried out on serial tissue sections including: the combination of SIMS and MALDI MSI for the analysis of elemental, lipid, peptide and proteins in musculoskeletal tissue [214]; the combination of laser ablation inductively coupled plasma mass spectrometry (LA ICP MS) and MALDI ion mobility MS imaging for the analysis of elements and lipids [215]. Whilst the use of serial sections can provide information that allows direct comparison of other altered variables, the data obtained is typically from tissue regions ~ 5 - 10 µm apart.

One little explored method which may allow increased information to be obtained without having to use serial tissue sections is the repeated analysis of a single tissue section. In 2007, Garrett *et al.* performed repeat analysis on a single rat brain tissue section [206]. They found much of the matrix still present on a tissue section after MALDI MSI. This enabled multiple MSI and MS/MS analyses of a rat brain tissue sections to be carried out, though the concept and data were only briefly discussed. More recently, repeat analysis using desorption electrospray ionization (DESI) and then MALDI was developed by Eberlin *et al.* (2011) to perform MSI analyses in both the lipid and protein *m/z* regions on the same tissue section [216]. First DESI MSI was used to analyse the lipid content of a mouse brain tissue section then MALDI MSI was used for analysis of the protein content of that same tissue section. These types of repeat analysis methodologies may allow the analysis of single tissue

sections where the choice of matrix and instrumentation of the first analysis will not preclude the use of other matrices, methodologies and instruments from also being used to analyse that same tissue section. Further to the identification of PNA as a useful matrix within MALDI MSI in Chapter 5, particularly for high throughput and lower energy analyses, the use of PNA and comparison to CHCA as a matrix for repeat analysis of single tissue sections can further extent the utility of these matrices for the acquisition of improved information within MALDI MSI.

6.2. Experimental Methods

6.2.1. Materials

Methanol, ethanol, acetonitrile and isopropanol (HPLC grade) were purchased from Fisher Scientific (Leicestershire, UK). The water used was purified by an ELGA Option 3 system (Marlow, UK). Trifluoroacetic acid (TFA) and MALDI matrices α-cyano-4-hydroxycinnamic acid (CHCA), sinapinic acid (SA) and *para*–nitroaniline (PNA) were purchased from Sigma Aldrich (Dorset, UK). Formal saline 10 % v/v (equivalent to 4 % formaldehyde) with 0.9 % w/v sodium chloride was purchased from Adams Healthcare (Leeds, UK).

6.2.2. Tissue Fixation

A whole mouse brain was fixed in a 10 mL volume of 10 % formal saline for 36 hours prior to sectioning.

6.2.3. Tissue Sectioning and Preparation

Mice were sacrificed humanly in accordance with the Home Office Animals (Scientific Procedures) Act 1986 [163]. Mouse brains were flash frozen in liquid nitrogen immediately after excision (fresh frozen) then fixed prior to refreezing for sectioning. Tissue sections (12 μm) were collected and thaw mounted onto an AB Sciex MALDI imaging plate (or ITO coated glass slide for Bruker UltrafleXtreme analysis). Sectioning was performed on a Leica CM 1850 Cryostat (Milton Keynes, UK). 15 mL CHCA, PNA (20 mg mL^{-1} in 85 % CH_3OH, 0.1 % TFA) or SA (20 mg mL^{-1} in 50 % Acetonitrile, 0.1 % TFA) was applied to the imaging plate using an artist airbrush purchased from Draper Air Tools Airbrush Kit (Hampshire, UK) propelled by dry N_2. The airbrush nozzle was held approximately 20 cm from the plate. Three consecutive spray passes were followed by fifteen seconds drying time. This process was repeated four times then the plate was rotated on the clamp stand by ninety degrees. This sequence was repeated until all matrix solution was used.

For the peptide and protein tissue analysis using the Bruker ultrafleXtreme the tissue was washed twice in isopropanol (70 % then 95% for 30 seconds per solution) as per the protocol by Seeley et al. [141] and then coated in SA as per the above protocol.

6.2.4. Mass Spectrometry

MALDI MSI data were acquired with a QSTAR XL QqToF instrument with an oMALDI 2 ion source using Analyst QS 1.1 with oMALDI server 5.1 (AB Sciex). An Nd:YVO_4 (Elforlight: SPOT-10-100-355) diode pumped solid state (DPSS) laser with λ = 355 nm, < 50kHz repetition rate and < 1.5 ns pulse length was used in this study. The Nd:YVO_4 laser was triggered by a Thurlby Thandar Instruments (Huntingdon, Cambridgeshire) TGP110

10 MHz Pulse Generator at 5 kHz for all experiments shown resulting in between ~500 laser pulses per pixel. The laser was coupled to the MALDI source via a 100 μm core diameter fibre optic patchcord (Edmund Optics, NA = 0.22). Matrix was applied to tissue section prior to each analysis. Images in Figures 6.1-6.3 were acquired at 50 × 50 μm and Figure 6.6 at 60 × 60 μm pixel size using a raster speed of 0.5 mm s^{-1} taking ~80 minutes per image. The same sample analysis region coordinates were used for each repeat analysis experiment on the same single tissue section. The tissue wash used (after analysis number 4 Figures 6.5 and 6.6) was composed of 50 % ethanol. 1 mL was pipetted over the tissue section, the MALDI plate was held at an angle to allow the wash to run off. To optimize the ethanol:water ratio within this wash four serial mouse brain tissue sections were mounted onto the same MALDI MSI plate, one in each corner, and coated with CHCA as per the above protocol. Washes of 25, 50, 75 and 100 % ethanol were pipetted over each section. Care was taken to pipette each wash over only one of the sections; the plate was held at the appropriate angle to allow each wash to run over its correct section and off the plate into different beakers. This runoff was then analysed by MALDI MS.

Further repeat MALDI MSI analysis mass spectrometric data was acquired with an UltrafleXtreme ToF/ToF mass spectrometer (Bruker Daltonics) employing a smartbeam-II Nd:YAG (355 nm) laser operated at 1 kHz. The first analysis was performed in reflectron ToF mode with an *m/z* range of 60-1200, a pixel size of 100 μm and laser energy of 50 % (absolute energy unknown). The second analysis was performed in linear ToF mode with an *m/z* range of 1480-20000, a pixel size of 200 μm and laser energy of 80 % (absolute energy unknown). For both analyses the laser power percentage was optimized to give the best signal-to-noise ratio from a separate identically prepared serial tissue section. 500 laser pulses were summed per pixel mass spectrum.

6.2.5. Data Analysis

MALDI data analysis for the QSTAR XL data was carried out using Analyst QS 1.1 and MATLAB (version 7.8.0 (2009a), Math Works Inc., USA). The data were converted from proprietary file format to mzML using AB MS Data Converter (AB Sciex version 1.3) and then converted to imzML using imzMLConverter [164] and processed in MATLAB. Image alignment for the display of summed images was performed with the aid of Image J (FIJI). UltrafleXtreme data visualization was carried out in FlexImaging v2.1 (Bruker Daltonics).

6.3. Results and Discussion

6.3.1. Investigation into repeat MALDI MSI of a single tissue section

Repeat MALDI MSI of a single tissue section has the potential to provide increased molecular information about said tissue section. Initial experiments investigated this *via* analysis of two fresh frozen mouse brain tissue sections coated with matrix and analysed by MALDI MSI in oversampling continuous raster mode [131, 133]. The use of oversampling [133] in continuous raster mode on the QSTAR XL instrument, in conjunction with the high repetition rates (5 kHz in this study) of the Nd:YVO_4 laser [165], allows the possibility of the ablation and visible removal of virtually all matrix within the imaged region (Figure 6.1 and Figure 6.4 sub-image 1 for MALDI MSI data and example photo showing removal of matrix after initial imaging experiment). This occurs due to the overlapping of laser pulses on the sample as it is moved continuously under the laser meaning all areas of the sample receive a considerable number of laser pulses (~ 500 per pixel per experiment).

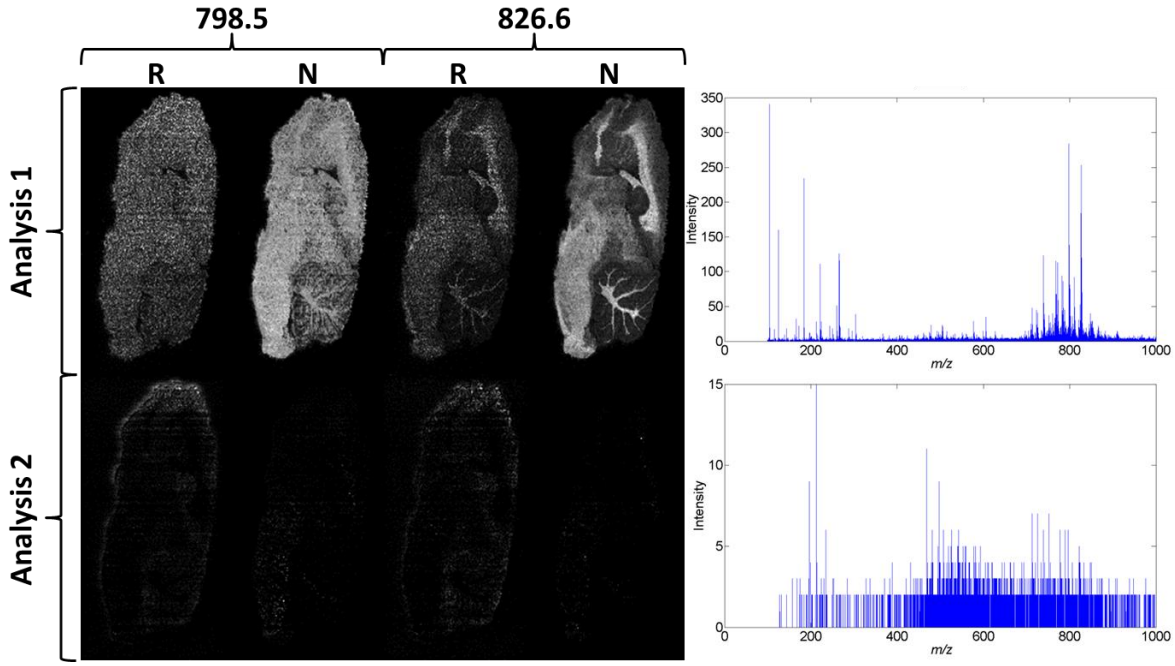

Figure 6.1. Repeat analysis of a single tissue section without matrix application prior to second analysis. CHCA was used as the matrix in this experiment. Representative spectra from the first and second analyses are displayed: top right and bottom right respectively. Images of lipid ions at *m/z* = 798.5 and 826.6 are displayed in bot their raw (R) and normalized to total ion count (N) form.

As a consequence of this the same tissue section can be re-coated in matrix material and re-analysed after each analysis, without having to wash away the previous matrix layer. This process was carried out using CHCA on one tissue section and PNA [175] on another (see Figure 6.2), taking 80 minutes per image for a 50 × 50 μm pixel size.

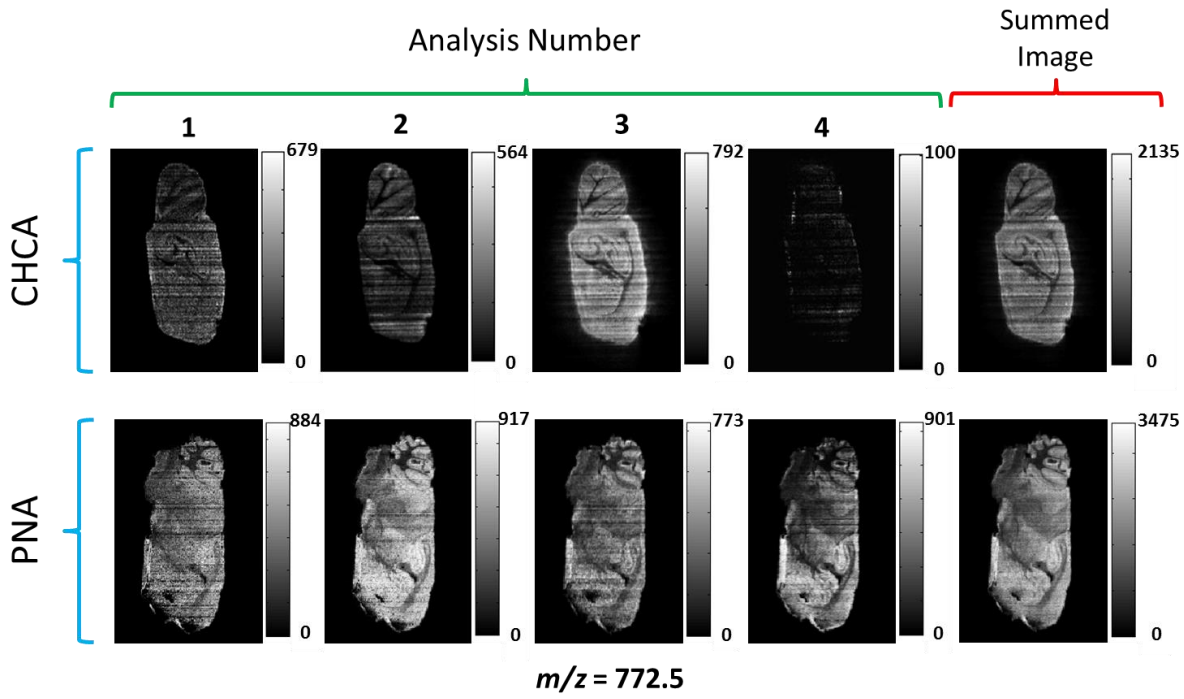

Figure 6.2. Images of *m/z* = 772.5 acquired by repeat MALDI MSI analysis of single tissue sections from fresh frozen mouse brain. PNA and CHCA were used on two different tissue sections; matrix was re-applied prior to each image acquisition. The summed image of each dataset is shown on the right hand side. Intensity scale bars show peak area ±0.1 Daltons around the peak centroid. Images have 50 × 50 µm pixel size. Images demonstrate that repeat analysis can be performed multiple times on the same tissue section with PNA performing better than CHCA.

The distribution of detected lipids (e.g. *m/z* = 772.5, tentatively assigned from literature as PC (16:0/16:0) $[M+K]^+$ [178]) appears to be the same for each of the first three images in the CHCA data and for all four analyses using PNA (Figure 6.2). Further to this the peak ion intensity in each of the four images acquired using PNA are similar. The methodology of repeat MALDI MSI analysis used in this study is therefore shown to be

consistent in ion yield and spatial distribution for at least four analyses using PNA as matrix. The horizontal line artefacts are believed to be due to slight inconstancies in the stepping motors in combination with the raster line to raster line oversampling resulting in variations in the total ion count per pixel along certain raster lines. As this issue directly affects the total ion count, normalizing the data to the total ion count (TIC) can largely remove these artefacts, an example of this is shown in Figure 6.3.

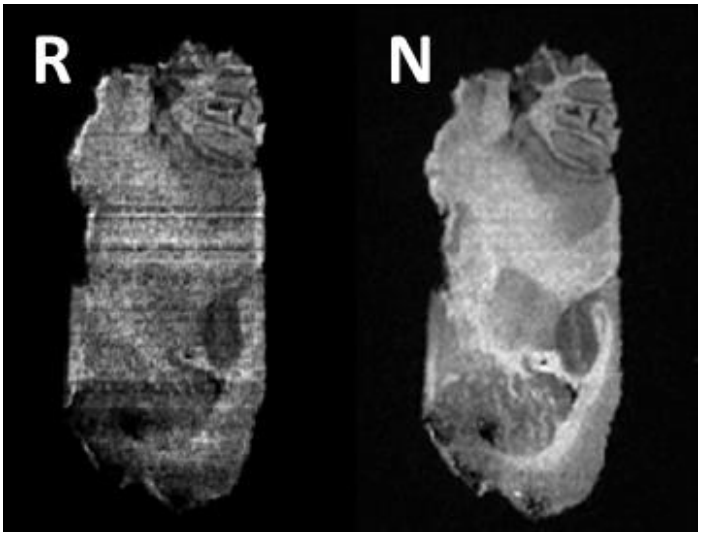

Figure 6.3. Image of *m/z* = 826.6 intensity from mouse brain tissue section comparing raw ion intensity data (R) to normalised by total ion count data (N). This demonstrates the use of normalization by total ion count per pixel for removal of horizontal image artefacts.

Repeat analysis of tissue using CHCA only provided three data sets of acceptable quality (Figure 6.2). This may be due to the build-up of un-ablated matrix material to such an extent that effective ablation and ionization cannot occur. The reason why the first few analyses should visibly remove all matrix but subsequent ones do not, isn't immediately

obvious, but the fact that this does not appear to be nearly as deleterious when using PNA suggests matrix modification effects may be the cause.

As discussed in Chapters 2 and 3, matrix hysteresis and modification effects have been shown to be caused by decarboxylation of matrix molecules during the desorption-ionization process. This results in a reduced spectral absorption efficiency and thus more energy is required to cause further ablation and desorption ionization from the sample [30-32]. In addition, Tarzi et al. showed this may be due to the heating of the matrix from the incident laser photons rather than photochemical processes [192]. If this process were occurring during every analysis and building up over several to a point where data could no longer be obtained, this may explain the inability to perform repeat analysis using CHCA passed a certain number of repeats. The increased utility of PNA for repeat analysis compared to CHCA could then be explained by its lack of a carboxyl group (Figure 6.4).

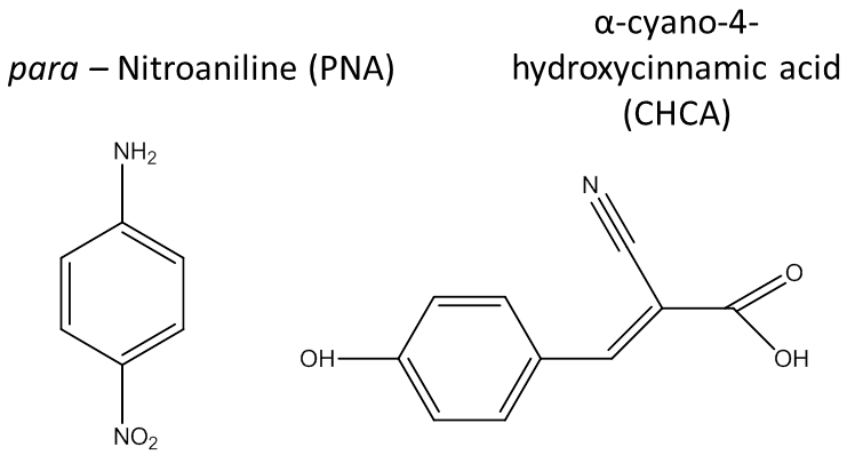

Figure 6.4. Molecular structures of CHCA and PNA.

To investigate this further a second data set was acquired using CHCA as the matrix. Images of the peak at *m/z* = 826.5 from each MALDI MS analysis and photographs of the tissue sample after each analysis are shown in Figures 6.5 and 6.6. In this analysis, poor data quality can be seen in analyses 3 and 4 (Figure 6.5 A3 and A4). A wash (1 mL of 50 % ethanol pipetted over the tissue section; optimization data shown in Figure 6.7) was employed after analysis four to remove the build-up of un-ablated matrix. The fifth analysis once again shows the same distribution of *m/z* = 826.6 (tentatively assigned as PC (18:0/18:1) $[M+K]^+$[179]) as was observed in the first analysis. This suggests that it is the build-up of un-ablated matrix which is causing the poor repeat analysis performance of CHCA. Though this does not give us any information regarding the modification or otherwise of the matrix, it remains a viable hypothesis.

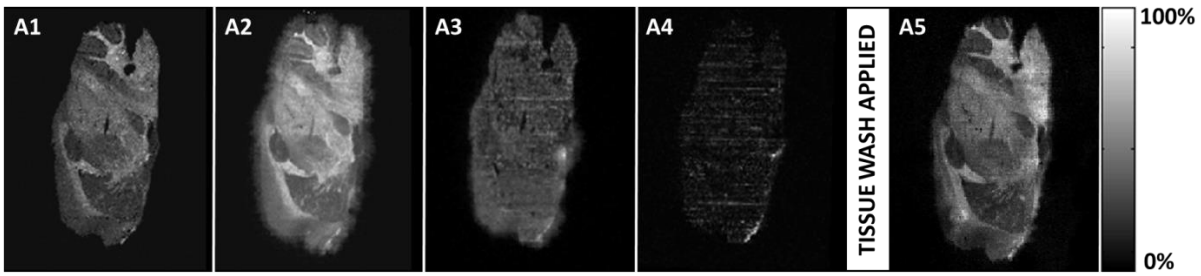

Figure 6.5. TIC normalized images of *m/z* = 826.5 from repeat analysis data set where CHCA was applied to the fresh frozen mouse brain tissue section prior to every analysis (A1 through to A5). A tissue wash (1 mL of 50 % ethanol) was pipetted over the tissue section after analysis 4 (A4) to remove matrix build up and enable further analysis. Poor data after several analyses due to build-up of un-ablated matrix can be alleviated by the application of a tissue wash.

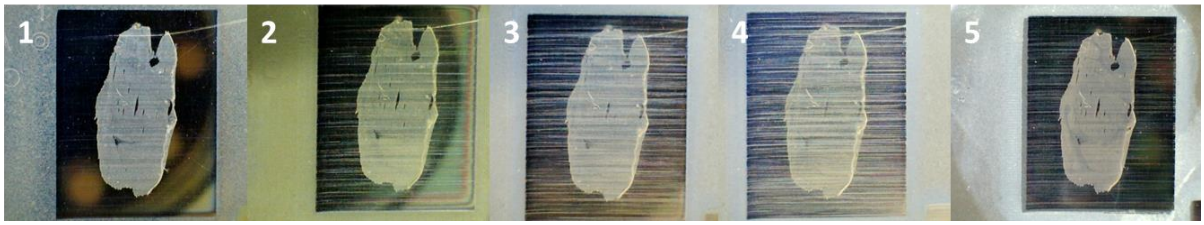

Figure 6.6. Image of build-up of unablated CHCA post analyses. Each image was taken after successive MALDI-MSI interrogations. Image five shows tissue section after 50 % ethanol wash step. Images correspond to data shown in Figure 6.5.

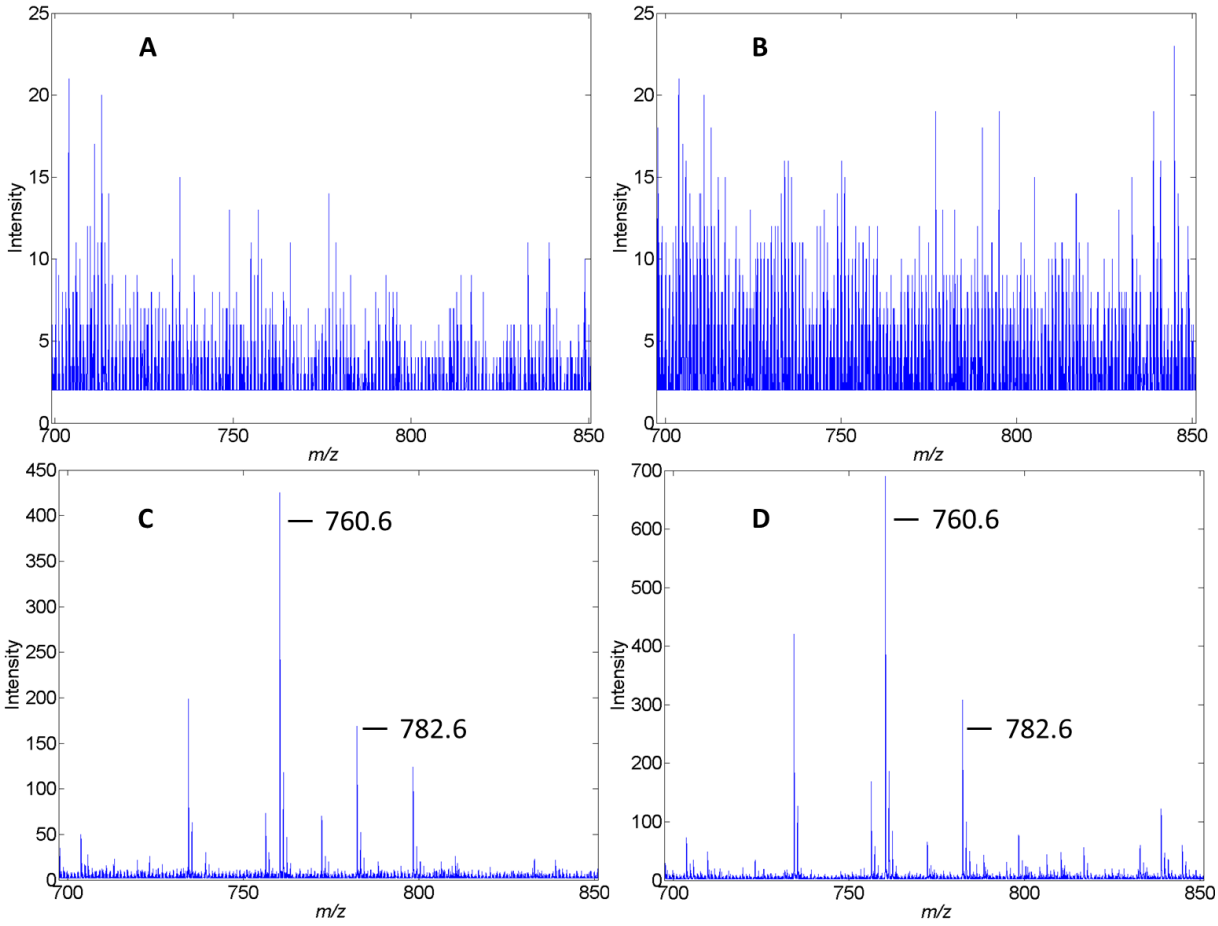

Figure 6.7. Ethanol - water wash run-off was collected and analysed by spot mode MALDI MS. Lipid region spectra for: A) 25 % ethanol, B) 50 % ethanol, C) 75 % ethanol and D) 100 % ethanol. 50 % ethanol was chosen for the subsequent wash due to the combination of no detected lipids in the collected wash run-off (shown here) and the visible removal of a larger portion of the matrix on the tissue as compared to the 25 % ethanol wash. Commonly detected ions at 760.6 and 782.6 Da are labelled in C) and D).

During matrix application using the airspray method, the solvent and matrix solution is thought to extract molecules from the tissue section prior to co-crystallization of matrix and tissue endogenous molecules [217]. This process should favour the molecules which are more soluble in the solvent-matrix solution used. Representative spectra from each of the four PNA

analyses discussed above (Figure 6.2) are shown in Figure 6.8. No substantial changes in spectral properties are observed across the four PNA repeat analyses. This was also found to be the case for the CHCA repeat analysis data set (spectra not shown). Commonly detected phosphocholine (PC) species, as discussed in Chapter 4, are dominant across all four analyses [178, 179, 195]. This suggests that there is still a relatively large amount of these molecules remaining after each analysis and that the abundance of these molecules doesn't significantly change in relation to other less abundant but similarly soluble lipid species. The observed consistency in spatial and spectral lipid abundance and distribution echoes the studies by Garrett *et al.* [206] and Eberlin *et al.* [216] and provides opportunity to use repeat analysis in further research.

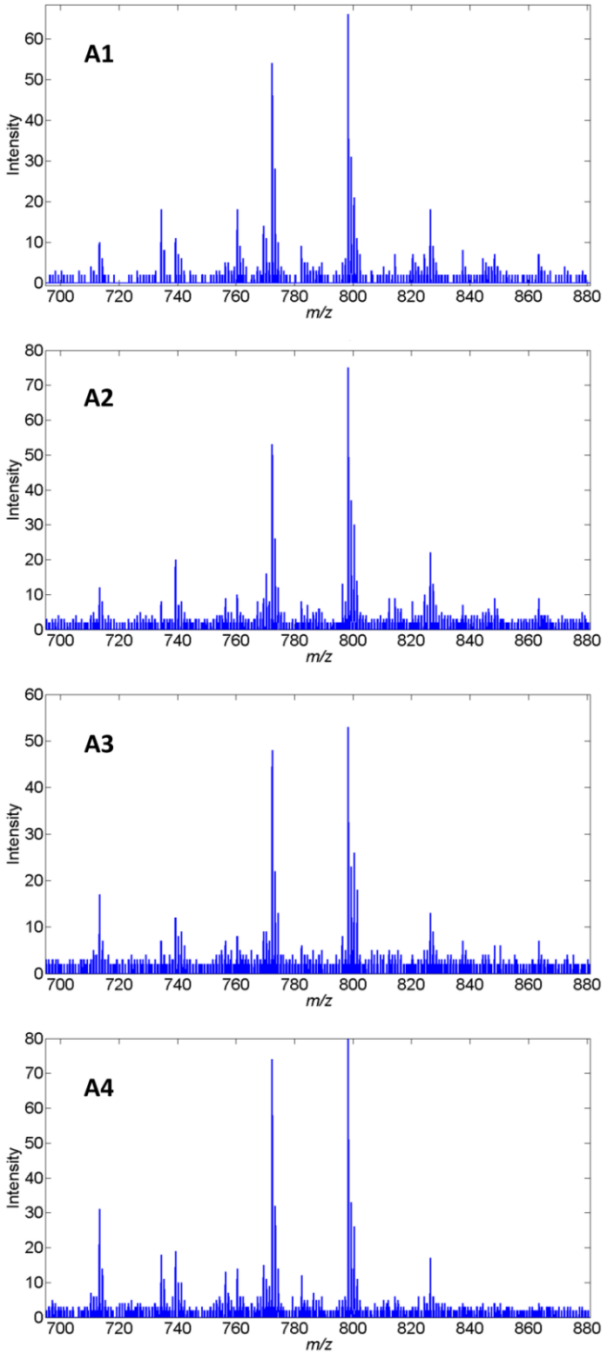

Figure 6.8. Single pixel spectra from the same anatomical region of the repeat analysis data set performed using PNA as the matrix (images shown in Figure 6.2). Analyses one to four are labelled A1 to A4. Spectra appear similar across all four MSI datasets demonstrating the consistency of detected analytes when using repeat analysis by MALDI MSI.

The summed images shown in Figure 6.2 do not, alone, provide any information that cannot be gained from one of the single analysis images. However, they do serve as an example that the data sets can be effectively combined. The combining of these data sets can also be achieved by summing the spatially equivalent spectral data, leading to a signal-to-noise ratio improvement of the order of ×8, an example of which can be seen in Figure 6.9.

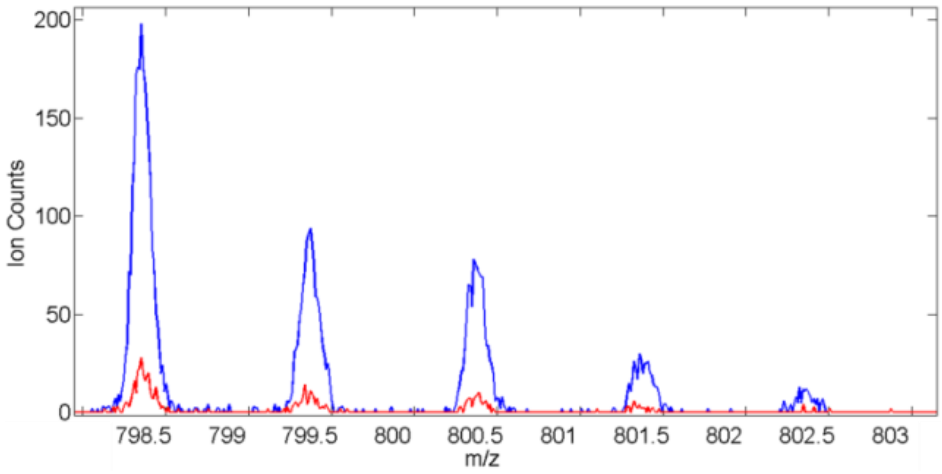

Figure 6.9. Example of a small *m/z* region from single pixel spectrum (red trace) and the sum spectra spatially equivalent pixels from the four PNA repeat analyses (blue trace). The single pixel spectrum has peaks which may not be considered to have a sufficiently large signal to noise to be trustworthy. However, by combining the data for the spatially equivalent pixels from all four of the PNA datasets (Figure 6.2) the signal-to-noise ratio is improved.

6.3.2. Repeat MALDI MS/MS imaging of a single tissue section

Tandem mass spectrometry (MS/MS) combined with collision induced dissociation (CID) can be used to obtain structural information about specifically selected molecules in MALDI MS. The fragmentation of sodium adducts of phospholipid molecules in positive ion

mode can provide improved structural information as compared to protonated species [218, 219]. In addition, the proportion of sodium adducts, as compared to potassium and protonated, increases substantially where formalin fixed tissue is analyzed as opposed to fresh frozen [116]. This is due to the introduction of sodium ions into the tissue from the salt buffer in the formalin fixative solution. Therefore, by using formalin fixed tissue to perform MS/MS studies it is likely that superior structural information can be obtained due to the increased abundance of the more informative sodium adducted lipids.

In-situ MALDI MS/MS imaging with CID has been carried out by groups in the past; enabling useful structural information to be obtained from tissue whilst maintaining the spatial information afforded by MALDI MSI [136, 220]. As pointed out by Caprioli *et al.* (Chapter 7.8 of [221]): "The MS/MS imaging analysis is practically limited to a discrete number of parent ions that can be recorded in a given experiment." Some groups have extended the number of experiments which can be performed in imaging mode by alternating between experiment types in different pixels [222]. However, this will compromise spatial resolution in the resulting images, which in some situations is not acceptable.

In order to demonstrate one way in which repeat analysis can be employed to obtain increased information from a tissue section, and to demonstrate its utility in other experiment methodologies, repeat analysis has been combined with MALDI MS/MS imaging to provide multiple MS/MS imaging analyses from a single tissue section (Figure 6.10). This enables the full accumulation time per pixel, for all pixels, to be dedicated to one MS experiment method per image acquisition; improving sensitivity whilst maintaining spatial resolution.

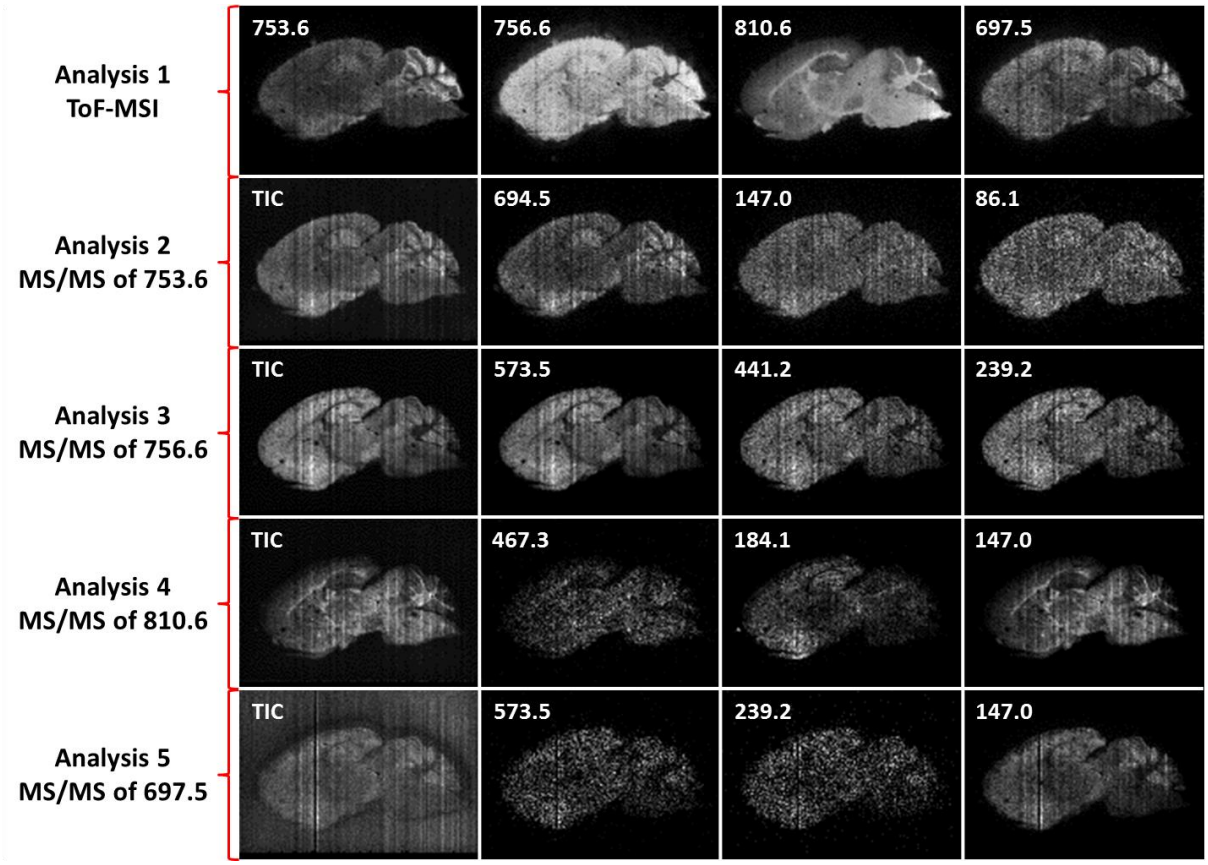

Figure 6.10. Tissue images from five repeat analyses of a single formalin fixed mouse brain tissue section using PNA as matrix. A ToF MS image data set was acquired in the first analysis. Subsequent analyses consisted of CID MS/MS image acquisitions from parent ions at *m/z* = 753.6, 756.6, 810.6 and 697.5. Images from MS/MS data sets show either the TIC or fragment abundances, mass-to-charge values corresponding to each image are displayed. Repeat MALDI MSI and MS/MS imaging of a single tissue section can allow structural information from an increased number of different spatially resolved species to be obtained from a single tissue section. Viewing the spatial distribution of fragment ions in comparison to the parent distribution can give further confirmation of the proposed structural assignment.

MALDI MSI and MS/MS imaging can be performed on the same tissue section using repeat analysis methodology. Repeat analysis of a tissue section by MALDI MSI doesn't appear to result in changing spatial distributions being detected for individual lipid peaks (Figure 6.2). Therefore performing MS/MS studies in imaging mode after having already acquired MALDI MSI data allows the spatial distribution of the MS/MS fragments to be compared with the MS image of the parent ion. This can provide an extra level of information for the assignment of molecules in tissue that would otherwise not be available.

Five analyses were carried out on a single section; images from the initial ToF MSI data acquisition are shown on the top row of Figure 6.10. MS/MS images were acquired in the four subsequent analyses using these ions as the parent ions. Images of the TIC and selected fragments are displayed for each of these MS/MS acquisitions (Figure 6.10). The TIC images from the MS/MS data sets essentially show the spatial distribution of the parent ions selected for each MS/MS experiment; as all fragments in the mass spectra are derived from the parent ion or ions. Consequently, the TIC images should match those of the corresponding ion from ToF MSI data in analysis 1. Comparison between images in Figure 6.10 shows that this is largely the case; notwithstanding the TIC image from analysis 5 which shows contribution in the off tissue regions, suggesting that a matrix derived ion is also being transmitted during the MS/MS parent ion selection. This provides us with further reassurance that the molecule(s) selected for MS/MS analysis are the same ones which we observed in our original ToF MSI experiment. A list of fragment peaks and corresponding assignments from the data in Figure 6.10 is shown in Table 6.1, the mean spectra and structural diagrams from this experiment are shown in Figures 6.11-6.14.

Table 6.1. Parent ions, detected fragments, proposed assignments and supporting references from repeat MALDI MS/MS imaging data shown in Figure 6.10. Full spectra and assignment structures are shown in Figures 6.11-6.14.

Analysis number	Parent *m/z*	Detected Fragment *m/z* and possible molecular formula	Tentative assignment and supporting references.
2	753.6	694.5 - $[M+Na-N(CH_3)_3]^+$ 570.5 - $[M+Na-PO_4HC_2H_4N(CH_3)_3]^+$ 548.5 - $[M+H- PO_4HC_2H_4N(CH_3)_3]^+$ 147.0 - $[PO_4HNaC_2H_3]^+$	SM 36:1 $[M+Na]^+$ [178, 195]
3	756.6	573.5 - $[M+Na- PO_4HC_2H_4N(CH_3)_3]^+$ 441.2 - $[M+Na-N(CH_3)_3- C_{15}H_{31}COOH]^+$ 239.2 - $[C_{15}H_{31}CO]^+$ 147.0 $[PO_4HNaC_2H_4]^+$	PC 16:0/16:0 $[M+Na]^+$ [178, 179, 185]
4	810.6	627.5 - $[M+Na- PO_4HC_2H_4N(CH_3)_3]^+$ 469.3 - $[M+Na-N(CH_3)_3-C_{17}H_{33}COOH]^+$ 467.3 - $[M+Na-N(CH_3)_3-C_{17}H_{35}COOH]^+$ 267.3 - $[C_{17}H_{35}CO]^+$ 265.3 - $[C_{17}H_{33}CO]^+$ 147.0 - $[PO_4HNaC_2H_4]^+$	PC 18:0/18:1 $[M+Na]^+$ [185]
5	697.5	573.5 - $[M+Na- PO_4HC_2H_4N(CH_3)_3]^+$ 441.2 - $[M+Na-N(CH_3)_3- C_{15}H_{31}COOH]^+$ 239.2 - $[C_{15}H_{31}CO]^+$ 147.0 - $[PO_4HNaC_2H_4]^+$	PC 18:0/18:1 $[M+Na-N(CH_3)_3]^+$ [146]

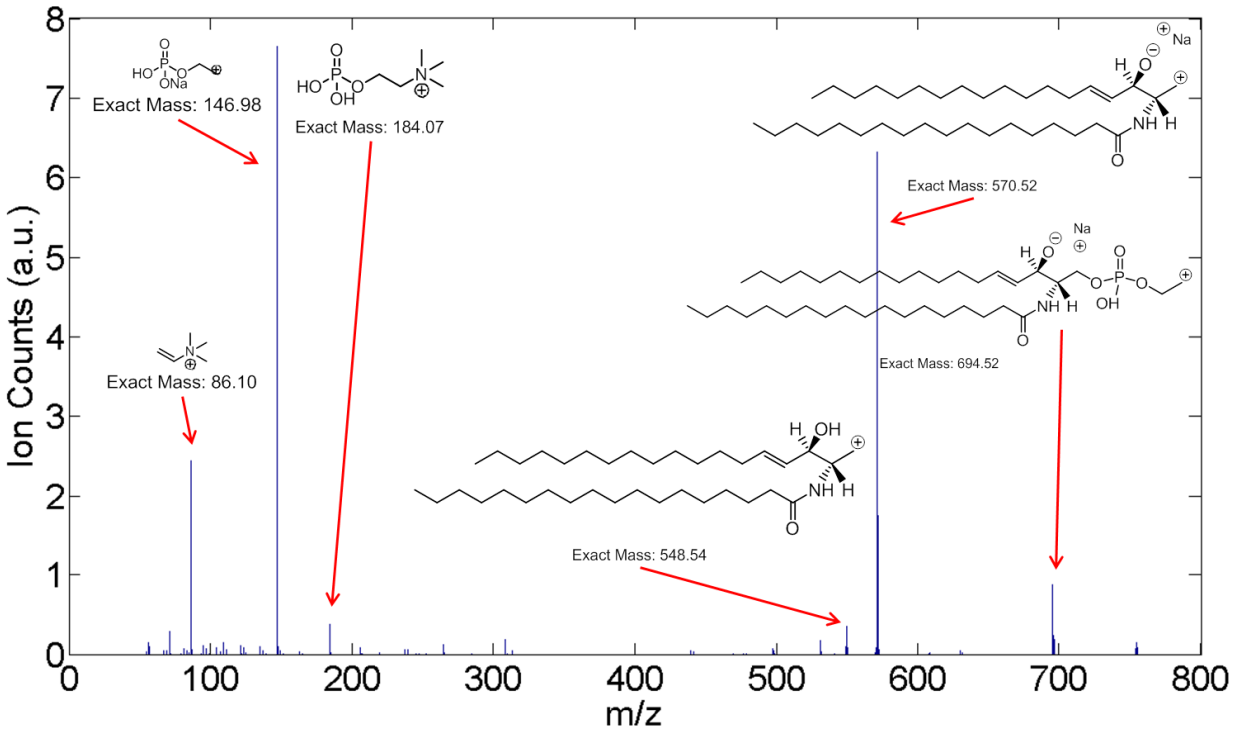

Figure 6.11. Mean mass spectrum from collision induced dissociation by MS/MS of parent molecule at *m/z* = 753.6. Possible structural assignments are labelled; double bond positions are for reference only. Data taken from that shown in analysis 2 of Figure 6.10.

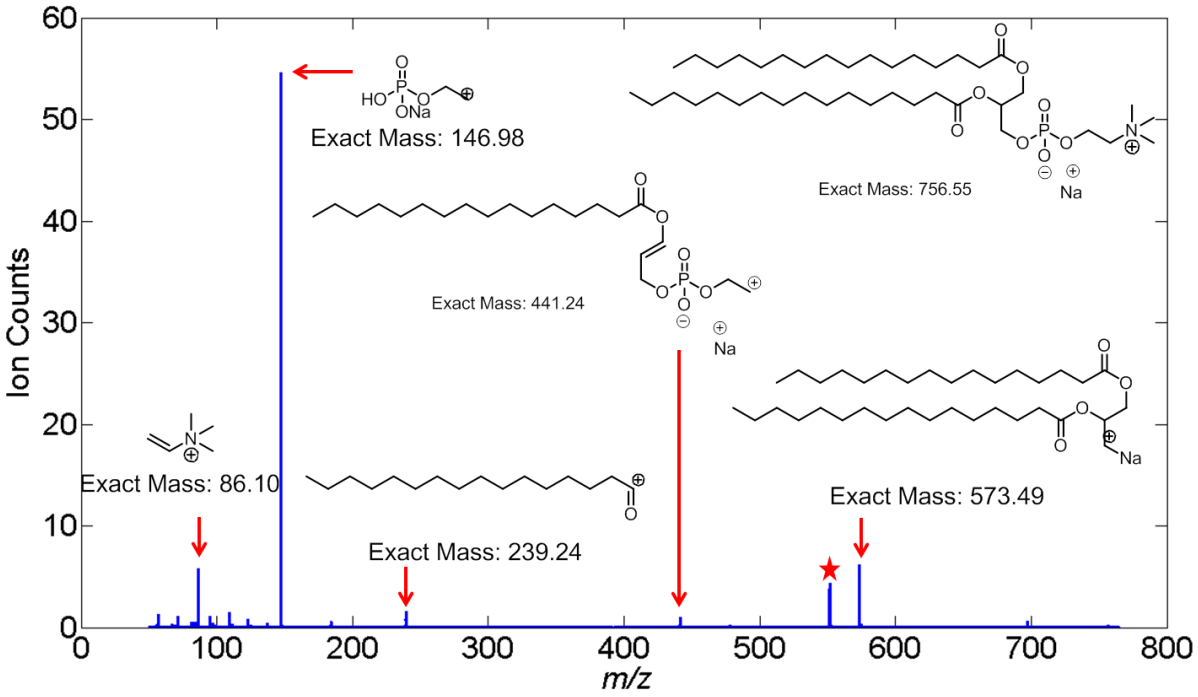

Figure 6.12. Mean mass spectrum from collision induced dissociation by MS/MS of parent molecule at *m/z* = 756.6. Possible structural assignments are labelled; double bond positions are for reference only. Data taken from that shown in analysis 3 of Figure 6.10. The peak marked with an asterisk is [573.5-Na+H].

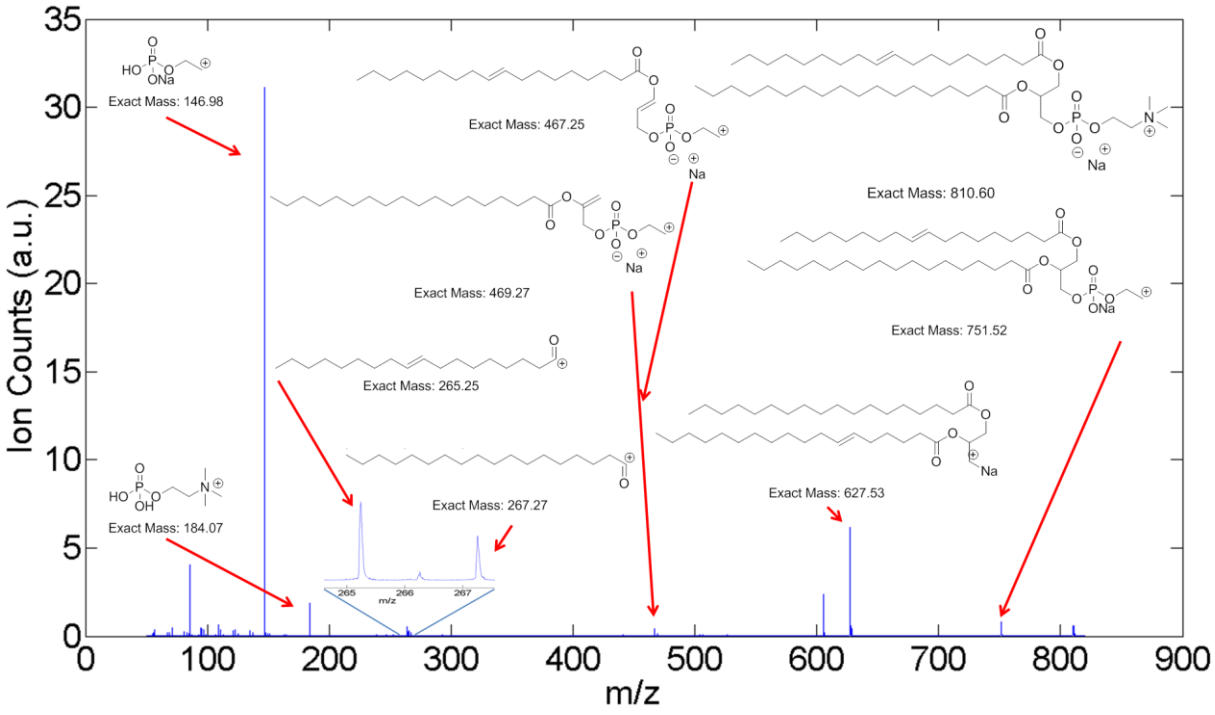

Figure 6.13. Mean mass spectrum from collision induced dissociation by MS/MS of parent molecule at *m/z* = 810.6. Possible structural assignments are labelled; double bond positions are for reference only. Data taken from that shown in analysis 4 of Figure 6.10.

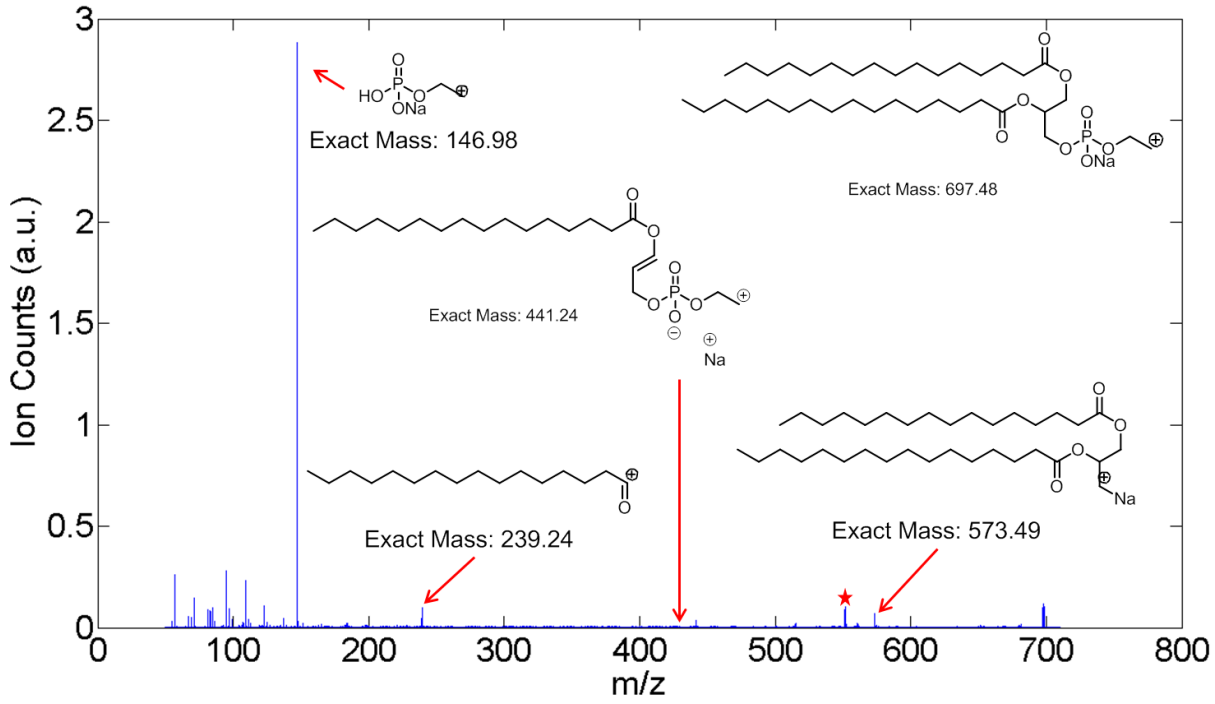

Figure 6.14. Mean mass spectrum from collision induced dissociation by MS/MS of parent molecule at *m/z* = 697.5. Possible structural assignments are labeled; double bond positions are for reference only. Data taken from that shown in analysis 3 of Figure 6.10. The peak marked with an asterisk is [573.5-Na+H].

It is well known that many tissue endogenous lipids can have very similar *m/z* values and on an instrument such as the one used in this study these lipids cannot be resolved in the mass spectrum (this issue was also discussed within Chapter 4) [210, 223, 224]. A consequence of this is that the peaks displayed in the images from analysis 1 and the TIC images of analyses 2-5 in Figure 6.10 may in fact have a contribution from several different ions; notwithstanding the transmission of several ions into the collision cell. Performing MS/MS on such peaks is therefore likely to only allow us to assign structures to the ions which contribute most to the selected peak (if there is indeed more than one contributing). However, by performing MS/MS in the imaging mode, as here, the spatial intensity

distributions of the fragment ions can give us further information regarding multiple contributions to the parent ion peak. If the spatial intensity distributions of one or more of the fragments differ then some judgment can be made as to the parent of said fragments. For example the spatial intensity distributions of the two PC head-group fragments at *m/z* = 184.1 and 147.0 from analysis 4 (Figure 6.10) show different spatial distributions suggesting that two PC lipids are contributing to the peak at *m/z* = 810.6.

Performing MALDI MS/MS with CID in imaging mode in this manor allows the full acquisition time per pixel to be allocated to the analysis of a single parent molecule, maximizing sensitivity. This can be contrasted with the implementation of multiple MS/MS experiments per pixel, where every additional parent molecule reduces the time available for each experiment, reducing sensitivity and restricting the number of experiments which can be performed. Under the conditions used in this study, utilizing the QSTAR XL (and likely other instrument incorporating ToF or Tof/ToF mass analyzers), the acquisition of a Δ*m/z* 50 - 1000 ToF and four MS/MS imaging data sets would not have been possible in one acquisition.

6.3.3. MALDI MSI of lipids and proteins from a single tissue section

Repeat MALDI MSI of a single tissue section can allow additional information to be obtained from that tissue section. A further application of this is for the acquisition of both lipid and peptide / protein data from a single tissue section by MALDI MSI. Typically, data from lipids and peptides / proteins are not simultaneously acquired as the matrices, laser energies and operational setups used for these two different *m/z* regimes are incompatible using MALDI TOF type instrumentation.

Repeat analysis was performed; incorporating a washing protocol after the first analysis allows the detection of lipids and peptides / proteins from the same tissue section. A Bruker Daltonics UltrafleXtreme was used to allow both *m/z* regimes to be accessed and to demonstrate the muli-platform applicability of the presented methodologies. Firstly the mass to charge region 60-1200 was analysed using CHCA as matrix (as PNA sublimes readily at the pressure this source is maintained at; as demonstrated in Chapter 5), with a 100 × 100 μm pixel size (see Figure 6.15 for example single pixel spectra and images).

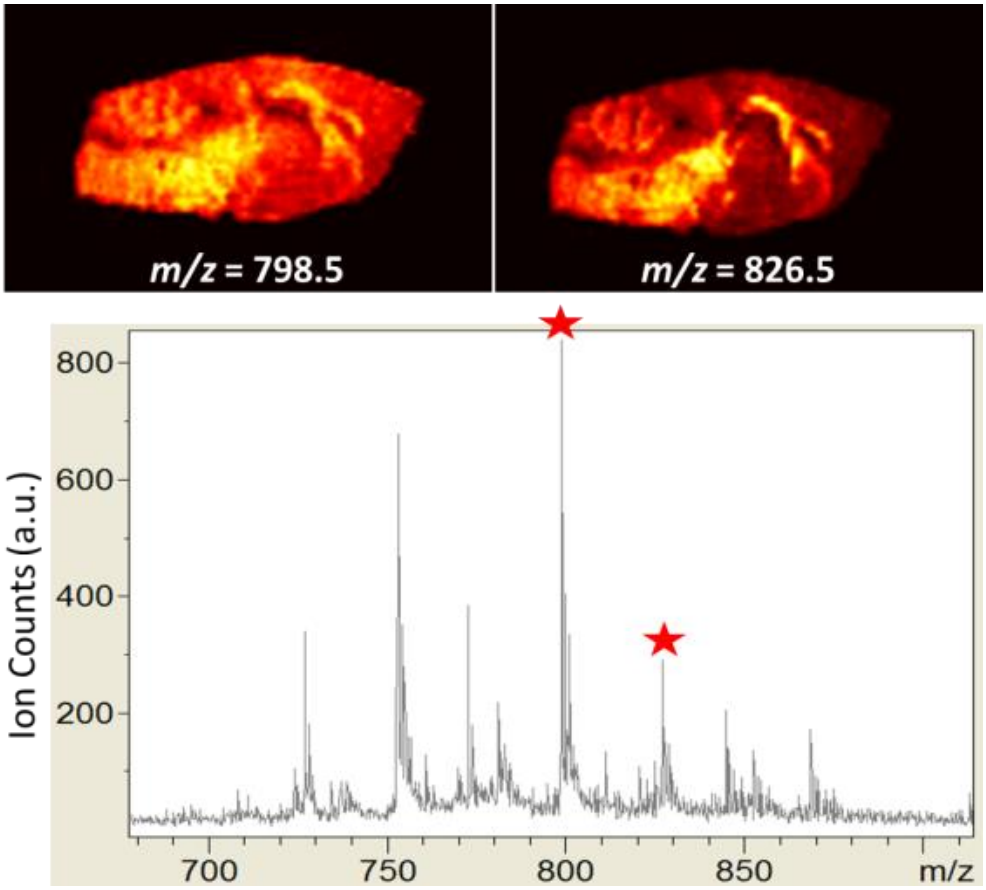

Figure 6.15. Example single pixel spectrum from lipid rich *m/z* region and two example images; starred peaks correspond to peaks used for image display. Spectra and images correspond well with existing mouse brain lipid analysis in published literature[116].

Data from the first acquisition are presented in Figure 6.15 showing spectral information in the lipid region and ion images of peaks at *m/z* = 798.5 and 826.5. The use of spot mode raster imaging results in much of the matrix material still being present on the tissue after MSI data acquisition [206]. This makes the application of SA for the next analysis problematic. However, many groups now employ tissue wash procedures prior to peptide / protein analysis [141]; these wash steps are also ideal for removing many commonly used MALDI MSI matrices, including CHCA. This allowed the application of SA prior to repeat analysis of the tissue section in the mass to charge region 1480-20,000 (see Figure 6.16) with a pixel size of 200 × 200 μm.

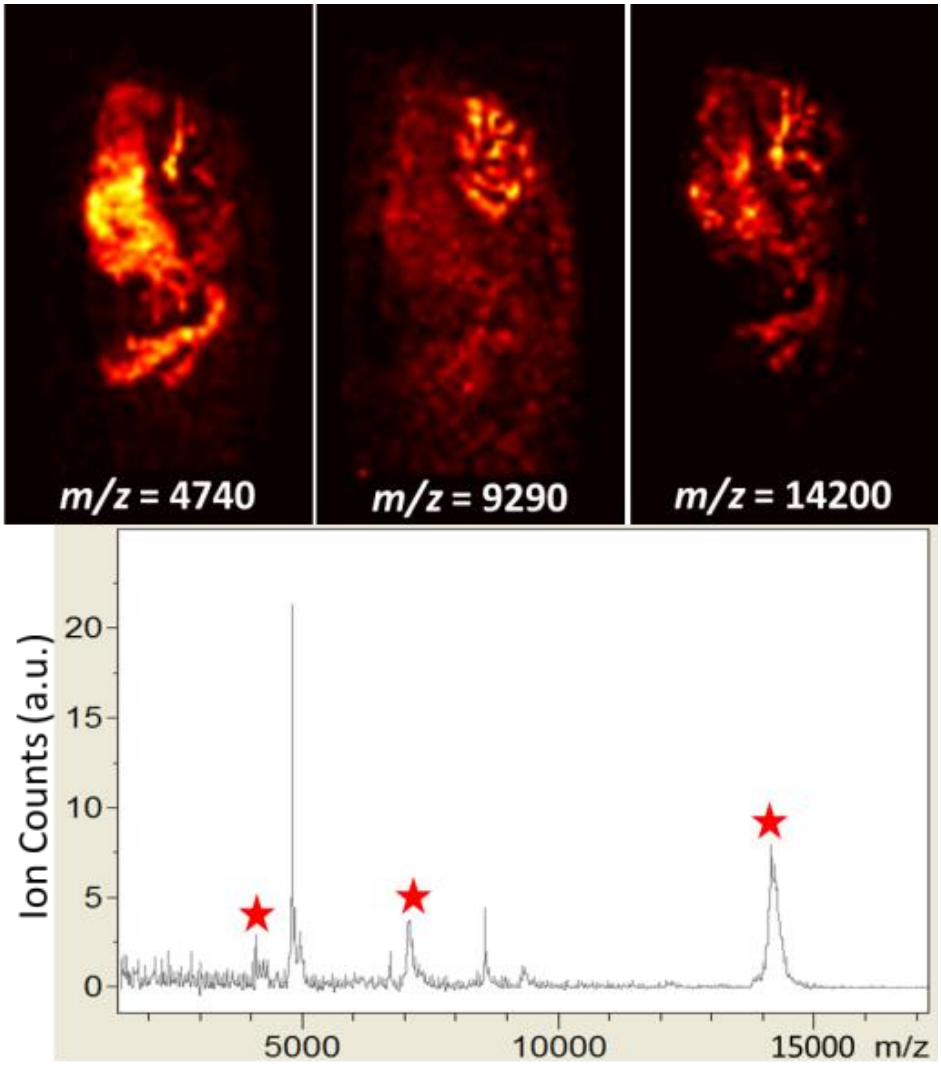

Figure 6.16. Example single pixel spectrum from peptide / protein *m/z* region and example images from a mouse brain tissue section upon second analysis; starred peaks correspond to peaks used for image data. Peptide and protein data can be obtained from the second MALDI MSI analysis of a tissue section.

Repeat analysis by MALDI MSI allows the acquisition of both lipid and peptide / protein data from the same tissue section. A single pixel mass spectrum and three ion intensity images are displayed from this second analysis in Figure 6.16. Ions are detected at up to approximately 15,000 *m/z*. The spectra obtained appear to broadly agree with previously

published analyses for brain tissue using SA for this *m/z* region [225]. Additionally, the initial low *m/z* MALDI MSI analysis doesn't appear to have significantly limited the detection of different peptides and proteins in the subsequent analysis. The co-localization of lipid and protein molecules can be seen when viewing Figures 6.15 and 6.16. For example the lipid peak at *m/z* = 826.6 and the peak at *m/z* = 4740 display similar distributions and both appear to be present in the corpus callosum and pons brain regions.

6.4. Conclusion

The process of multiple MALDI MSI data acquisitions of a single tissue section by repeat analysis is shown to increase the quality of information which can be obtained from a single tissue section. The opportunity for applying multiple MALDI MSI methodologies to a single tissue section, whilst maintaining the sensitivity afforded by a single experimental acquisition, is a potentially very useful and powerful feature of the repeat analysis methodologies shown here. The utility of this methodology for analysis of molecules which require different matrices, instrumental setups or laser energies by MALDI MSI opens the way for new applications such as imaging the co-localization of drugs, their metabolites and proteins from the same tissue section. This is not possible with current methodologies where the analysis of serial sections is currently the standard practice where multiple matrices, instrumental setups or instruments are required. Further to this, repeat analysis can provide security from the wastage of precious samples. If an error, human or mechanical, should occur during a MALDI MSI data acquisition a repeat analysis can be used to prevent the need to start again with a new sample.

Chapter 7

Future Work

Within Chapter 2 the fluorescent properties of white paper were exploited to enable a low cost UV laser beam profiling method. This method was then applied within the source of the mass spectrometer. The precise and accurate profiling of the laser beam profile within the source of a MALDI mass spectrometer is the main priority where the extension of this work is concerned. As mentioned within the conclusions of Chapter 2, the structure of the paper fibres is the dominant feature within the in-source beam profile image. The development of a substrate which is homogenous on the length scales typically probed within MALDI MS will enable the imaging of the photon distribution within the beam profile, as well as the beam profile dimensions.

One possibility is the creation of a home-made solution / suspension of appropriate fluorophores which can be applied onto the sample plate. An important part of selecting the appropriate fluorophore would be to carefully characterise the fluorescent response under a wide range of MALDI MS relevant fluences. The ideal fluorophore would provide information of an acceptable quality over as wide a fluence range as possible. Therefore, a low level of photo-bleaching and photo-chemical reaction would be desirable. Another option, not investigated within this study, is to place the fluorescing media directly in-front of the

camera and not on the sample plate; creating a transmission mode fluorometric beam profiling setup. If the sample plate is made of a material which reflects sufficiently well (in a suitably diffuse manner) at the laser wavelength used then this alternative configuration could allow the use of substances which are not suitable on-plate. For example, the fluorescent glass investigated within this study could be used within this alternative setup.

Ultimately, an improved fluorometric beam profiling methodology would enable the on-line, in-source imaging of the laser photon distribution. This information would then be correlated with corresponding pulse energy measurements to enable a more sophisticated consideration of the effect of beam profile on ion yield in MALDI MS and MSI. A high frame rate source camera and energy meter would additionally allow single pulse images and energy measures to be correlated.

Chapters 3 and 4 deal with similar topics and so will be addressed together here. The trends seen and discussed within Chapters 3 and 4 demonstrate that the interplay of variables within these high repetition-rate continuous raster mode experiments lead to complex effects; the causes of which are difficult to elucidate. The possibility of matrix modification and hysteresis effects contributing to the trends observed is a priority for the future work in this area. Repeating the experimental protocols used here with different matrices, analytes and a larger fluence range will help uncover whether this is the case. Within the work by Fournier *et al.* [31, 32] and Tarzi *et al.* [192] matrix modification and hysteresis effects were seen to vary depending upon the matrix investigated. Therefore, indirect evidence as to whether this was at play within these studies would be provided by utilising matrices with a variety of structures and physical properties. For example, decarboxylation is has been put forward as potentially

being responsible for some matrix modification and hysteresis effects [30-32, 192]. CHCA was used within the repetition rate and raster speed variation experiments within this thesis and does possess a carboxyl group. Therefore, repeating this work with PNA would be an obvious first step.

The use of a number of analytes from varying molecular classes would not only add to the overall knowledge of the suitability of continuous raster mode sampling with high repetition rate lasers, it would also allow evidence to be gathered regarding potential charge transfer and plume dynamics related factors which may be contributing to the trends and phenomena seen within Chapters 3 and 4. The use of molecules which exhibit very little fragmentation under typical UV MALDI MS conditions would simplify the process of data analysis and, more importantly, would further rule out fragmentation as the cause of the observed trends.

To further probe the observed shift in $[M+H]^+$ / $[M+Na]^+$ ratio with changing fluence, sample solutions could be purified further in an attempt to remove sodium. However the enthusiasm with which sodium makes itself present within mass spectrometric experiments, even at very low levels, makes this problematic. An alternative would be to dope the sample solution with varying levels of sodium or even other alkali metals such as potassium, lithium or caesium [82]. Whilst this may complicate matters in terms of altering the analyte fragmentation behaviour; it may allow the underlying reason for the changing adduct ratio to be elucidated. For example, if matrix crystal regions with higher sodium salt content require a higher fluence to fully ablate then the decrease in $[M+H]^+$ / $[M+Na]^+$ with increasing fluence would potentially make sense. Doping with additional alkali salt would potentially ensure that there was always a large amount of that metal cation available regardless of the energy delivered.

Aside from exploring other possibilities within the mass spectrometric process for this experiment, other analytical methods could be employed. SEM imaging can be used to analyse the morphology of matrix crystals both before and after analysis. Matrix / analyte crystals which have undergone modification and remain on the sample plate should be visible. Further to this, the use of techniques such as ramen, or UV/VIS spectroscopy could provide information regarding chemical changes which may have occurred during the MALDI MS process; further enabling judgements to be made as to the likelihood of matrix modification as a significant factor.

Within Chapter 5 PNA was shown to be a promising matrix for high-throughput MALDI MSI analysis of lipids in mouse brain tissue sections using a high repetition rate laser. Part of the reasoning behind the utility of PNA is the relatively low ion detection fluence threshold energy which ensures the lower energy per pulse delivered by the Nd:YVO_4 laser remains within a useful range (at the spot size used). In early work (not shown) 2,5-DHB was not found to provide data of acceptable quality within our experimental setup, despite often being quoted as the best matrix for lipid analysis. It is known, however, that 2,5-DHB has a higher threshold energy than CHCA, a matrix which was found to be useful. The first extension of the work in this chapter would be to establish the ion intensity response of PNA, CHCA and other matrices over a wide range of fluences, thus establishing the threshold energy in the process. In addition, the absorption properties of these matrices over the UV MALDI MS relevant range of wavelengths should be measured. This information would allow the comparison of PNA to other more common MALDI MS imaging matrices to be made more rigorously and for the relevant underlying properties to be compared.

Further to this, the investigation into useful matrices and the underlying reasons for their performance could be extended into the analysis of other analytical classes. Typically, in this type of investigation, single analyte molecules are assessed using each matrix studied. Promising matrices then tend to jump straight into use in imaging. A sensible intermediate step would be to create relatively complex solutions of multiple biologically relevant analytes from multiple classes for examining the applicability of different matrix compounds. These data could then be related to the response of subsequent imaging studies for the same or similar analytes endogenous to the tissue being examined.

The repeat analysis of single tissue sections is investigated and applied to the analysis of both lipids and proteins within Chapter 6. The ultimate benifit of these methodologies will be in their application. Therefore, future work using repeat analysis would aim to both further demonstrate their utility and to apply them to real world problems in MALDI MSI applications.

The next confirmatory experiment necessary is to rigorously demonstrate that certain analyses and washes do not alter the detected distributions of different molecules. Whilst this was investigated for lipids with both PNA and CHCA within Chapter 6, it also needs to be demonstrated for other analyte classes such as peptides and proteins. Additionally, serial tissue sections could be analysed by traditional single interrogation MALDI MSI to provide further validation of these repeat analysis methods. To demonstrate the promise of these methods the analysis of multiple analyte classes using multiple matrices and tissue washes can be investigated further. For example, the MALDI MSI analysis of a single tissue section could proceed as follows: positive mode analysis of lipids using CHCA; matrix removal

tissue wash; negative mode analysis of lipids using 9-aminoacridine (9-AA) [196]; matrix removal tissue wash; positive mode peptide / protein analysis using SA; negative mode peptide / protein analysis using SA. The tissue could then be revisited in discrete regions or by further imaging using MS/MS analysis for structural conformation, as in Chapter 6. Thus, a huge amount of data is potentially returned from a single tissue section. The further confirmation of these methods would be to perform an analysis similar to the one just outlined on medically relevant and important samples, such as those from a drug dosing animal study within which this breadth of knowledge is required from a small amount of sample material.

References

1. Haakansson, P., Kamensky, I., Sundqvist, B., Fohlman, J., Peterson, P., McNeal, C. J., and Macfarlane, R. D. Iodine-127-plasma desorption mass spectrometry of insulin. Journal of the American Chemical Society, 1982. **104**(10): p. 2948-2949.
2. Dell, A. and Morris, H. R. Fast atom bombardment-high field magnet mass spectrometry of 6000 dalton polypeptides. Biochemical and biophysical research communications, 1982. **106**(4): p. 1456-1462.
3. Barber, M., Green, B. N., and Jennings, K. The analysis of small proteins in the molecular weight range 10–24 kDa by magnetic sector mass spectrometry. Rapid Communications in Mass Spectrometry, 1987. **1**(5): p. 80-83.
4. Karas, M., Bachmann, D., and Hillenkamp, F. Influence of the wavelength in high-irradiance ultraviolet laser desorption mass spectrometry of organic molecules. Analytical Chemistry, 1985. **57**(14): p. 2935-2939.
5. Tanaka, K., Waki, H., Ido, Y., Akita, S., Yoshida, Y., Yoshida, T., and Matsuo, T. Protein and polymer analyses up to m/z 100 000 by laser ionization time? of? flight mass spectrometry. Rapid Communications in Mass Spectrometry, 1988. **2**(8): p. 151-153.
6. Karas, M., Bachmann, D., Bahr, U., and Hillenkamp, F. Matrix-Assisted Ultraviolet-Laser Desorption of Nonvolatile Compounds. International Journal of Mass Spectrometry and Ion Processes, 1987. **78**: p. 53-68.
7. Karas, M. and Hillenkamp, F. Laser desorption ionization of proteins with molecular masses exceeding 10,000 daltons. Analytical chemistry, 1988. **60**(20): p. 2299-2301.
8. Horneffer, V., Dreisewerd, K., Ludemann, H. C., Hillenkamp, F., Lage, M., and Strupat, K. Is the incorporation of analytes into matrix crystals a prerequisite for matrix-assisted laser desorption/ionization mass spectrometry? A study of five positional isomers of dihydroxybenzoic acid2. International Journal of Mass Spectrometry, 1999. **185**: p. 859-870.
9. Soltwisch, J., Jaskolla, T. W., and Dreisewerd, K. Color Matters—Material Ejection and Ion Yields in UV-MALDI Mass Spectrometry as a Function of Laser Wavelength and Laser Fluence. Journal of The American Society for Mass Spectrometry, 2013. **24**(10): p. 1477-1488.
10. Beavis, R. C., Chait, B. T., and Standing, K. Factors affecting the ultraviolet laser desorption of proteins. Rapid Communications in Mass Spectrometry, 1989. **3**(7): p. 233-237.
11. Chen, X., Carroll, J. A., and Beavis, R. C. Near-ultraviolet-induced matrix-assisted laser desorption/ionization as a function of wavelength. Journal of the American Society for Mass Spectrometry, 1998. **9**(9): p. 885-891.
12. Allwood, D. A., Dreyfus, R. W., Perera, I. K., and Dyer, P. E. UV optical absorption of matrices used for matrix-assisted laser desorption/ionization. Rapid Communications in Mass Spectrometry, 1996. **10**(13): p. 1575-1578.
13. Soltwisch, J., Jaskolla, T. W., Hillenkamp, F., Karas, M., and Dreisewerd, K. Ion yields in UV-MALDI mass spectrometry as a function of excitation laser wavelength and optical and physico-chemical properties of classical and halogen-substituted MALDI matrixes. Analytical chemistry, 2012. **84**(15): p. 6567-6576.
14. Wiegelmann, M., Soltwisch, J., Jaskolla, T. W., and Dreisewerd, K. Matching the laser wavelength to the absorption properties of matrices increases the ion yield in UV-MALDI mass spectrometry. Analytical and bioanalytical chemistry, 2013. **405**(22): p. 6925-6932.
15. Wu, K. J., Steding, A., and Becker, C. H. Matrix assisted laser desorption time of flight mass spectrometry of oligonucleotides using 3 hydroxypicolinic acid as an ultraviolet sensitive matrix. Rapid Communications in Mass Spectrometry, 1993. **7**(2): p. 142-146.

16. Allwood, D. A., Dreyfus, R. W., Perera, I. K., and Dyer, P. E. Optical absorption of matrix compounds for laser-induced desorption and ionization (MALDI). Applied Surface Science, 1997. **110**: p. 154-157.
17. Bökelmann, V., Spengler, B., and Kaufmann, R. Dynamical parameters of ion ejection and ion formation in matrix-assisted laser desorption/ionization. Eur. Mass Spectrom, 1995. **1**: p. 81-93.
18. Ehring, H. and Sundqvist, B. U. R. Studies of the MALDI process by luminescence spectroscopy. Journal of Mass Spectrometry, 1995. **30**(9): p. 1303-1310.
19. Ingendoh, A., Karas, M., Hillenkamp, F., and Giessmann, U. Factors affecting the resolution in matrix-assisted laser desorption--ionization mass spectrometry. International journal of mass spectrometry and ion processes, 1994. **131**: p. 345-354.
20. Westman, A., Huth-Fehre, T., Demirev, P., Bielawski, J., Medina, N., Sundqvist, B. U. R., and Karas, M. Matrix-assisted laser desorption/ionization: Dependence of the ion yield on the laser beam incidence angle. Rapid Communications in Mass Spectrometry, 1994. **8**(5): p. 388-393.
21. Dreisewerd, K., Schurenberg, M., Karas, M., and Hillenkamp, F. Influence of the Laser Intensity and Spot Size on the Desorption of Molecules and Ions in Matrix-Assisted Laser-Desorption Ionization with a Uniform Beam Profile. International Journal of Mass Spectrometry, 1995. **141**(2): p. 127-148.
22. Yau, P., Dominic Chan, T. W., Cullis, P. G., Colburn, A., and Derrick, P. J. Threshold fluences for production of positive and negative ions in matrix-assisted laser desorption/ionisation using liquid and solid matrices. Chemical physics letters, 1993. **202**(1-2): p. 93-100.
23. Qiao, H., Spicer, V., and Ens, W. The effect of laser profile, fluence, and spot size on sensitivity in orthogonal-injection matrix-assisted laser desorption/ionization time-of-flight mass spectrometry. Rapid Communications in Mass Spectrometry, 2008. **22**(18): p. 2779-2790.
24. Guenther, S., Koestler, M., Schulz, O., and Spengler, B. Laser spot size and laser power dependence of ion formation in high resolution MALDI imaging. International Journal of Mass Spectrometry, 2010. **294**(1): p. 7-15.
25. Westmacott, G., Ens, W., Hillenkamp, F., Dreisewerd, K., and Schurenberg, M. The influence of laser fluence on ion yield in matrix-assisted laser desorption ionization mass spectrometry. International Journal of Mass Spectrometry, 2002. **221**(1): p. 67-81.
26. Zhigilei, L. V. and Garrison, B. J. Molecular dynamics simulation study of the fluence dependence of particle yield and plume composition in laser desorption and ablation of organic solids. Applied physics letters, 1999. **74**(9): p. 1341-1343.
27. Zhigilei, L. V., Yingling, Y. G., Itina, T. E., Schoolcraft, T. A., and Garrison, B. J. Molecular dynamics simulations of matrix-assisted laser desorption—connections to experiment. International Journal of Mass Spectrometry, 2003. **226**(1): p. 85-106.
28. Liu, B.-H., Charkin, O. P., Klemenko, N., Chen, C. W., and Wang, Y.-S. Initial ionization reaction in matrix-assisted laser desorption/ionization. The Journal of Physical Chemistry B, 2010. **114**(33): p. 10853-10859.
29. Dreisewerd, K. The desorption process in MALDI. Chemical Reviews, 2003. **103**(2): p. 395-425.
30. Fournier, I., Marinach, C., Tabet, J. C., and Bolbach, G. Irradiation effects in MALDI, ablation, ion production, and surface modifications. PART II: 2,5-dihydroxybenzoic acid monocrystals. Journal of the American Society for Mass Spectrometry, 2003. **14**(8): p. 893-899.
31. Fournier, I., Tabet, J. C., and Bolbach, G. Irradiation effects in MALDI and surface modifications - Part I: Sinapinic acid monocrystals. International Journal of Mass Spectrometry, 2002. **219**(3): p. 515-523.

32. Fournier, I., Beavis, R., Blais, J., Tabet, J., and Bolbach, G. Hysteresis effects observed in MALDI using oriented, protein-doped matrix crystals. International journal of mass spectrometry and ion processes, 1997. **169**: p. 19-29.
33. Holle, A., Haase, A., Kayser, M., and Hohndorf, J. Optimizing UV laser focus profiles for improved MALDI performance. Journal of Mass Spectrometry, 2006. **41**(6): p. 705-716.
34. Sherrod, S. D., Castellana, E. T., McLean, J. A., and Russell, D. H. Spatially dynamic laser patterning using advanced optics for imaging matrix assisted laser desorption/ionization (MALDI) mass spectrometry. International Journal of Mass Spectrometry, 2007. **262**(3): p. 256-262.
35. Dreisewerd, K., Schürenberg, M., Karas, M., and Hillenkamp, F. Matrix-assisted laser desorption/ionization with nitrogen lasers of different pulse widths. International journal of mass spectrometry and ion processes, 1996. **154**(3): p. 171-178.
36. Vertes, A., Luo, G., Ye, L., Chen, Y., and Marginean, I. Laser pulse length dependence of internal energy transfer in UV-MALDI-MS. Applied Physics A, 2004. **79**(4-6): p. 823-825.
37. Yingling, Y., Conforti, P., and Garrison, B. Theoretical investigation of laser pulse width dependence in a thermal confinement regime. Applied Physics A, 2004. **79**(4-6): p. 757-759.
38. Zhigilei, L. V. and Garrison, B. J. Microscopic mechanisms of laser ablation of organic solids in the thermal and stress confinement irradiation regimes. Journal of Applied Physics, 2000. **88**(3): p. 1281-1298.
39. Knochenmuss, R. and Zhigilei, L. V. Molecular dynamics simulations of MALDI: laser fluence and pulse width dependence of plume characteristics and consequences for matrix and analyte ionization. Journal of Mass Spectrometry, 2010. **45**(4): p. 333-346.
40. Knochenmuss, R. and Vertes, A. Time-delayed 2-pulse studies of MALDI matrix ionization mechanisms. The Journal of Physical Chemistry B, 2000. **104**(23): p. 5406-5410.
41. Tang, X., Sadeghi, M., Olumee, Z., and Vertes, A. Matrix-assisted laser desorption/ionization by two collinear subthreshold laser pulses. Rapid communications in mass spectrometry, 1997. **11**(5): p. 484-488.
42. Fournier, I., Brunot, A., Tabet, J., and Bolbach, G. Delayed extraction experiments using a repulsing potential before ion extraction: evidence of non-covalent clusters as ion precursor in UV matrix-assisted laser desorption/ionization. Part II—Dynamic effects with α-cyano-4-hydroxycinnamic acid matrix. Journal of mass spectrometry, 2005. **40**(1): p. 50-59.
43. Fournier, I., Brunot, A., Tabet, J., and Bolbach, G. Delayed extraction experiments using a repulsive potential before ion extraction: evidence of clusters as ion precursors in UV-MALDI. Part I: dynamical effects with the matrix 2, 5-dihydroxybenzoic acid. International Journal of Mass Spectrometry, 2002. **213**(2): p. 203-215.
44. Glückmann, M. and Karas, M. The initial ion velocity and its dependence on matrix, analyte and preparation method in ultraviolet matrix-assisted laser desorption/ionization. Journal of mass spectrometry, 1999. **34**(5): p. 467-477.
45. Asakawa, D., Sakakura, M., and Takayama, M. Influence of initial velocity of analytes on in-source decay products in MALDI mass spectrometry using salicylic acid derivative matrices. International Journal of Mass Spectrometry, 2013. **337**: p. 29-33.
46. Jaskolla, T. W., Karas, M., Roth, U., Steinert, K., Menzel, C., and Reihs, K. Comparison between vacuum sublimed matrices and conventional dried droplet preparation in MALDI-TOF mass spectrometry. Journal of the American Society for Mass Spectrometry, 2009. **20**(6): p. 1104-1114.
47. Beavis, R. C. and Chait, B. T. Velocity distributions of intact high mass polypeptide molecule ions produced by matrix assisted laser desorption. Chemical physics letters, 1991. **181**(5): p. 479-484.
48. Juhasz, P., Vestal, M. L., and Martin, S. A. On the initial velocity of ions generated by matrix-assisted laser desorption ionization and its effect on the calibration of delayed extraction

time-of-flight mass spectra. Journal of the American Society for Mass Spectrometry, 1997. **8**(3): p. 209-217.
49. Kinsel, G. R., Gimon-Kinsel, M. E., Gillig, K. J., and Russell, D. H. Investigation of the dynamics of matrix-assisted laser desorption/ionization ion formation using an electrostatic analyzer/time-of-flight mass spectrometer. Journal of mass spectrometry, 1999. **34**(6): p. 684-690.
50. Kinsel, G. R., Edmondson, R. D., and Russell, D. H. Profile and Flight Time Analysis of Bovine Insulin Clusters as a Probe of Matrix-assisted Laser Desorption/Ionization Ion Formation Dynamics. Journal of mass spectrometry, 1997. **32**(7): p. 714-722.
51. Karas, M., Bahr, U., Fournier, I., Glückmann, M., and Pfenninger, A. The initial-ion velocity as a marker for different desorption-ionization mechanisms in MALDI. International Journal of Mass Spectrometry, 2003. **226**(1): p. 239-248.
52. Rohlfing, A., Leisner, A., Hillenkamp, F., and Dreisewerd, K. Investigation of the Desorption Process in UV Matrix-Assisted Laser Desorption/Ionization with a Liquid 3-Nitrobenzyl Alcohol Matrix by Photoacoustic Analysis, Fast-Flash Imaging, and UV-Laser Postionization†. The Journal of Physical Chemistry C, 2009. **114**(12): p. 5367-5381.
53. Liang, C. W., Lee, C. H., Lin, Y.-J., Lee, Y. T., and Ni, C. K. MALDI Mechanism of Dihydroxybenzoic Acid Isomers: Desorption of Neutral Matrix and Analyte. The Journal of Physical Chemistry B, 2013. **117**(17): p. 5058-5064.
54. Spengler, B. and Bökelmann, V. Angular and time resolved intensity distributions of laser-desorbed matrix ions. Nuclear Instruments and Methods in Physics Research Section B: Beam Interactions with Materials and Atoms, 1993. **82**(2): p. 379-385.
55. Spengler, B. and Kirsch, D. On the formation of initial ion velocities in matrix-assisted laser desorption ionization: Virtual desorption time as an additional parameter describing ion ejection dynamics. International Journal of Mass Spectrometry, 2003. **226**(1): p. 71-83.
56. Puretzky, A., Geohegan, D., Hurst, G., Buchanan, M., and Luk'yanchuk, B. Imaging of vapor plumes produced by matrix assisted laser desorption: a plume sharpening effect. Physical review letters, 1999. **83**(2): p. 444.
57. Puretzky, A. A. and Geohegan, D. B. LIF imaging and gas-phase diagnostics of laser desorbed MALDI-matrix plumes. Applied surface science, 1998. **127**: p. 248-254.
58. Schmitz, T. A., Koch, J., Gunther, D., and Zenobi, R. Early plume and shock wave dynamics in atmospheric-pressure ultraviolet-laser ablation of different matrix-assisted laser ablation matrices. Journal of Applied Physics, 2011. **109**(12): p. 123106-123106-15.
59. Hillenkamp, F., Karas, M., Holtkamp, D., and Klüsener, P. Energy deposition in ultraviolet laser desorption mass spectrometry of biomolecules. International journal of mass spectrometry and ion processes, 1986. **69**(3): p. 265-276.
60. Spengler, B., Karas, M., Bahr, U., and Hillenkamp, F. Excimer laser desorption mass spectrometry of biomolecules at 248 and 193 nm. Journal of Physical Chemistry, 1987. **91**(26): p. 6502-6506.
61. Fitzgerald, M. C., Parr, G. R., and Smith, L. M. Basic matrixes for the matrix-assisted laser desorption/ionization mass spectrometry of proteins and oligonucleotides. Analytical Chemistry, 1993. **65**(22): p. 3204-3211.
62. Krause, J., Stoeckli, M., and Schlunegger, U. P. Studies on the selection of new matrices for ultraviolet matrix-assisted laser desorption/ionization time-of-flight mass spectrometry. Rapid communications in mass spectrometry, 1996. **10**(15): p. 1927-1933.
63. Wang, X., Han, J., Chou, A., Yang, J., Pan, J., and Borchers, C. H. Hydroxyflavones as a New Family of Matrices for MALDI Tissue Imaging. Analytical chemistry, 2013. **85**(15): p. 7566-7573.

64. Batoy, S., Akhmetova, E., Miladinovic, S., Smeal, J., and Wilkins, C. Developments in MALDI mass spectrometry: the quest for the perfect matrix. Applied Spectroscopy Reviews, 2008. **43**(6): p. 485-550.
65. Strupat, K., Karas, M., and Hillenkamp, F. 2, 5-Dihydroxybenzoic acid: a new matrix for laser desorption--ionization mass spectrometry. International journal of mass spectrometry and ion processes, 1991. **111**: p. 89-102.
66. Eskinja, M., Zollner, P., and Schmid, E. R. Determination of mercapturic acids using 1, 4-dihydroxynaphthalene, a new matrix for matrix-assisted UV laser desorption/ionization mass spectrometry. European Mass Spectrometry, 1998. **4**(3): p. 157-162.
67. Li, J., Inutan, E. D., Wang, B., Lietz, C. B., Green, D. R., Manly, C. D., Richards, A. L., Marshall, D. D., Lingenfelter, S., and Ren, Y. Matrix assisted ionization: new aromatic and nonaromatic matrix compounds producing multiply charged lipid, peptide, and protein ions in the positive and negative mode observed directly from surfaces. Journal of The American Society for Mass Spectrometry, 2012. **23**(10): p. 1625-1643.
68. Nonami, H., Fukui, S., and Erra-Balsells, R. β-Carboline Alkaloids as Matrices for Matrix-assisted Ultraviolet Laser Desorption Time-of-flight Mass Spectrometry of Proteins and Sulfated Oligosaccharides: a Comparative Study Using Phenylcarbonyl Compounds, Carbazoles and Classical Matrices. Journal of mass spectrometry, 1997. **32**(3): p. 287-296.
69. Jespersen, S., Niessen, W., Tjaden, U., and Van der Greef, J. Basic matrices in the analysis of non-covalent complexes by matrix-assisted laser desorption/ionization mass spectrometry. Journal of mass spectrometry, 1998. **33**(11): p. 1088-1093.
70. Beavis, R. C., Chait, B. T., and Fales, H. Cinnamic acid derivatives as matrices for ultraviolet laser desorption mass spectrometry of proteins. Rapid Communications in Mass Spectrometry, 1989. **3**(12): p. 432-435.
71. Porta, T., Grivet, C., Knochenmuss, R., Varesio, E., and Hopfgartner, G. Alternative CHCA-based matrices for the analysis of low molecular weight compounds by UV-MALDI-tandem mass spectrometry. Journal of Mass Spectrometry, 2011. **46**(2): p. 144-152.
72. Godfrey, A., Brenton, A., and Forbes-Robertson, S. Investigating dansyl compounds as novel matrices for matrix-assisted laser desorption/ionisation proteomics. Rapid Communications in Mass Spectrometry, 2010. **24**(1): p. 160-164.
73. Xu, N., Huang, Z.-H., Watson, J. T., and Gage, D. A. Mercaptobenzothiazoles: A new class of matrices for laser desorption ionization mass spectrometry. Journal of the American Society for Mass Spectrometry, 1997. **8**(2): p. 116-124.
74. Meier, M. A., Adams, N., and Schubert, U. S. Statistical approach to understand MALDI-TOFMS matrices: Discovery and evaluation of new MALDI matrices. Analytical chemistry, 2007. **79**(3): p. 863-869.
75. Glückmann, M., Pfenninger, A., Krüger, R., Thierolf, M., Karasa, M., Horneffer, V., Hillenkamp, F., and Strupat, K. Mechanisms in MALDI analysis: surface interaction or incorporation of analytes? International Journal of Mass Spectrometry, 2001. **210**: p. 121-132.
76. Horneffer, V., Glückmann, M., Krüger, R., Karas, M., Strupat, K., and Hillenkamp, F. Matrix–analyte-interaction in MALDI-MS: Pellet and nano-electrospray preparations. International Journal of Mass Spectrometry, 2006. **249**: p. 426-432.
77. Trimpin, S., Räder, H. J., and Müllen, K. Investigations of theoretical principles for MALDI-MS derived from solvent-free sample preparation: Part I. Preorganization. International Journal of Mass Spectrometry, 2006. **253**(1): p. 13-21.
78. Bouschen, W. and Spengler, B. Artifacts of MALDI sample preparation investigated by high-resolution scanning microprobe matrix-assisted laser desorption/ionization (SMALDI) imaging mass spectrometry. International Journal of Mass Spectrometry, 2007. **266**(1): p. 129-137.

79. Luxembourg, S. L., McDonnell, L. A., Duursma, M. C., Guo, X., and Heeren, R. M. Effect of local matrix crystal variations in matrix-assisted ionization techniques for mass spectrometry. Analytical chemistry, 2003. **75**(10): p. 2333-2341.
80. Hanton, S. D., Cornelio Clark, P. A., and Owens, K. G. Investigations of matrix-assisted laser desorption/ionization sample preparation by time-of-flight secondary ion mass spectrometry. Journal of the American Society for Mass Spectrometry, 1999. **10**(2): p. 104-111.
81. Dai, Y., Whittal, R. M., and Li, L. Confocal fluorescence microscopic imaging for investigating the analyte distribution in MALDI matrices. Analytical chemistry, 1996. **68**(15): p. 2494-2500.
82. Griffiths, R. L. and Bunch, J. A survey of useful salt additives in matrix-assisted laser desorption/ionization mass spectrometry and tandem mass spectrometry of lipids: introducing nitrates for improved analysis. Rapid Communications in Mass Spectrometry, 2012. **26**(13): p. 1557-1566.
83. Toh-Boyo, G. M., Wulff, S. S., and Basile, F. Comparison of Sample Preparation Methods and Evaluation of Intra-and Intersample Reproducibility in Bacteria MALDI-MS Profiling. Analytical chemistry, 2012. **84**(22): p. 9971-9980.
84. Kim, S. H., Shin, C. M., and Yoo, J. S. First application of thermal vapor deposition method to matrix-assisted laser desorption ionization mass spectrometry: determination of molecular mass of bis (p-methyl benzylidene) sorbitol. Rapid communications in mass spectrometry, 1998. **12**(11): p. 701-704.
85. Sadeghi, M. and Vertes, A. Crystallite size dependence of volatilization in matrix-assisted laser desorption ionization. Applied surface science, 1998. **127**: p. 226-234.
86. Önnerfjord, P., Ekström, S., Bergquist, J., Nilsson, J., Laurell, T., and Marko-Varga, G. Homogeneous sample preparation for automated high throughput analysis with matrix-assisted laser desorption/ionisation time-of-flight mass spectrometry. Rapid communications in mass spectrometry, 1999. **13**(5): p. 315-322.
87. Gusev, A. I., Wilkinson, W. R., Proctor, A., and Hercules, D. M. Improvement of signal reproducibility and matrix/comatrix effects in MALDI analysis. Analytical Chemistry, 1995. **67**(6): p. 1034-1041.
88. Knochenmuss, R., Karbach, V., Wiesli, U., Breuker, K., and Zenobi, R. The matrix suppression effect in matrix-assisted laser desorption/ionization: application to negative ions and further characteristics. Rapid communications in mass spectrometry, 1998. **12**(9): p. 529-534.
89. McCombie, G. and Knochenmuss, R. Small-molecule MALDI using the matrix suppression effect to reduce or eliminate matrix background interferences. Analytical chemistry, 2004. **76**(17): p. 4990-4997.
90. Wang, B. H., Dreisewerd, K., Bahr, U., Karas, M., and Hillenkamp, F. Gas-phase cationization and protonation of neutrals generated by matrix-assisted laser desorption. Journal of the American Society for Mass Spectrometry, 1993. **4**(5): p. 393-398.
91. Knochenmuss, R. Ion formation mechanisms in UV-MALDI. Analyst, 2006. **131**(9): p. 966-986.
92. Karas, M. and Krüger, R. Ion formation in MALDI: the cluster ionization mechanism. Chemical Reviews, 2003. **103**(2): p. 427-440.
93. Karas, M., Glückmann, M., and Schäfer, J. Ionization in matrix-assisted laser desorption/ionization: singly charged molecular ions are the lucky survivors. Journal of Mass Spectrometry, 2000. **35**(1): p. 1-12.
94. Jaskolla, T. W. and Karas, M. Compelling evidence for lucky survivor and gas phase protonation: The unified MALDI analyte protonation mechanism. Journal of The American Society for Mass Spectrometry, 2011. **22**(6): p. 976-988.
95. Knochenmuss, R. MALDI mechanisms: wavelength and matrix dependence of the coupled photophysical and chemical dynamics model. Analyst, 2013. **139**(1): p. 147-156.

96. Knochenmuss, R. A quantitative model of ultraviolet matrix-assisted laser desorption/ionization including analyte ion generation. Analytical chemistry, 2003. **75**(10): p. 2199-2207.
97. Krüger, R., Pfenninger, A., Fournier, I., Glückmann, M., and Karas, M. Analyte incorporation and ionization in matrix-assisted laser desorption/ionization visualized by pH indicator molecular probes. Analytical chemistry, 2001. **73**(24): p. 5812-5821.
98. Krüger, R. and Karas, M. Formation and fate of ion pairs during MALDI analysis: anion adduct generation as an indicative tool to determine ionization processes. Journal of the American Society for Mass Spectrometry, 2002. **13**(10): p. 1218-1226.
99. Trimpin, S., Wang, B., Inutan, E. D., Li, J., Lietz, C. B., Harron, A., Pagnotti, V. S., Sardelis, D., and McEwen, C. N. A mechanism for ionization of nonvolatile compounds in mass spectrometry: considerations from MALDI and inlet ionization. Journal of The American Society for Mass Spectrometry, 2012. **23**(10): p. 1644-1660.
100. Trimpin, S., Wang, B., Lietz, C. B., Marshall, D. D., Richards, A. L., and Inutan, E. D. New ionization processes and applications for use in mass spectrometry. Critical reviews in biochemistry and molecular biology, 2013. **48**(5): p. 409-429.
101. Karbach, V. and Knochenmuss, R. Do single matrix molecules generate primary ions in ultraviolet matrix-assisted laser desorption/ionization. Rapid communications in mass spectrometry, 1998. **12**(14): p. 968-974.
102. Hoteling, A., Nichols, W., Giesen, D., Lenhard, J., and Knochenmuss, R. Electron transfer reactions in LDI and MALDI: factors influencing matrix and analyte ion intensities. Eur. J. Mass Spectrom, 2006. **12**: p. 345.
103. Setz, P. D. and Knochenmuss, R. Exciton mobility and trapping in a MALDI matrix. The Journal of Physical Chemistry A, 2005. **109**(18): p. 4030-4037.
104. Knochenmuss, R. and Zhigilei, L. V. What determines MALDI ion yields? A molecular dynamics study of ion loss mechanisms. Analytical and bioanalytical chemistry, 2012. **402**(8): p. 2511-2519.
105. Bae, Y. J., Choe, J. C., Moon, J. H., and Kim, M. S. Why do the Abundances of Ions Generated by MALDI Look Thermally Determined? Journal of The American Society for Mass Spectrometry, 2013. **24**(11): p. 1807-1815.
106. Knochenmuss, R. MALDI ionization mechanisms: the coupled photophysical and chemical dynamics model correctly predicts 'temperature'-selected spectra. Journal of Mass Spectrometry, 2013. **48**(9): p. 998-1004.
107. Caprioli, R. M., Farmer, T. B., and Gile, J. Molecular imaging of biological samples: Localization of peptides and proteins using MALDI-TOF MS. Analytical Chemistry, 1997. **69**(23): p. 4751-4760.
108. Schwamborn, K. and Caprioli, R. M. MALDI imaging mass spectrometry–painting molecular pictures. Molecular oncology, 2010. **4**(6): p. 529-538.
109. Sugiura, Y., Shimma, S., and Setou, M. Thin sectioning improves the peak intensity and signal-to-noise ratio in direct tissue mass spectrometry. JOURNAL-MASS SPECTROMETRY SOCIETY OF JAPAN, 2006. **54**(2): p. 45.
110. Carter, C. L., The analysis and imaging of lipids from complex samples by matrix-assisted laser desorption/ionisation mass spectrometry. 2012, University of Birmingham.
111. Schwartz, S. A., Reyzer, M. L., and Caprioli, R. M. Direct tissue analysis using matrix-assisted laser desorption/ionization mass spectrometry: practical aspects of sample preparation. Journal of Mass Spectrometry, 2003. **38**(7): p. 699-708.
112. Page, J. S., Rubakhin, S. S., and Sweedler, J. V. Direct cellular assays using off-line capillary electrophoresis with matrix-assisted laser desorption/ionization time-of-flight mass spectrometry. Analyst, 2000. **125**(4): p. 555-562.

113. Bunch, J., Clench, M. R., and Richards, D. S. Determination of pharmaceutical compounds in skin by imaging matrix-assisted laser desorption/ionisation mass spectrometry. Rapid Communications in Mass Spectrometry, 2004. **18**(24): p. 3051-3060.
114. Goodwin, R. J. Sample preparation for mass spectrometry imaging: Small mistakes can lead to big consequences. Journal of proteomics, 2012. **75**(16): p. 4893-4911.
115. Chen, Y., Allegood, J., Liu, Y., Wang, E., Cachón-González, B., Cox, T. M., Merrill, A. H., and Sullards, M. C. Imaging MALDI mass spectrometry using an oscillating capillary nebulizer matrix coating system and its application to analysis of lipids in brain from a mouse model of Tay-Sachs/Sandhoff disease. Analytical chemistry, 2008. **80**(8): p. 2780-2788.
116. Carter, C. L., McLeod, C. W., and Bunch, J. Imaging of phospholipids in formalin fixed rat brain sections by matrix assisted laser desorption/ionization mass spectrometry. Journal of the American Society for Mass Spectrometry, 2011. **22**(11): p. 1991-1998.
117. Deutskens, F., Yang, J., and Caprioli, R. M. High spatial resolution imaging mass spectrometry and classical histology on a single tissue section. Journal of Mass Spectrometry, 2011. **46**(6): p. 568-571.
118. Schuerenberg, M., Luebbert, C., Deininger, S.-O., Ketterlinus, R., and Suckau, D. MALDI tissue imaging: mass spectrometric localization of biomarkers in tissue slices. Nature Methods, 2007. **4**(5).
119. Mounfield III, W. P. and Garrett, T. J. Automated MALDI matrix coating system for multiple tissue samples for imaging mass spectrometry. Journal of The American Society for Mass Spectrometry, 2012. **23**(3): p. 563-569.
120. Shimma, S., Furuta, M., Ichimura, K., Yoshida, Y., and Setou, M. A novel approach to in situ proteome analysis using chemical inkjet printing technology and MALDI-QIT-TOF tandem mass spectrometer. Journal of the Mass Spectrometry Society of Japan, 2006. **54**(4): p. 133-140.
121. Baluya, D. L., Garrett, T. J., and Yost, R. A. Automated MALDI matrix deposition method with inkjet printing for imaging mass spectrometry. Analytical chemistry, 2007. **79**(17): p. 6862-6867.
122. Cornett, D. S., Frappier, S. L., and Caprioli, R. M. MALDI-FTICR Imaging Mass Spectrometry of Drugs and Metabolites in Tissue. Analytical Chemistry, 2008. **80**(14): p. 5648-5653.
123. Aerni, H.-R., Cornett, D. S., and Caprioli, R. M. Automated acoustic matrix deposition for MALDI sample preparation. Analytical chemistry, 2006. **78**(3): p. 827-834.
124. Hankin, J. A., Barkley, R. M., and Murphy, R. C. Sublimation as a method of matrix application for mass spectrometric imaging. Journal of the American Society for Mass Spectrometry, 2007. **18**(9): p. 1646-1652.
125. Puolitaival, S. M., Burnum, K. E., Cornett, D. S., and Caprioli, R. M. Solvent-free matrix dry-coating for MALDI imaging of phospholipids. Journal of the American Society for Mass Spectrometry, 2008. **19**(6): p. 882-886.
126. Goodwin, R. J., Scullion, P., MacIntyre, L., Watson, D., and Pitt, A. Use of a solvent-free dry matrix coating for quantitative matrix-assisted laser desorption ionization imaging of 4-bromophenyl-1, 4-diazabicyclo (3.2. 2) nonane-4-carboxylate in rat brain and quantitative analysis of the drug from laser microdissected tissue regions. Analytical chemistry, 2010. **82**(9): p. 3868-3873.
127. Murphy, R. C., Hankin, J. A., Barkley, R. M., and Zemski Berry, K. A. MALDI imaging of lipids after matrix sublimation/deposition. Biochimica et Biophysica Acta (BBA)-Molecular and Cell Biology of Lipids, 2011. **1811**(11): p. 970-975.
128. Thomas, A., Charbonneau, J. L., Fournaise, E., and Chaurand, P. Sublimation of new matrix candidates for high spatial resolution imaging mass spectrometry of lipids: Enhanced information in both positive and negative polarities after 1, 5-diaminonapthalene deposition. Analytical Chemistry, 2012. **84**(4): p. 2048-2054.

129. Bouschen, W., Schulz, O., Eikel, D., and Spengler, B. Matrix vapor deposition/recrystallization and dedicated spray preparation for high-resolution scanning microprobe matrix-assisted laser desorption/ionization imaging mass spectrometry (SMALDI-MS) of tissue and single cells. Rapid Communications in Mass Spectrometry, 2010. **24**(3): p. 355-364.
130. Ferguson, L., Bradshaw, R., Wolstenholme, R., Clench, M., and Francese, S. Two-step matrix application for the enhancement and imaging of latent fingermarks. Analytical Chemistry, 2011. **83**(14): p. 5585-5591.
131. Simmons, D. A. Improved MALDI-MS Imaging Performance Using Continuous Laser Rastering. Applied Biosystems Technical Note, 2008.
132. Robichaud, G., Barry, J. A., and Muddiman, D. C. IR-MALDESI Mass Spectrometry Imaging of Biological Tissue Sections Using Ice as a Matrix. Journal of The American Society for Mass Spectrometry, 2014. **25**(3): p. 1-10.
133. Jurchen, J. C., Rubakhin, S. S., and Sweedler, J. V. MALDI-MS imaging of features smaller than the size of the laser beam. Journal of the American Society for Mass Spectrometry, 2005. **16**(10): p. 1654-1659.
134. Caprioli, R. and Spraggins, J. M. High-Speed MALDI-TOF Imaging Mass Spectrometry: Rapid Ion Image Acquisition and Considerations for Next Generation Instrumentation. Journal of the American Society for Mass Spectrometry, 2011. **22**(6): p. 1022-1031.
135. Prideaux, B. and Stoeckli, M. Mass spectrometry imaging for drug distribution studies. Journal of proteomics, 2012. **75**(16): p. 4999-5013.
136. Prideaux, B., Dartois, V. r., Staab, D., Weiner, D. M., Goh, A., Via, L. E., Barry III, C. E., and Stoeckli, M. High-Sensitivity MALDI-MRM-MS Imaging of Moxifloxacin Distribution in Tuberculosis-Infected Rabbit Lungs and Granulomatous Lesions. Analytical Chemistry, 2011. **83**(6): p. 2112-2118.
137. Römpp, A., Guenther, S., Takats, Z., and Spengler, B. Mass spectrometry imaging with high resolution in mass and space (HR2 MSI) for reliable investigation of drug compound distributions on the cellular level. Analytical and bioanalytical chemistry, 2011. **401**(1): p. 65-73.
138. Porta, T., Grivet, C., Kraemer, T., Varesio, E., and Hopfgartner, G. Single hair cocaine consumption monitoring by mass spectrometric imaging. Analytical chemistry, 2011. **83**(11): p. 4266-4272.
139. Stoeckli, M., Staab, D., and Schweitzer, A. Compound and metabolite distribution measured by MALDI mass spectrometric imaging in whole-body tissue sections. International Journal of Mass Spectrometry, 2007. **260**(2): p. 195-202.
140. Angel, P. M. and Caprioli, R. M. Matrix-assisted laser desorption ionization imaging mass spectrometry: in situ molecular mapping. Biochemistry, 2013. **52**(22): p. 3818-3828.
141. Seeley, E. H., Oppenheimer, S. R., Mi, D., Chaurand, P., and Caprioli, R. M. Enhancement of protein sensitivity for MALDI imaging mass spectrometry after chemical treatment of tissue sections. Journal of the American Society for Mass Spectrometry, 2008. **19**(8): p. 1069-1077.
142. Oezdemir, R. F., Gaisa, N. T., Lindemann-Docter, K., Gostek, S., Weiskirchen, R., Ahrens, M., Schwamborn, K., Stephan, C., Pfister, D., and Heidenreich, A. Proteomic tissue profiling for the improvement of grading of noninvasive papillary urothelial neoplasia. Clinical biochemistry, 2012. **45**(1): p. 7-11.
143. Elsner, M., Rauser, S., Maier, S., Schöne, C., Balluff, B., Meding, S., Jung, G., Nipp, M., Sarioglu, H., and Maccarrone, G. MALDI imaging mass spectrometry reveals COX7A2, TAGLN2 and S100-A10 as novel prognostic markers in Barrett's adenocarcinoma. Journal of proteomics, 2012. **75**(15): p. 4693-4704.
144. Stauber, J., MacAleese, L., Franck, J., Claude, E., Snel, M., Kaletas, B. K., Wiel, I. M., Wisztorski, M., Fournier, I., and Heeren, R. On-tissue protein identification and imaging by

MALDI-ion mobility mass spectrometry. Journal of the American Society for Mass Spectrometry, 2010. **21**(3): p. 338-347.
145. Franck, J., El Ayed, M., Wisztorski, M., Salzet, M., and Fournier, I. On-tissue N-terminal peptide derivatizations for enhancing protein identification in MALDI mass spectrometric imaging strategies. Analytical chemistry, 2009. **81**(20): p. 8305-8317.
146. Zemski Berry, K. A., Hankin, J. A., Barkley, R. M., Spraggins, J. M., Caprioli, R. M., and Murphy, R. C. MALDI Imaging of Lipid Biochemistry in Tissues by Mass Spectrometry. Chemical Reviews, 2011. **111**(10): p. 6491-6512.
147. Zaima, N., Sasaki, T., Tanaka, H., Cheng, X. W., Onoue, K., Hayasaka, T., Goto-Inoue, N., Enomoto, H., Unno, N., and Kuzuya, M. Imaging mass spectrometry-based histopathologic examination of atherosclerotic lesions. Atherosclerosis, 2011. **217**(2): p. 427-432.
148. Woods, A. S., Colsch, B., Jackson, S. N., Post, J., Baldwin, K., Roux, A., Hoffer, B., Cox, B. M., Hoffer, M., and Rubovitch, V. Gangliosides and Ceramides Change in a Mouse Model of Blast Induced Traumatic Brain Injury. ACS chemical neuroscience, 2013. **4**(4): p. 594-600.
149. Vrkoslav, V., Muck, A., Cvačka, J., and Svatoš, A. MALDI imaging of neutral cuticular lipids in insects and plants. Journal of the American Society for Mass Spectrometry, 2010. **21**(2): p. 220-231.
150. Passarelli, M. K. and Ewing, A. G. Single-cell imaging mass spectrometry. Current opinion in chemical biology, 2013. **17**(5): p. 854-859.
151. Schober, Y., Guenther, S., Spengler, B., and Römpp, A. Single cell matrix-assisted laser desorption/ionization mass spectrometry imaging. Analytical chemistry, 2012. **84**(15): p. 6293-6297.
152. Hoffmann, E. d. and Stroobant, V., Mass spectrometry : principles and applications. 3rd ed. 2007, Chichester: Wiley. xii, 489 p.
153. Brown, R. S. and Lennon, J. J. Mass resolution improvement by incorporation of pulsed ion extraction in a matrix-assisted laser desorption/ionization linear time-of-flight mass spectrometer. Analytical chemistry, 1995. **67**(13): p. 1998-2003.
154. Mamyrin, B. Time-of-flight mass spectrometry (concepts, achievements, and prospects). International Journal of Mass Spectrometry, 2001. **206**(3): p. 251-266.
155. Stafford Jr, G., Kelley, P., Syka, J., Reynolds, W., and Todd, J. Recent improvements in and analytical applications of advanced ion trap technology. International journal of mass spectrometry and ion processes, 1984. **60**(1): p. 85-98.
156. Koestler, M., Kirsch, D., Hester, A., Leisner, A., Guenther, S., and Spengler, B. A high-resolution scanning microprobe matrix-assisted laser desorption/ionization ion source for imaging analysis on an ion trap/Fourier transform ion cyclotron resonance mass spectrometer. Rapid Communications in Mass Spectrometry, 2008. **22**(20): p. 3275-3285.
157. Soltwisch, J. and Dreisewerd, K. An ultraviolet/infrared matrix-assisted laser desorption ionization sample stage integrating scanning knife-edge and slit devices for laser beam analysis. Rapid Communications in Mass Spectrometry, 2011. **25**(9): p. 1266-1270.
158. Feldhaus, D., Menzel, C., Berkenkamp, S., Hillenkamp, F., and Dreisewerd, K. Influence of the laser fluence in infrared matrix-assisted laser desorption/ionization with a 2.94 µm Er: YAG laser and a flat-top beam profile. Journal of Mass Spectrometry, 2000. **35**(11): p. 1320-1328.
159. Wenzel, R. J. and Prather, K. A. Improvements in ion signal reproducibility obtained using a homogeneous laser beam for on-line laser desorption/ionization of single particles. Rapid Communications in Mass Spectrometry, 2004. **18**(13): p. 1525-1533.
160. Farkas, B. and Geretovszky, Z. On determining the spot size for laser fluence measurements. Applied surface science, 2006. **252**(13): p. 4728-4732.
161. Shrivastava, B., Benerji, N., Bhatnagar, P., Vora, H., and Nundy, U. Development of automated ultraviolet laser beam profiling system using fluorometric technique.

International Conference in Photonics 2004; Available from: http://een.iust.ac.ir/profs/sadr/Papers/disp19.pdf.
162. Häkkänen, H. and Korppi-Tommola, J. Laser-induced fluorescence imaging of paper surfaces. Applied spectroscopy, 1993. **47**(12): p. 2122-2125.
163. Hollands, C. The Animals (scientific procedures) Act 1986. The Lancet, 1986. **328**(8497): p. 32-33.
164. Race, A. M., Styles, I. B., and Bunch, J. Inclusive sharing of mass spectrometry imaging data requires a converter for all. Journal of Proteomics, 2012. **75**(16): p. 5111-5112.
165. Clench, M. R., Trim, P. J., Djidja, M. C., Atkinson, S. J., Oakes, K., Cole, L. M., Anderson, D. M. G., Hart, P. J., and Francese, S. Introduction of a 20 kHz Nd:YVO4 laser into a hybrid quadrupole time-of-flight mass spectrometer for MALDI-MS imaging. Analytical and Bioanalytical Chemistry, 2010. **397**(8): p. 3409-3419.
166. Moskovets, E. and Vertes, A. Fast dynamics of ionization in ultraviolet matrix-assisted laser desorption ionization of biomolecules. The Journal of Physical Chemistry B, 2002. **106**(12): p. 3301-3306.
167. Niederhofer, J. DPSS UV Lasers: Improve Mass Spectrometry and Laser Microdissection. Biophotonics International 2006 January 2006]; Available from: http://assets.newport.com/webDocuments-EN/images/12195.PDF.
168. Amadei, G. A., Cho, C. F., Lewis, J. D., and Luyt, L. G. A fast, reproducible and low cost method for sequence deconvolution of 'on bead'peptides via 'on target'maldi TOF/TOF mass spectrometry. Journal of Mass Spectrometry, 2010. **45**(3): p. 241-251.
169. Jackson, S. N., Colsch, B., Egan, T., Lewis, E. K., Schultz, J. A., and Woods, A. S. Gangliosides' analysis by MALDI-ion mobility MS. Analyst, 2010. **136**: p. 463-466.
170. Sundarapandian, S., May, J. C., and McLean, J. A. Dual Source Ion Mobility-Mass Spectrometer for Direct Comparison of Electrospray Ionization and MALDI Collision Cross Section Measurements. Analytical Chemistry, 2010. **82**(8): p. 3247-3254.
171. Moskovets, E., Preisler, J., Chen, H. S., Rejtar, T., Andreev, V., and Karger, B. L. High-throughput axial MALDI-TOF MS using a 2-kHz repetition rate laser. Analytical Chemistry, 2006. **78**(3): p. 912-919.
172. McLean, J. A., Russell, W. K., and Russell, D. H. A high repetition rate (1 kHz) microcrystal laser for high throughput atmospheric pressure MALDI-quadrupole-time-of-flight mass spectrometry. Analytical Chemistry, 2003. **75**(3): p. 648-654.
173. Murphy, R. C. and Hankin, J. A. Relationship between MALDI IMS Intensity and Measured Quantity of Selected Phospholipids in Rat Brain Sections. Analytical Chemistry, 2010. **82**(20): p. 8476-8484.
174. Folch, J., Lees, M., and Stanley, G. H. S. A Simple Method for the Isolation and Purification of Total Lipides from Animal Tissues. Journal of Biological Chemistry, 1957. **226**(1): p. 497-509.
175. Steven, R. T., Race, A. M., and Bunch, J. Para-Nitroaniline is a promising matrix for MALDI-MS imaging on intermediate pressure MS systems. Journal of The American Society for Mass Spectrometry, 2013. **24**(5): p. 801-804.
176. Griffiths, R. L. and Bunch, J. A survey of useful salt additives in matrix-assisted laser desorption/ionization mass spectrometry and tandem mass spectrometry of lipids: introducing nitrates for improved analysis. Rapid Communications in Mass Spectrometry, 2012. **26**(13): p. 1557-1566.
177. Jackson, S. N., Ugarov, M., Egan, T., Post, J. D., Langlais, D., Albert Schultz, J., and Woods, A. S. MALDI-ion mobility-TOFMS imaging of lipids in rat brain tissue. Journal of Mass Spectrometry, 2007. **42**(8): p. 1093-1098.
178. Jackson, S. N., Ugarov, M., Post, J. D., Egan, T., Langlais, D., Schultz, J. A., and Woods, A. S. A study of phospholipids by ion mobility TOFMS. Journal of the American Society for Mass Spectrometry, 2008. **19**(11): p. 1655-1662.

179. Wang, H. Y. J., Liu, C. B., Wu, H. W., and Kuo, J. S. Direct profiling of phospholipids and lysophospholipids in rat brain sections after ischemic stroke. Rapid Communications in Mass Spectrometry, 2010. **24**(14): p. 2057-2064.
180. Horneffer, V., Dreisewerd, K., Ludemann, H. C., Hillenkamp, F., Lage, M., and Strupat, K. Is the incorporation of analytes into matrix crystals a prerequisite for matrix-assisted laser desorption/ionization mass spectrometry? A study of five positional isomers of dihydroxybenzoic acid. International Journal of Mass Spectrometry, 1999. **187**: p. 859-870.
181. Jackson, S. N., Wang, H. Y. J., and Woods, A. S. In situ structural characterization of phosphatidylcholines in brain tissue using MALDI-MS/MS. Journal of the American Society for Mass Spectrometry, 2005. **16**(12): p. 2052-2056.
182. Sugiura, Y. and Setou, M. Selective imaging of positively charged polar and nonpolar lipids by optimizing matrix solution composition. Rapid Communications in Mass Spectrometry, 2009. **23**(20): p. 3269-3278.
183. Goodwin, R. J. A., Pitt, A. R., Harrison, D., Weidt, S. K., Langridge Smith, P. R. R., Barrett, M. P., and Logan Mackay, C. Matrix free mass spectrometric imaging using laser desorption ionisation Fourier transform ion cyclotron resonance mass spectrometry. Rapid Communications in Mass Spectrometry, 2011. **25**(7): p. 969-972.
184. Shanta, S. R., Zhou, L. H., Park, Y. S., Kim, Y. H., Kim, Y., and Kim, K. P. Binary Matrix for MALDI Imaging Mass Spectrometry of Phospholipids in Both Ion Modes. Analytical Chemistry, 2011. **83**(4): p. 1252-1259.
185. Shrivas, K., Hayasaka, T., Goto-Inoue, N., Sugiura, Y., Zaima, N., and Setou, M. Ionic matrix for enhanced MALDI imaging mass spectrometry for identification of phospholipids in mouse liver and cerebellum tissue sections. Analytical Chemistry, 2010. **82**(21): p. 8800-8806.
186. Wang, H.-Y. J., Wu, H.-W., Tsai, P.-J., and Liu, C. B. MALDI-mass spectrometry imaging of desalted rat brain sections reveals ischemia-mediated changes of lipids. Analytical and bioanalytical chemistry, 2012. **404**(1): p. 113-124.
187. Zhang, J. and Zenobi, R. Matrix-dependent cationization in MALDI mass spectrometry. Journal of Mass Spectrometry, 2004. **39**(7): p. 808-816.
188. Luo, G., Marginean, I., and Vertes, A. Internal energy of ions generated by matrix-assisted laser desorption/ionization. Analytical Chemistry, 2002. **74**(24): p. 6185-6190.
189. Luo, G., Marginean, I., Ye, L., and Vertes, A. Competing ion decomposition channels in matrix-assisted laser desorption ionization. The Journal of Physical Chemistry B, 2008. **112**(23): p. 6952-6956.
190. Campbell, J. M., Vestal, M. L., Blank, P. S., Stein, S. E., Epstein, J. A., and Yergey, A. L. Fragmentation of leucine enkephalin as a function of laser fluence in a MALDI TOF-TOF. Journal of the American Society for Mass Spectrometry, 2007. **18**(4): p. 607-616.
191. Knochenmuss, R. and Zenobi, R. MALDI ionization: the role of in-plume processes. Chemical Reviews, 2003. **103**(2): p. 441-452.
192. Tarzi, O. I., Nonami, H., and Erra-Balsells, R. The effect of temperature on the stability of compounds used as UV-MALDI-MS matrix: 2, 5-dihydroxybenzoic acid, 2, 4, 6-trihydroxyacetophenone, α-cyano-4-hydroxycinnamic acid, 3, 5-dimethoxy-4-hydroxycinnamic acid, nor-harmane and harmane. Journal of Mass Spectrometry, 2009. **44**(2): p. 260-277.
193. Koubenakis, A., Frankevich, V., Zhang, J., and Zenobi, R. Time-resolved surface temperature measurement of MALDI matrices under pulsed UV laser irradiation. The Journal of Physical Chemistry A, 2004. **108**(13): p. 2405-2410.
194. Palmer, A. D., Griffiths, R., Styles, I., Claridge, E., Calcagni, A., and Bunch, J. Sucrose cryo-protection facilitates imaging of whole eye sections by MALDI mass spectrometry. Journal of Mass Spectrometry, 2012. **47**(2): p. 237-241.

195. Vidová, V., Pól, J., Volný, M., Novák, P., Havlíček, V., Wiedmer, S. K., and Holopainen, J. M. Visualizing spatial lipid distribution in porcine lens by MALDI imaging high-resolution mass spectrometry. Journal of lipid research, 2010. **51**(8): p. 2295-2302.
196. Cerruti, C. D., Benabdellah, F., Laprévote, O., Touboul, D., and Brunelle, A. MALDI Imaging and Structural Analysis of Rat Brain Lipid Negative Ions with 9-Aminoacridine Matrix. Analytical Chemistry, 2012. **84**(5): p. 2164-2171.
197. Veloso, A., Astigarraga, E., Barreda-Gómez, G., Manuel, I., Ferrer, I., Teresa Giralt, M., Ochoa, B., Fresnedo, O., Rodríguez-Puertas, R., and Fernández, J. A. Anatomical Distribution of Lipids in Human Brain Cortex by Imaging Mass Spectrometry. Journal of the American Society for Mass Spectrometry, 2011. **22**(2): p. 329-338.
198. Le, C. H., Han, J., and Borchers, C. H. Dithranol as a MALDI Matrix for Tissue Imaging of Lipids by Fourier Transform Ion Cyclotron Resonance Mass Spectrometry. Analytical Chemistry, 2012. **84**(19): p. 8391-8398.
199. Jackson, S. N., Wang, H. Y. J., and Woods, A. S. In situ structural characterization of glycerophospholipids and sulfatides in brain tissue using MALDI-MS/MS. Journal of the American Society for Mass Spectrometry, 2007. **18**(1): p. 17-26.
200. Marto, J. A., White, F. M., Seldomridge, S., and Marshall, A. G. Structural characterization of phospholipids by matrix-assisted laser desorption/ionization Fourier transform ion cyclotron resonance mass spectrometry. Analytical Chemistry, 1995. **67**(21): p. 3979-3984.
201. Estrada, R. and Yappert, M. C. Alternative approaches for the detection of various phospholipid classes by matrix-assisted laser desorption/ionization time-of-flight mass spectrometry. Journal of Mass Spectrometry, 2004. **39**(4): p. 412-422.
202. Rujoi, M., Estrada, R., and Yappert, M. C. In situ MALDI-TOF MS regional analysis of neutral phospholipids in lens tissue. Analytical Chemistry, 2004. **76**(6): p. 1657-1663.
203. Estrada, R. and Yappert, M. C. Regional phospholipid analysis of porcine lens membranes by matrix-assisted laser desorption/ionization time-of-flight mass spectrometry. Journal of Mass Spectrometry, 2004. **39**(12): p. 1531-1540.
204. Astigarraga, E., Barreda-Gómez, G., Lombardero, L., Fresnedo, O., Castaño, F., Giralt, M. T., Ochoa, B., Rodríguez-Puertas, R., and Fernández, J. A. Profiling and imaging of lipids on brain and liver tissue by matrix-assisted laser desorption/ionization mass spectrometry using 2-mercaptobenzothiazole as a matrix. Analytical Chemistry, 2008. **80**(23): p. 9105-9114.
205. Fernández, J., Ochoa, B., Fresnedo, O., Giralt, M., and Rodríguez-Puertas, R. Matrix-assisted laser desorption ionization imaging mass spectrometry in lipidomics. Analytical and Bioanalytical Chemistry, 2011. **401**(1): p. 29-51.
206. Garrett, T. J., Prieto-Conaway, M. C., Kovtoun, V., Bui, H., Izgarian, N., Stafford, G., and Yost, R. A. Imaging of small molecules in tissue sections with a new intermediate-pressure MALDI linear ion trap mass spectrometer. International Journal of Mass Spectrometry, 2007. **260**(2): p. 166-176.
207. Goodwin, R. J. A., Mackay, C. L., Nilsson, A., Harrison, D. J., Farde, L., Andren, P. E., and Iverson, S. L. Qualitative and quantitative MALDI imaging of the positron emission tomography ligands raclopride (a D2 dopamine antagonist) and SCH 23390 (a D1 dopamine antagonist) in rat brain tissue sections using a solvent-free dry matrix application method. Analytical Chemistry, 2011. **83**(24): p. 9694-9701.
208. Veloso, A., Fernández, R., Astigarraga, E., Barreda-Gómez, G., Manuel, I., Giralt, M. T., Ferrer, I., Ochoa, B., Rodríguez-Puertas, R., and Fernández, J. A. Distribution of lipids in human brain. Analytical and Bioanalytical Chemistry, 2011. **401**(1): p. 89-101.
209. Wiseman, J. M., Puolitaival, S. M., Takáts, Z., Cooks, R. G., and Caprioli, R. M. Mass spectrometric profiling of intact biological tissue by using desorption electrospray ionization. Angewandte Chemie, 2005. **117**(43): p. 7256-7259.

210. Römpp, A., Guenther, S., Schober, Y., Schulz, O., Takats, Z., Kummer, W., and Spengler, B. Histology by Mass Spectrometry: Label-Free Tissue Characterization Obtained from High-Accuracy Bioanalytical Imaging. Angewandte chemie international edition, 2010. **49**(22): p. 3834-3838.
211. Ridenour, W. B., Kliman, M., McLean, J. A., and Caprioli, R. M. Structural characterization of phospholipids and peptides directly from tissue sections by MALDI traveling-wave ion mobility-mass spectrometry. Analytical Chemistry, 2010. **82**(5): p. 1881-1889.
212. Hsu, F. F. and Turk, J. Electrospray ionization/tandem quadrupole mass spectrometric studies on phosphatidylcholines: The fragmentation processes. Journal of the American Society for Mass Spectrometry, 2003. **14**(4): p. 352-363.
213. Lorkiewicz, P. and Cecilia Yappert, M. 2-(2-Aminoethylamino)-5-nitropyridine as a basic matrix for negative-mode matrix-assisted laser desorption/ionization analysis of phospholipids. Journal of Mass Spectrometry, 2009. **44**(1): p. 137-143.
214. Chughtai, S., Chughtai, K., Pastor, B. C., Kiss, A., Agrawal, P., MacAleese, L., and Heeren, R. A multimodal mass spectrometry imaging approach for the study of musculoskeletal tissues. International Journal of Mass Spectrometry, 2012. **325**: p. 150-160.
215. Matusch, A., Fenn, L. S., Depboylu, C., Klietz, M., Strohmer, S., McLean, J. A., and Becker, J. S. Combined Elemental and Biomolecular Mass Spectrometry Imaging for Probing the Inventory of Tissue at a Micrometer Scale. Analytical Chemistry, 2012. **84**(7): p. 3170-3178.
216. Eberlin, L. S., Liu, X., Ferreira, C. R., Santagata, S., Agar, N. Y. R., and Cooks, R. G. Desorption electrospray ionization then MALDI mass spectrometry imaging of lipid and protein distributions in single tissue sections. Analytical Chemistry, 2011. **83**(22): p. 8366-8371.
217. Amstalden van Hove, E. R., Smith, D. F., and Heeren, R. A concise review of mass spectrometry imaging. Journal of Chromatography A, 2010. **1217**(25): p. 3946-3954.
218. Al-Saad, K. A., Siems, W. F., Hill, H., Zabrouskov, V., and Knowles, N. R. Structural analysis of phosphatidylcholines by post-source decay matrix-assisted laser desorption/ionization time-of-flight mass spectrometry. Journal of the American Society for Mass Spectrometry, 2003. **14**(4): p. 373-382.
219. Stübiger, G. and Belgacem, O. Analysis of lipids using 2, 4, 6-trihydroxyacetophenone as a matrix for MALDI mass spectrometry. Analytical Chemistry, 2007. **79**(8): p. 3206-3213.
220. Khatib-Shahidi, S., Andersson, M., Herman, J. L., Gillespie, T. A., and Caprioli, R. M. Direct molecular analysis of whole-body animal tissue sections by imaging MALDI mass spectrometry. Analytical Chemistry, 2006. **78**(18): p. 6448-6456.
221. Alzate, O., Neuroproteomics. 2009: CRC.
222. Yagnik, G. B., Korte, A. R., and Lee, Y. J. Multiplex mass spectrometry imaging for latent fingerprints. Journal of Mass Spectrometry, 2013. **48**(1): p. 100-104.
223. Steven, R., Race, A., and Bunch, J. para-Nitroaniline is a Promising Matrix for MALDI-MS Imaging on Intermediate Pressure MS Systems. Journal of The American Society for Mass Spectrometry, 2013. **24**(5): p. 801-804.
224. Steven, R. and Bunch, J. Repeat MALDI MS imaging of a single tissue section using multiple matrices and tissue washes. Analytical and Bioanalytical Chemistry, 2013. **405**(14): p. 4719-4728.
225. Crecelius, A. C., Cornett, D. S., Caprioli, R. M., Williams, B., Dawant, B. M., and Bodenheimer, B. Three-dimensional visualization of protein expression in mouse brain structures using imaging mass spectrometry. Journal of the American Society for Mass Spectrometry, 2005. **16**(7): p. 1093-1099.